The Pennsylvania State University

The Graduate School

Department of Aerospace Engineering

TRANSFER AND CAPTURE INTO DISTANT RETROGRADE ORBITS

A Dissertation in

Aerospace Engineering

by

Christopher J. Scott

© 2010 Christopher J. Scott

Submitted in Partial Fulfillment
of the Requirements
for the Degree of

Doctor of Philosophy

May 2010

The dissertation of Christopher J. Scott was reviewed and approved* by the following:

David B. Spencer
Associate Professor of Aerospace Engineering
Thesis Advisor
Chair of Committee

Robert G. Melton
Professor of Aerospace Engineering

Jack W. Langelaan
Assistant Professor of Aerospace Engineering

Joseph P. Cusumano
Professor of Engineering Science and Mechanics

George A. Lesieutre
Professor of Aerospace Engineering, Head of the Department of Aerospace Engineering

*Signatures are on file in the Graduate School

ABSTRACT

This dissertation utilizes theory and techniques derived from the fields of dynamical systems theory, astrodyanamics, celestial mechanics, and fluid mechanics to analyze the phenomenon of satellite capture and interrelated spacecraft transfers in restricted three-body systems. The results extend current knowledge and understanding of capture dynamics in the context of astrodynamics and celestial mechanics.

Manifold theory, fast Lyapunov indicator maps, and the classification of space structure facilitate an analysis of the transport of objects from the chaotic reaches of the solar system to the distant retrograde region in the sun-Jupiter system. Apart from past studies this dissertation considers the role of the complex lobe structure encompassing stable regions in the circular restricted three-body problem. These structures are shown to be responsible for the phenomenon of sticky orbits and the transport of objects among stable regions. Since permanent capture can only be achieved through a change in energy, fast Lyapunov indicator maps and other methods which reveal the structure of the conservative system are used to discern capture regions and identify the underpinnings of the dynamics. Fast Lyapunov indicator maps provide an accurate classification of orbits of permanent capture and escape, yet monopolize computational resources. In anticipation of a fully three-dimensional analysis in the dissipative system a new mapping parameter is introduced based on energy degradation and averaged velocity. Although the study specifically addresses the sun-Jupiter system, the qualitative results and devised techniques can be applied throughout the solar system and to capture about extrasolar planets.

Extending the analysis beyond the exterior of the stable distant retrograde region fosters the construction of transfer orbits from low-Earth orbit to a stable periodic orbit at the center of the stable distant retrograde region. Key to this analysis is the predictability of collision orbits within the highly chaotic region commonly recognized as a saddle point on the energy manifold.

The pragmatic techniques derived from this analysis solve a number of complications apparent in the literature. Notably a reliable methodology for the construction of an arbitrary number of transfer orbits circumvents the requirement of computing specialized periodic orbits or extensive numerical sampling of the phase space. The procedure provides a complete description of the design space accessing a wide range of distant retrograde orbits sizes, insertion points, and parking orbit altitudes in an automated manner. The transfers are studied in a similar fashion to periodic orbits unveiling the intimate relationship among design parameters and phase space structure. An arbitrary number of Earth return periodic orbits can be generated as a by-product. These orbits may be useful for spacecraft that must make a number of passes near the second primary without a reduction in energy.

Further analysis of the lobe dynamics and a modification of the transfers to the center of the stable region yields sets of single impulse transfers to sticky distant retrograde orbits. It is shown that the evolution of the phase space structures with energy corresponds to the variation of capture time and target size. Capture phenomenon is related to the stability characteristics of the unstable periodic orbit and the geometry of the corresponding homoclinic tangle at various energies. Future spacecraft with little or no propulsive means may take advantage of these natural trajectories for operations in the region.

Temporary capture along a sticky orbit may come before incremental stabilization of the spacecraft by way of a series of small impulsive or a low continuous thrust maneuvers. The requirements of small stabilization maneuver are calculated and compared to a direct transfer to the center of stable region. This mission design may be desirable as any failure in the classic set of maneuvers to the center of the stable region could result in the loss of the spacecraft. A simple low-thrust stabilization method is analyzed in a similar manner to nebular drag. It is shown that stabilization maneuvers initiated within the sticky region can be achieved via a simple control law. Moreover, the sticky region can be used as a staging point for both spiral-in and spiral-out

maneuvers. For the spiral in maneuver this negates a large, initial maneuver required to reach the center of the stable region. It is shown that large lengths of orbits exist within the sticky regions which reliably lead to permanent capture. In the case of spiral-out the spacecraft is transported to a highly energetic yet stable orbit about the second primary. From here a small maneuver could allow the spacecraft to access other regions of the solar system.

TABLE OF CONTENTS

LIST OF FIGURES viii

LIST OF TABLES xii

ACKNOWLEDGEMENTS xiii

Chapter 1 Introduction 1

- Historical Background 4
- Contribution and Document Organization 10
- References 15

Chapter 2 Theory 19

- The Circular Restricted Three-Body Problem 19
  - Equations of Motion 20
  - Symmetry of Solutions 27
  - Equilibrium Points 29
  - The Jacobi Integral and Hill's Regions 35
  - Symmetric, Planar-Periodic Orbits 38
- The Kolmogorov-Arnold-Moser (KAM) Theorem 41
- Area Preserving Maps and the Poincaré-Birkoff Fixed Point Theorem 44
- The Lyapunov Exponent and the Fast Lyapunov Indicator 50
  - The State Transition Matrix and the Maximum Lyapunov Exponent 51
  - Fast Lyapunov Indicator 56
- The Mean FLI and Practical Implementation 59
- Relevance 71
- References 72

Chapter 3 Satellite Capture and Transport in the Outer Solar System 75

- Background 76
- Dynamical Analysis 79
  - Capture Distributions 82
  - The Capture Process 94
- Summary and Extension 117
- References 119

Chapter 4 Transfers to Periodic Distant Retrograde Orbits 122

- Phase Space Analysis 125
- Initial Guess 134
- Predictor-Corrector Algorithms 137
  - Predictor-Corrector for Transfers to the *x*-axis 137
  - Predictor-Corrector for Variable Parking Orbit Altitudes 142
  - Predictor-Corrector for Variable Insertion Points 143

Application and Results 145
Transfers Terminating on the *x*-axis 145
Earth Return Periodic Orbits 158
Variable Parking Orbit Altitude 161
Variable Insertion Points 165
Summary and Extension 174
References 177

Chapter 5 Transfers to Sticky Distant Retrograde Orbits 179

Differential Correction 182
Phase Space Structure 184
The Role of the BUPO and its Manifolds 192
Monte Carlo Simulations 192
Stability Index 196
Single Impulse Transfers 198
Transfer Characteristics 199
Capture 205
Stabilization Maneuver to a Quasi-Periodic Orbit 213
Low-Thrust Stabilization 217
Summary and Extension 227
References 230

Chapter 6 Conclusion 233

Appendix 236

Chapter 4 Variables 236
Chapter 5 Variables 238

LIST OF FIGURES

Figure **1-1**: Heliocentric velocity of the Voyager 2 spacecraft as a function of radial distance from the sun 5

Figure **1-2**: Halo oribt about the Earth-Moon L_1 equilibrium point 7

Figure **1-3**: Artist's interpretation of the IPS. 9

Figure **2-1**: CR3BP in the inertial reference frame 21

Figure **2-2**: The CR3BP in a rotating reference frame 24

Figure **2-3**: The CR3BP and its equilibrium points 29

Figure **2-4**: Local phase portraits in the u_1-v_1, u_2-v_2, and u_3-v_3 planes 32

Figure **2-5**: Hill's region(s) for increasing values of Jacobi constant 37

Figure **2-6**: Unperturbed twist map 48

Figure **2-7**: Perturbed twist map 48

Figure **2-8**: *F* subjected to mapping 49

Figure **2-9**: Representation of a Hyperbolic Point in Two-Dimensional Space 61

Figure **2-10**: Forward and backward FLI maps showing the stable and unstable manifolds, respectively 62

Figure **2-11**: Mean FLI map of the region shown in Fig. 2-10 63

Figure **2-12**: Sketch and computation of the basins of attraction 64

Figure **2-13**: Unstable limit cycle of the forced Duffing oscillator 66

Figure **2-14**: Progression of FLI maps for the forced Duffing oscillator 67

Figure **2-15**: Progression of FLI maps for the forced Duffing oscillator after homoclinic bifurcation 69-70

Figure **3-1**: Typical orbits within the distant retrograde region. 81

Figure **3-2**: Mapping of Monte Carlo simulations. 83

Figure **3-3**: The distribution of semi-major axis and eccentricity about the Jupiter of the BUPO and surviving particles....85

Figure **3-4**: Mapping of the first and last *x*-axis crossings of an assortment of particles surviving 95 years against a mean FLI stability map....86

Figure **3-5**: Demonstration of capture and escape mechanism....88

Figure **3-6**: Distribution of semi-major axis and eccentricity for particles surviving a simulation of 100 Jupiter years....90

Figure **3-7**: Distribution of sun-centered unstable periodic orbits bounding stable regions...91

Figure **3-8**: Resonant periodic orbits in physical space....92-93

Figure **3-9**: FLI map of *C* versus *x* for orbits satisfying the mirror theorem....95

Figure **3-10**: Collision map in the sun-Jupiter system....96

Figure **3-11**: Maps of collisions and manifolds near the distant retrograde region....98

Figure **3-12**: Mean FLI map demonstrating a high-energy, direct transport from the 4:3 resonance region to the distant retrograde region....99

Figure **3-13**: Direct transport trajectory from the 4:3 resonance region to the distant retrograde region....101

Figure **3-14**: Close-up of the distant retrograde region on a mean FLI map....102

Figure **3-15**: Close-up of the right-most hyperbolic point in Fig.3-14 showing the homoclinic tangle....104

Figure **3-16**: Forward FLI maps of the distant retrograde region for a variety of drag parameters....108

Figure **3-17**: Forward FLI maps of the distant retrograde region for a variety of drag parameters....110

Figure **3-18**: Capture and escape orbits over a time-span 150 TU subjected to drag....111

Figure **3-19**: Close up the capture region using a map of $\langle v^2 \rangle$ values with γ=7×10^{-5}....112

Figure **3-20**: $\langle v^2 \rangle$ maps of the distant retrograde region for drag parameters of 7×10^{-6}, 7×10^{-5}, and 7×10^{-4}....113

Figure **3-21**: The migration of a particle over a period of 2000 TU or 3800 years....114

Figure **3-22**: Mean FLI map of the 4:3 resonance region....116

Figure **3-23**: Mean FLI map with an expanded view of the distant retrograde, 4:3, and 3:2 resonant islands 117

Figure **4-1**: Orbits and maps of the distant retrograde region 128-129

Figure **4-2**: Collision maps over a period of one and two years 131

Figure **4-3**: Initial guess for the predictor-corrector algorithm 136

Figure **4-4**: F1 transfers at C=-1.5001, -1.4997, -1.499, and -1.496 141

Figure **4-5**: F1 transfers starting from unadjusted parking orbit altitudes of 250, 500, 1000, and 2000 km 143

Figure **4-6**: F1 transfers to insertion points of α=7, 91, 178, and 274 deg. 145

Figure **4-7**: Termination point of five families of transfer orbits versus Jacobi constant 147

Figure **4-8**: F1-5 transfers at a Jacobi constant of -1.5 148

Figure **4-9**: SPDROs of sizes 5, 10, 15, 20, 25, and 30 M km 149

Figure **4-10**: Variation of ΔV_T and transfer time with SPDRO size 151

Figure **4-11**: ΔV_1 and ΔV_2 versus SPDRO size. 152

Figure **4-12**: ΔV_2 as percentage of ΔV_T. 153

Figure **4-13**: Termination point of five families of transfer orbits 155

Figure **4-14**: Evolution of phase space structure with energy 157

Figure **4-15**: Variation of Vx_o with energy for each transfer family 158

Figure **4-16**: Unstable periodic orbits, Earth return orbits, corresponding to the F1-5 transfers 160

Figure **4-17**: Variation of ΔV_T with unadjusted parking orbit altitude 162

Figure **4-18**: Variation of transfer time with unadjusted parking orbit altitude for an F1 transfer to a 20 M km. SPDRO 164

Figure **4-19**: Transfer characteristics versus insertion point. 167

Figure **4-20** Evolution of transfer orbits at high gradients 169

Figure **4-21**: Variation of transfer time and ΔV with insertion point for a 30×10^6 km SPDRO 170

Figure **4-22**: Percent change in transfer time and ΔV_T at insertion points corresponding to the minimum transfer time relative to transfers terminating on the *x*-axis 171

Figure **4-23**: Geometry and evolution of F2 transfers.....173

Figure **5-1**: F1 and F2 transfers terminating on the *x*-axis at the indicated terminal velocities 184

Figure **5-2**: Orbits, FLI map, and phase space structure near the distant retrograde region ...186

Figure **5-3**: Backward collision maps over a period of two years.....188

Figure **5-4**: Phase space structure and transfer families.....191

Figure **5-5**: Monte Carlo simulation in the sun-Earth system.....195

Figure **5-6**: Stability index versus Jacobi constant for the BUPO 197

Figure **5-7**: Continuations of the F1-5 with maps of the manifolds of the BUPO at various energies.....200-201

Figure **5-8**: ΔV versus final Jacobi constant for all single impulse transfers 203

Figure **5-9**: Transfer time versus *x* and *Vx* for single impulse transfers.....204

Figure **5-10**: Variation of capture time with *x*-position for F5 transfers.....207-208

Figure **5-11**: Variation of capture time with *x*-position for F1-4 209-210

Figure **5-12**: Approximate amplitude along *x*-axis of temporarily captures orbits with energy.....211

Figure **5-13**: Extended capture orbits.....213

Figure **5-14**: Impulsive stabilizing maneuver from *C*=-1.4997 215

Figure **5-15**: Impulsive stabilizing maneuver from *C*=-1.499 216

Figure **5-16**: Low-thrust stabilizing maneuver starting from *C*=-1.5001.....221

Figure **5-17**: Spiral-down transfer starting from *C*=-1.4997.....223

Figure **5-18**: Low-thrust stabilizing maneuver starting from *C*=-1.4997.....225

Figure **5-19**: Evolution of capture region with thrust magnitude starting from *C*=-1.4997....226

Figure **5-20**: Low-thrust stabilizing maneuver starting from *C*=-1.499.....227

LIST OF TABLES

Table **2-1**: DOF versus dimension of phase space, energy shell, and tori... 44

ACKNOWLEDGEMENTS

Throughout the years, many have selflessly contributed to my education. I hope that this work at least partially meets their expectations. I will strive to live a life worthy of their efforts.

Julianna Ondecko taught, and continues to teach, algebra at Glendale Jr./Sr. High School. I doubt she recalls a quiet student like me, but I remember her quite well. She had the challenging task of delivering abstract fundamentals to an unwieldy group of 8th and 9th graders. The class contained students who were destined to become secretaries, soldiers, counselors, auto-mechanics, doctors, engineers, drug addicts, and even criminals. Despite its eclectic composition, she refused to lower the standards of the class. If she is ever to read this, I ask that she tell her students that with hard work they are capable of accomplishments greater than this.

Besides my parents, Thomas Terza was the first individual who I felt believed in my potential. He went above and beyond to reach not only me, but all students who he thought he could help. He taught calculus and geometry with a style that managed to be highly entertaining, humorous, strict, intriguing, and, most importantly, effective all at the same time. Both my father and I had the privilege of sitting in his classroom. He will live on through his students as I am confident none will forget him.

Richard Burmeister was also one of my father's teachers in high school. Many years later he introduced me to both chemistry and physics at level much higher than one would expect in a rural high school. He was my first mentor many times sitting me down to render valuable advice that I implement to this day. During one such instance, he told me to go to college and make a name for myself. He told me to make an impression on the right people.

I am certain that he was speaking of a person like Dr. David B. Spencer. As a junior in 2001, Dr. Spencer introduced me to the wonderful field of astrodynamics. Subsequently, he

became my advisor for my undergraduate thesis, master thesis, and Ph.D. dissertation. From the beginning, he had an unwavering belief that I was capable of outstanding work. He has provided valuable mentorship for both my research and career. His influence on my life and future can not be understated. It has been a pleasure and one greatest privileges of my life; thank you very much Dr. Spencer.

I have served as a teaching assistant for many classes throughout my education at Penn State. Any student, whatever his or her grade, will be quick to praise the teaching ability of Dr. Robert Melton. Both actively and passively he has shown me both the practical and innovative ways to approach education at the collegiate level. I have grown both personally and professionally, because of his influence. I take many of these lessons with me into the workforce.

I would also like to thank the remaining members of my committee for their interest and careful consideration, namely, Dr. Jack Langelaan, Joseph P. Cusumano, and the department head Dr. George A. Lesieutre. Specifically, I would like to thank Dr. Cusumano for fostering my interest in dynamical systems to topics beyond astrodynamics. His enthusiasm was contagious.

If credit is to be given, it must be shared equally with my parents. My mother, my first teacher, instilled in me from an early age the importance that education would play in my life. Due her efforts, I have enjoyed a confidence that has propelled my education for over two decades. My father was my first role model who taught by steadfast example things that can not be attained from books. I am the first of my direct line of the Scotts to successfully complete college. I can not repay them; yet, some satisfaction will come when they live to see their gifts passed on to future generations

Chapter 1

Introduction

This dissertation starts by investigating the dynamical processes responsible for the placement of irregular satellites in the outer solar system. This topic is not new to the fields of celestial mechanics and dynamical astronomy. Many cited references attempt to make progress towards an answer. They often involve complex simulations taking into account from one to many of the planets and their influence both on each other and on smaller celestial bodies, such as comets and asteroids. The dynamical analyses are primarily statistical in nature with, often times, nebulous explanations to justify the results. Sometimes analytical approximations to specific regions of space are utilized, yet break down when the particle is transported from one region to another. Despite this criticism, these studies were by no means trivial and have contributed tremendously to our understanding of the problem.

Orbits similar to those of irregular satellites have been identified in the circular restricted three-body problem where spacecraft travel along chaotic orbits well-beyond Earth's influence, yet remain on Earth-centered orbits. This dissertation answers the vital question, "What is the cause of these so called 'natural trajectories'?" The answer to this question opens the door to the development of new techniques for design and analysis in both celestial mechanics and astrodynamics. Many works involving the transport of spacecraft from Earth to distant retrograde orbits, similar to the aforementioned "natural trajectories", rely on "blackbox" methods, reporting trends that go unexplained in the context of the underlying dynamics. Although practical engineering solutions are available, the procedures can not progress until the physical nature of the results is revealed.

Consider the following analogy: Imagine trying to understand the nature of a simple game such as a single soccer player attempting to kick a goal from mid-field with only knowledge of the time history of the ball's position and velocity. Now consider this task with the introduction of deterministic chaos and with rules, such as field, goal, and sideline geometries, that change with ball position, velocity, and time. Despite these complications, suppose you get lucky finding a ball trajectory that results in a goal by some ad-hoc method. Although finding a goal may have been the preferred outcome, perhaps it is an undesirable solution that involves a time-period much longer than the game or a ball velocity that requires super-human strength. Unfortunately, you can not know if a better solution actually exists without blind experimentation. More importantly, you have an incomplete understanding of how the rules change with the conditions of the game.

Analogous complexities arise in models such as the circular restricted three-body problem. Fortunately, a field of applied mathematics, called dynamical systems theory, is tailor-made to infer the "rules" of a particle chaotically transported among distinct regions of space. The "rules" are defined by invariant phase space structures, analogous geometric boundaries that evolve with the energy of the particle and time, for time-dependent systems. The theory provides a framework in order to classify broad sets of orbits which can be used not only to physically understand important trends and phenomena, but to infer methodologies for analysis and the construction of efficacious orbits.

It follows that a major contribution of this dissertation includes the identification via dynamical systems theory of the mechanisms responsible for the capture of irregular satellites in the outer solar system. These mechanisms provide a comprehensive explanation to why these objects are both captured and reside in orbits distant from the central planet. From here new methods of analysis are introduced. They provide a means for understanding the statistical data found in this dissertation and throughout the literature. Furthermore, results of the conservative

system act as a guide for capture phenomenon in the presence of nebular drag, a hypothesized stabilization mechanism. For the dissipative system, analogous geometric structures are utilized in the analyses using both newly developed techniques and mapping procedures often applied to problems in fluid mechanics. All of these developments constitute original contributions to the satellite capture problem.

The orbits occupied by irregular satellites are often called distant retrograde orbits. In the sun-Earth, and other systems visited by spacecraft, distant retrograde orbits have been identified as ideal for spacecraft for a number of applications. Here the length and timescales have changed while the qualitative dynamics are the same. Using underlying structures, a new and efficient technique is developed to both construct and identify optimal spacecraft transfers to this region. The technique considers the evolution of both the transfer orbits and the dominant dynamical structures to provide physical explanation for the variation of important mission design parameters. Captured spacecraft reside on the equivalent orbits to those thought to be occupied by irregular satellites. The analysis of these orbits and the aforementioned transfers act as the foundation for the construction of transfers into what are coined “sticky orbits”. These transfer types are new to astrodynamics. Both small stabilization and low thrust maneuvers can be initiated from these types of orbits. The same techniques developed to analyze the capture of irregular satellites subjected to nebular drag are extended to the spacecraft with continuous thrusting capabilities. These are a new class of transfers, original to this dissertation.

The overall philosophy of this dissertation can be summarized in a few sentences. First, a better understanding of the complex dynamical phenomena of the outer solar system starts by reducing the problem to the relatively simple model of the circular restricted three-body problem. Thus, this model constitutes the dynamical underpinnings of the capture of irregular satellites in systems of greater complexity. Second, related problems in the fields of astrodynamics and celestial mechanics can not only be developed in parallel, but the same techniques for analysis

can be utilized. This cross fertilization facilitates discoveries that may not have been made independently by approaching the problems from the perspective of a single application or discipline.

This next section briefly introduces the historical placement of this dissertation relative to an assortment of pertinent works over the past thirty years. The survey, by no means complete, essentially provides a starting point for further investigation. The past decade has witnessed an acceleration of interest in the application of dynamical systems theory in these fields due to the efforts of researchers at The California Institute of Technology, Jet Propulsion Laboratory, Purdue University, The Pennsylvania State University, University of Michigan, University of Colorado, and Virginia Tech., to name a few. It is impossible to do justice to the collection of works produced by these and other institutions in just one section. The last section delves into the greater details of the specific contributions of the dissertation and document organization. Although the results are significant, the reader may gain an appreciation that the topics addressed in this dissertation are minutia compared to what will be produced in the coming century.

Historical Background

In 2001, Martin Lo of the Jet Propulsion Laboratory voiced that in general the mathematical tools used in the past fifty years by the applied and engineering communities were mostly developed during the 18^{th} and 19^{th} centuries [1]. Modern mathematics had often been overlooked because of the inaccessibility of the subject matter and lack of computational resources. In recent years, many researchers in a variety of fields are beginning to utilize the tools left behind by the great mathematicians of the 20^{th} century often with the assistance of modern computing. Lo's assertion seems to be motivated by his hope that astrodynamicists will embrace modern mathematical tools for the design of spacecraft trajectories in the 21^{st} century.

For many applications involving spacecraft dynamics and control traditional methodologies have worked well. Nevertheless, the prospect of accelerated human and robotic exploration of the solar system demands a broader set of skills that must be utilized by the practicing astrodynamicist.

Advanced astrodynamics courses and texts cover a methodology, known as the patched conic method, for spacecraft encountering multiple gravitational sources. This method works well to model spacecraft trajectories utilizing what are commonly known as gravity assists. Core to this methodology is the decomposition of a multi-body system into single two-body problems which possess analytical solutions. To maintain consistency with accurate solar system models ad-hoc numerical routines must be implemented. Fundamentally, gravity assists increase or decrease heliocentric velocity in order to access regions of the solar system with minimal fuel consumption. The heliocentric velocity of Voyager 2 is plotted in Fig. 1-1 before and after assists from Jupiter, Saturn, Uranus, and Neptune.

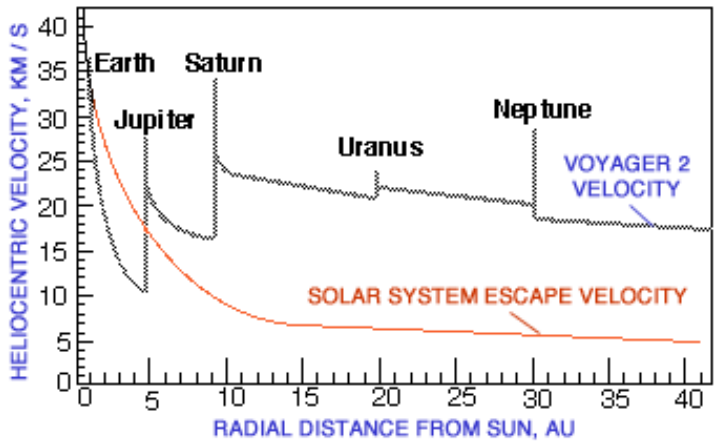

Fig. 1-1 Heliocentric velocity of the Voyager 2 spacecraft as a function of radial distance from the sun. Image courtesy of NASA (http://www2.jpl.nasa.gov/basics/bsf4-1.php).

Notably, Galileo and Cassini followed trajectories planned using this methodology [2,3]. Galileo's complex orbit passed by Venus then twice by Earth before departing the inner solar system for Jupiter. A more recent example is the New Horizons spacecraft, currently en route to Pluto on a highly energetic trajectory [4]. The spacecraft encountered Jupiter on February 28, 2007 and will reach Pluto on July 14, 2015, before an extended mission to the Kuiper Belt region. At the time of this writing the Messenger spacecraft, launched on August 3, 2004, had traveled approximately 3.8 billion miles. After insertion into an orbit about Mercury it will have performed a flyby of Earth once, Venus twice, and Mercury three times. The solutions to these complex designs are not trivial and have been integral to the success of sophisticated space missions. Many, akin to the well-known traveling salesman problem, can be just one of millions of possibilities.

Although the patched conic method proved useful for numerous missions, the general criticism is that it considers only a subset of the design space. By definition a mission designer can not tap the rich dynamics of the three-body problem. The first missions to utilize these intricate dynamics were those to the sun-Earth libration points. These are equilibrium points in a simplified version of the three-body problem, called the circular restricted three-body problem, where the centripetal acceleration of the spacecraft balances the gravitational forces. Thus, these points and their associated orbits do not exist in the two-body problem. Specifically, spacecraft visit the vicinity of three-dimensional periodic orbits known as halo orbits, as coined by their discoverer Robert Farquhar, and quasi-periodic orbits often called Lissajous orbits. Viewed from Earth in the Earth-Moon system, halo orbits appear as halos about the Moon. Figure 1-2 shows a halo orbit in the Earth-Moon system in three-dimensions and as it would appear from Earth.

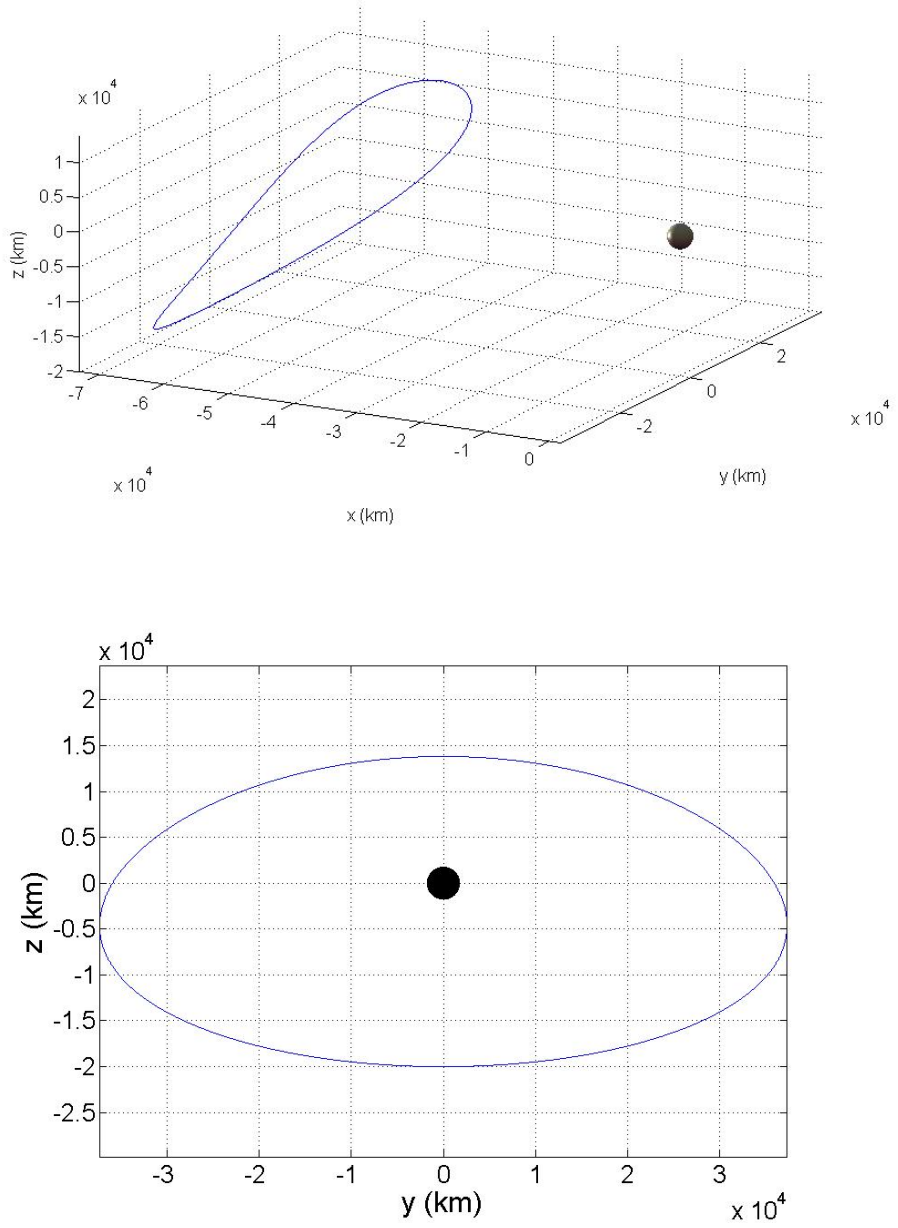

Fig. 1-2 Type 1 Halo orbit about L_1 with negative *z*-amplitude of 20,000 km. and period of 14.75 days in the Earth-Moon system. The positive *x*-axis points towards the Earth, while the *x*-*y* plane lies in the plane of the orbits of Earth and Moon about their center of mass. Image produced by software developed by the author for the undergraduate spacecraft design class.

Missions to libration points in the sun-Earth system include ISEE-3, Wind, SOHO, ACE, and MAP which were inserted into their orbits in 1978, 1995, 1996, 1997, and 2001, respectively [5]. However, the first mission to have its transfer trajectory designed through the three-body formulation was Genesis through extensive phase space analysis [6]. Genesis was inserted into an orbit about the sun-Earth L_1 libration point in 2001 in order to collect solar wind particles for analysis on Earth. Much to the delight of scientists and engineers who study nonlinear dynamics, Genesis has its place in history as the first spacecraft whose trajectory was designed using dynamical systems theory. This design marked change in the outlook of project managers in the United States to the application of dynamical systems theory to trajectory design. The European Space Agency and the Moscow Space Research Institute had been studying the control of halo orbits via manifold theory since the 1980s [7].

As stated in the last section, the advantages of dynamical systems theory to trajectory design can not be overstated. It provides a solid framework for otherwise inexplicable phenomena in multi-body systems. The cogent methodology provides classifications for the role and behavior of orbits. Armed with this knowledge, an astrodynamicist may not only construct a single highly efficient orbit, but may classify entire families of orbits and clear methodologies for their construction. The alternative is to discover such orbits through trial and error which leads to inefficiencies in the design process and promotes a basic disregard for the fundamental dynamics.

The concept of utilizing orbits derived from three-body systems led to the development of what has popularly known as the “interplanetary superhighway system” (IPS) which can be visualized as a vast network of tubes connecting the eight sun-planet systems. Within the systems themselves, such as Jupiter, the tubes connect the many moon-Jupiter systems. The tubes are composed of invariant manifolds that originate from the unstable region encompassing the L_1 and L_2 equilibrium points. Figure 1-3 shows an artist’s conception of the IPS.

Fig. 1-3 An artist's interpretation of the interplanetary superhighway system. Image courtesy of NASA (http://www.jpl.nasa.gov/images/superhighway_square_browse.jpg).

A strong case can be made that the sun-Earth libration points should be used as a staging point for future human space activities in the Earth's neighborhood along the IPS [5]. Regardless of its future use, the astrodynamics community is just beginning to discover what is possible using the IPS and more generally dynamical systems theory. Using these concepts, theories and methodologies have been developed over the past decade for the construction of highly efficient spacecraft transfers along segments of the IPS [8, 9]. One must keep in mind that the IPS, as it is classically defined, considers only the manifolds emanating near the libration points. The circular restricted three-body problem contains an infinite number of unstable periodic orbits and associated manifolds. Many may prove useful for space missions. This is clearly demonstrated by Lo and Parker in their study of unstable resonant orbits in the Earth-Moon system [10].

The concepts of the IPS naturally extend to the motion of comets throughout the solar system. One example is the phenomenon of resonance transition exhibited by short period comets such as Oterma and Gehrels 3 [11-13]. The motion of these objects can be described by

chains of tubes in phase space, the same tubes which that make up the IPS. The manifold tubes have other extensions including estimating the collision probabilities of comets and asteroids with the planets [14]. Tubes controlling transport are thought to exist on galactic distance and time scales leading to a physical explanation to the 'evaporation' of some star clusters over tens of billions of years [15].

Remarkable parallels between astrodynamics, celestial mechanics, and a variety of other fields exist. For example, the same chaotic motions that are traversed by celestial bodies in our solar system are traced out on the atomic scale by Rydberg electrons. The transition state theory that can be applied to asteroids and comets can be used to study reaction rates that include atom ionization, cluster rearrangement, and conductance through microjunctions [16]. Due to these similarities, it is not surprising that Lo worked closely with Jaffé, a chemist from The University of West Virginia, when designing the Genesis mission.

Contribution and Document Organization

Chapter 2 provides a brief overview of the theory required to understand the basic structure of phase space and the tools utilized in this dissertation. Additionally, it includes a section which outlines the algorithm utilized by this dissertation to find symmetric periodic orbits. Any of the topics could constitute a complete text. Therefore, readers unfamiliar with the subject matter should refer to the references.

The general problem of satellite capture in three-body systems is considered from a dynamical systems perspective. This topic is of relevance to temporarily capture comets and the irregular satellites of the outer solar system. The irregular satellites, hypothesized to have been captured during the final stages of planetary formation, exist only about the gas giants of the outer solar system. These satellites are comparatively small, on the order of a few kilometers in

diameter, to the large interior moons and are clumped into distinct families distinguished by their orbital characteristics. Many follow highly elongated orbits revolving in the retrograde direction about the planet. These orbits are often called distant retrograde orbit. Most have been discovered after 1997 by way of improvements in digital-camera technology [17]. Spacecraft missions such as Cassini and Voyager 2 have revealed that irregular satellites resemble the composition of captured comets and asteroids, with those of Jupiter missing the volatile compounds. Consequently, astronomers have postulated that irregular satellites have a capture origin.

Many works have studied this phenomenon largely from a statistical point of view where capture probabilities were understood within the framework of classical orbital elements [18-21]. Brunini hypothesized that captured orbits originate from chaotic region of space with preferred eccentricities and semimajor axes loosely corresponding to first order resonances about the sun [21]. He introduced the notion of an energy threshold where collision orbits prohibit capture and escape These studies have approached the problem via statistical methods and with a flavor dynamical systems theory by visualization of the stable regions with surface of sections.

Chapter 3 presents a detailed and original analysis of satellite capture into distant retrograde orbits in the sun-Jupiter system. A number of fields influenced this chapter including techniques adapted from astrodynamics, fluid mechanics, and dynamical systems theory. To the author's knowledge this is the first analysis of the capture of irregular satellites from the perspective of dynamical systems theory, specifically, lobe dynamics. By Monte Carlo simulations the lobes, geometric phase-space structures contiguous to the stable distant retrograde region, are shown to be the primary mechanism responsible for extended capture about Jupiter. This is an important first step as only these orbits will linger long enough so that nebular drag may facilitate permanent capture.

Similar structures exist which surround the stable sun-centered resonant orbits. In fact, orbits contained within these structures are those that have been classified as sticky orbits in the literature, but without consideration of the lobes. Thus, this dissertation studies the physical mechanism responsible for sticky phenomenon [22, 23]. By this definition, orbits lying at the exterior of the stable distant retrograde region are shown to exhibit sticky behavior.

Visualization of the phase space is achieved via manifold theory and fast Lyapunov indicator maps. These tools work well to identify precise dynamical pathways, certainly contained within the macroscopic influence of the IPS, from chaotic regions about the sun to the distant retrograde region. The evolution of the lobes surrounding the distant retrograde are shown to be responsible for the energy threshold, described by Brunini [21], below which capture and escape are impossible. Moreover, the orbital element distributions of unstable periodic orbits encompassing the stable resonant regions and the size and geometry of the associated homoclinic tangle, the total collection of lobes, are demonstrated to be responsible for the distribution of sun-centered orbits before capture.

The notion of manifolds and lobes breaks down after the introduction of nebular drag. However, like a pendulum with friction, the structure of the conservative systems embodies the underpinnings of the dynamics. The fast Lyapunov indicator map provides reliable discernment among capture and escape orbits in the dissipative system. However, analysis in the three-dimensional system would involve computation times, even on modern computers, that would encumber any meaningful analysis. A function of the degradation of energy, drag parameter, and simulation time, a new parameter derived from the integral of motion is introduced which decreases computation time by a factor of three. Although the analysis was performed specifically for the sun-Jupiter system, the techniques have application throughout the solar system and within extrasolar planetary systems.

Chapter 4 extends the dynamical analysis of chapter 3 beyond the fringe of the stable distant retrograde region for astrodynamical applications. Many uses for distant retrograde orbits have been proposed. In the sun-Earth system there is avoidance of near-Earth phenomena including stellar occultation and thermal perturbations for applications such as spaceborne telescopes, radio imaging of the sun [24], and solar storm warning systems [25]. In the Jupiter-Europa system distant retrograde orbits have been identified as ideal quarantine orbits for derelict spacecraft. Additionally, continuous families of stable orbits through energy provide instantaneous transfer paths to orbits of both capture and escape, which are sometimes referred to as spiral-in and spiral-out transfers [26].

Of particular importance is the region between the stable zone and the Lyapunov orbit where orbits transition many times between retrograde and both retrograde and prograde motion about the second primary. Within this region lie numerous, perhaps an infinity of, periodic orbits which pass especially near the second primary in the prograde direction. These special orbits, called Earth return periodic orbits, have been used as an initial guess for the construction of transfer orbits [25]. To bypass the often tedious search for these orbits, a recent paper applied manifold theory, yet largely constrained the design space [24].

Chapter 4 derives transfers from the fundamental dynamics of the system. It constitutes an original work in the field of astrodynamics showing that the regions holding the Earth return periodic orbits also contain orderly regions of collision orbits. Due to the nature of the dynamics, the orbits are transported to the surface of the Earth in a predictable order. This facilitates a straight-forward algorithm to not only find an arbitrary number of transfer orbits, but to continue them through energy in a manner analogous to periodic orbits. It is shown numerically that an Earth return periodic orbit exists for each transfer family, facilitating the generation of an arbitrary number. This essentially solves the problem of tedious sampling to find such orbits. Algorithms are presented that enable an astrodynamist to surf the design space in an automated

manner. Trends involving variable insertions points and distant retrograde orbit size are understood by way of the manifolds of Lyapunov orbits, globally links along the IPS, and the morphology of stable regions through energy. Because of a detailed understanding of the collision regions and a reliable method to follow their borders through energy, the broader impacts involve the calculation of collision probabilities, an understanding of the paths of comets like Shoemaker-Levy 9, and a platform to analyze the process of accretion of the outer planets during solar system formation.

Chapter 5 builds on both chapters 3 and 4 for the construction of single impulse transfers from low-Earth orbit to the outer fringes of the distant retrograde region. These transfers come by way of a simple adaptation of those discussed in chapter 4 and are new development of this dissertation. In this case the spacecraft inserts directly into a sticky orbit at the exterior of the stable distant retrograde region. These transfers are preferable to spacecraft with little or no propulsive means. Additionally, it gives the spacecraft time, on the order of many years, to stabilize itself by a series of small maneuvers or by continuous low-thrust control.

A proposed mission of the former Soviet Union had utilized what the author believes to be a sticky orbit about the Earth in the sun-Earth system [27]. This is the first study to identify the dynamical mechanisms responsible and to provide a means for the systematic construction of transfers to the region. This is achieved by an extension of the dynamical analysis largely performed in chapter 3. The evolution of the lobes and the stability characteristics of the periodic orbits from which they emanate is investigated relative to the morphology of the transfer orbits with energy. This analysis facilitates direct targeting of the lobes and provides a detailed understanding of the size of the target region, length of capture, collision probability, and capture orbit characteristics.

Both small impulsive and continuous low-thrust maneuvers are investigated to stabilize the spacecraft. It is found, in the case of a small impulsive maneuver, that substantial fuel saving

can be achieved over the classical maneuver to the center of the stable region. Simple low-thrust maneuvers are studied in a manner similar to chapter 3. Depending on the energy, the evolution of the stable region with energy dictates whether thrusting with or against the direction of the velocity vector stabilizes the spacecraft.

The sticky region at the exterior of the distant retrograde region may constitute valuable orbits for spacecraft traveling along the IPS which require temporary capture about a body of interest. Additionally, it may be an ideal location for spiral-out and spiral-in low-thrust maneuvers. Initiated from these orbits, both spiral-in and spiral-out maneuvers are investigated. It is shown that large lengths of orbits with the sticky region, in terms of position and velocity, can be used as staging point for these maneuvers. In the case of the spiral-out maneuver the spacecraft may evolve into a high energy orbit centered about the second primary. Thus, the the region acts much like "coiled spring" from which, after a small maneuver, the spacecraft may visit other location within the solar system.

References

[1] Lo, M.W., "The Lunar L1 Gateway: Portal to the Stars and Beyond", *AIAA Space 2001 Conferenc*e, 2001.

[2] The Galileo Tour Guide. Press Kit. *National Aeronautics and Space Administration*, 1996.

[3] Cassini Launch Press Kit. *National Aeronautics and Space Administration*, 1997.

[4] Guo, Y. and Farquhar, R., "New Horizons Mission Design", *Space Sci. Rev.*, Vol. 140, pg. 49-74, 2008.

[5] Farquhar, R., Dunham, D., Guo, Y., McAdams, J., "Utilization of Libration Points for Human Exploration in the Sun-Earth-Moon system and Beyond", *Acta Astronautica*, Vol. 55, pg. 687-700, 2004.

[6] Lo, M., B. G. Williams, W. E. Bollman, D. Han, Y. Hahn, J. L. Bell, E. A. Hirst, R. A. Corwin, P. E. Hong, K. C. Howell, B. Barden, and R. Wilson, "Genesis Mission Design", *The Journal of the Astronautical Sciences*, Vol. 49, No. 1, pp. 169-184, 2001.

[7] Lo, M., "Libration Point Trajectory Design", *Numerical Algorithms*, Vol. 14, pp. 153-164, 1997.

[8] Gómez, G., Koon, W., Lo, M., Marsden, J., Masdemont, J., and Ross, S., "Invariant manifolds, the spatial three-body problem and space mission design", *AAS/AIAA Astrodynamics Specialist Conference, Quebec City, Canada*, AAS 01-301, 2001.

[9] Yamato, H. and Spencer, D., "Transit-Orbit Search for Planar Restricted Three-Body Problems with Perturbations", *Journal of Guidance, Control and Dynamics*, Vol. 27, No. 6, pp. 1035-1045, 2004.

[10] Lo, M. and Parker, J., "Unstable Resonant Orbits near Earth and their Applications in Planetary Missions", *AIAA Guidance, Navigation and Control Conference and Exhibit, Providence, Rhode Island, August 16-19,* AIAA 2004-5304, 2004.

[11] Wilczak, D. and Zgliczyński, P., "Heteroclinic Connections between Periodic Orbits in Planar Restricted Circular Three Body Problem. Part II", *Communications in Mathematical Physics*, Vol. 259, pp. 561-576, 2005.

[12] Koon, W., Lo, M., Marsden, J., Ross, S., "Heteroclinic connections between periodic orbits and resonance transitions in celestial mechanics", Chaos, Vol. 10, No. 2, pp. 427-469, 2000.

[13] Koon, W., Lo, M., Marsden, J., Ross, S., "Resonance and Capture of Jupiter Comets", *Celestial Mechanics and Dynamical Astronomy*, Vol. 81, pp. 27-38, 2001.

[14] Statistical theory of interior-exterior transition and collision probabilities for minor bodies in the solar system, *Libration Point Orbits and Applications* (Eds. G Gomez, M.W. Lo and J.J. Masdemont), World Scientific, pp. 637-652, 2003.

[15] Marsden, J. and Ross, S., "New Methods in Celestial Mechanics and Mission Design", *Bulletin of the American Mathematical Society*, Vol. 43, No. 1, pp. 43-73, 2005.

[16] Porter, M. and Cvitanovic, P., "Ground Control to Niels Bohr: Exploring Outer Space with Atomic Physics", *Notices of the AMS*, Vol. 52, No. 9, pp. 1020-1025, 2005.

[17] Hamilton, D., "Jupiter's Moonopoly", *Nature*, Vol. 423, pp. 235-236, 2003.

[18] Astakhov, S., Burbanks, A., Wiggins, S. and Farrely, D., "Dynamics of Capture in the Restricted Three-Body Problem," *Order and Chaos in Stellar and Planetary Systems, ASP Conference Series*, Vol. 316, 2004.

[19] Astakhov, S. and Farrely, D., "Capture and Escape in the Elliptic Restricted Three-Body Problem," *Monthly Notices of the Royal Astronomical Society*, Vol. 354, pp. 971-979, 2004.

[20] Astakhov, S.A., Burbanks, A.D., Wiggins, S., and Farrelly, D., "Chaos-assisted capture of irregular moons", *Nature*, Vol. 423, pp. 264-267, 2003.

[21] Brunini, A., "On the satellite capture problem. Capture and stability regions for planetary satellites", *Celestial Mechanics and Dynamical Astronomy*, Vol. 64, No. 1, 1996.

[22] Alvarez, A. and Roig, F., "The role of the resonant "stickiness" in the dynamical evolution of Jupiter family comets", *Dynamics of Populations of Planetary Systems Proceedings IAU Colloquium*, No. 197, 2005.

[23] Malyshkin, L. and Tremaine, S., "The Keplerian Map for the Planar Restricted Three-Body Problem as a Model of Comet Evolution", *Icarus*, Vol. 141, 1999, pp. 341-353.

[24] Demeyer, J. and Gurfil, Pini, "Transfer to Distant Retrograde Orbits Using Manifold Theory", *Journal of Guidance, Control, and Dynamics*, Vol. 30, No. 5, pp. 1261-1267, 2007.

[25] Ocampo, C., and Rosborough, G., "Transfer Trajectories for Distant Retrograde Orbiters of the Earth", *Advances in the Astronautical Sciences,* Vol. 82, No. 2, pp. 1177–1200, 1993.

[26] Lam, T., "Exploration of distant retrograde orbits around Europa", *Advances in Astronautical Sciences*, Vol. 120, pp. 135-153, 2005.

[27] Dunham, D., "Astrodynamics-Natural Trajectories", *Space for Peace and Progress, 41st International Astronautical Congress, Dresden Germany, October 1990*.

Chapter 2

Theory

The current chapter is intended as a theoretical primer to the core topics of this dissertation. The derivations of the circular restricted three-body problem (CR3BP) using both Langrange's and Hamilton's equations are provided. Details essential to interpretation of any study in the CR3BP are covered, including the Jacobi constant, the five equilibrium points, Hill's regions, and symmetry. The basic principles of Kolmogorov-Arnold-Moser (KAM) theory and the Poincaré-Birkoff fixed point theorem are introduced yielding a qualitative guide to the complex and often chaotic dynamics of the CR3BP. Both the practical and theoretical details of the maximum Lyapunov exponent (MLE) and the fast Lyapunov indicator (FLI) are discussed in conjunction with a simple example.

The Circular Restricted Three-Body Problem

The *n*-body problem involves the motion of *n* point masses moving in three-dimensional space mutually governed by Newton's law of gravitation. An analytical solution can be found for n=2, but no closed-form solution is available for n>2. Despite the work of Kepler, Newton, Laplace, Lagrange, Weierstrass, Mittag-Leffler, Poincaré, Birkoff, Siegel, Kolmogorov, Moser, and Arnold there are many open questions pertaining to the *n*-body problem. Interestingly, there are no proofs establishing the existence of quasi-periodic orbits for $n \geq 4$. Many open questions exist, in part, because of the degeneracy of the *n*-body problem. As a result, the *n*-body problem does not fall into the class of general Hamiltonian systems for which KAM theory applies. However, special cases, such as the planar circular restricted three body problem (CR3BP), are

iso-energetically non-degenerate. Therefore, KAM theory can be applied to establish the existence of quasi-periodic orbits.

In 1966, Hénon stated that a simple application of Arnold's theorem to the restricted three-body problem established the existence of invariant tori for mass ratios less than 10^{-333}. Although, Moser's theorem established a value of 10^{-50}, the result was of no practical use to astronomers. In fact, as stated by Celletti [1], this is close to the mass ratio of proton with respect to the sun. It was not until 1997 that the existence of KAM tori for the CR3BP for a mass ratio up to 10^{-6} was established [1]. In 2003 it was reported that KAM theory had been applied to mass ratios up to 10^{-3}, specifically for the Jupiter-Sun-Victoria system. The outline of the specific algorithm and theory required 127 pages of explanation and 12,000 lines of code to execute. This study relies on numerical evidence of stability while using the general results of KAM and other theories as a guide to infer long-term evolution, stability, and chaotic transport.

This section introduces the pertinent theory and equations of the CR3BP. A thorough study of the problem usually starts with Szebehely's classic book *Theory of Orbits* [2]. Certainly any questions relating to the basic formulation of the problem can be resolved by consulting this work. Interestingly, the late Szebehely got his start researching engines here at University Park.

Equations of Motion

Consider an inertial coordinate frame that has an origin at the center of mass of two bodies revolving in circular orbits influenced only by their mutual gravitational attraction as illustrated in Fig. 2-1. A third body, which will be referred to as a particle or spacecraft, moves within this system influenced by the gravity of the other two bodies, but has no effect on the gravity field. Since the motion of the two massive bodies has been predefined, the CR3BP is concerned only with the motion of the third "massless" particle.

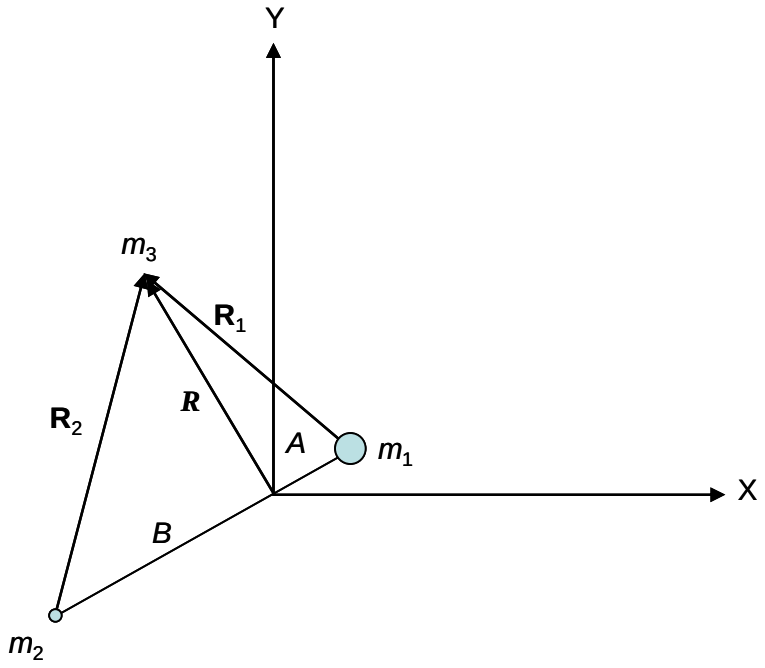

Fig 2-1 CR3BP in the inertial reference frame.

Here the relative position vectors $\boldsymbol{R}_1$ and $\boldsymbol{R}_2$ originate at the center of mass of m_1 and m_2. At the present, the masses are assumed to have any distribution and will be referred to as the primaries. The quantities A and B are the distances from the origin to the first and second primaries. Defining a specific gravitational potential function, $U(X,Y,t)$, that includes contributions of both m_1 and m_2, the equations of motion of the particle in an inertial coordinate frame are

$$\frac{d^2X}{dt^2}=\frac{\partial U\left(X,Y,t\right)}{dX}\quad \frac{d^2Y}{dt^2}=\frac{\partial U\left(X,Y,t\right)}{dY}\quad \frac{d^2Z}{dt^2}=\frac{\partial U\left(X,Y,t\right)}{dZ} \tag{2.1}$$

The assumptions of the CR3BP violate the conservation of energy since the particle has no effect on the gravity field. Note that because U is defined as a continuous function of its variables the differential takes on the familiar form.

$$dU = \frac{\partial U}{\partial X}dX + \frac{\partial U}{\partial Y}dY + \frac{\partial U}{\partial Z}dZ + \frac{\partial U}{\partial t}dt \tag{2.2}$$

Using the equations of motion, an expression that relates the specific kinetic energy and the function U is found.

$$\begin{aligned}\int_{t_o}^{t_f}\left(\frac{d^2X}{dt^2}\frac{dX}{dt}+\frac{d^2Y}{dt^2}\frac{dY}{dt}+\frac{d^2Z}{dt^2}\frac{dZ}{dt}\right)dt &= \frac{1}{2}\left[\left(\frac{dX}{dt}\right)^2+\left(\frac{dY}{dt}\right)^2+\left(\frac{dZ}{dt}\right)^2\right]=\frac{1}{2}v^2 \\ = \int_{t_o}^{t_f}\left(\frac{\partial U}{\partial X}\frac{dX}{dt}+\frac{\partial U}{\partial Y}\frac{dY}{dt}+\frac{\partial U}{\partial Z}\frac{dZ}{dt}\right)dt &= \int_{t_o}^{t_f}\left(dU-\frac{\partial U}{\partial t}dt\right)=U-\int_{t_o}^{t_f}\frac{\partial U}{\partial t}dt\end{aligned} \tag{2.3}$$

Defining the inertial velocity as V yields the following invariant relationship

$$\frac{1}{2}V^2 - U = -\int_{t_o}^{t_f}\frac{\partial U}{\partial t}dt \tag{2.4}$$

Since the expression on the right side is a function of time the total energy of the system is not conserved. The motion of the two primaries is considered to be known, therefore, only terms involving the motion of particle are of interest in the Lagrangian and/or the Hamiltonian.

$$L = T + U = \frac{1}{2}\left(\dot{X}^2+\dot{Y}^2+\dot{Z}^2\right)+U \tag{2.5}$$

Here the units are energy per unit mass. The momentum variables become

$$\mathbf{p} = \left(\frac{\partial L}{\partial \dot{\mathbf{q}}} \right)^T = \begin{bmatrix} \dot{X} \\ \dot{Y} \\ \dot{Z} \end{bmatrix} \tag{2.6}$$

where **q** are generalized coordinates. Thus, the Hamiltonian is

$$H = \frac{1}{2} \langle \mathbf{p}, \mathbf{p} \rangle - U \tag{2.7}$$

where $\langle *, * \rangle$ denotes the inner product and the equations of motion in Hamiltonian form are

$$\dot{\mathbf{q}} = \frac{\partial H}{\partial \mathbf{p}} \quad \mathbf{p} = -\frac{\partial H}{\partial \mathbf{q}} \tag{2.8}$$

Since *U* is a function of time, the Hamiltonian is not a constant of motion, as would be expected since it is simply another form of the energy in the inertial reference system.

A convenient coordinate system that will be shown to yield a constant of motion is a rotating set that matches the angular velocity of the primaries. Assume that the angular velocity is $\boldsymbol{\omega} = n\hat{\mathbf{K}}$. Also, let the rotating coordinate axes be denoted by x', y', and z' with unit vectors $\hat{\mathbf{i}}'$, $\hat{\mathbf{j}}'$, $\hat{\mathbf{k}}'$ and the position vector of the particle be given by $\mathbf{r}'$, shown in Fig. 2-2.

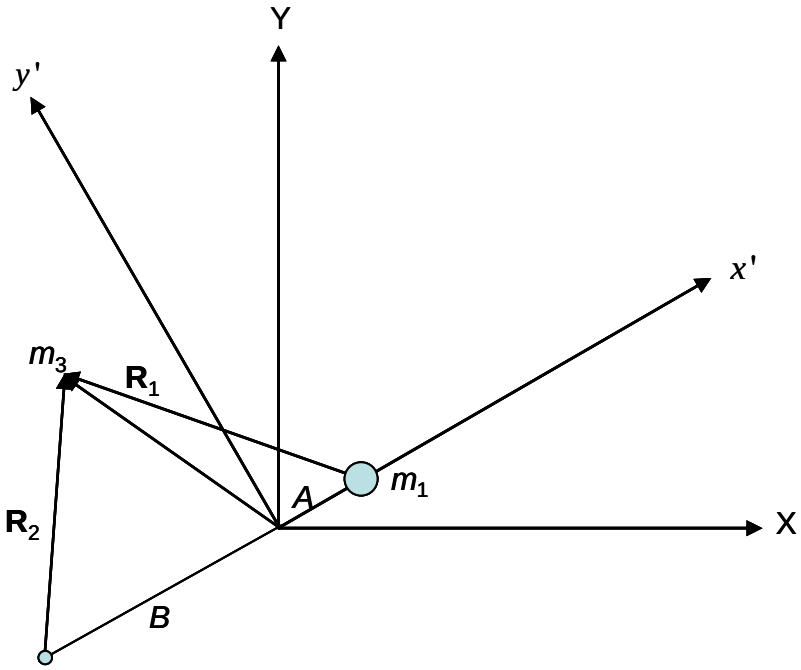

Fig. 2-2 The CR3BP in a rotating reference frame.

Under some circumstances the transformed Lagrangian is not explicitly a function of time. Letting the subscript "r" signify that coordinates are expressed in the rotating reference frame,

$$\begin{aligned} L_r &= \frac{1}{2}\left\langle \left(n\hat{\mathbf{k}}'\times\mathbf{r}'\right)+\dot{\mathbf{r}}', \left(n\hat{\mathbf{k}}'\times\mathbf{r}'\right)+\dot{\mathbf{r}}' \right\rangle + U_r\left(\mathbf{r}'\right) \\ &= \frac{1}{2}\left[\left(\dot{x}'-ny'\right)^2+\left(\dot{y}'+nx'\right)^2+\dot{z}'^2\right]+U_r\left(x',y',z'\right) \end{aligned} \tag{2.9}$$

These circumstances occur when the potential is of the form of a gravitational potential for a point mass and for certain forms of an aspherical potential function. For now assume that the Lagrangian is not explicitly a function of time. Lagrange's equations give the equations of motion

$$\begin{aligned} \ddot{x}' - 2n\dot{y}' - n^2 x' &= \frac{\partial U_r}{\partial x'} \\ \ddot{y}' + 2n\dot{x}' - n^2 y' &= \frac{\partial U_r}{\partial y'} \\ \ddot{z}' &= \frac{\partial U_r}{\partial z'} \end{aligned} \tag{2.10}$$

Setting $(A+B)=L$ and m_1+m_2=M, it is convenient to choose dimensionless units such that

$$\begin{aligned} x &= \frac{x'}{L} \quad & \mathbf{r}_1 &= \frac{\mathbf{R}_1}{L} \quad & t &= nt' \\ y &= \frac{y'}{L} \quad & \mathbf{r}_2 &= \frac{\mathbf{R}_2}{L} \quad & \mu &= \frac{m_2}{M} \\ z &= \frac{z'}{L} \quad & \mathbf{r} &= \frac{\mathbf{r}'}{L} \quad & 1-\mu &= \frac{m_1}{M} \end{aligned} \tag{2.11}$$

These relationships implicitly set the gravitational constant to 1, this is easily demonstrated by applying Newton's second law to the primaries in a rotating coordinate system. It is also easily shown, by the definition of the center of mass, that A=μ and B=1-μ. Assuming that the derivative with respect to time is taken in the new time units and dropping the subscripts on the potential, the equations of motion are

$$\begin{aligned} \ddot{x} - 2\dot{y} - x &= \frac{\partial U}{\partial x} \\ \ddot{y} + 2\dot{x} - y &= \frac{\partial U}{\partial y} \\ \ddot{z} &= \frac{\partial U}{\partial z} \end{aligned} \tag{2.12}$$

These equations can be written in Hamiltonian form since linear transformations by way of rotation matrices are canonical. The generalized momentum vector is

$$\mathbf{p} = \left(\frac{\partial L}{\partial \dot{\mathbf{q}}} \right)^T = \begin{bmatrix} \dot{x} - y \\ \dot{y} + x \\ \dot{z} \end{bmatrix} \tag{2.13}$$

and the Hamiltonian becomes

$$\begin{aligned} H &= \frac{1}{2}\langle \mathbf{p}, \mathbf{p} \rangle - \langle \mathbf{p}, \hat{\mathbf{k}} \times \mathbf{r} \rangle - U(\mathbf{r}) \\ &= \frac{1}{2}\left(p_x^2 + p_y^2 + p_z^2 \right) + \left(p_x y - p_y x \right) - U(x, y, z) \end{aligned} \tag{2.14}$$

which yields the equations of motion in Hamiltonian form

$$\begin{aligned} \dot{x} &= \frac{\partial H}{\partial p_x} = p_x + y \qquad \dot{p}_x = -\frac{\partial H}{\partial x} = p_y + \frac{\partial U}{\partial x} \\ \dot{y} &= \frac{\partial H}{\partial p_y} = p_y - x \qquad \dot{p}_y = -\frac{\partial H}{\partial y} = -p_x + \frac{\partial U}{\partial y} \\ \dot{z} &= \frac{\partial H}{\partial p_z} = p_z \qquad\qquad \dot{p}_z = -\frac{\partial H}{\partial z} = \frac{\partial U}{\partial z} \end{aligned} \tag{2.15}$$

If both of the primaries have uniform mass distributions and can be considered point masses then the potential is

$$U = \frac{(1-\mu)}{r_1} + \frac{\mu}{r_2} \tag{2.16}$$

where $r_1 = \left[\left(x-\mu \right)^2 + y^2 + z^2 \right]^{1/2}$ and $r_2 = \left[\left(x+1-\mu \right)^2 + y^2 + z^2 \right]^{1/2}$. It is common in the literature to set $\Omega = \frac{x^2+y^2}{2} + \frac{(1-\mu)}{r_1} + \frac{\mu}{r_2} + \frac{\mu(1-\mu)}{2}$ which allows for a more compact expression for the equations of motion.

$$\begin{aligned} \ddot{x} - 2\dot{y} &= \Omega_x \\ \ddot{y} + 2\dot{x} &= \Omega_y \\ \ddot{z} &= \Omega_z \end{aligned} \tag{2.17}$$

Here the subscripts indicate partial derivatives. Using this notation and making a few simplifications, the Hamiltonian takes the form

$$H = \frac{1}{2}\left(\left(p_x + y \right)^2 + \left(p_y - x \right)^2 + p_z^2 \right) - \Omega \tag{2.18}$$

and the equations of motion are

$$\begin{aligned} \dot{x} &= \frac{\partial H}{\partial p_x} = p_x + y & \dot{p}_x &= -\frac{\partial H}{\partial x} = p_y - x + \Omega_x \\ \dot{y} &= \frac{\partial H}{\partial p_y} = p_y - x & \dot{p}_y &= -\frac{\partial H}{\partial y} = -p_x - y + \Omega_y \\ \dot{z} &= \frac{\partial H}{\partial p_z} = p_z & \dot{p}_z &= -\frac{\partial H}{\partial z} = \Omega_z \end{aligned} \tag{2.19}$$

Symmetry of Solutions

If a particular solution of the CR3BP is known then another solution can be found by considering that the system is invariant to the following transformation.

$$t \to -t \quad y \to -y \tag{2.20}$$

This is easily verified by making the following substitutions into the equations of motion.

$$\begin{array}{lll} \ddot{x} \to \ddot{x} & \dot{y} \to \dot{y} & \Omega_x \to \Omega_x \\ \ddot{y} \to -\ddot{y} & \dot{x} \to -\dot{x} & \Omega_y \to -\Omega_y \\ \ddot{z} \to \ddot{z} & \Omega_z \to \Omega_z & \end{array} \tag{2.21}$$

This is often called *x*-*z* plane symmetry. Similarly, a symmetry about the *x*-axis can be shown by proving invariance under the transformation

$$t \to -t \quad y \to -y \quad z \to -z \tag{2.22}$$

It follows that symmetry of about the x-y plane can easily be shown via the following transformation

$$z \to -z \tag{2.23}$$

Symmetry in the planar-CR3BP is of particular importance when numerically calculating initial conditions for periodic orbits, fast Lyapunov exponent maps, and transfer orbits which return to the second primary. A point on a backwards collision map (x, Vx) in the planar problem implies a collision at $(x, -Vx)$ on a forward map. Similarly, if a point of the mapping of an unstable manifold of a symmetric periodic orbit lies at (x, Vx) then a point corresponding to the stable manifold lies at $(x, -Vx)$. In all cases, the symmetry of the model can be used to reduce computing time.

Equilibrium Points

An important starting point for the analysis of any dynamical system is to solve for the equilibrium points and investigate the nature of the phase space near these solutions. In general, the full three-body problem in an inertial reference system has no equilibrium points. It does, however, have the specific solutions of the equilateral triangular and collinear points that fix positions for each of the bodies in a rotating reference frame. Since it can be shown that the CR3BP can be considered a limiting case of the full three-body problem, one may predict that equilibrium points possessing some these characteristic will be present. Figure 2-3 shows the arrangement of these points.

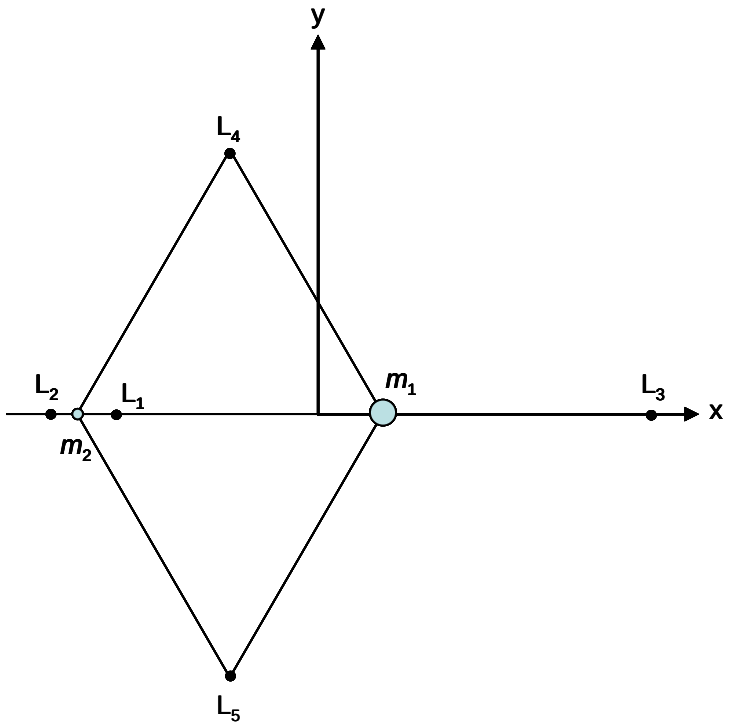

Fig. 2-3 The CR3BP and its equilibrium points.

A connection between the local linear analysis and the local nonlinear dynamics is given by Moser's generalization of the theorem of Lyapunov. This theorem indicates that the

qualitative results of the linear analysis carry over to the full nonlinear equation. Specifically, a power series can be constructed to describe the evolution of each of the six state variables with time, which converge in some neighborhood of the equilibrium point. Locally the collinear points, the three points on the *x*-axis, have the form saddle×center×center. The remaining points, the triangular points, are stable to for a wide range of mass ratios including all scenarios within our solar system.

Let the eigenvalues of any particular collinear point be denoted as $\pm\alpha$, $\pm\gamma i$, and $\pm\omega i$. As an application of the eigen-decomposition theorem, the coordinate axes can be transformed so that the linear differential equations take on a simple form. Using this transformation, and expressing the state vector as $\left[u_1, u_2, u_3, v_1, v_2, v_3\right]^T$, the linearized equations of motion become

$$\begin{aligned} \dot{u}_1 &= \alpha u_1 \quad & \dot{v}_1 &= -\alpha v_1 \\ \dot{u}_2 &= \gamma v_2 \quad & \dot{v}_2 &= -\gamma u_2 \\ \dot{u}_3 &= \omega v_3 \quad & \dot{v}_3 &= -\omega u_3 \end{aligned} \tag{2.24}$$

here the subscripts indicate a direction along one of the three eigen-directions. The Hamiltonian corresponding to these equations can easily be inferred by inspection.

$$H = \alpha u_1 v_1 + \frac{\gamma}{2}\left(u_2^2 + v_2^2\right) + \frac{\omega}{2}\left(u_3^2 + v_3^2\right) \tag{2.25}$$

The Hamiltonian indicates that the dynamics lie on a five-dimensional energy surface. Additional constants of motion can be found by solving the equations of motion.

$$\begin{array}{ll} u_1(t) = u_1^0 e^{\alpha t} & v_1(t) = v_1^0 e^{-\alpha t} \\ u_2(t) = u_2^0 \cos(\gamma t) + v_2^0 \sin(\gamma t) & v_2(t) = v_2^0 \cos(\gamma t) - u_2^0 \sin(\gamma t) \\ u_3(t) = u_3^0 \cos(\omega t) + v_3^0 \sin(\omega t) & v_3(t) = v_3^0 \cos(\omega t) - v_3^0 \sin(\omega t) \end{array} \tag{2.26}$$

Here the superscript (0) indicates an initial condition. It is trivial to show that $u_1 v_1$, $u_2^2 + v_2^2$, and $u_3^2 + v_3^2$ are local constants of motion. Also notice that for any local solution, the $\mathrm{sgn}(u_1)$ and $\mathrm{sgn}(v_1)$ can each take three possible values $(-1, 0, 1)$, which indicates that the solution can fall into nine different classes. Figure 2-4 shows the local phase portraits.

The next developments summarize a few pertinent results, presented in the plane by Conley [3], which have been extended to the general case of three-degrees-of-freedom [4]. Interpretation in the plane comes by discarding the u_3 and v_3 coordinates. Consider now, only the regions where these power series converge. Call this a closed ball *B* and consider a set of points, referred to by region *R*, on a level energy surface in this ball satisfying

$$H(u_1, u_2, u_3, v_1, v_2, v_3) = h, \quad |u_1 - v_1| \le c \tag{2.27}$$

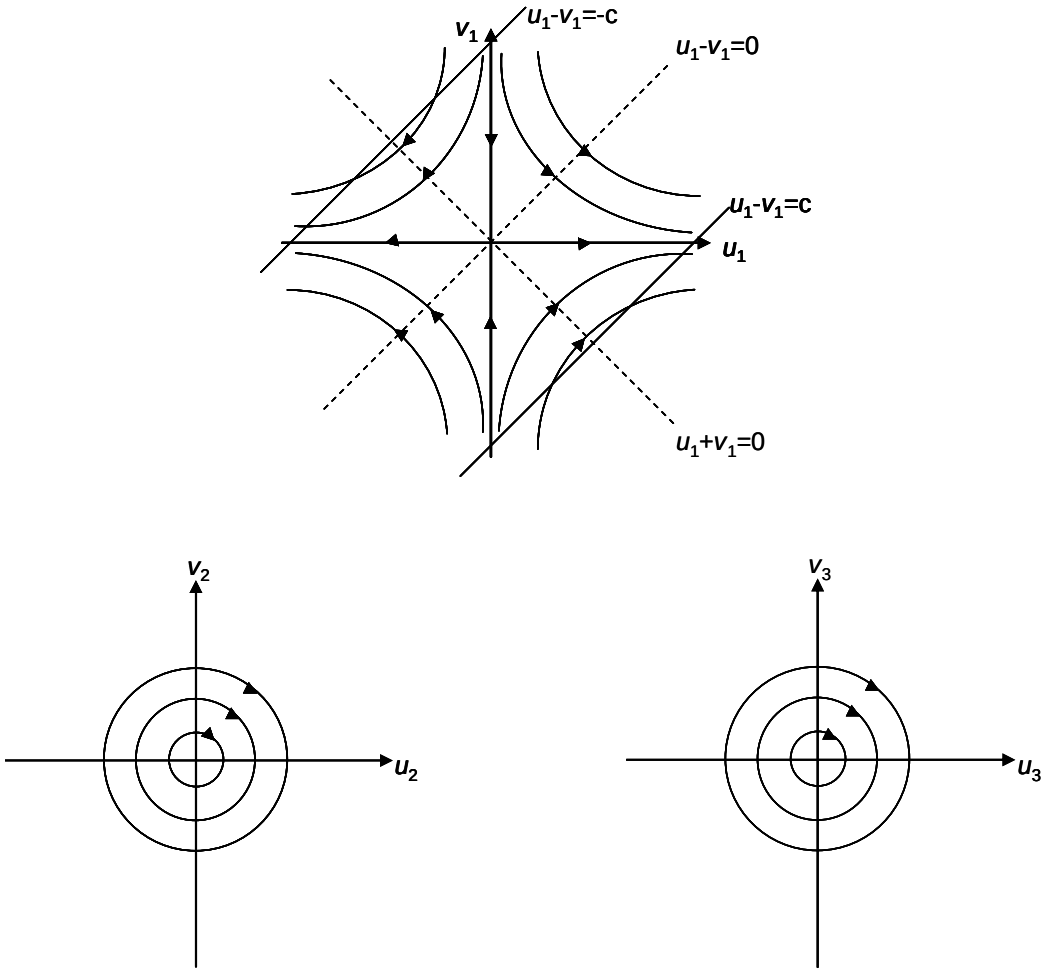

Fig. 2-4 Local phase portraits in the u_1-v_1, u_2-v_2, and u_3-v_3 planes.

A level energy surface can be expressed as

$$\frac{\alpha}{2}\left(u_1+v_1\right)^2+\frac{\gamma}{2}\left(u_2^2+v_2^2\right)+\frac{\omega}{2}\left(u_3^2+v_3^2\right)=h+\frac{\alpha}{4}\left(u_1-v_1\right)^2\le h+\frac{\alpha}{4}c^2 \qquad (2.28)$$

If only positive values of h are considered, the bounded region is topologically equivalent to the product of a four-sphere (a sphere with a four-dimensional surface) and a closed interval, which

can be verified with a simple change of variables and rescaling. Thus, the bounding line segments can be interpreted as two bounding four-spheres.

Every fixed point in the u_1-v_1 plane corresponds to a three-sphere. Furthermore, the projection of any trajectory in R in the u_1-v_1 plane is a hyperbola, since $u_1 v_1$ is a local constant of motion. For some fixed energy level, moving along $u_1 - v_1 = 0$ in either direction, the motion is bounded by two hyperbola $u_1 v_1 = \frac{h}{\alpha}$. In this case, all other state variables are zero and the 3-spheres corresponding to points in the u_1-v_1 plane collapse to single points on the bounding hyperbolas.

$$u_1 v_1 = \frac{1}{\alpha}\left(h - \frac{\gamma}{2}\left(u_2^2 + v_2^2\right) - \frac{\omega}{2}\left(u_3^2 + v_3^2\right)\right) \tag{2.29}$$

The boundaries in four-dimensional space for any fixed u_1-v_1 within B can be described by defining a four-dimensional "scaled radius" function, $\rho = \frac{\gamma}{2}\left(u_2^2 + v_2^2\right) + \frac{\omega}{2}\left(u_3^2 + v_3^2\right)$. Thus, $0 \le \rho \le h + \frac{\alpha}{4}\left(u_1 - v_1\right)^2$ bounds R.

Recall any particular solution in R can fall in to one of nine classes of motion. Each of these cases is listed below:

1) First is motion confined to the center manifold, $u_1 = v_1 = 0$, where periodic and quasi-period orbits are known to exists. Except for a few special cases these solutions lie on an invariant two-torus within a three-sphere, S^3 [5]. If the frequencies are equal or relatively prime integers every solution is periodic. Encompassing a larger set of the solution space is when the ratio of the frequencies is irrational. In this case, number theory can be used to show that the solutions are dense on the two-torus [5]. Turning to the nonlinear equations and citing the

classical Lyapunov theorem, in an arbitrarily close neighborhood to the equilibrium point there are two families of periodic orbits. The first is contained within the *x*-*y* plane and the other is tangent to the (z, p_z) direction. Halo orbits are a bifurcation of the planar family of Lyapunov orbits, where the in-plane and out-of-plane frequencies are equal.

2-5) Orbits that are asymptotic to the center manifold correspond to $u_1 v_1 = 0$. These orbits approach the center manifold when $v_1 = 0$ as time increases or when $u_1 = 0$ as time decreases. They lie on the stable and unstable manifolds, which both admit the same local constant of motion.

$$h = \frac{\gamma}{2}\left(u_2^2 + v_2^2\right) + \frac{\omega}{2}\left(u_3^2 + v_3^2\right) \tag{2.30}$$

Thus, these manifolds have the form $S^3 \times R$. These can be thought of as higher dimensional "tubes" which form a subset in six-dimensional space and the five-dimensional energy manifold.

6-7) When $u_1 v_1 > 0$ the orbits cross from one bounding three-sphere to another. Since the orbits are crossing from one region of phase space to another, this type of orbit is referred to as a transit orbit. This corresponds to the transit of the orbits among regions specified by Hill's regions to be discussed below. These correspond to five-dimensional elliptic cylinders in the linearized phase space.

8-9) If $u_1 v_1 < 0$ the orbits enter *R* by entering and leaving across the same bounding four-sphere. These will be referred to as non-transit orbits. As with the transit orbits, these are five-dimensional elliptic cylinders in the linearized phase space.

The Jacobi Integral and Hill's Regions

If the Lagrangian is not dependent on time and minimum number of coordinates has been used, it should be possible to derive a constant of motion. Jacobi's constant can be written as

$$C = \dot{\mathbf{q}}^T \left(\frac{\partial L}{\partial \dot{\mathbf{q}}} \right)^T - L \tag{2.31}$$

where C is a constant. Using this equation with the general form of the Lagrangian gives a constant of motion,

$$C = \frac{1}{2}\left(\dot{x}^2 + \dot{y}^2 + \dot{z}^2 \right) - \frac{1}{2}\left(x^2 + y^2 \right) - U\left(x, y, z \right) \tag{2.32}$$

If the primaries can be considered point masses this equation can be used to yield a common form of the Jacobi constant for this system.

$$C = \frac{1}{2}\left(\dot{x}^2 + \dot{y}^2 + \dot{z}^2 \right) - \frac{1}{2}\left(x^2 + y^2 \right) - \frac{1-\mu}{r_1} - \frac{\mu}{r_2} \tag{2.33}$$

Although the CR3BP technically violates conservation of energy, C is often called the energy of the system. The Jacobi integral is a multiple of the Hamiltonian function and defines an invariant five-dimensional manifold, often denoted as M, for this system. Defining a function $K\left(x, y, z, \dot{x}, \dot{y}, \dot{z}\right)$=$C$, the manifold is given by

$$M = \left\{ \left(x, y, z, \dot{x}, \dot{y}, \dot{z}\right) \middle| K\left(x, y, z, \dot{x}, \dot{y}, \dot{z}\right) = const. \right\} \tag{2.34}$$

Setting the velocity components to zero gives the projection of this surface into position space. This projection defines a boundary (ies) or a surface(s) in space over which the particle cannot cross, forming a region(s) known as Hill's region(s) where the particle is "trapped" for all time. There are five cases, four of which are shown below in Fig. 2-5 for a mass ratio of 0.1. Here the exterior and the regions about the large and small primaries are labeled as "E" and, "P_1" and "P_2", respectively.

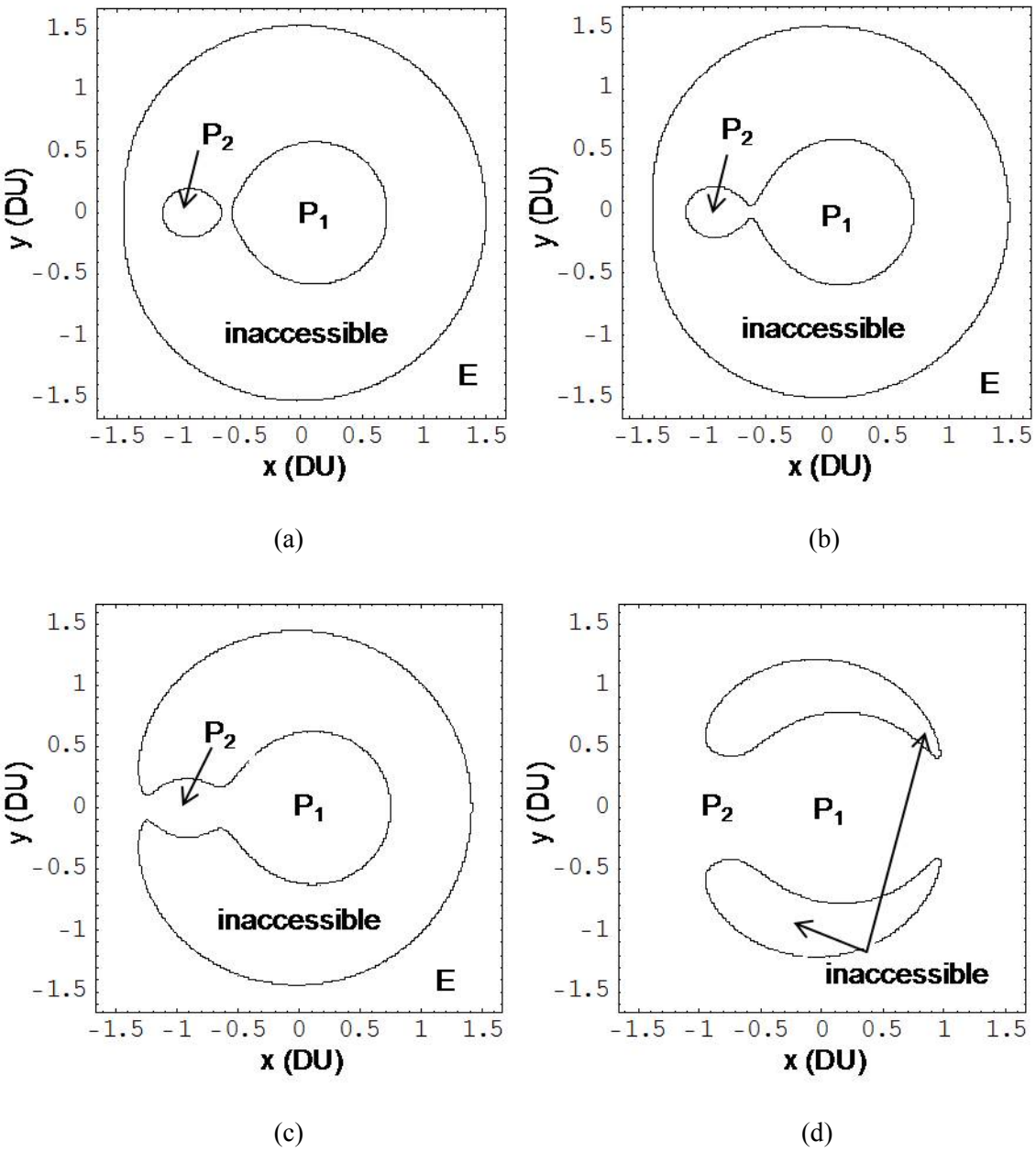

Fig. 2-5 Hill's region(s) for increasing values of Jacobi constant.

At the energy of the Hills curves shown in Fig. 2-5a motion is possible in the vicinity of both primaries; however, it is energetically impossible to pass among primaries. Increasing the energy to Fig. 2-5b the particle can pass between primaries, yet cannot escape to exterior of the

three-body system. By Fig. 2-5c the particle can escape to the exterior region via the smaller primary. Further increases render escape on the opposite side of the smaller primary possible leaving only the L_4 and L_5 equilibrium points inaccessible. Finally, after further increases the particle may access all regions within the CR3BP. Note that these curves do not guarantee that a particle will transition from one region to another. For example, if it evolves along a KAM torus then it is forbidden from leaving the surface of the torus. Additionally, motion along a periodic orbit which does not transition among regions and orbits asymptotically approaching an unstable periodic orbit (stable manifold) that does not transition, are other examples.

Symmetric, Planar-Periodic Orbits

Many types of periodic orbits exist in the CR3BP including the symmetric varieties, namely, axi-symmetric, doubly-symmetric, and planar. There also exists the more difficult to find asymmetric periodic orbits. This dissertation investigates the planar type. The predictor-corrector method utilized to study the evolution of planar-periodic orbits with energy is introduced in this section.

The initial and final conditions of a planar-periodic orbit,

$$\begin{aligned} \mathbf{X}_o &= \mathbf{X}(\mathbf{X}_o, 0) = \begin{bmatrix} x_o & 0 & 0 & \dot{y}_o \end{bmatrix}^T \\ \mathbf{X}_1 &= \mathbf{X}(\mathbf{X}_1, T) = \begin{bmatrix} x_o & 0 & 0 & \dot{y}_o \end{bmatrix}^T = \begin{bmatrix} x_1 & 0 & 0 & \dot{y}_1 \end{bmatrix}^T \end{aligned} \tag{2.35}$$

are dictated by symmetry and a constraint dictated by the integral of motion. Here the subscripts "o" and "1" indicate initial and final conditions and T is the period. Within the algorithm, a set of initial conditions satisfying the constraints are differentially corrected until the final velocity in the x-direction is zero, within a certain tolerance, for a specified constant of motion. After

differential correction the predictor step is performed to rectify any violations of the constraint. Differential correction is continued until the final velocity in the *x*-direction is zero. This procedure is repeated until the constraint and end conditions are satisfied to a specified tolerance. To access periodic orbits at nearby energies, the constraint on the Jacobi constant is modified to a new value during the prediction step and process is continued.

Expanding the equation of motion to first order about $(\mathbf{X}_o, T)$,

$$\delta \mathbf{X}_1 = \Phi(T)\delta \mathbf{X}_o + \frac{\partial \mathbf{X}_1}{\partial t}\delta T \tag{2.36}$$

where $\Phi(T) = \dfrac{\partial \mathbf{X}_1}{\partial \mathbf{X}_o}$ is the 4×4 state transition matrix. Eq. (2.36) provides the variation of the final state as a function of small changes in the initial conditions and transfer time. A differential correction routine is established where $\delta \dot{x}_1 = -\dot{x}_1$ at each step. Expanding the third element of Eq. (2.36),

$$\delta \dot{x}_1 = \Phi_{31}\delta x_o + \Phi_{34}\delta \dot{y}_o + \ddot{x}_1 \delta T \tag{2.37}$$

yields one equation and three unknowns. δT can be eliminated by recalling that $y_o = 0 \Rightarrow \delta y_o = 0$; therefore, the second element of Eq. (2.36) can be modified to give,

$$\delta T = -\frac{1}{\dot{y}_1}\left(\Phi_{21}\delta x_o + \Phi_{24}\delta \dot{y}_o\right) \tag{2.38}$$

The variation of the constant of motion can be used to eliminate $\delta \dot{y}_o$,

$$\delta C = C_{x_o}\delta x_o + C_{\dot{y}_o}\delta \dot{y}_o = 0$$
$$\Rightarrow \delta \dot{y}_o = -\frac{C_{x_o}}{C_{\dot{y}_o}}\delta x_o \tag{2.39}$$

Combining Eqs. (2.37)-(2.40) yields the necessary equation for differential correction,

$$\delta x_o = -\frac{\delta \dot{x}_1}{\Phi_{31} - \frac{C_{x_o}}{C_{\dot{y}_o}}\Phi_{34} + \frac{\ddot{x}_1}{\dot{y}_1}\left(-\Phi_{21} + \frac{C_{x_o}}{C_{\dot{y}_o}}\Phi_{24}\right)} \tag{2.40}$$

The prediction step is derived by assuming that the differential corrector has successfully converged to a periodic orbit and $\delta C \neq 0$. Thus, a prediction of the initial condition of the same family of periodic orbits at a nearby energy is given by the following equation,

$$\delta x_o = -\frac{\frac{\Phi_{14}}{C_{\dot{y}_o}}\delta C}{\left(\Phi_{11} - 1 - \frac{C_{x_o}}{C_{\dot{y}_o}}\Phi_{14}\right)} \tag{2.41}$$

Initial guesses are often obtained by any means necessary, i.e. by random sampling, surface of sections, or analytical approximations. Most of the periodic orbits relevant to this work had initial guesses derived from fast Lyapunov indicator maps. This methodology provides adequate guesses for both stable and unstable periodic orbits, although a substantially more accurate guess is required for unstable periodic orbit.

The Kolmogorov-Arnold-Moser (KAM) Theorem

For an unperturbed, integrable system there is a foliation in invariant tori. Classical perturbation theory assumes that the energy manifold continues to be foliated by invariant tori under perturbation. In general, this assumption fails due to the problem of small divisors. Kolmogorov took a different point of view and decided investigate if, and under what conditions, some invariant tori survive under perturbation. In other words, the goal was to find a solution for the motion of the system for specific values of the actions, corresponding to a unique set of frequencies, which turn out to be the nonresonant frequencies [6]. In 1954 he outlined a theorem that was later proven by Arnold and Moser in the early 1960's [6].

In Arnold's notation, a Hamiltonian system of the form

$$H\left(\boldsymbol{\theta},\mathbf{I}\right)=H_0\left(\mathbf{I}\right)+H_1\left(\boldsymbol{\theta},\mathbf{I}\right) \tag{2.42}$$

is considered where $H_1\left(\boldsymbol{\theta},\mathbf{I}\right)<<1$, periodic in the angle variables, and differentiable up to a sufficiently high order. It is also assumed that the unperturbed system is non-degenerate,

$$\det\left|\frac{\partial\omega_i\left(\mathbf{J}\right)}{\partial J_k}\right|=\det\left|\frac{\partial H\left(\mathbf{J}\right)}{\partial J_i\partial J_k}\right|\neq 0 \tag{2.43}$$

which implies that there cannot exist a relationship of the form $f\left(\omega_1,\omega_2\ldots\omega_n\right)=0$ unless some elements of **J** occur explicitly. To understand the importance of this equation differentiate $f\left(\omega_1,\omega_2\ldots\omega_n\right)=0$, to obtain the following system of equations,

$$\begin{aligned} \frac{\partial f}{\partial \omega_1}\frac{\partial \omega_1}{\partial J_1}+\ldots\frac{\partial f}{\partial \omega_n}\frac{\partial \omega_n}{\partial J_1}&=0\\ \vdots \qquad\qquad \vdots &= \vdots\\ \frac{\partial f}{\partial \omega_1}\frac{\partial \omega_1}{\partial J_n}+\ldots\frac{\partial f}{\partial \omega_n}\frac{\partial \omega_n}{\partial J_n}&=0 \end{aligned} \tag{2.44}$$

This system can only have the trivial solution

$$\frac{\partial f}{\partial \omega_k}=0 \quad k=1,\ldots,n \tag{2.45}$$

if $\det\left|\frac{\partial \omega_i(\mathbf{J})}{\partial J_k}\right|\neq 0$. This excludes any solution of the type,

$$f\left(\omega_1,\omega_2\ldots\omega_n\right)=a_1\omega_1+a_2\omega_2\ldots a_n\omega_n=0 \quad \forall a_i\neq 0 \tag{2.46}$$

thus the frequencies must be linearly independent. It follows that a set of frequencies satisfying the condition of non-degeneracy can be used to label unique non-resonant tori embedded in a (2*n*-1)-dimensional energy manifold. The resonant tori are everywhere dense, but of zero measure. The non-resonant tori are also everywhere dense, but of full measure. Another possibility is to have a set of $i<n$ independent frequencies. In this case there will be a resonant torus of dimension n-i.

An essential assumption is that the location in phase space must be sufficiently far from a resonance, satisfying the Diophantine condition. A vector $\boldsymbol{\omega}$ is said to satisfy this condition if for any integer vector, $\mathbf{k}$, $\mathbf{k}\neq 0$.

$$\left|\mathbf{k}\cdot\boldsymbol{\omega}\right|\geq\gamma\left|\mathbf{k}\right|^{-\mu} \tag{2.47}$$

Here γ is dependent on the size of the perturbation and μ is dependent on the number of degrees of freedom and the smoothness of the perturbation. A transcription of Kolmogorov's theorem will now be stated and can be found in Boccaletti [6].

> If the unperturbed system is non-degenerate or isoenergetically non-degenerate, then for a sufficiently small Hamiltonian perturbation most non-resonant invariant tori do not vanish but are only slightly deformed, so that in the phase space of the perturbed system there are invariant tori densely filled with conditionally periodic phase curves winding around them, with a number of independent frequencies equal to the number of degrees of freedom. These invariant tori form a majority in the sense that the measure of the complement of their union is small when the perturbation is small. In the case of iso-energetic non-degeneracy the invariant tori form a majority on each level manifold of the energy.

A system is iso-energetically non-degenerate if for a fixed energy the frequency ratios vary smoothly from torus to torus. For a system with *n*-degrees of freedom this is equivalent to satisfying the following condition.

$$\det\begin{vmatrix} \dfrac{\partial H_0}{\partial I_i I_j} & \dfrac{\partial H_0}{\partial I_i} \\ \dfrac{\partial H_0}{\partial I_j} & 0 \end{vmatrix} \neq 0 \tag{2.48}$$

In general, the frequency of the perturbed tori will depend on the size of the perturbation. For an isoenergetically non-degenerate the frequency ratio will be preserved for changes in the size of the perturbation.

The set of actions corresponding to the set of frequencies satisfying the Diophantine condition has the structure of a Cantor set. Stated simply, KAM theory indicates that for frequencies satisfying the Diophantine condition the perturbed system is integrable. Therefore, it is possible to find *n* integrals of motion for the set of actions corresponding to the set of

frequencies satisfying the condition. It is important to point out that KAM theory states nothing of the fate of resonant tori, this will be discussed next. In addition, there is the open question of how small the perturbation must be for the theorem to hold. If the perturbation is large enough all tori will be destroyed.

An instructive table relating the degrees of freedom (DOF) with dimensions of the phase space, energy shell, and tori is provided below [7].

Table 2-1 DOF versus dimension of phase space, energy shell, and tori.

DOF	1	2	3	4
Dimension of phase space	2	4	6	8
Dimension of energy shell	1	3	5	7
Dimension of tori	1	2	3	4

If the DOF is 2, the tori can divide the energy shell into distinct regions. Therefore, if the system is nonintegrable and there are chaotic regions lying between two distinct tori, the trajectory will be confined between these tori. For $n \geq 3$, the tori cannot divide the energy shell into distinct regions. As a result, the trajectories are not prohibited from traveling among the tori. This phenomenon is known as Arnold diffusion.

Area Preserving Maps and the Poincaré-Birkoff Fixed Point Theorem

KAM theory states that for a non-degenerate or iso-energetically non-degenerate system most non-resonant tori persist under a small perturbation. The theory states nothing pertaining the persistence or destruction of the resonant tori. This section introduces the main ideas of the Poincaré-Birkoff fixed point theorem and provides a basic explanation for the onset of chaos.

Consider a two DOF integrable system written in action angle variables. Such a system describes linear flow on a torus, embedded in the energy shell $H\left(I_1, I_2\right)$.

$$\begin{aligned} \theta_1(t) &= \omega_1 t + \theta_1(0) \\ \theta_2(t) &= \omega_2 t + \theta_2(0) \end{aligned} \tag{2.49}$$

The time it takes for θ_2 to complete one cycle is, $T_2 = 2\pi / \omega_2$ and the corresponding change in θ_1 can easily be found.

$$\theta_1\left(t + T_2\right) = \theta_1(t) + 2\pi\alpha \tag{2.50}$$

where $\alpha = \omega_1 / \omega_2$, is the rotation number. Noting that α can be written as only a function of I_1, since the energy is constant. A mapping, known as a twist map, T can be constructed in the $\left(I_1, \theta_1\right)$-plane. Setting $I = I_1$,

$$T : \begin{cases} \theta_{i+1} = \theta_i + 2\pi\alpha\left(I_i\right) \\ I_{i+1} = I_i \end{cases} \tag{2.51}$$

If the system is isoenergetically non-degenerate the rotation number will vary smoothly with I. It is obvious that, T, simply maps points on a circle with a radius defined by I_1. In fact, given any arbitrary circle it will map that circle into itself. It is also easy to show that this map is area preserving,

$$\frac{\partial\left(\theta_{i+1}, I_{i+1}\right)}{\partial\left(\theta_i, I_i\right)} = \begin{vmatrix} \dfrac{\partial\theta_{i+1}}{\partial\theta_i} & \dfrac{\partial I_{i+1}}{\partial I_i} \\ \dfrac{\partial I_{i+1}}{\partial\theta_i} & \dfrac{\partial I_{i+1}}{\partial I_i} \end{vmatrix} = \begin{vmatrix} 1 & 2\pi\alpha \\ 0 & 1 \end{vmatrix} = 1 \tag{2.52}$$

These ideas can be extended to systems with many degrees of freedom. If a constant value of θ_i is chosen as the surface of section, the rotation number becomes a vector $\boldsymbol{\omega}$ with *n*-1 components.

$$\omega_j / \omega_i \quad j = 1, 2 \ldots i-1, i+1, \ldots n-1 \tag{2.53}$$

Consider a nearly integrable system with the Hamiltonian

$$H\left(\boldsymbol{\theta}, \mathbf{I}\right) = H_0\left(\mathbf{I}\right) + \varepsilon H_1\left(\boldsymbol{\theta}, \mathbf{I}\right) \tag{2.54}$$

The twist map will be perturbed taking the general form,

$$T_\varepsilon : \begin{cases} \theta_{i+1} = \theta_i + 2\pi\alpha\left(I_{i+1}\right) + \varepsilon g\left(\theta_i, I_{i+1}\right) \\ I_{i+1} = I_i + \varepsilon f\left(\theta_i, I_{i+1}\right) \end{cases} \tag{2.55}$$

The map can be thought of as a canonical transformation, therefore a generating function of the form

$$S\left(\theta_i, I_{i+1}\right) = I_{i+1}\theta_i + 2\pi A\left(I_{i+1}\right) + \varepsilon F\left(\theta_i, I_{i+1}\right) \tag{2.56}$$

yields the map

$$T_\varepsilon : \begin{cases} \theta_{i+1} = \theta_i + 2\pi \dfrac{\partial A}{\partial I_{i+1}} + \varepsilon \dfrac{\partial F}{\partial I_{i+1}} \\ I_{i+1} = I_i - \varepsilon \dfrac{\partial F}{\partial \theta_i} \end{cases} \tag{2.57}$$

Comparing equations,

$$f = -\frac{\partial F}{\partial \theta_i} \quad g = \frac{\partial F}{\partial I_{i+1}} \quad \alpha = \frac{\partial A}{\partial I_{i+1}} \tag{2.58}$$

To preserve area the following condition must hold

$$\frac{\partial f}{\partial I_{i+1}} + \frac{\partial g}{\partial \theta_i} = 0 \tag{2.59}$$

Note that it is always possible to pass from a Hamiltonian system to its corresponding twist map. The preservation of circles defined by the unperturbed twist map was answered by Moser's contribution to KAM theory. He proved that for a sufficiently small perturbation and sufficiently irrational winding numbers most circles are preserved. Yet, KAM theory says nothing about circles with rational winding numbers. This question is answered by the Poincaré-Birkoff fixed point theorem. The main ideas of this theorem are outlined below.

Consider two invariant curves of the unperturbed twist map, C^+ and C^- lying on either outside and inside of a curve C with a rational winding number. Here it is assumed that α varies smoothly with I and that C^+ rotates counterclockwise whereas C^- rotates clockwise. It is easy to show that each point lying on C is a fixed point of the unperturbed twist map.

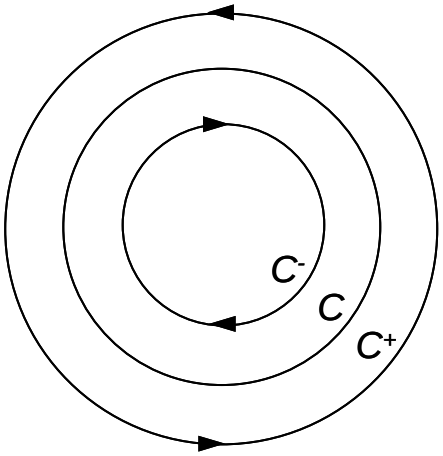

Fig. 2-6 Unperturbed twist map.

By the KAM theorem, C^+ and C^- will be preserved, although distorted. Thus, there will be two invariant curves, C_ε^+ and C_ε^-, of the perturbed twist map. If the perturbation is sufficiently weak, the direction of twist will be preserved for C^+ and C^-. Since, C_ε^+ and C_ε^- twist in opposite directions, for each radius vector drawn from the center there must be a point on that vector such that the angular coordinate is preserved under the mapping. The locus of these points is a curve labeled as F in Fig. 2-7. Note that I is permitted to change for arbitrary points on F.

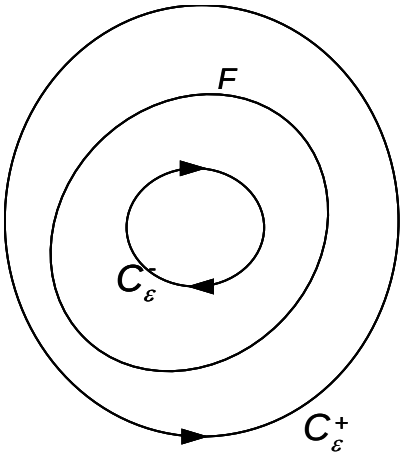

Fig. 2-7 Perturbed twist map.

The rotation number of *C*, which is an integer ratio, will be denoted by r/s. The goal is now to find the fixed points on *F*. To do this *F* will be subjected to the mapping T_ε, *s* times. The image of *F* after the mapping must intersect *F*, since the center must remain as an internal point and areas are preserved. Moreover, by a simple geometric argument, it must intersect *F* an even number of times. Each of these intersections are a fixed point for T_ε^s. Applying this map to one of the 2*k* intersection points, *P*, gives $P, T_\varepsilon P, T_\varepsilon^2 P, \ldots, T_\varepsilon^{s-1} P, T_\varepsilon^s P = P$. Each of the points in this series will be a fixed point of T_ε^s. Thus, there are $2ks \quad k = 1, 23, \ldots$ fixed points in all. It is straightforward to show that each of these fixed points will alternate as hyperbolic and elliptic fixed points by following the directions of the flow, shown in Fig. 2-8. The KAM theorem will be applicable to each of these elliptic fixed points. Within these elliptic regions will be tori with frequencies that can be expressed as an integer ratio. Thus, there will self-similar pattern on all scales.

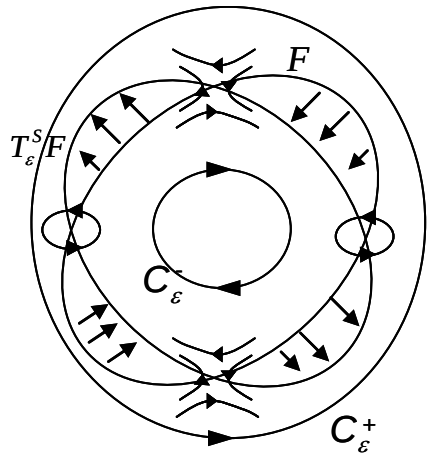

Fig. 2-8 *F* subjected to mapping.

A qualitative sketch shows the massive complexity of the perturbed dynamics. Under a large enough perturbation there will appear heteroclinic intersections between the stable and unstable manifolds of individual fixed point families. Since this requires a perturbation that destroys tori with irrational frequency ratios, one may expect widespread chaos under this condition. Upon this realization Poincaré stated [8]**:**

> One is struck by the complexity of this figure that I am not even attempting to draw. Nothing can give us a better idea of the complexity of the three-body problem and of all problems of dynamics where there is no holomorphic integral and Bohlin's series diverge.

This work will explore many cases where both heteroclinic points and widespread chaos are present. One widely accepted method for loosely predicting the onset of widespread chaos is to use the resonance overlap criterion developed by Chirkov. Walker provides an insightful numerical analysis that provides impetus for the criterion labeling the phenomenon as amplitude instability [9]. Wisdom was the first to use the ideas of the resonance overlap criterion to provide an approximation for the onset of widespread chaos in the CR3BP [10]. Under certain circumstances, a simple calculation using this approximation allows one to predict which first order resonant islands will persist under perturbation. The next section will discuss in detail the methods that will be used to numerically explore the stable regions predicted by the KAM theory and chaotic regions expected by interpretation of the Poincaré-Birkoff fixed point theorem.

The Lyapunov Exponent and the Fast Lyapunov Indicator

This section outlines theory that, for most systems, must be implemented numerically. First the maximum Lyapunov exponent (MLE), used as an indicator of chaos, will be introduced. Then the fast Lyapunov indicator (FLI) and related indicators will be described along with an

approach to stability mapping. These maps are shown to provide insight into the complex structure of phase space for non-integrable systems. As will be demonstrated this insight can be used to describe the evolution objects throughout the solar system.

The State Transition Matrix and the Maximum Lyapunov Exponent

Consider a general dynamical system defined by a vector field

$$\dot{\mathbf{x}} = f(\mathbf{x}) \quad \mathbf{x} \in R^n \tag{2.60}$$

Note that if the vector field is time dependent then an extra phase space coordinate can be introduced. If a certain solution $\mathbf{x}^*(t)$ is known, the perturbed solution becomes

$$\mathbf{x}(t) = \mathbf{x}^*(t) + \boldsymbol{\varepsilon}(t) \tag{2.61}$$

The equations describing the motion of this perturbed solution can be expressed as

$$\dot{\mathbf{x}}^* + \dot{\boldsymbol{\varepsilon}} = f(\mathbf{x}^* + \boldsymbol{\varepsilon}) \tag{2.62}$$

Noting that $\dot{\mathbf{x}}^* = f(\mathbf{x}^*)$ and taking only the first order terms of a Taylor's series, the expression can be approximated for small perturbations

$$\dot{\boldsymbol{\varepsilon}} \approx A(t)\boldsymbol{\varepsilon} \tag{2.63}$$

where $A(t)$ is the Jacobian of *f*. Thus, if ***x**** is evolving on some manifold *M* the prior expression will describe how any vector in the tangent space will evolve. This equation is called the first variational equation. A differential equation of this form has a unique solution [11].

$$\boldsymbol{\varepsilon}(t) = e^{At}\boldsymbol{\varepsilon}_0 \tag{2.64}$$

A fundamental solution matrix of the linear system

$$\dot{\boldsymbol{\varepsilon}} = A\boldsymbol{\varepsilon} \tag{2.65}$$

is any nonsingular *n*x*n* matrix, Φ, satisfying

$$\dot{\Phi} = A\Phi \quad \forall t \in R \tag{2.66}$$

It is trivial to show that $\Phi(t) = e^{At}$ is a fundamental solution matrix satisfying $\Phi(0) = I$. In fact, the solution of the linear system can be expressed as

$$\boldsymbol{\varepsilon}(t) = \Phi(t)\Phi^{-1}(0)\boldsymbol{\varepsilon}_0 \tag{2.67}$$

which can be verified by differentiating with respect to time. The introduction of the MLE follows from these fundamental results.

The coefficient of expansion about a trajectory $\mathbf{x}(t)$ through $\mathbf{x}_0$ in some direction, specified by the vector **e** in R^n, is given by

$$\lambda_t\left(\mathbf{x}_0,\mathbf{e}\right)=\frac{\left\|\Phi\left(t\right)\mathbf{e}\right\|}{\left\|\mathbf{e}\right\|}=\sqrt{\frac{\left\langle\Phi\left(t\right)\mathbf{e},\Phi\left(t\right)\mathbf{e}\right\rangle}{\left\langle\mathbf{e},\mathbf{e}\right\rangle}} \tag{2.68}$$

where $\|\cdot\|$ signifies the standard scalar product on R^n. Note that this entire expression is the Riemannian metric that has been chosen when speaking of the general theory [12, 13]. The Lyapunov characteristic exponent in the direction **e** along a particular orbit with an initial condition at $\mathbf{x}_0$ is defined, in terms of the coefficient of expansion, as

$$\chi\left(\mathbf{x}_0,\mathbf{e}\right)=\lim_{t\to\infty}\sup\log\lambda_t \tag{2.69}$$

Computationally it is easier to evaluate a limit instead of a limit supremum. Some terminology is necessary in order to introduce the applicable theorem.

An orthonormal basis in R^n is a normal basis if the quantity $\sum_{i=1}^{n}\chi\left(\mathbf{x}_0,\mathbf{e}_i\right)$ attains a minimum on that basis. This basis has been shown to exist [12]. A fundamental solution matrix is regular if the following limit exists and is finite

$$\lim_{t\to\infty}\log\left|\det\Phi\left(t\right)\right| \tag{2.70}$$

and if for every normal basis $\left\{\mathbf{e}_1,\ldots\mathbf{e}_n\right\}$

$$\sum_{i=1}^{n}\chi\left(\mathbf{x}_0,\mathbf{e}_i\right)=\lim_{t\to\infty}\log\left|\det\Phi\left(t\right)\right| \tag{2.71}$$

Now the following theorem can be introduced, which states existence in terms of the fundamental solution matrix [14].

Theorem:

If $\Phi(t)$ *is regular , then*

$$\chi(\mathbf{x}_0, \mathbf{e}) = \lim_{t\to\infty} \frac{1}{t} \log \lambda_t$$

The Lyaponuv exponent of a particular orbit is independent of the initial condition, since the time limit is taken to infinity.

Lyapunov exponents give information concerning the local expansion and contraction of phase space, yet reveal nothing of twisting or folding. In general the MLE is not a smooth function of initial conditions. As one would predict, the MLE on a KAM torus is zero. This can be shown by transforming the Hamiltonian of a torus into the Kolmogorov normal form [15]. In addition the evolution of $\frac{1}{t}\log \lambda_t$, specifically the oscillations, can be used to indicate the distance from a resonance [15] .

Before introducing the MLE algorithm, a mention of numerical reliability must be made. The theorems stated above do not take into account numerical errors incurred on a computer. But it has been found that if the orbit is sufficiently stochastic and the precision at each time step is high enough then one may conjecture that the computation of the LCEs is reliable [12]. The primary challenge of the MLE is that any randomly chosen initial vector will grow exponentially if $\chi_{\max}(x) > 0$. As a result the vector could exceed the limitations of the computer. The algorithm outlined below uses a renormalization procedure to overcome this problem.

For the purpose of this work we are concerned with computing a truncated version of the MLE. The renormalization procedure can be used when seeking a converged or truncated MLE value. This turns out to have an easy numerical algorithm, although computationally expensive.

The algorithm described by Benettin [13], chosen for its renormalization procedure, will be outlined below. To introduce the algorithm and some relevant theory a bit of terminology will first be introduced.

Consider a compact and connected manifold, *M* (the energy surface, for example), and a diffeomorphism, *T*, which maps the manifold into itself (as described by the flow). The differentiable flow generated by the vector field will be signified by T^t, thus for any *t*, $\mathbf{x}(t) = T^t\mathbf{x}$ where $\mathbf{x} \in M$. The tangent space at **x** to *M* will be denoted by $E_{\mathbf{x}}$. The mapping of $E_{\mathbf{x}}$ into $E_{T^t\mathbf{x}}$ will be denoted by $dT^t_{\mathbf{x}}$. Note that the Lyapunov characteristic exponent of the mapping is the same as that of the flow. Also, the mapping is linear, $dT^{t+s}_{\mathbf{x}} = dT^t_{\mathbf{x}_s}\left(dT^s_{\mathbf{x}}\mathbf{e}\right)$, where $\mathbf{x}_s$ is the position at time, *s*. Randomly choosing **e** with $\|\mathbf{e}\| = 1$ and setting $s \geq 1$, computing recursively yields the following algorithm.

MLE Algorithm [13]:

$$\mathbf{w}_o = \mathbf{e} \in E_0$$

$$\alpha_k = \left\| dT^s_{\mathbf{x}_{(k-1)s}}\mathbf{w}_{k-1} \right\|$$

$$\mathbf{w}_k = \frac{dT^s_{\mathbf{x}_{(k-1)s}}\mathbf{w}_{k-1}}{\alpha_k} \in E_{ks}$$

Thus, for $k \geq 1$

$$\left\| dT^{ks}_{\mathbf{x}}\mathbf{w}_{k-1} \right\| = \alpha_1 \ldots \alpha_n$$

and

$$\chi_{\max}(\mathbf{x}) = \lim_{k\to\infty} \frac{1}{ks}\sum_{i=1}^{k} \ln \alpha_i$$

This is a reliable algorithm for computing the MLE or a truncated version that solves the problem of computer overflow. Other algorithms have been conjured that try to estimate the MLE by calculating the difference of nearby trajectories so that integration of the variational equations can be avoided. Since these methodologies are prone to erroneous results, they will not be considered.

Fast Lyapunov Indicator

Since computation of the MLE requires integration of the variational equations, integration time can become prohibitively long. Typically, in the case of weak chaos, it can take over ten times the inverse of the MLE, the Lyapunov time. To solve this problem Froeschle et al. defined a closely related indicator, the FLI [16, 17]. Although there are multiple definitions of the FLI, in general it can be thought of as indicating the time necessary for a tangential vector to reach a given value or as the time for the angle between two vectors to reach a given value. Given some initial *n*-dimensional basis $\{\mathbf{e}_1(0),\ldots\mathbf{e}_n(0)\}$, Froeschlé et al. studied three variations of the FLI listed below,

$$\psi_1(t)=\frac{1}{\|\mathbf{e}_1(t)\|^n} \quad \psi_2(t)=\frac{1}{\Pi_{i=1}^n\|\mathbf{e}_i(t)\|} \quad \psi_3(t)=\frac{1}{\sup_i\|\mathbf{e}_i(t)\|^n} \tag{2.72}$$

The second and third expressions require finding the time evolution of *n* vectors. Computation time of the third indicator may be shortened by noting that after a certain time span the largest $\mathbf{e}_i$ will always persist as the largest. Thus, after this amount of time the evolution of only one vector will need to be tracked. The last indicator appears to be advantageous because it has exhibited little dependence on the initial basis.

Unlike the MLE, for a given orbit, the FLI does depend on the chosen initial condition. It also depends on the threshold chosen for the vector or angle. Therefore, the FLI is not intrinsically related to an individual orbit and as a result it cannot be used as an absolute measure of chaoticity [15]. It can, however, be used to compare the nature of one orbit relative to another with the MLE of one orbit acting as a calibration. For the exact relationship between the FLI, as defined above, and the MLE see Froeschlé [16].

The main advantage of the FLI over the MLE is the speed of computation. The FLI, specifically ψ_3, has also been shown to effectively indicate the presence of thin chaotic layers. It can be used to efficiently discriminate between regions of chaos and regions of regular motion. Moreover, it is possible to discern regions of macroscopic diffusion (Chirikov regime) and exponentially slow diffusion (Arnold web).

Another closely related parameter, known as the effective Lyapunov exponent, has been utilized by Doerner et al. [18]. The advantages of using this parameter is that it is closely related to the MLE and it can be interpreted as a function of the average "rate-of-strain" matrix over a finite segment of an orbit starting at $\mathbf{x}_0$. Using the coefficient of expansion, and some perturbation defined by the unit vector, $\mathbf{e} = \frac{\boldsymbol{\varepsilon}_o}{\varepsilon_o}$,

$$\lambda_t\left(\mathbf{x}_0, \mathbf{e}\right) = \sqrt{\frac{\left\langle \Phi\left(t\right)\mathbf{e}\varepsilon_o, \Phi\left(t\right)\mathbf{e}\varepsilon_o \right\rangle}{\left\langle \mathbf{e}\varepsilon_o, \mathbf{e}\varepsilon_o \right\rangle}} = \sqrt{\left\langle \Phi\left(t\right)\mathbf{e}, \Phi\left(t\right)\mathbf{e} \right\rangle} = \sqrt{\left\langle \mathbf{e}^T\Phi^T\left(t\right), \Phi\left(t\right)\mathbf{e} \right\rangle} \quad (2.73)$$

At an arbitrary time , t_f, $\Phi^T\left(t_f\right)\cdot\Phi\left(t_f\right)$ is a symmetric matrix with a set of orthonormal eigenvectors, $\left\{\mathbf{e}_{t_f}^{(1)}, \mathbf{e}_{t_f}^{(2)} \ldots \mathbf{e}_{t_f}^{(n)}\right\}$. Using the definition of a Lyapunov exponent and computing over a finite time, t_f, gives the effective Lyapunov exponent,

$$\chi_{eff}^{(i)}\left(\mathbf{x}_o, t_f\right) = \frac{1}{2t_f}\log\left(\left\langle \mathbf{e}_{t_f}^{(i)T}\Phi^T\left(t_f\right), \Phi\left(t_f\right)\mathbf{e}_{t_f}^{(i)}\right\rangle\right) \tag{2.74}$$

As in the case of the MLE, for any vector **e** chosen at random the largest effective Lyapunov exponent, $\chi_{eff}^{(n)}\left(\mathbf{x}_o, t_f\right)$, will be found. The analysis to follow will closely follow that given by Doerner [18].

To illuminate its relationship with the rate of strain matrix consider a solution $\varphi^t\left(\mathbf{x}_o\right)$ and the Jacobian $D\varphi^{t_f}\left(\mathbf{x}_o\right)$ at $t = t_f$. Breaking the orbit up into *N* segments with initial conditions $\mathbf{x}_o \ldots \mathbf{x}_{N-1}$ and realizing that the mapping is linear yields,

$$D\varphi^{t_f}\left(\mathbf{x}_o\right) = D\varphi^{t_f/N}\left(\mathbf{x}_o\right)\cdot D\varphi^{t_f/N}\left(\mathbf{x}_1\right)\ldots D\varphi^{t_f/N}\left(\mathbf{x}_{N-1}\right) \tag{2.75}$$

In general these factors do not commute, so that a time ordering operator, T, is needed,

$$D\phi^T\left(\mathbf{x}_o\right) = \mathrm{T}\left\{\prod_{\tau=0}^{N-1} D\phi^{t_f/N}\left(\mathbf{x}_\tau\right)\right\} \tag{2.76}$$

Using the Taylor series expansion with respect to time and taking the limit as the number of time increments goes to infinity,

$$\begin{aligned} D\varphi^{t_f}\left(\mathbf{x}_o\right) &= \lim_{N\to\infty}\left\{\prod_{\tau=0}^{N-1}\left(I + \frac{t_f}{N}Df\left(\mathbf{x}_\tau\right) + O\left(\left(\frac{t_f}{N}\right)^2\right)\right)\right\} \\ &= \lim_{N\to\infty}\left\{1 + \frac{t_f}{N}\sum_{\tau=0}^{N-1}Df\left(\mathbf{x}_\tau\right) + \left(\frac{t_f}{N}\right)^2\sum_{\tau=1}^{N-1}\sum_{\tau'=0}^{\tau-1}Df\left(\mathbf{x}_\tau\right)\cdot Df\left(\mathbf{x}_{\tau'}\right) + \ldots\right\} \end{aligned} \tag{2.77}$$

With considerable effort this expression can be expanded and simplified using the definition of an integral,

$$D\varphi^{T}\left(\mathbf{x}_{o}\right)=\mathrm{T}\left\{I+\sum_{j=0}^{\infty}\frac{1}{j}\left(\int_{0}^{t_{f}}Df\left(\varphi\left(\mathbf{x}_{o}\right)\right)dt\right)^{j}\right\} \tag{2.78}$$

Setting $S\left(\mathbf{x}_{o},t_{f}\right)=\frac{1}{t_{f}}\int_{0}^{t_{f}}Df\left(\varphi\left(\mathbf{x}_{o}\right)\right)dt$ it is clear that

$$\Phi\left(t_{f}\right)=D\varphi^{t_{f}}\left(\mathbf{x}_{o}\right)=\mathrm{T}\exp\left(t_{f}S\left(\mathbf{x}_{o},t_{f}\right)\right) \tag{2.79}$$

Finally, the effective Lyapunov exponent becomes

$$\chi_{eff}^{(i)}\left(\mathbf{x}_{o},T\right)=\frac{1}{t_{f}}\log\sqrt{\left\langle\left(\mathbf{e}_{t_{f}}^{(i)T}\mathrm{T}\exp\left(t_{f}S\left(\mathbf{x}_{o},t_{f}\right)\right)^{T},\mathrm{T}\exp\left(t_{f}S\left(\mathbf{x}_{o},t_{f}\right)\right)\mathbf{e}_{t_{f}}^{(i)}\right)\right\rangle} \tag{2.80}$$

Thus, the effective Lyapunov exponent is a function of the average over the rate of strain matrices. Because of this property, FLI or effective Lyapunov exponents will often show structures in regions of relatively high strain that do not necessary correspond to invariant manifolds. Thus, some caution must be exercised when interpreting FLI maps.

The Mean FLI and Practical Implementation

Although the FLI has a number of definitions, for the purpose of this study, an indicator closely resembling the MLE and effective Lyapunov exponent at some final time *T* will be used,

$$FLI\left(T,\mathbf{x}_0,\mathbf{e}\right)=\log\lambda_T \tag{2.81}$$

An FLI map is simply the mapping of FLI values over a grid of initial conditions which have commonly been expressed as density plots. The concept of mapping these types of parameters has history in both dynamical systems theory and in fluid mechanics where, for time-dependent flows, it is has been called the finite time Lyapunov exponent [19]. The first case of these values being mapped in the manner described is currently not known by the author. The first application to a spacecraft control problem appears to be by Villac in 2005 [20, 21].

To show how FLI maps illuminate the pathways and boundaries in phase space consider a hyperbolic point represented here in a two-dimensional phase space. Note that this could correspond to a hyperbolic point on a two-dimesional map defined by a surface of section/Poincaré section. If two initial conditions, represented in Fig. 2-9 by black dots on either side of a stable manifold, are integrated forward in time they will, after a certain period of time, diverge after passing the hyperbolic point. Conversely, if two initial conditions are integrated backward in time along the unstable manifold, they too will diverge. Thus, in many cases initial conditions lying very close to invariant manifolds will have relatively high FLI values. However, if the invariant manifold is embedded within a large chaotic zone and the integration times are low it may exhibit lower FLI values, since over a finite time the local expansion and contraction of phase space will be less than conditions in surrounding regions. As will be demonstrated in the next chapter, manifolds, marking the boundary of lobes emanating from sticky regions in the CR3BP, exhibit lower FLI values due to lobe dynamics.

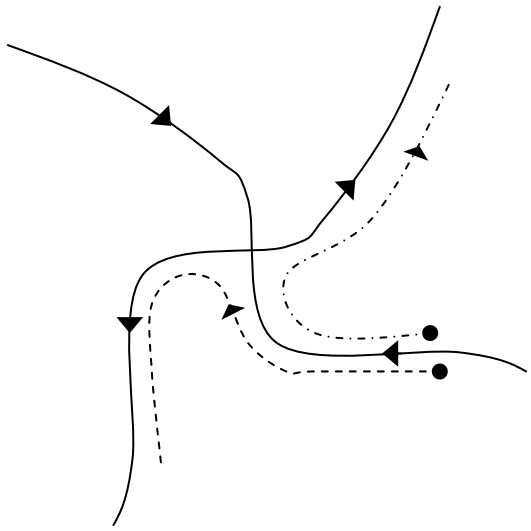

Fig. 2-9 Representation of a Hyperbolic Point in Two-Dimensional Space

Integrating forward and backward in time reveals stable and unstable manifold structures. If the forward FLI is denoted by FLI^{+} and the backward FLI by FLI^{-}, a highbrid parameter, called the mean FLI, FLI_m, can be formed

$$FLI_m = \frac{1}{2}\left(FLI^{+} + FLI^{-}\right) \tag{2.82}$$

such that both the stable and unstable manifolds are revealed when this parameter is mapped on a grid of initial conditions. For an autonomous system these structures will mark the invariant manifolds emanating from a hyperbolic point. For time-dependent systems analogous structures still exist, although they may evolve with time. These are often called coherent structures (CS) [19]. Flux across well defined CS structure is almost negligibly small. In order to effectively

utilize this mapping approach a few technical issues must be discussed. This will be done by way of a well studied example, the Duffing oscillator.

The damped, forced Duffing oscillator is described by the following set of equations.

$$\begin{aligned} \dot{x} &= y \\ \dot{y} &= x - x^3 - \varepsilon y + \gamma \cos \omega t \end{aligned} \tag{2.83}$$

where ε, γ, and ω are constants representing the damping, forcing amplitude, and angular rate, respectively. Consider the unforced oscillator where γ is set to zero. This system has three equilibrium points along the *x*-axis at $x = 0, \pm 1$. For $0 < \varepsilon < \sqrt{8}$ the equilibrium points, from left to right, are a sink, a saddle, and a sink where the sinks have an imaginary component of their eigenvalues. As mentioned, to illuminate the stable manifolds at the origin FLI^{+} must be utilized. Conversely, to show the unstable manifold FLI^{-} must be used. Figure 2-10 shows a these maps near the origin.

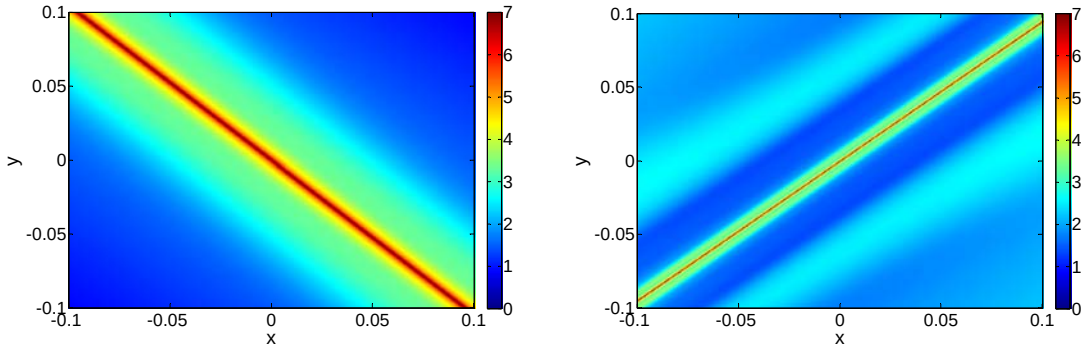

Fig. 2-10 Forward and backward FLI maps showing the stable and unstable manifolds, respectively. The color scale defines the FLI value at each initial condition.

Notice that the unstable manifolds, shown on the right are less prominent than the stable manifolds. This is a result of the initial vector, **e,** chosen by the algorithm. In this case, **e** is

nearly parallel to the unstable manifold. Obviously, it is impossible to avoid this situation under all circumstances for a set value of **e**. One solution is to randomly pick **e** for each initial condition, yet this leads to maps which are grainy in appearance. The mean FLI map, shown in Fig. 2-11, shows all manifolds of the (0, 0) equilibrium point.

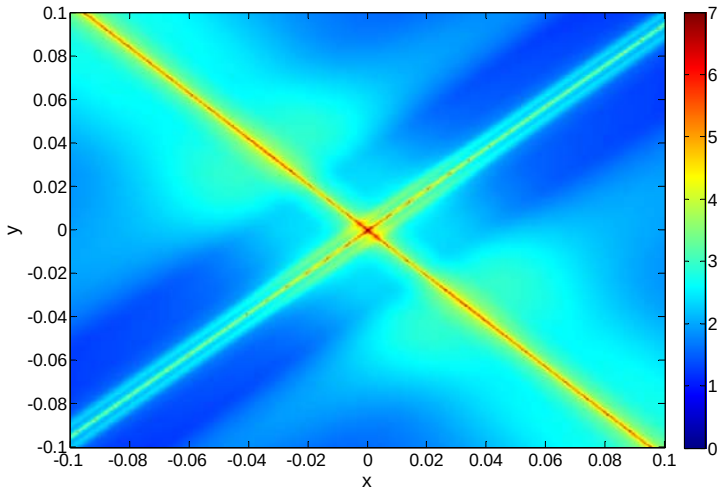

Fig. 2-11 Mean FLI map of the region shown in Fig. 2-10. The color scale defines the FLI value at each initial condition.

The mean FLI map has the advantage of showing all of the manifolds, but the average dims them with respect to the background. This dimming effect does not occur if stable and unstable manifolds intersect at either a homoclinic or heteroclinic point. As will be demonstrated later, this helps locate regions of dynamical connections for more complicated systems. Important to analysis of the unforced Duffing oscillator are the basins of attraction, which separate orbits that converge on each of the equilibrium points corresponding to sinks. Without any numerical analysis a simple sketch can be constructed that shows that the stable manifold forms the boundary of the basins, as shown in Fig. 2-12. The black line represents the stable and

unstable manifolds. The unstable manifold approaches the sinks, due to damping. The second plot shows the computation of the basins of attraction using the forward FLI map.

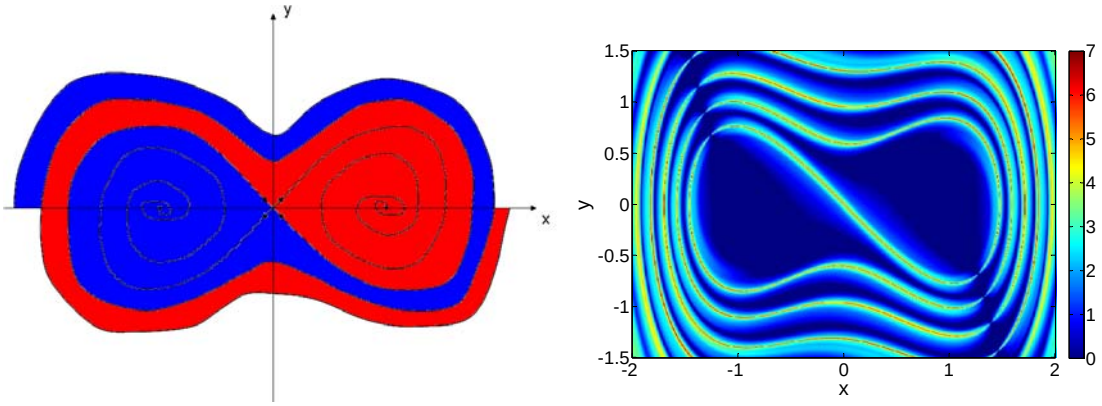

Fig. 2-12 Sketch and computation of the basins of attraction. The black lines indicate sketches of the stable and unstable manifolds. The color scale defines the FLI value at each initial condition.

High and low FLI values correspond to red and blue hues, respectively. An artifact of the initial **e** chosen by the algorithm can be seen by the apparent blue streak on the upper left and lower right corners of the map. Again, accepting this imperfection must be weighed against other options such as randomly choosing **e** for each initial condition. Notice that as the stable manifolds are followed from the origin they become less distinct. This occurs because a significant divergence of nearby orbits does not take place until they reach the vicinity of the origin. In fact using a highly simplified model, Doerner [18] has shown that the length of these structures increases linearly with time, yet the width decreases exponentially with time.

The manifolds comprise of an infinite set of exceptional initial conditions, of measure zero. This means that if the grid of initial conditions possessed an infinite number of points there is a probability of zero of randomly picking one of the exceptional conditions. Practically, one must work with both a finite grid of initial conditions and a finite integration time. At lower

integration times the FLI structure, in this case the stable manifold, will appear as a thick fuzzy line. Here the test particle has had insufficient time to depart from the region near the stable manifold. At higher integration times the structures will appear more distinct, yet if the initial condition grid is not fine enough the structure may not be detected at all. In this case, many of the initial conditions that started out close to the set of exceptional points have had time diverge into the surrounding regions.

By these arguments, in order to make the length of the structure longer or the line more distinct both the integration time and the number of grid points must be increased. This translates to a compounding effect on the computation time required to build a map. With modern computers computation times for the Duffing oscillator are not prohibitively long, yet when dealing with more complex models, such as the CR3BP, an increase in grid size or integration time can have a significant effect. The FLI map is effective for the global visualization of phase space, while traditional techniques, such as seeding manifolds, are used for a more precise representation of phase space in a certain regions. This appears to be a valid technique when dealing with autonomous systems, yet methods such as seeding break down for non-autonomous systems. Perhaps techniques that exploit an adaptive grid size may provide a solution.

One of the advantages of using FLI maps is that they can easily be used for non-autonomous systems. For these systems there are no fixed points. Accordingly, the invariant manifolds observed in autonomous systems no longer exist, yet analogous time-dependent structures in which an initial condition has a low probability of crossing do exist. As mentioned before, these structures are often called CS in fluid mechanics, yet they will simply be referred to as FLI structures in this discussion. Consider again the Duffing oscillator, this time with a forcing term. For low values of forcing, there appears an unstable limit cycle about the origin. After some simplification, this limit cycle can be shown to exist analytically [14]. Taking a "stroboscopic" Poincaré section (only considering a time series whose elements are exactly a

period of the forcing apart) a point on the limit cycle appears as an unstable equilibrium point. A qualitative sketch is shown in Fig. 2-13.

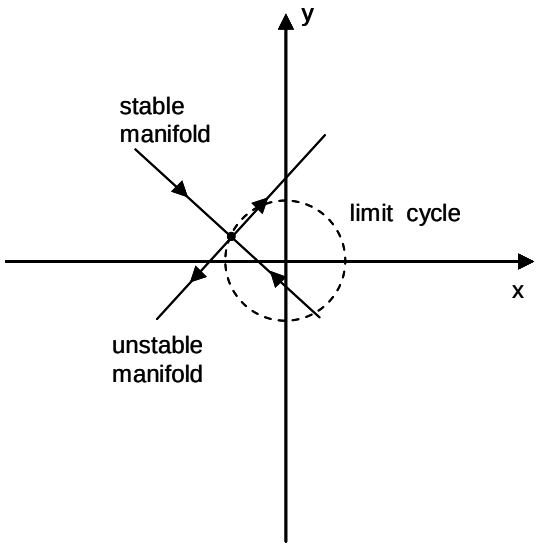

Fig. 2-13 Unstable limit cycle of the forced Duffing oscillator.

For low values of the forcing amplitude the stable and unstable manifolds do not intersect. Therefore, there is no homoclinic tangle accompanied by "Smale horseshoe-like" dynamics. In other words, the system is not chaotic. It is possible to construct a set of FLI maps each with a different epoch time. Examining these maps sequentially, the FLI structures will evolve with time. Each epoch will correspond to a different point on the limit cycle. Therefore, as shown in Fig. 2-14 the FLI structure evolve with a point on the limit cycle revolving about the origin.

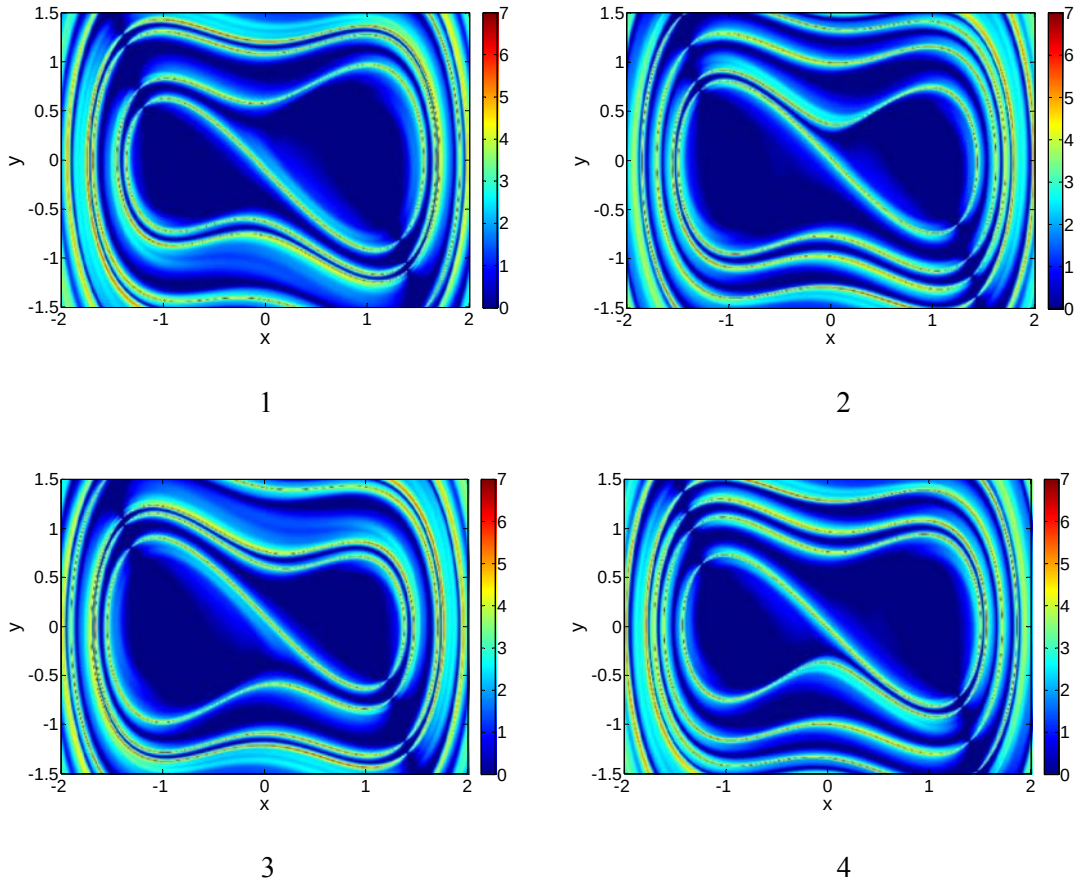

Fig. 2-14 Progression of FLI maps for the forced Duffing oscillator where the color scale defines the FLI value at each initial condition

Plot 1 shows the FLI map at the beginning of the period. Each subsequent plot shows the map one quarter of a forcing period later. Due to the symmetry of the system plots 1 and 2 rotated by 180 deg. yields plots 3 and 4 respectively. Notice the expansion and contraction of the basins of attraction. These act as moving boundaries that determine the ultimate fate of a particle influenced by the dynamics. Thus, inserting a particle into the system at some arbitrary epoch, an accurate prediction of which basin a particle will fall into can be made. A simple experiment shows that placing a particle on the FLI structure itself will cause it to converge to the unstable limit cycle.

A statement pertaining to the fate of this particle can be made without prior knowledge of the limit cycle. As proved in Shadden [25], it is known for time dependent systems that a particle has a low probability of crossing a well defined FLI structure. Thus, the converse must be true. If a particle starts on an FLI structure then it must have a low probability of leaving that structure. Note the term "starts on" is used loosely since the structure has a measure of zero. A more intuitive argument may be stated as follows. If a particle is integrated from an apparent structure on the map, then that initial condition must have a distinctly different FLI value compared to the surrounding phase space. Thus, if the particle left the vicinity of the structure during the integration time, it would have a value more closely matching the surrounding phase space.

If the forcing amplitude is increased above a certain threshold, the stable and unstable manifolds of the limit cycle will cross marking a homoclinic bifurcation. If the manifolds cross once on a "stroboscopic" Poincaré section then they must cross an infinite number of times due to well known theorems of existence and uniqueness. At this point the dynamics take on the characteristics of the Smale horseshoe map. Namely, there are a countable infinity of unstable periodic orbits, an uncountable infinity of bounded nonperiodic orbits, and a dense orbit. The sensitive dependence on initial conditions, one of the characteristics of chaos, can be demonstrated by using symbolic dynamics, see the Smale-Birkhoff homoclinic theorem presented in Ref. 14.

Often visualization of the flow is achieved by stringing together a succession of stroboscopic Poincaré maps. Although some of the flow structure can be seen on these maps, one must rely on the positioning of points relative to one another to identify major structures in phase space. These maps often become cluttered making exact quantification of flow structure difficult. In addition, if a particle has a low probability of returning to a certain region of phase space then structure in these regions may be difficult attain using this method. Using the FLI map on a grid of initial conditions overcomes some of these shortcomings especially in complex systems such

as the CR3BP. Figure 2-15 shows the evolution of the FLI map with the epoch time. A test particle, a white dot with a red rim, has been inserted into the flow.

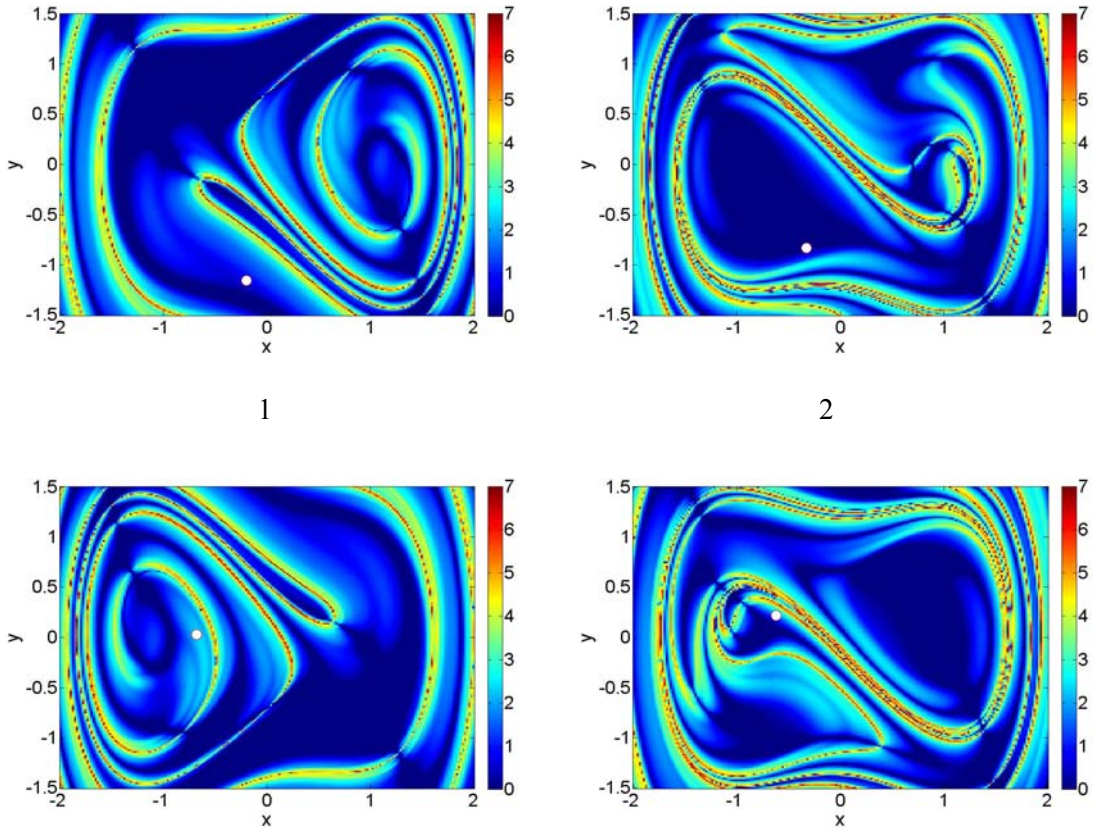

1 2

3 4

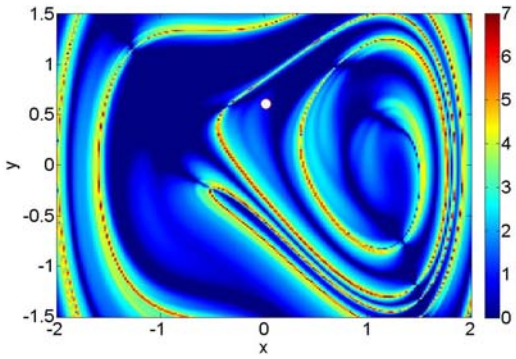

5

Fig. 2-15 Progression of FLI maps, values indicated by the color scale, for the forced Duffing oscillator after homoclinic bifurcation.

Here each epoch is incremented by approximately a quarter of the forcing period. Therefore, the fifth map is nearly identical to the first, showing the position of the test particle a forcing period into the future. The maps show how the test particle is transported from one region to another, essential being "pushed" by the evolving FLI structure. There is a continuous mixing and folding of phase space consistent with the horseshoe map. As before, the symmetry of the equations of motion is evident by rotating plots 1 and 2 by 180 deg. or half of the forcing period.

The techniques that were used to analyze the Duffing oscillator can be extended to systems of greater dimension and complexity. In order to achieve reasonable integration times for such systems, parallel computing must be implemented. Alternatively, the use of system specific parameters can be used to classify distinct regions of phase space. One such parameter is provided for the CR3BP including a simple dissipation model.

Relevance

The remainder of the dissertation utilizes the theoretical foundation provided in this chapter to analyze the complexities of the CR3BP. Without this knowledge the revealed structures have no explanation taking on an almost mysterious quality. KAM theory states that objects on stable orbits (KAM tori) remain on them for all time, thus a change in energy is necessary for transport to other regions. Moreover, the Poincaré-Birkoff fixed point theorem indicates that finite portions of the stable regions are infinitely complex containing saddle and center points at all scales. Therefore, there exist bounded chaotic orbits within what are commonly referred to as stable regions. These orbits are bound between KAM tori in the planar problem and for practical purposes can be considered bound in the three-dimensions. Thus, in most cases, Arnold diffusion may be ignored.

By past numerical studies and observation of both spacecraft and celestial bodies, it is known that tori with irrational frequency ratios have been destroyed in the CR3BP for mass ratios within the solar system. By creating dynamical connections among resonant orbits of distinct frequency ratios the perturbation to the two-body problem is large enough to facilitate transport for sufficient energies. For example, an object may be transported from chaotic regions within the solar system to the fringe of the stable distant retrograde region about a planet in the outer solar system. This object, however, cannot be stabilized (follow a KAM torus) without a change in energy. These observations essentially state that the information inferred from the two-body problem is insufficient to describe transport phenomena.

FLI maps efficiently discriminate between chaotic and stable regions of phase space. They are utilized to show the evolution of stable regions and other phase space structures through energy. Such classifications are difficult to obtain using traditional surface of sections and manifold seeding, especially through energy, where identification of homoclinic points would

have to be obtained by some automated manner. They are used to identify dynamical pathways through phase space, especially among stable resonant regions, before precise analysis through tedious manifold seeding. The maps discern regions of various capture times contained within complex homoclinic tangles that are difficult to analyze given current mathematical theory. The practical details for constructing FLI maps outlined in chapter are applied throughout the dissertation.

The notion of invariant manifolds in the CR3BP breaks down with the inclusion of dissipation, such as nebular drag, or a spacecraft maneuver over a finite time period. The evolution of CSs with time was clearly demonstrated on the FLI maps. Because of the time-scales involved in the problems addressed in this dissertation, distinct CS structures generally do no appear. However, clear discernment can be made among orbits which remain on chaotic trajectories and those which are either stabilized or remain on stable orbits. The idea of the CS structure, as it was interpreted in the previous section, is manifested as a clear phase space boundary separating these two outcomes.

References

[1] Celletti, A., Chierchia, L., "On the stability of realistic three-body problems", *Commun. Math. Phys.*, Vol. 186, pp. 413-449, 1997.

[2] Szebehely, V., *Theory of Orbits: The Restricted Problem of Three Bodies*, Academic Press, New York, 1967.

[3] Conley, C., "Low Energy Transit Orbits in the Restricted Three-Body Problem", *SIAM J. Appl. Math*, Vol. 16, No. 4, 1968.

[4] Gómez, G., Koon, W., Lo, M., Marsden, J., Masdemont, J., and Ross, S., "Invariant manifolds, the spatial three-body problem and space mission design", *AAS/AIAA Astrodynamics Specialist Conference, Quebec City, Canada*, , AAS 01-301, 2001.

[5] Myers, K., "The Geometry of Harmonic Oscillators", *The American Mathematical Monthly*, Vol. 97, No. 6, pp. 457-465, 1990

[6] Boccaletii, D. and Pucacco, G., *Theory of Orbits: 2: Perturbative and Geometrical Methods*, Springer, 1998.

[7] Tabor, M, *Chaos and Integrability in Nonlinear Dynamic*s, John Wiley & Sons, New York, 1989.

[8] Arnold, V.I. and Avez, A., *Ergodic Problems of Classical Mechanics*, Addison-Wesley Publishing Company, Inc., New York, 1989.

[9] Walker, G.H., Ford, J., "Amplitude Instability and Ergodic Behavior for Conservative Nonlinear Oscillator Systems", *Physical Review*, Vol. 188, No. 1, pp. 416-431, 1969.

[10] Wisdom, J., "The Resonance Overlap Criterion and the Onset of Stochastic Behavior in the Restricted Three-Body Problem, *The Astronomical Journal*, Vol. 85, No. 8, 1980.

[11] Perko, L., *Differential Equations and Dynamical Systems*. *Texts in Applied Mathematics 7.* Springer-Verlag, New York, 2000.

[12] Benettin, G., Galgani, L., Giorgilli, A. and Strelcyn, J., "Lyapunov characteristic exponents for smooth dynamical systems and for Hamiltonian systems; A method for computing all of them. Part 1: Theory", *Meccanica*, Vol. 15, No. 1, pp. 9-20, 1980.

[13] Benettin, G., Galgani, L., Giorgilli, A. and Strelcyn, J., "Lyapunov characteristic exponents for smooth dynamical systems and for Hamiltonian systems; A method for computing all of them. Part 2: Numerical application.", *Meccanica*, Vol. 15, No. 1, pp. 21-30, 1980.

[14] Wiggins, S., *Introduction to Applied Nonlinear Dynamical Systems and Chaos*, Springer-Verlag, New York, 1990.

[15] Morbidelli, A., *Modern Celestial Mechanics: Aspects of Solar System Dynamics*, Talor and Francis, New York, 2002.

[16] Froeschlé, C., Lega, E., and Gongczi, R, "Fast Lyapunov indicators. Application to asteroidal motion", *Celestial Mechanics and Dynamical Astronomy*, Vol. 67, pp. 41-62, 1997.

[17] Froeschlé, C., Lega, E., and Gongczi, R, "The fast Lyapunov indicator: a simple tool to detect weak chaos. Application to the structure of the main asteroidal belt. *Planetary and Space Sci.*, Vol. 45, pp. 881-886, 1997.

[18] Doerner, R., Hubinger, B., Martienssen, W., Grossman, S., and Thomae, S., "Stable Manifolds and the Predictability of Dynamical Systems", *Chaos, Solitons, & Fractals*, pp. 1759-1782, 1999.

[19] Shadden, S.C., Lekien, F., and Marsden, J. E., "Definition and properties of Lagrangian coherent structures from finite-time Lyapunov exponents in two-dimensional aperiodic flows", Physica D, Vol. 212, pp. 271-304, 2005.

[20] Villac, B.F., Mapping long-term stability regions using the fast Lyapunov indicator, *Advances in Astronautical Sciences, 15th AAS/AIAA Spaceflight Mechanics Meeting, Copper Mountain, CO*, January 23-27, AAS 05-188, 2005.

[21] Villac, B.F., Lara, M., "Stability maps, global dynamics and transfers", *Proceedings of the 2005 AAS/AIAA Astrodynamics Specialist Conference,* AAS 05-378, 2005.

Chapter 3

Satellite Capture and Transport in the Outer Solar System

The developments of this chapter constitute an original study pertaining to the capture of irregular satellites in the plane of the sun-Jupiter system. Physical explanations are provided for statistical data found in the literature. This work distinguishes itself by approaching the satellite capture problem from a dynamical systems perspective. In particular, dynamical phenomena are analyzed by way of geometric structures in phase space rather than solely on statistical data. Since this viewpoint is largely absent in the literature, this chapter entails not only new work but a new viewpoint to the problem of satellite capture. The techniques introduced in this chapter may be further developed to analyze other complex problems such as the transport of Kuiper belt objects in the outer solar system and more intricate formulations of the restricted problem, such as the elliptic restricted problem, the circular restricted four-body problem, and three-dimensional models. Additionally, the general dynamical analysis lays the foundation for topics involving spacecraft transfers in the sun-Earth system to be covered in chapters 4 and 5.

This chapter was inspired by a number of sources including recent work in astrodynamics, the classical problem of satellite capture in celestial mechanics, and mathematical techniques commonly applied to fluid mechanics and, more recently, astrodynamics. Statistical evidence is provided that suggests that particles trapped by Jupiter originate near the fringes of stable, sun-centered resonant islands. Moreover, transport is shown to be controlled by unstable periodic orbits lying at fringes of the stable regions, known as bounding unstable periodic orbits (BUPOs).

The role of the BUPOs and their manifolds is analyzed by utilization of FLI maps, manifold theory, and statistical evidence. A new mapping parameter is introduced that speeds up

the computation of capture regions in the dissipative problem by a factor of three. Heteroclinic connections are demonstrated among manifolds emanating from unstable periodic orbits bordering the distant retrograde region about the smaller primary and the stable resonant islands of about the larger primary. A mapping technique is developed that facilitates the classification of the widths and locations of the stable regions and the energy threshold necessary to avoid collision with the second primary. This threshold for capture and escape is identified with a physical explanation involving the morphology manifolds emanating from the fringes of the stable region. The manifolds which make the connections dictate direct transport into and out of the so called sticky regions that border the surviving KAM tori of the two-body problems. These sticky regions retain motion that is referred to as "stable chaos". A simple analysis of the lobes facilitates the classification of short and long term temporarily captured orbits in the distant retrograde region.

Permanent capture is demonstrated by the addition of dissipation to the circular restricted three-body problem (CR3BP). Regions of capture are identified in both the conservative and dissipative system by way of FLI maps, manifold theory, and a newly introduced mapping parameter. Structures presented in this chapter aid the comprehension of the classical satellite capture problem, lay the foundation for problems of greater complexity, and efficacious spacecraft transfers throughout the solar system. In particular, later chapters will build on these developments for the construction of spacecraft trajectories to both stable and sticky distant retrograde orbits.

Background

The Jovian planets each possess a population of regular satellites revolving in nearly circular equatorial orbits. These satellites reside in prograde orbits about their planets, indicative

of the disks of gas which coalesced into each of the Jovian systems. Quite different from regular satellites, populations of irregular satellites have highly tilted, elongated orbits. Most of these irregular satellites evolve in retrograde orbits, often called distant retrograde orbits (DROs), which contradicts the popular formation scenario. The existence of this class of satellites has been recognized for over 150 years, starting with the discovery of Neptune's satellite Triton in 1846. By the end of the twentieth century only ten irregular satellites had been discovered. However, in recent times there has been an explosion of discoveries that parallels the aftermath of the detection of the first trans-Neptunian object [1]. In the last decade astronomers, using modern technology, have discovered dozens of these objects dispersed over a wide region of space. This vastness of this region, on the order of the size of the Hill sphere[1], explains why most irregular satellites had gone undetected for centuries.

Astronomers have found that the majority of irregular satellites are comparatively small, on the order of a few kilometers in diameter, and are clumped into distinct families distinguished by their orbital characteristics. Spacecraft missions such as Cassini and Voyager 2 have revealed that they resemble the composition of captured comets and asteroids, with those of Jupiter missing the volatile compounds. As a result, astronomers have long theorized that many irregular satellites have a capture origin with large fractions residing in stable distant retrograde orbits [2, 3]. Some examples are those that reside in Saturn's Norse group and Jupiter's Ananke group.

Early numerical work was conducted by Hénon using Hill's equations, an approximation of the CR3BP about the second primary. He demonstrated that essentially all retrograde periodic orbits around the smaller body are stable for $0 \le \mu < 0.0477$ [4]. This range includes all natural and artificial bodies within the solar system with the exception of the Pluto-Charon system. Many studies have numerically integrated numerous test particles to study capture phenomena. Results have shown that captured satellites most likely originated from chaotic regions about the

[1] A planet's Hill sphere comprises the approximate volume where it dominates the attraction satellites.

sun [2]. Additionally, temporary capture has been studied from a dynamical systems approach. The invariant manifolds emanating from periodic orbits about L_1 and L_2 act as gatekeepers to the second primary. This approach has been used to describe the phenomenon of resonance transition exhibited by short period comets such as Oterma [5, 6].

DROs have drawn the attention of the astrodynamics community due to the possibility of achieving highly energetic, yet stable orbits or orbits or long-term stability [7-11]. A notable overview of their utility can be found in Lam et al. [7] where a realistic dynamical model is utilized. Stability boundaries and a variety of transfers were investigated including spiral in and spiral out maneuvers. In 2005, Villac introduced the notion of using FLI maps to discover thrust-free transfers among resonant regions in the circular restricted three-body problem, specifically, in the Jupiter-Europa system [10, 11]. This chapter draws on a number of observations and concepts developed in the field of astrodynamics. In particular, the structures apparent on FLI maps are examined in greater detail.

In the plane, if a particle initially lies outside of an invariant torus, it is forbidden to enter for all time, see Table 2-1. This can be inferred by noting that the energy shell and a KAM torus possess a three and two-dimensional surface, respectively. Thus, the energy shell can be divided into closed regions by the KAM tori. Practically speaking this is also the case in the spatial problem. Here the time to enter a volume of nearly integrable phase space is super-exponentially long [12]. Since most irregular satellites currently reside in stable orbits, this points to other dynamical mechanisms that must have dissipated energy from the system. One prevalent theory is that nebular drag acted to ensure capture. Another theory states a scenario where the satellite is initially part of a binary system. One of the masses is ejected, thus depleting enough energy for capture. This chapter will investigate the case nebular drag. As mentioned, most studies have relied on integration of numerous test particles. A modern example integrated 80 million test

particles in the Hill's sphere and plotted capture probability distribution with inclination and Jacobi constant [3].

This chapter takes a complementary approach for capture in the plane. Brunini [2] found that satellites escaping Jupiter tended to collect near the major resonance zones in the sun-Jupiter system. Similarly, he found that satellites captured by Jupiter originated from the same regions of space. The impetus for this study comes from two hypotheses. The first is that for a range of energies a dynamical connection, by way of invariant manifolds, exists between the sun-centered mean motion resonances with Jupiter and the DROs about Jupiter. Moreover, these manifolds are responsible for transport into and out of the fringes of these regions. The second is that edges of invariant tori are sufficiently sticky. In other words, orbits lying on the frontier of a stability region tend to remain in its vicinity for long segments of time. If this time is long enough, nebular drag can dissipate adequate energy for permanent capture. This stickiness near the separatrix of mean motion resonances has been identified to be the cause of so called "stable chaos". "Stable chaos", a prototypical oxymoron, refers to particles that have dynamical lifetimes longer than one would expect from the Lyapunov time [13].

Dynamical Analysis

The CR3BP can be thought of as a perturbation of the two-body problem. Since the two-body problem is an integrable Hamiltonian system, it is foliated with invariant tori. Expressing the system in action angle variables, for instance Delaunay variables, the twist map resembles Fig. 2-5. Under small perturbations, the rational tori are destroyed leaving a structure of center-saddle-center on all scales around a circle of rational frequency ratios. In this case, KAM theory predicts that most non-resonant invariant tori do not vanish and are only slightly deformed. If the perturbation is large enough some irrational tori will be destroyed, allowing for the possibility of

heteroclinic connections between distinct regions space. Therefore, the system is neither ergodic nor everywhere integrable and will possess a divided phase space filled with both chaotic and stable orbits. This situation must exist if there are connections between the resonant and distant retrograde regions.

Using these observations, the phase space can be pictured as a chaotic sea marked by islands of stability. Each island is composed of quasi-periodic orbits and bounded chaotic orbits surrounding a stable periodic orbit. Here the classification of stable also applies to the bounded chaotic orbits within each island. A 2006 Scientific American article, authored by a prominent astronomer, points out that the orbits of many irregular satellites are akin to figures from the children's toy Spirograph [14]. These are in fact the bounded chaotic and quasi-periodic orbits interior to the stability region. Typical examples in the sun-Jupiter system of each of these orbits are shown in Fig. 3-1 where intersections with the *x*-axis are shown in Fig. 3-1d. Since an orbit traversing the chaotic sea can not enter a KAM torus, unstable periodic orbits are sought near the edge of the stable regions. It follows that invariant manifolds of these orbits will form connections with other regions of space and may control transport at the fringes of stability regions.

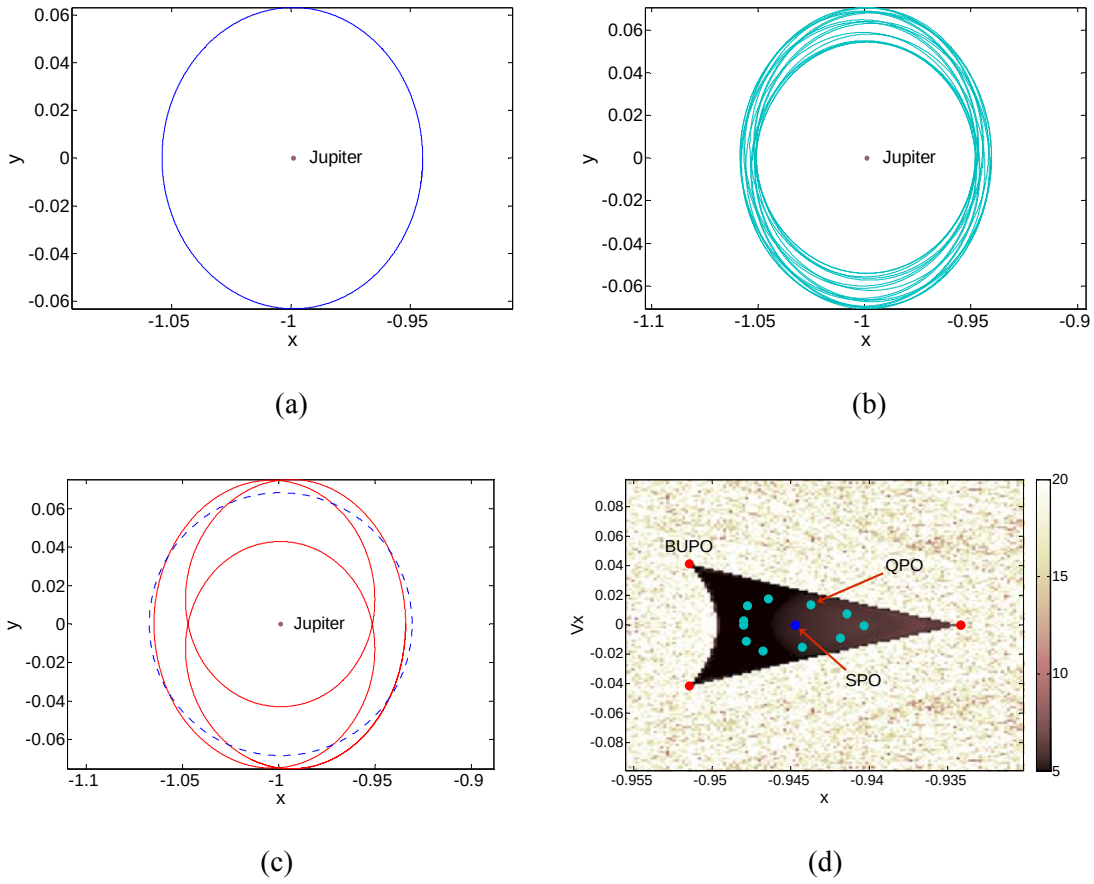

Fig. 3-1 Typical orbits within the distant retrograde region. (a-c) Examples of a stable periodic orbit, quasi-periodic orbit, and a BUPO orbit about Jupiter. The dotted line in (c) marks the edge of the Hill sphere. (d) The intersection of the bounding unstable periodic orbit, quasi-periodic orbit, and stable periodic orbit with the *x*-axis against a mean FLI stability mapping where the shades indicate FLI values. A Jacobi constant of -1.5 was used for each orbit.

A Jacobi constant of -1.5 allows access to all of the collinear Lagrange points, slightly above the energy of L_3, forming curves of zero velocity qualitatively similar to Fig. 2-5d. The precise value of the energy is irrelevant in respect to the mechanisms responsible for satellite capture. However, the geometry of the structures at C=-1.5, chosen after some trial and error, are such that they are easily identifiable, marking tightly knit paths, in the Monte Carlo simulations to follow. Additionally, the geometry of the lobes is such that it eases demonstration in the analysis

to follow. The evolution of these phase space structures in this and future chapters will be shown to effect both capture and collision probabilities.

Capture Distributions

Previous studies have statistical analyzed the distribution of particles bombarding the Hill sphere [3, 15, 16]. This section begins with a similar approach presenting a Monte Carlo simulation of 6 million particles bombarding the Hill sphere in the CR3BP. However, this study is the first to use this method in order to identify the precise paths of capture and escape and the associated dynamical mechanisms. The notion of a sphere is a misnomer when considering only the plane of Jupiter's orbit. Yet, to avoid confusion, this outlying region will continue to be referred to as the Hill sphere. Initial conditions were chosen in the following manner: First, an initial position was uniformly and randomly selected on a circle 10% greater than the Hill Sphere. This is necessary so that the sample space does not intersect the stable region. Next, using the Jacobi constant the magnitude of the velocity vector was calculated. After uniformly and randomly generating the direction of the velocity vector the simulation continued until one of three criteria was satisfied, viz., a predetermined cut-off time was reached, the particle collided with Jupiter, or the particle evolved beyond the vicinity of the circle of radius 10% greater than the Hill sphere up to specified threshold.

To illuminate the mechanisms of capture the first and last x-axis crossings of the surviving particles are recorded. To visualize the distribution in the Cartesian frame, these points can be plotted on the x-V_x plane against a mean FLI stability map, where V_x is the velocity in the x-direction in the rotating frame at the point of crossing. Figure 3-2a shows the first and last x-axis crossings of particles surviving 95 years by green and red dots. Figure 3-2b and c show only the last x-axis crossing of particles surviving a 190 and 227 year simulation.

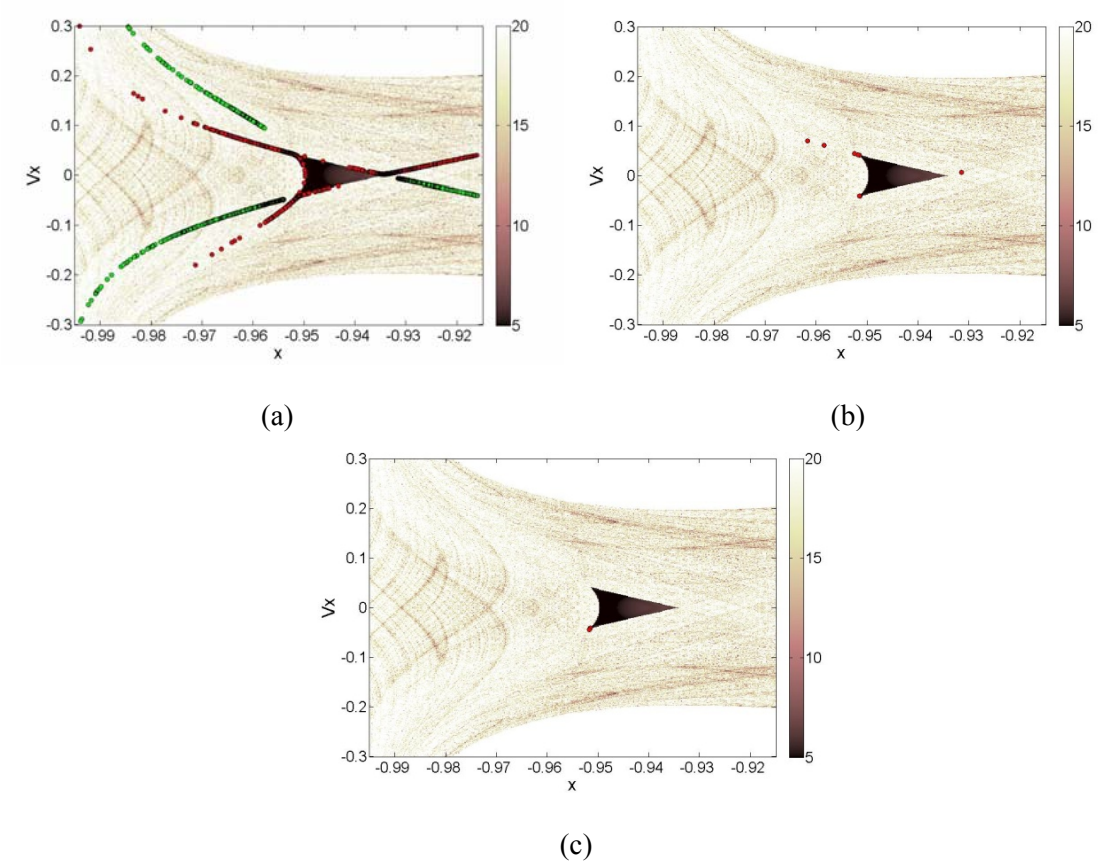

Fig. 3-2 Mapping of Monte Carlo simulations, (a) Mapping of the first and last *x*-axis crossings of particles surviving a 95 year simulation. (b) and (c) The last *x*-crossings of particles surviving simulations lasting approximately 190 and 227 years, respectively. The first and last *x*-axis crossings are indicated by green and red dots. Points are plotted against a mean FLI stability map where the color scale indicates the FLI value and the dark, triangular region constitutes a stable region. A Jacobi constant of -1.5 was used for all test particles and maps.

Evidenced by the vast decrease of red points in Fig 3-2b and c, the number of surviving particles depends on the simulation time. A particle has approximately a 1 in 5,200 chance of surviving a simulation of 95 years, whereas a particle has 1 in 750,000 chance of surviving 190 years and a 1 in 2,000,000 chance of surviving 227 years. Each plot shows a clustering of particles on the outer fringes, the sticky frontier, of the stability region. Only those near the corners of this region survive for longer integration times. Notice that the first *x*-axis crossings

follow well defined paths in Fig. 3-2a approaching the corners of the stable region. Similarly, the last crossing occurs on lines emanating from the same points. These structures indicate that temporarily captured particles follow precise paths through space. A deviation from this path results in an expedient escape or collision. An understanding of the final distributions of surviving objects certainly follows from a detailed knowledge of these structures.

Particles surviving the simulations collect near the fringes of the stability region, corresponding to the *x*-axis crossings of a bounding unstable periodic orbit (BUPO) and its manifolds. It will be shown that the manifolds are responsible for the transport of particles into and out of a thin, sticky region just outside of the impenetrable realm of the stable quasi-periodic orbits.

Figure 3-3a and b show the distribution of eccentricity and semi-major axis, as a fraction of the radius of the Hill sphere, about Jupiter for the BUPO. Each data point was taken at the end of 24,000 equally spaced time intervals up to the period of the orbit, approximately 11.8 years. For comparison, Fig. 3c and 3d show the distribution of data points from the last 11.8 years of particles surviving a Monte Carlo simulation of 227 years. The sampling rate was chosen to match 24,000 data points. Here *N* represents the number of particles falling within each bin separated by the vertical lines. These figures show that the orbital elements of captured objects closely track the orbital elements of the BUPO. Due to the dynamical similarities of the homoclinic tangle, the BUPOs for any stable region may be used to estimate/predict peaks in capture distributions prevalent in the literature [2, 3]. Below it is shown that that this approach also applies to distributions for particles trapped near the fringes of the stable resonant islands.

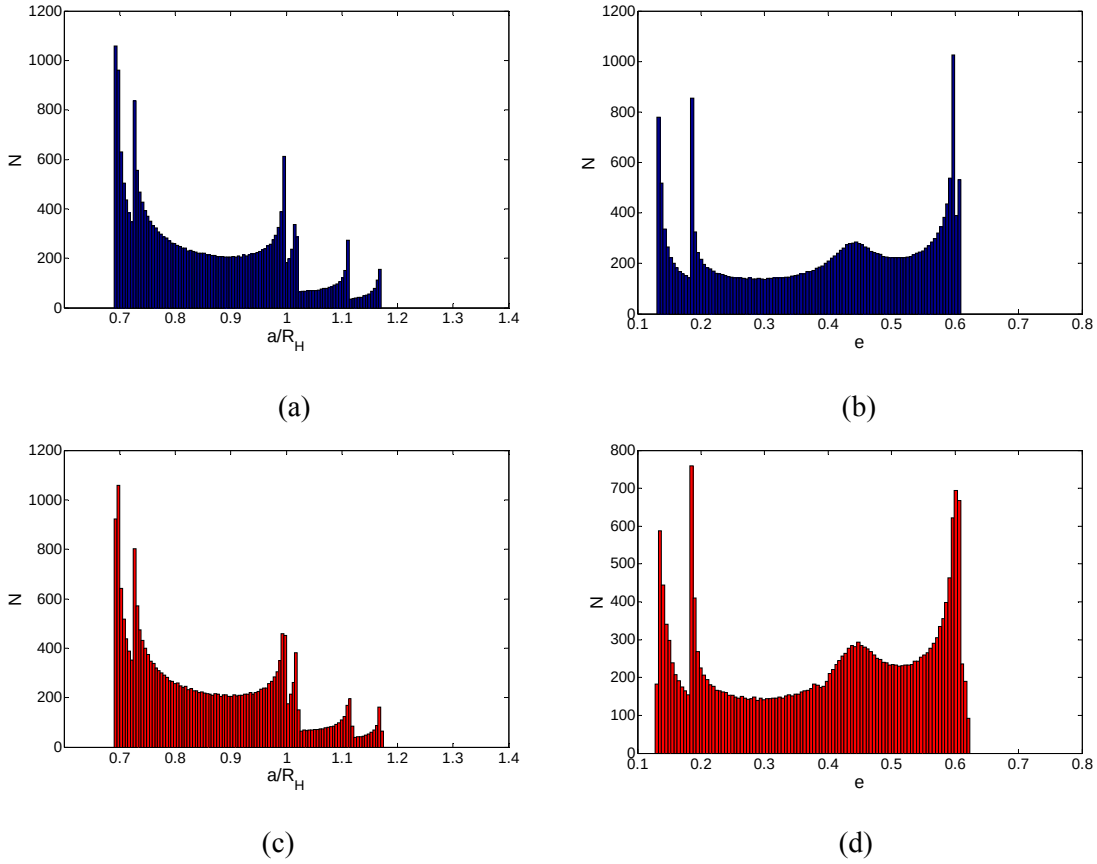

Fig. 3-3 Orbital element distributions resulting from a Monte Carlo simulation and BUPO. (a) and (b), The distribution of semi-major axis and eccentricity about the Jupiter of the BUPO. (c) and (d) similar distributions for the last 11.8 years of particles surviving a Monte Carlo simulation of 227 years.

At this particular energy, as the simulation time is increased only the points closest to the edge of the stable distant retrograde region survive. This indicates that the stickiest regions lie near to these structures, yet, as will be demonstrated in chapter 5, is a function of the stability index and the size of the homoclinic tangle. Knowing, a priori, the capture orbits and where they intersect the Hill sphere the probability that a randomly sampled orbit would fall within a capture region can be calculated. This may be a fruitful exercise, since a recent study required 80 million test particles in order to find 23,000 capture orbits [3].

Figure 3-2a attests that particles surviving Monte Carlo simulations travel along distinct paths in space. These paths are a manifestation of the stability characteristic of the BUPO. Moving forward in time, stable manifolds converge to the BUPO. Thus, a logical conclusion is that the collection of green dots in Fig. 3-2a corresponds to a stable manifold. Likewise, unstable manifolds diverge from the BUPO; therefore the assortment red dots lie on the unstable manifold. Indeed, Fig. 3-4 provides verification that particles surviving the simulations follow paths drawn out by the stable and unstable manifolds. In fact, these are elongated lobes manifolds of homoclinic tangle surrounding the stable region. Here the *x*-axis crossings of the stable and unstable manifolds are shown by the thin green and red lines, respectively. So that they are not obscured, only surviving particles of the first one million randomly selected initial conditions are displayed.

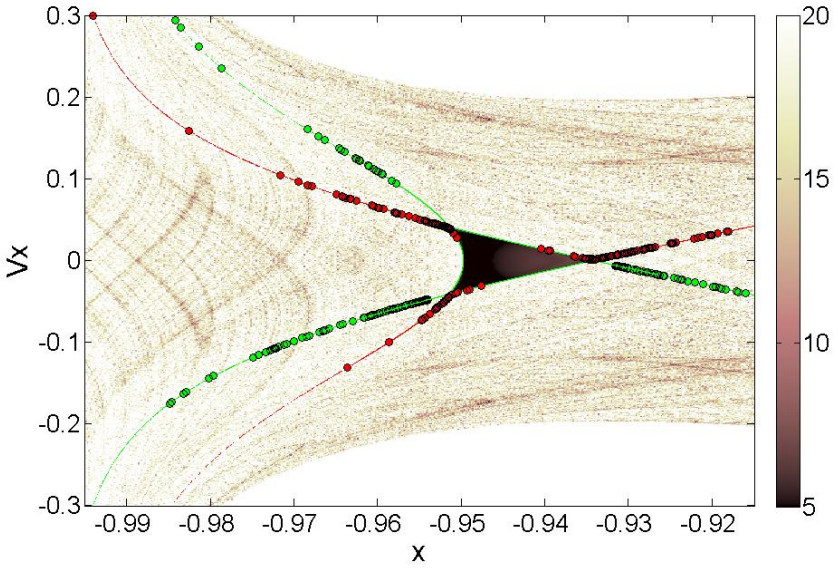

Fig. 3-4 Mapping of the first and last *x*-axis crossings of an assortment of particles surviving 95 years against a mean FLI stability map where the hues indicate the FLI value. Crossings of the stable and unstable manifolds are shown by green and red lines, respectively. The dark triangular region constitutes a stability region. A Jacobi constant of -1.5 was used for all test particles.

BUPO and their associated manifolds control the flux of particles into and out of the region of space surrounding the stability region. Particles approaching the region will follow the stable manifolds, whereas diverging particles will follow the unstable manifolds. Along the border of the stability region the manifolds become tangled, sowing the seeds of chaos, yet causing particles to be cycled many times through the local lobe dynamics. This is the root of the sticky behavior within the thin region surrounding the stability zone.

Figure 3-5b shows a close-up of the BUPO's right-most *x*-axis crossing. The unstable manifold emanating from the upper-left crossing approaches the right-most crossing and begins to form loops. These loops, also called lobes, stretch farther into space as upon their approach. The stable manifold behaves in a similar manner on the lower half of the plot. These loops are crucial to understanding the transport of objects into and out of this region. All captured particles remaining near the stable region for an extended time period must approach via the lobes formed by the stable manifold. Other potential mechanisms of extended capture have been ruled out by way of the Monte Carlo simulations.

Figure 3-5a shows a capture and escape orbits passing near the same region of phase space. The *x*-axis crossings are shown in Fig. 3-5b along with the first three crossings of capture and escape orbits. Notice that the first crossing of the capture orbit (1C) starts inside of a lobe formed by the stable manifold. Each orbit traverses near the edge of the stable region, but the escape orbit deviates from a Jupiter-centered trajectory after only one circumnavigation (many times about Jupiter) of the stable region. It does not experience an extended period of capture, because it starts outside of the lobes. The captured orbit will circumnavigate the region for an extended time period before delayed escape due to the lobe dynamics.

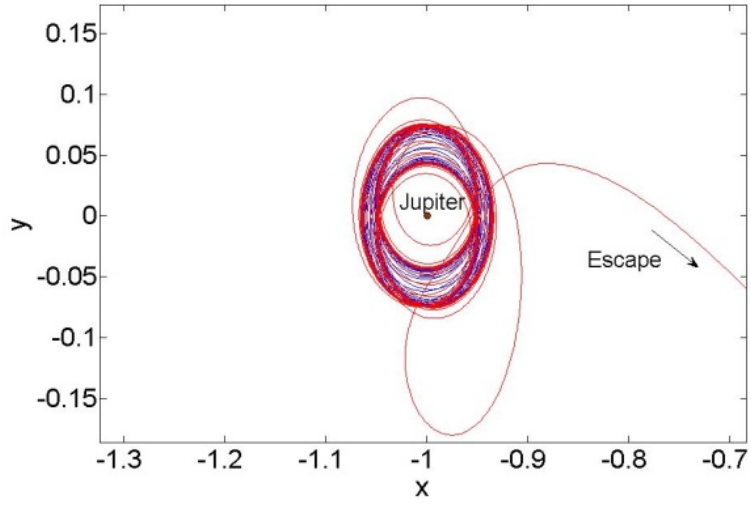

(a)

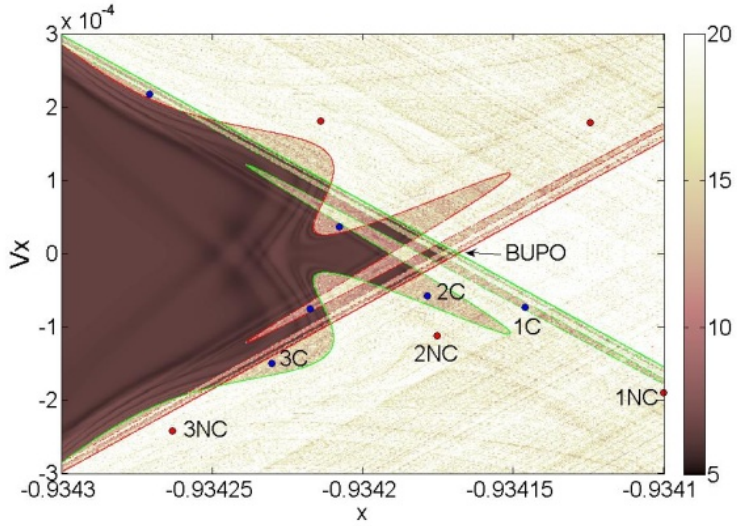

(b)

Fig. 3-5 Demonstration of capture and escape mechanism, *C*=-1.5. (a) Capture and escape trajectories in physical space in blue and red. (b) FLI map where color indicates the FLI value. Mapping of the *x*-axis crossings of an escape and capture trajectory signified by red and blue dots, in that order. Crossings of the stable and unstable manifolds are shown by green and red lines, respectively.

Homoclinic tangles near the edge of stable regions in the CR3BP hold vital importance, because they are a generic phenomenon. All of the major mean motion resonances about the sun

possess BUPOs and associated manifolds which control transport. Extending to three-degrees-freedom higher dimensional analog of this behavior are find. Lobes from distinct region of space may cross. It is at these crossings where all orbits transported from the fringes of one stability region to another must pass. The author hypothesizes that this is the mechanism responsible for resonance transitions observed during the evolution of many short-period comets including Oterma and Gehrels. These are the precise connections within the IPS.

It is possible to infer the origin of captured objects by integrating backwards along the stable manifold of the BUPO. Figure 3-6 shows the final distribution of particles surviving a simulation of 100 Jupiter years. In this case, a particle survives if it has not collided with the sun or Jupiter. Compared to Brunini's [2] results, there exists many more surviving particles at low eccentricities. This is due to disparate criteria for survival and methodologies to generate initial conditions. More importantly this simulation only tests one energy level. The distribution spikes in semi-major axis at approximately 4, 7, and 8.6 AU are associated with the 3:2, 2:3, and 1:2 mean motion resonances. Other than at low eccentricities, the spikes agree with those found by Brunini [2]. Knowing a priori the final location of captured orbits in phase space, along the stable manifold, much numerical effort was saved compared to methodologies involving random sampling.

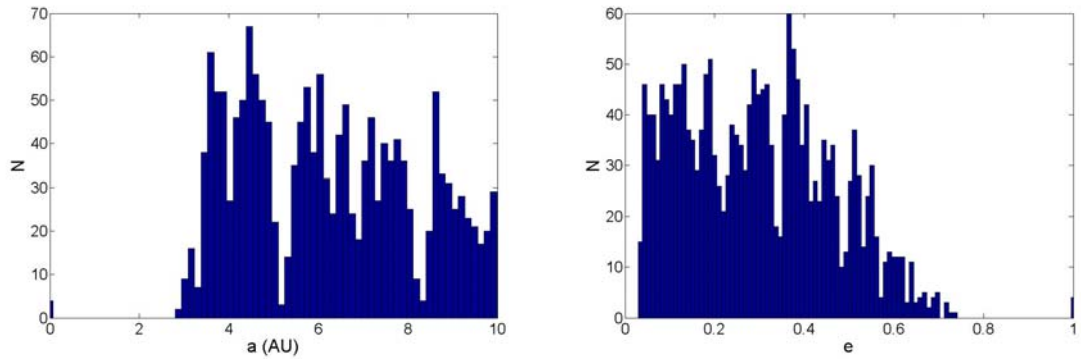

Fig. 3-6 Distribution of semi-major axis and eccentricity for particles surviving a simulation of 100 Jupiter years.

By dimensionality, the test particles are forbidden from entering stable resonant islands, see Table 2-1. Therefore, the spikes in orbital elements are better understood by examining the dynamics on the sticky fringes of these islands. The spikes in orbital distributions can be examined by considering the distribution of orbital elements along unstable periodic orbits bounding the stable regions. Figure 3-7 shows the orbital element distributions of these orbits in the sun-Jupiter system. These plots are constructed by calculating the semi-major axis and eccentricity at 200 equally spaced intervals over the period of the orbit.

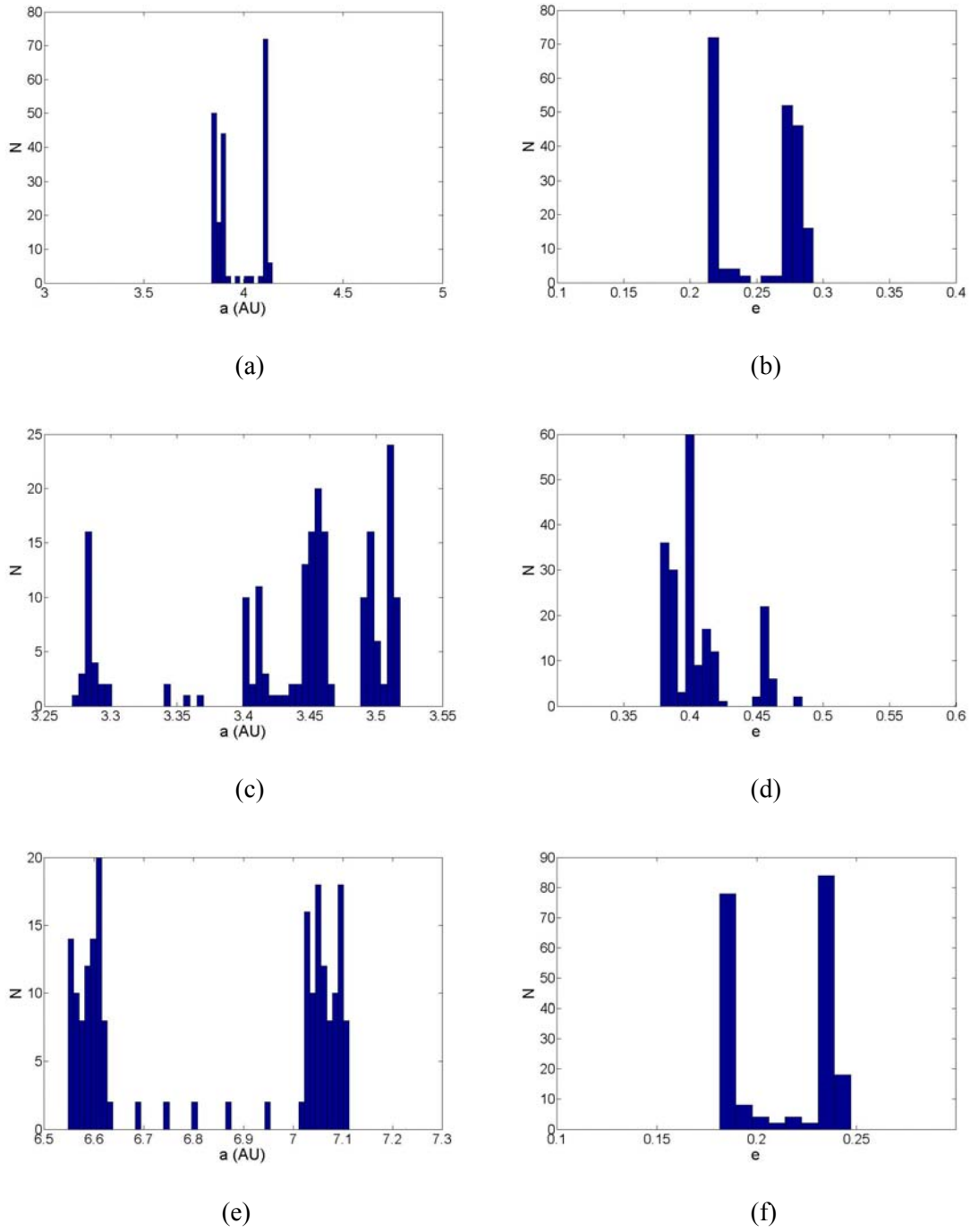

Fig. 3-7 Distribution of sun-centered unstable periodic orbits bounding stable regions. (a) and (b) Distributions along the 18:12 resonant periodic orbit bordering the 3:2 stable island. (c) and (d) 28:14 bordering the 2:1 island. (e) and (f) 10:15 resonant periodic orbit lying at the fringes of the 2:3 island.

A comparison of Figs. 3-7 and 3-6 indicates that particles destined to be captured by Jupiter have a high probability of originating from the vicinity of the 2:1 and 3:2 resonant islands. Some of the smaller spikes can be attributed to the 2:3 and 1:2 exterior resonances. Thus, the spikes in Fig. 3-6 are associated with the BUPO and its homoclinic tangle on the frontier of each stable region.

Figure 3-8 shows many of the resonant periodic orbits marking the interiors and borders the stability regions in the sun-Jupiter system. The qualitative features of the geometries hold for a large range of mass ratios. The next section takes a closer look at the dynamics near the distant retrograde region and the use of FLI maps and an alternative method in the context of global transport.

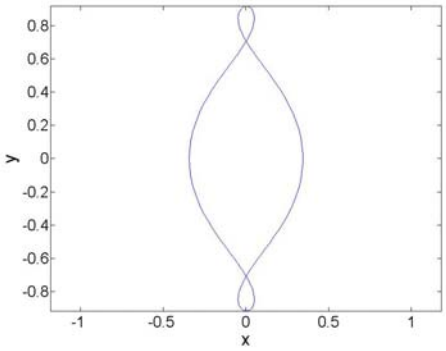

(a)

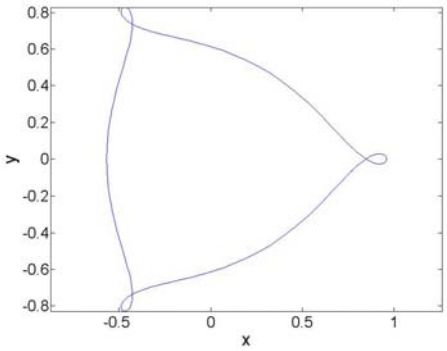

(b)

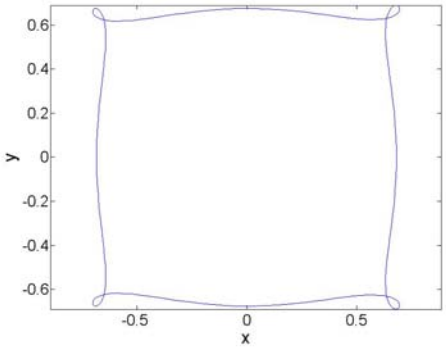

(c)

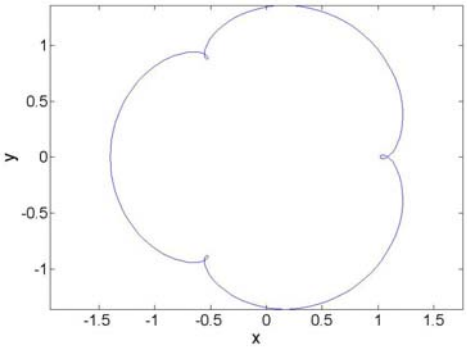

(d)

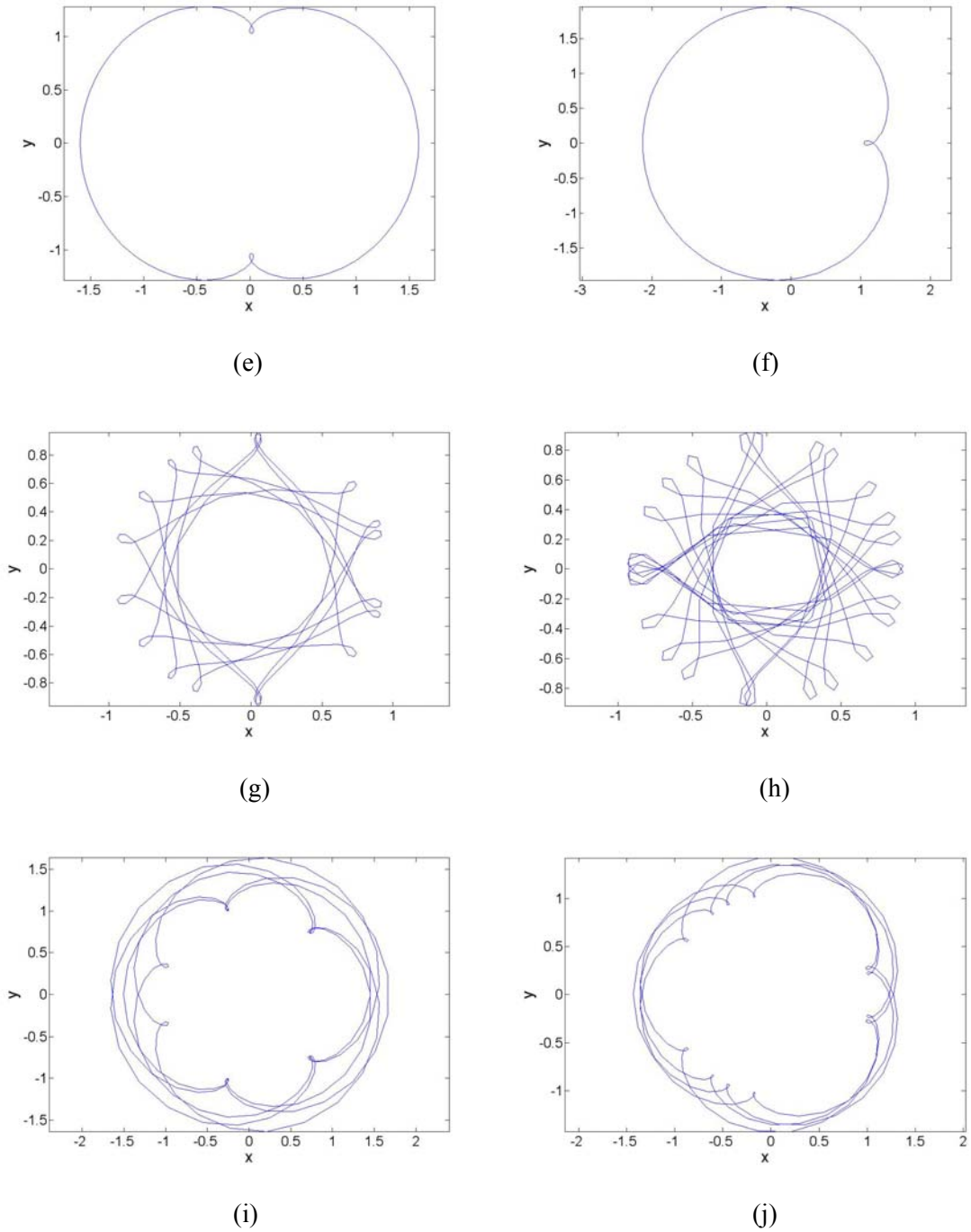

Fig. 3-8 Resonant periodic orbits in physical space. (a-f) Plots of 2:1, 3:2, 4:3, 3:4, 2:3, and 1:2 first order resonant periodic orbits. (g-j) Plots of 18:12, 28:14, 10:15, and 12:16 resonant periodic orbits associated with the 3:2, 2:1, 2:3, and 3:4 stable resonant islands in the sun-Jupiter system.

The Capture Process

The Conservative Problem

This section takes a closer look at the mechanisms responsible for transport into the distant retrograde region. In the conservative system the structure of the lobes at a specific energy are analyzed along with the consequences of a particular orbit being transported to the fringes of the distant retrograde region. The structure of the conservative system provides the framework for transport in the dissipative system. An energy threshold below which capture is not possible is identified along with a physical explanation of probable collision.

An estimate of which first order resonant islands will be destroyed can be attained by applying the resonant overlap criterion to the CR3BP [17]. If an interior resonance is given by $(s+1):s$, the criterion predicts that resonances should begin to overlap when $s \cong .51\mu^{-2/7}$. Rounding to the nearest integer, the interior first order resonances should begin to overlap at the 5:4 resonance in the sun-Jupiter system.

At low energies the stable retrograde orbits are located in the vicinity of the planet and are nearly circular. As the energy is increased the stable region moves past L_1, $x \cong -0.9323$, and approaches a 2:1 axis ratio, with the shortest axis parallel to the Jupiter-sun line. Further increases destroy the apparent symmetry about Jupiter. Using Hénon's classification system, the quasi-periodic orbits in the distant retrograde region encompass the family *f* period orbits. The division between Jupiter and sun-centered orbits is marked by a wide region of chaotic orbits near the "bottleneck" of the energy manifold exhibiting "Smale horseshoe-like" dynamics that dictate capture and escape from Jupiter. This chaotic region is caused by a homoclinic tangle of the of the center manifold encompassing L_1 and a heteroclinic tangle among the of the L_1 and L_2 center manifolds.

The positions and widths of the stable regions can be calculated by building a mean FLI map of Jacobi constant versus position on the *x*-axis. The initial conditions of Fig. 3-9 were first calculated by setting a value for *x* and *C*, leaving *y*, V_x, and V_y to be determined. With no loss of generality *y* can be set to zero. This leaves two unknowns and one constant of motion. The center of libration, the stable periodic orbit, lies at V_x=0 for the first order resonances. If the initial conditions are restricted to this hyper-plane, corresponding to the thickest region of the resonance, they satisfy what is sometimes called the mirror theorem. This theorem indicates that all orbits will be symmetric about the *x*-axis, a restatement of symmetry in the CR3BP. Thus, any orbit initially trapped by Jupiter must, by symmetry arguments, eventually escape. V_y, restricted to only negative values, corresponding to retrograde motion about Jupiter and prograde motion about sun, is calculated from the Jacobi constant. Figure 3-9 shows the maximum widths and positions of stable resonant regions for a range of Jacobi constants.

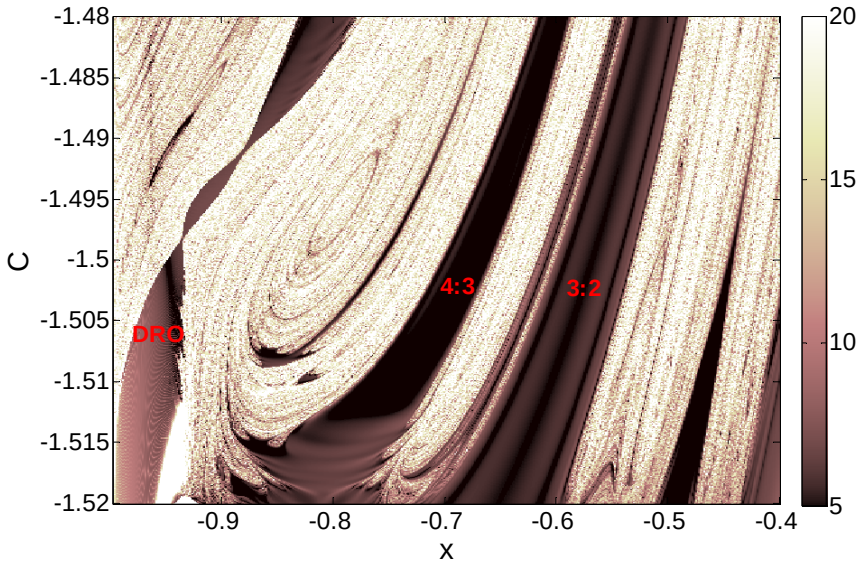

Fig. 3-9 FLI map of *C* versus *x* for orbits satisfying the mirror theorem. Color tones indicate the FLI values.

Notice that the prediction of the resonance overlap criteria was accurate, as first order resonances equal to or higher than 5:4 have been virtually destroyed. Also, notice the erosion of the 4:3 and 3:2 regions with increasing energy. The stable DRO disappears at two distinct energies where the BUPO and stable periodic distant retrograde orbit intersect. This is a generic phenomenon for a wide range of mass ratios in the CR3BP and in certain Hamiltonian systems, the "squeeze effect", marking the disappearance of the stable distant retrograde region.

It is common knowledge that many orbits starting near the distant retrograde regions are on collision paths [2, 7]. These collision orbits have been shown to be ubiquitous for specific energies on the lower range of the *C*-axis of Fig. 3-9. To form a complete picture, it is instructive to build a similar map indicating collision or no collision for a wide range of energies. Figure 3-10 shows such a map where black and white specify collision and no collision with either primary, respectively. Here the integration time is 150 TU or approximately 283 years.

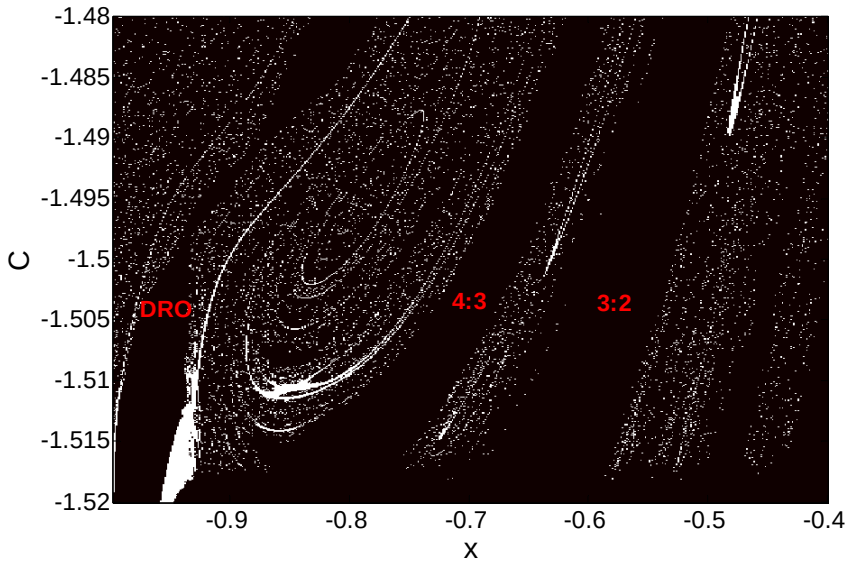

Fig. 3-10 Collision map where white indicates that a collision has taken place during an integration time of 150 TU or approximately 283 years.

The solid black regions running the vertical length of this plot correspond to the stable regions in Fig. 3-9. At low energies there is a wide region of collision orbits bordering the stable distant retrograde region. For energies below ~-1.51, capture into a DRO is impossible. It will be demonstrated in chapter 5 that collision probability significantly increases with decreasing energy.

Figure 3-11 shows a typical example of the distant retrograde region bounded by collision orbits. The proximity of the collision orbits indicates that the lobes of the BUPO carry objects on collision trajectories. Indeed, plotting the manifolds shows that they asymptotically approach Jupiter's center of mass, marked by the vertical line. Thus, any particle escaping the region must be on a collision orbit. This is not the case for higher energies where transport into and out of the distant retrograde region is possible. This circumstance is characterized by the intersection of manifolds emanating from the fringes of the prograde stable resonant regions about the sun and distant retrograde region. Thus, well-documented collision orbits bordering the stable region are controlled by the evolution of the manifolds of the BUPO through energy.

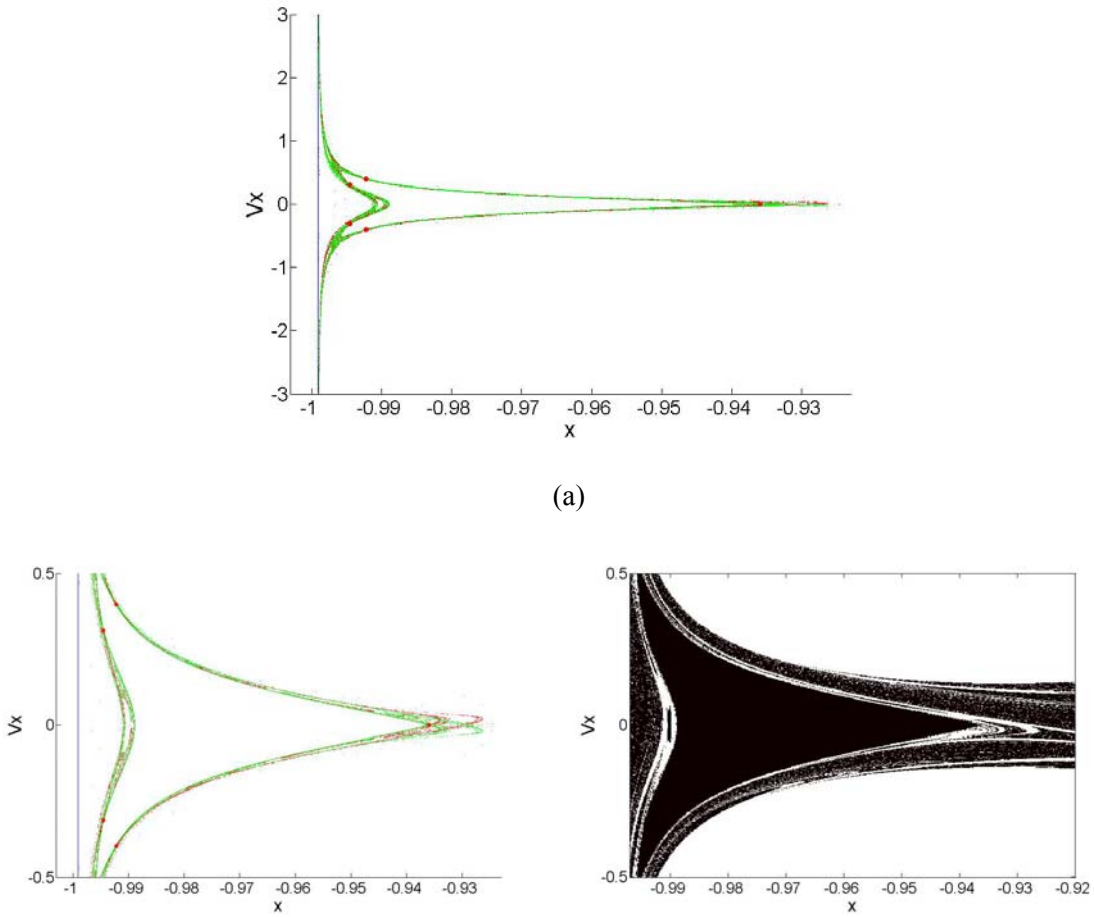

Fig. 3-11 Maps of collisions and manifolds near the distant retrograde region. (a) and (b) Mapping of invariant manifolds of the bounding periodic orbit. Jupiter's center of mass is marked by the vertical line. Red dots mark hyperbolic points. (c) Collision map of the distant retrograded region integration time of 150 TU or approximately 283 years, *C*=-1.51. White regions indicate collision orbits which bound the stability region.

The transport of a high-energy particle is inspected for a Jacobi constant of -1.49, greater than the value of the Jacobi constant at the L_3 equilibrium point. Examining the mean FLI map shown Fig. 3-12 reveals dynamical connection among the resonant islands and distant retrograde region. Similar structures were demonstrated by Villac [10, 11] in the Europa-Jupiter aiding the construction of efficient spacecraft maneuvers, yet the precise elements which form the dynamical connections were not identified. Comparison with Fig. 3-20 shows that the darker

regions and their associated connections mark lobes emanating from BUPOs bordering resonant islands and distant retrograde region. These structures, more prominent at lower simulation times, display slower divergence times (darker shades) despite following chaotic orbits. This is a result of subjection to lobe dynamics in the vicinity of each region delaying divergence. A high-energy, direct capture from the 4:3 island to the distant retrograde region is also shown in Fig. 3-12.

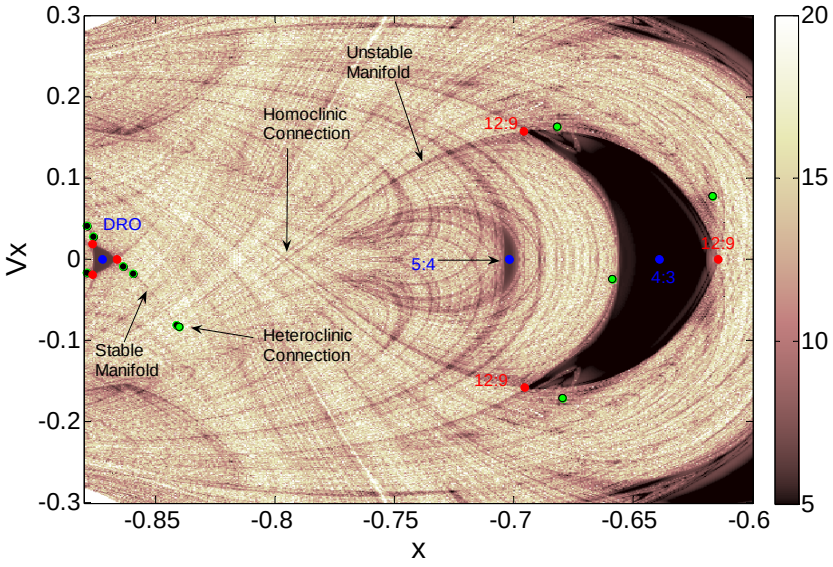

Fig. 3-12 Mean FLI map demonstrating a high-energy, direct transport from the 4:3 resonance region to the distant retrograde region. Stable and unstable periodic orbits are represented by blue and red dots, respectively. Green and black dots represent the Poincaré map of a direct transfer orbit, C=-1.49.

Here stable and unstable periodic orbits are represented by blue and red dots, respectively. These orbits were calculated using differential correction routine outlined in chapter 2. On the left side of the plot, the distant retrograde region can be found at x~-0.8873. A period-3 unstable periodic orbit, surrounds this triangular region of stability. The 4:3 resonance region lies at x~-0.639 and also has a period-3, 12:9 resonant unstable periodic orbit at its boundary. For

a direct transfer, the lobes of the unstable manifold of the 12:9 periodic orbit must intersect the lobes of the stable manifold BUPO abut the distant retrograde region. This intersection can be found by following the structures from their origin to the heteroclinic connection labeled on the plot.

An approximate initial condition can be found by zooming in on this connection. If this initial condition is integrated backwards in time the particle is transported to the outskirts of the 4:3 resonance region. This leg of the orbit is represented as green Poincaré map points in Fig. 3-12. In this case, the particle migrates to the sticky region lying near the boundary of the quasiperiodic orbits of the 4:3 resonance. Conversely, integrating forward in time, the particle follows the stable manifold and is transported to outer parts of the distant retrograde region. Patching these orbits together to form a continuous trajectory yields a direct transport from the 4:3 resonance region to the distant retrograde region. Figure 3-13 shows this trajectory in physical space which takes about 95 TU or 179 years. A set of trajectories that are transported from the distant retrograde region to the fringe of the 4:3 resonant island can be found by symmetry.

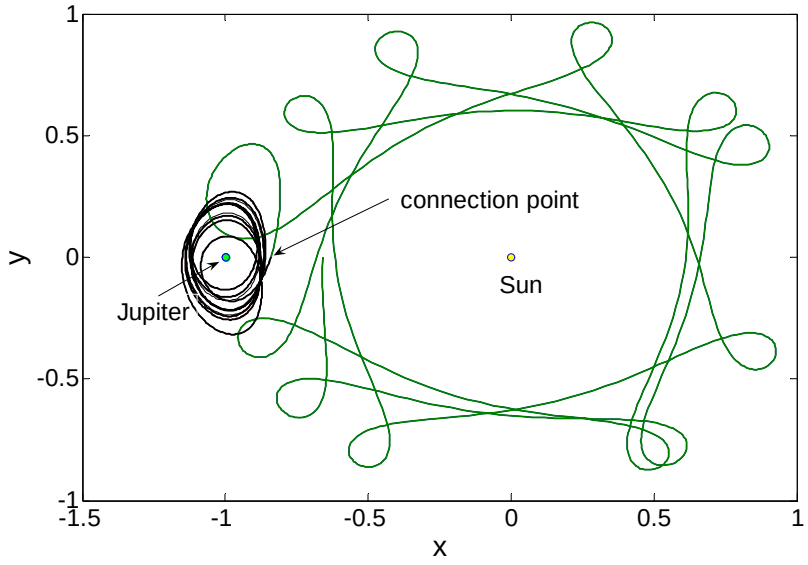

Fig. 3-13 Direct transport trajectory from the 4:3 resonance region to the distant retrograde region. Total integration time is 150 TU or ~179 years, C=-1.49. Note that Jupiter and the sun are not drawn to scale.

Precise transport conditions can be found by seeding along the eigen-directions of the hyperbolic points. The invariant manifolds, which are responsible for transport into and out of the vicinities of the stable regions, will now be examined in greater detail. Figure 3-14 shows a close-up of the distant retrograde region for a Jacobi constant of -1.5. The stable and unstable manifolds of the bounding periodic orbit are shown in green and red, respectively. The directions of motion outside of the homoclinic tangle are shown by the blue arrows.

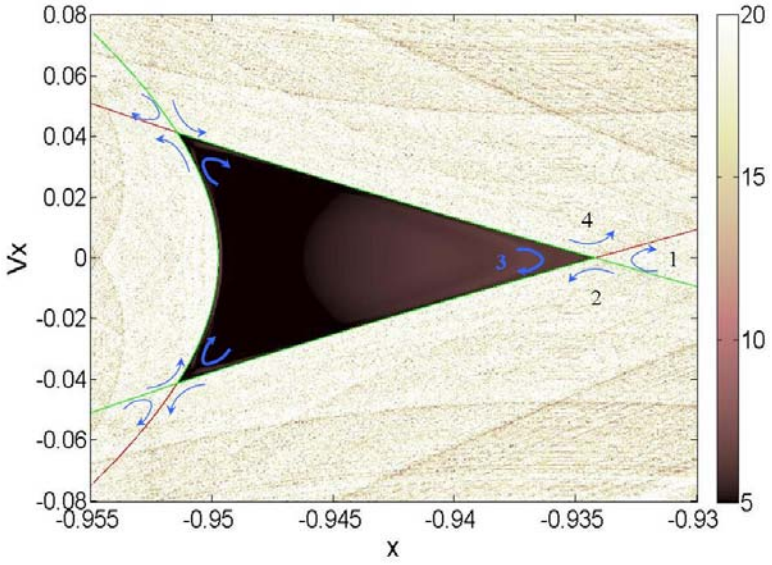

Fig. 3-14 Close-up of the distant retrograde region on a mean FLI map where the colors indicate the values. Total integration time is 150 TU or ~179 years and *C*=-1.5. Stable and unstable manifolds are plotted in green and red.

Near the unstable periodic orbit the phase space locally takes on the structure of a saddle point. Since the manifolds track the nebulous boundary of the stability region (the homoclinic tangle is thin at this particular energy), particles approaching the distant retrograde region while remaining close to the stable manifold will more likely become trapped, perhaps for extended time periods, along the border. Moreover, the saddle points separate four classes of motion outside of the homoclinic tangle, viz. orbits approaching then turning away from the stable region (1), orbits approaching then turning nearly parallel to the stability boundary (2), orbits traveling nearly parallel to quasi-periodic orbits residing in the stability zone (3), and orbits traveling parallel to the stability boundary then turning away from the region. These types of motions are labeled by their respective numbers for one of the hyperbolic points.

Zooming in near an equilibrium point shows the existence of a homoclinic tangle where the motion is governed by lobe dynamics. The lobes are the small regions of phase space

enclosed by segments of the stable and unstable manifolds. Transport between regions of phase space enclosed by intersecting manifolds can be completely described by the dynamical evolution of these lobes [18]. Using this method, the map can naturally be partitioned by segments of the stable and unstable manifolds up to their first intersection, often called a primary intersection point [19]. This corresponds to an outline of the triangular stability region which is generally called a pseudo-separatrix. The transport rates into and out of this region in terms of volume of phase per iterate of the map can be calculated by way of the area contained by the lobes [18]. Figure 3-15 shows that this area is extremely small relative to the area occupied by the stable region. Therefore, it can be stated that at this particular energy the transport of an object across the pseudo-separatrix is an event of low probability even for objects passing near the stable distant retrograde region. This, however, is not the case for all energies and, in fact, can grow quite large as will be demonstrated in later chapters.

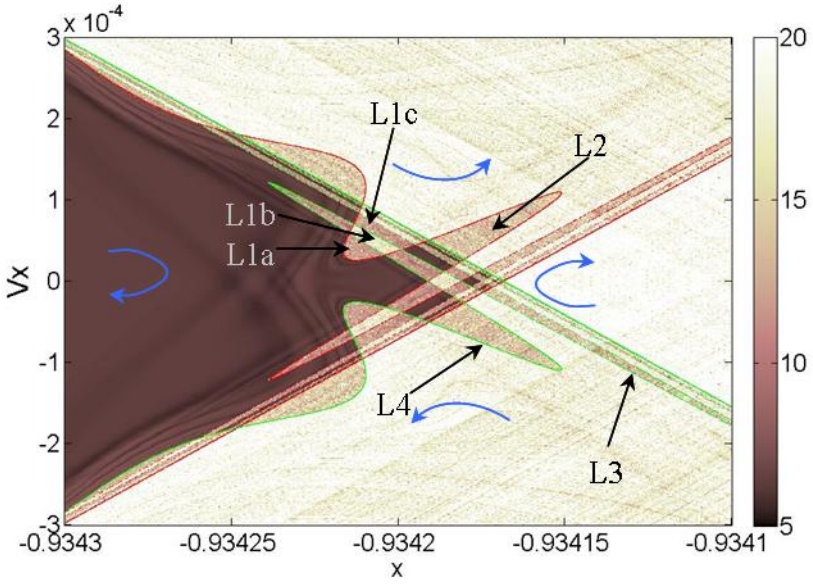

Fig. 3-15 Close-up of the right-most hyperbolic point in Fig.3-14 showing the homoclinic tangle. Here colors indicate the FLI values. The three largest strips of lobe, L1, are labeled. FLI map integration time is 150 TU and C=-1.5.

Precise, transport analysis using lobe dynamics is complex, involving many technical and theoretical considerations, and will not be considered here. However, some observations can be made using the mean FLI map. For any pseudo-separatrix on an area preserving map it can be shown that all points that leave the interior entering the exterior region must have at some earlier time entered the interior from the exterior, although this time may be arbitrarily large [19]. Orbits contained within the lobes comprise the set of extended, yet finite, capture. The relative length of capture can be inferred by map. For example, lobe L1, shown in Fig. 3-15, has been broken up into three major strips out of infinity, with sides bordered by the manifolds. By the relative FLI values, strips L1a and L1c will have longer capture times than L1b. Indeed, random samples indicate that initial conditions within L1a and L1c have capture times that range from 3-15 times that of L1b. Initial conditions starting in lobe L2 will diverge to other regions of space as iterates

of L2 are stretched parallel to the unstable manifold. By symmetry orbits approaching the region along the stable manifolds evolve along lobes that compress length-wise into L3 and L4. Notice that the region of space containing no lobes, bounded by the right-most stable and unstable manifolds and labeled as quadrant 1 in Fig. 3-14, has no capture orbits. Therefore, the stable manifold acts as a separatrix among all possible capture and non-capture orbits approaching the region.

Permanent Capture

Initial conditions are sought that will remain in the vicinity of the distant retrograde region for a sufficient time to allow entrance into the stability region via nebular drag. For the conservative system entrainment into the lobes will occur for orbits approaching the distant retrograde region parallel to the stable manifold in quadrant 2. These orbits will migrate into L3 and L4 before being cycled through the local dynamics which determines the capture-time. Using the conservative system as a guide, the effects of nebular drag can be anticipated. Dissipation will cause the areas of capture to expand around the regions of length-wise contracting lobes such as L3 and L4. The extent of this expansion will depend both on the strength of the dissipation, the manner in which it is modeled, and the initial energy level. An analogous capture boundary nearly parallel to the stable manifold will exist with a second running roughly in the same direction before turning in the direction of the blue arrow in quadrant two. The orbits inside of the bounded region will correspond to permanent capture if the map integration time is of sufficient length.

Below, the time rate of change of energy in terms of an arbitrary acceleration $\mathbf{a} = \begin{bmatrix} a_x & a_y \end{bmatrix}^T$ is quantified. To this end, the modified time-dependent equations of motions become,

$$\begin{aligned} \ddot{x} - 2\dot{y} &= \Omega_x + H(t)a_x \\ \ddot{y} + 2\dot{x} &= \Omega_y + H(t)a_y \end{aligned} \tag{3.1}$$

$H(t)$ is the Heaviside step function,

$$H(t) = \begin{cases} 0, & t < t_1 \\ 1, & t_1 < t < t_2 \\ 0, & t > t_2 \end{cases} \tag{3.2}$$

where t_1 and t_2 mark the times at the beginning end of the period acceleration produced by drag. There is no constant of motion, yet a simple expression for the change in Jacobi constant during the segment can be derived.

$$\frac{dC}{dt} = C_x\dot{x} + C_y\dot{y} + C_{\dot{x}}\ddot{x} + C_{\dot{y}}\ddot{y} = a_x\dot{x} + a_y\dot{y} \tag{3.3}$$

In this case, nebular drag will be modeled such that $\mathbf{a} = -\gamma\mathbf{v}$ where $\mathbf{v} = \begin{bmatrix} \dot{x} & \dot{y} \end{bmatrix}^T$ and γ is the drag parameter. Astakhov has found that variations in γ have the most effect on the final semimajor axes of captured objects [3] and that this simple model compared well with other forms of dissipation. He heuristically chose a value of 7×10^{-5} for integration times of 10,000

years to match the observed range of semi-major axes in the sun-Jupiter system [3]. This value is used as baseline in this study. Using this model,

$$\frac{dC}{dt} = -\gamma v^2 \Rightarrow \Delta C := C_2 - C_1 = -\gamma \Delta t \left\langle v^2 \right\rangle \tag{3.4}$$

therefore,

$$\left\langle v^2 \right\rangle = -\frac{\Delta C}{\gamma \Delta t} \tag{3.5}$$

where $\left\langle v^2 \right\rangle = \frac{1}{\Delta t}\int_{t_1}^{t_2} v^2 dt$, the average of velocity squared relative to the rotating frame of the spacecraft during thrust and, C_2 and C_1 are the Jacobi constants at the start and end of the period of nebular drag.

The equations state that for a fixed time increment and drag parameter the change in Jacobi constant depends linearly on the average velocity squared. This average, of course, depends on the length of the time increment, drag parameter, and initial conditions. As the captured orbit progress deeper in the Hill sphere the rate of energy dissipation will increase as more of the potential is exchanged for kinetic energy.

It was shown that orbital elements of captured objects are statistically similar to each other and the BUPOs on the edges of stable regions. Based on Eq. (3.5), capture regions starting from an initial region will share similar $\left\langle v^2 \right\rangle$ values. Thus, the value could provide a useful tool for the identification of capture regions and will be investigated along with the use of forward FLI maps. Additionally, it provides a descriptive quantity for particular sets of capture and escape orbits.

A forward FLI map reveals regions of capture, which expand along the stable manifold with increasing γ. Figure 3-16 shows forward FLI maps for drag parameters of 7×10^{-6}, 7×10^{-5}, and 7×10^{-4}. The stable manifolds of the conservative system are shown by the green lines.

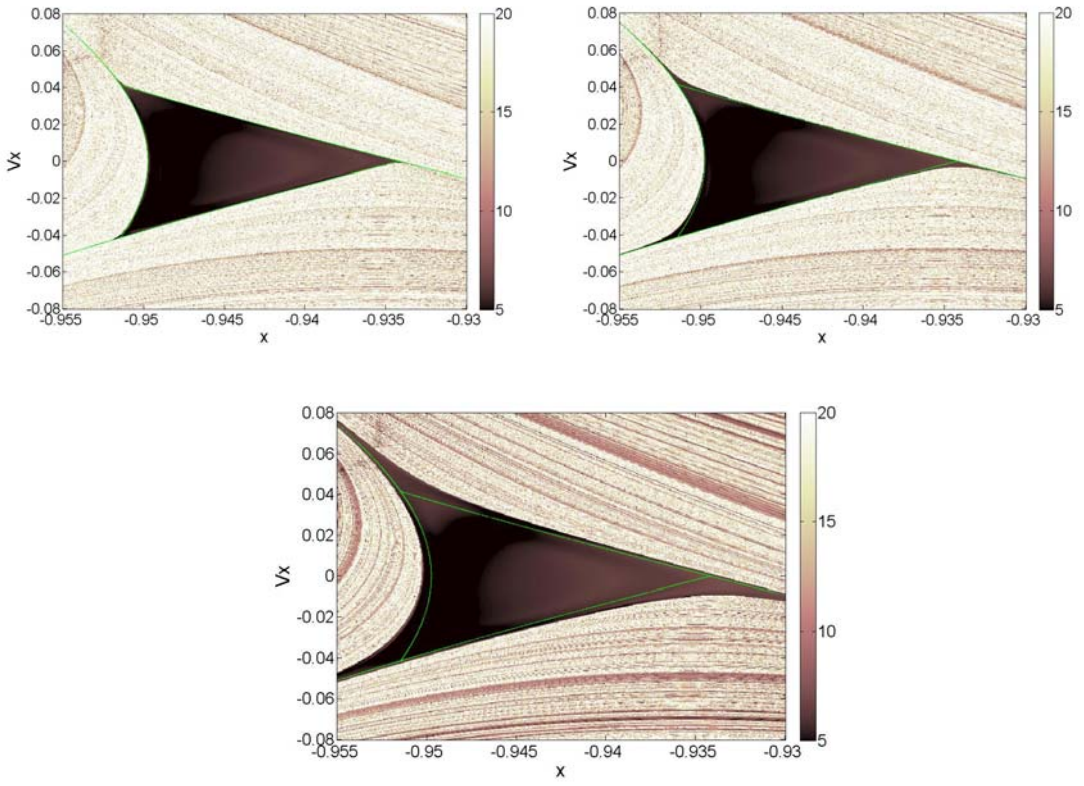

Fig. 3-16 Forward FLI maps of the distant retrograde region for drag parameters of 7×10^{-6}, 7×10^{-5}, and 7×10^{-4}, respectively, where the color scale indicates FLI value. Integration time is 150 TU with a starting Jacobi constant of -1.5. Stable manifolds of the conservative system are shown in green.

At the lowest value of the drag parameter the region of capture is already larger than the lobes. As the parameter is increased to 7×10^{-5} a noticeable region of capture begins to form getting thinner as it is followed away from the region. The largest value forms a substantial area of capture, which likewise, languishes away from the region. For all strengths of dissipation one of the boundaries closely follows the stable manifold of the conservative system. For the largest

value a noticeable region of capture forms in quadrant 1. These plots illustrate that even with substantial dissipation an approaching particle will track the stable manifold of the conservative system.

The distinct difference of FLI values between capture and escape orbits shows the efficacy of using an FLI map to identify capture regions. Figure 3-17 shows a close up of the second of Fig. 3-16. Capture trajectories can be identified by picking initial conditions within the capture region surrounding the stable manifold. Here two initial conditions starting in the lower right corner inside and outside of the capture region are shown by blue and red dots respectively. The initial conditions share an *x*-coordinate and are separated by 5×10^{-4} in the *Vx* direction. These trajectories quickly diverge as the blue particle enters and the red is swept away from the stability region. At this map resolution and integration time capture and non-capture initial conditions as close as 6×10^{-5} can be found in the *Vx* direction. Greater accuracy can be achieved by increasing the resolution.

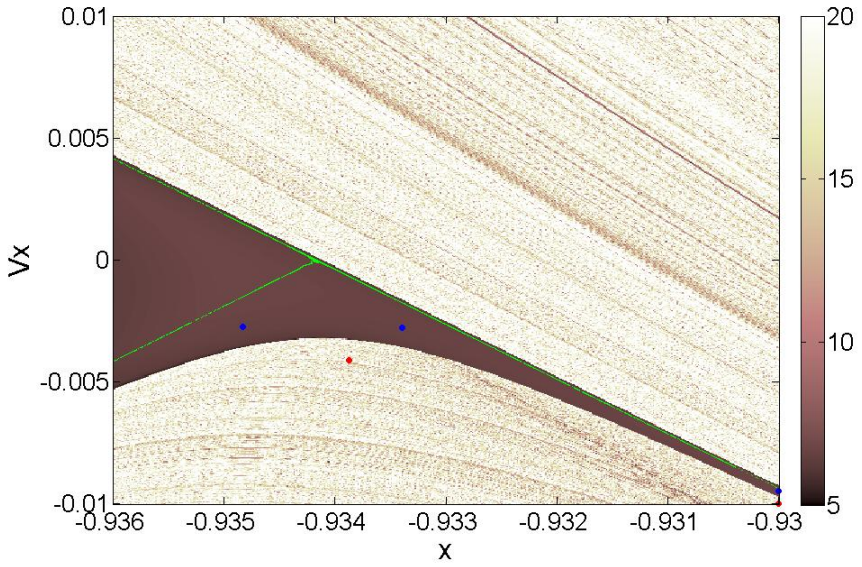

Fig. 3-17 Close-up the capture region using a forward FLI map with γ=7×10^{-5} where the color bar indicated the FLI value. The map integration time is 150 TU with an initial Jacobi constant of -1.5. Stable manifolds of the conservative system are shown in green.

Figure 3-18 shows a capture and escape orbit starting at *x*-positions of -0.93 and *Vx* -0.0095 and -0.01 on the map, respectively. Integrated over 150 TU these orbits yield distinct $\langle v^2 \rangle$ values of approximately 0.03 and 0.10, nearly an order of magnitude difference. At 80 TU the values are much closer at 0.03 and 0.05, yet capture orbits will have values which have little deviation.

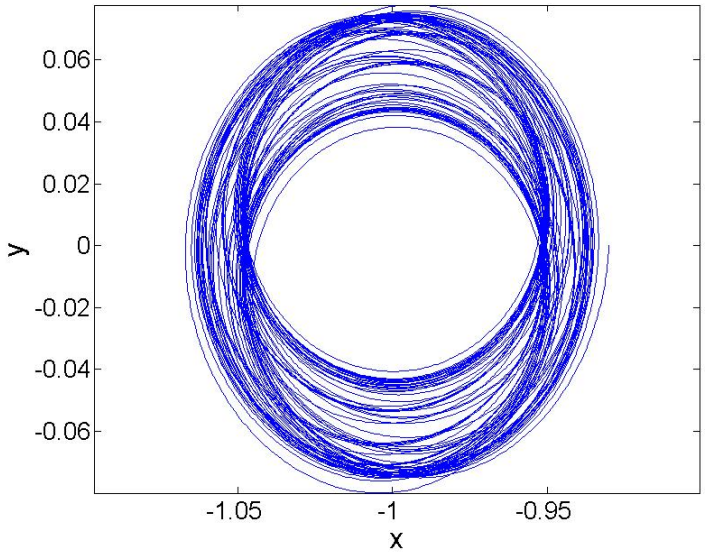

(a)

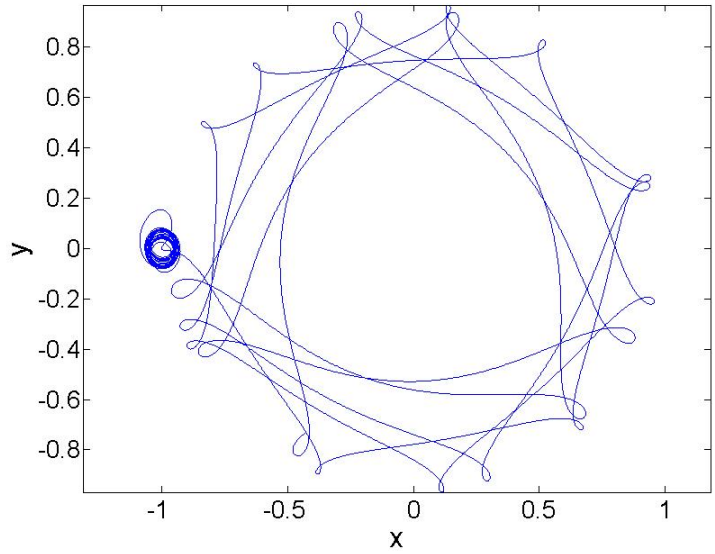

(b)

Fig. 3-18 Capture and escape orbits over a time-span 150 TU subjected to drag with γ=7×10^{-5}. Initial conditions started from the map shown in Fig. 3-17 are x=-0.93 and Vx=-0.0095, -0.01.

The FLI map provides a distinct classification of capture and escape orbits in the dissipative CR3BP. Now the use of a map of the $\langle v^2 \rangle$ values is investigated. Figure 3-19 shows such a map for the initial conditions of Fig. 3-17 integrated over 80 TU.

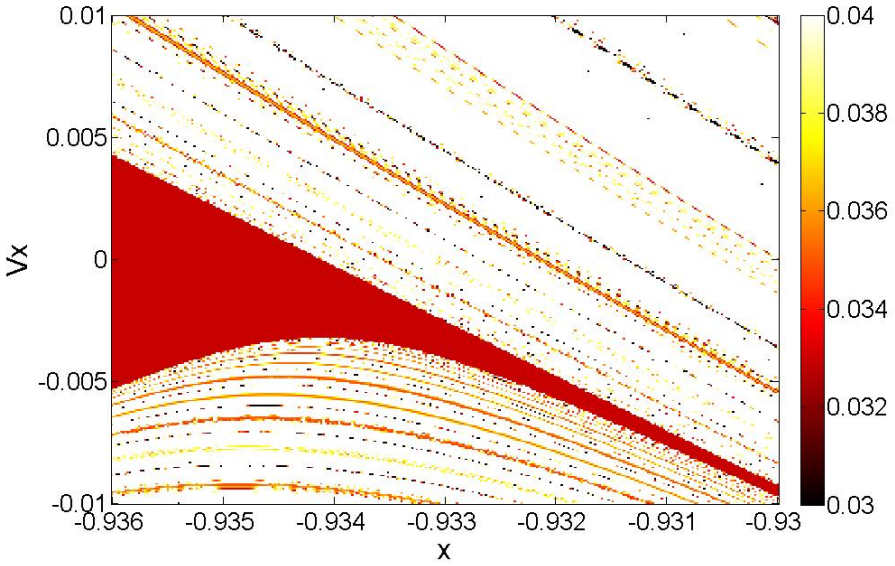

Fig. 3-19 Close up the capture region using a map of $\langle v^2 \rangle$ values, indicated by the color bar, with γ=7×10^{-5}. The map integration time is 80 TU with an initial Jacobi constant of -1.5.

Notice that an identical capture region can be identified with a distinct difference among escape and orbits of permanent capture. Specifying a strip of capture orbits of $x \in [-0.934, -0.933]$ and $x \in \left[-3\times10^{-3}, -2.9\times10^{-3}\right]$ and sampling over 2,500 evenly grid points yields a mean and standard deviation of 0.033 and 5.7×10^{-7}, respectively. Thus, a clear distinction between escape and orbits of permanent capture can be drawn by consideration of this narrow range. Utilization of the $\langle v^2 \rangle$ map comes with a clear computational advantage requiring the numerical integration of four differential equations versus 20 for FLI maps. The clock-time

of each computation decreases by a factor of three for 2.8 GHz Pentium processor. The parameter could yield a substantial speed-up for other studies which have constructed capture regions by use of FLI maps [20]. The addition of manifold theory and computational advances will certainly improve understanding of past studies and lay the foundation for the three-dimensional problem. Figure 3-20 shows $\langle v^2 \rangle$ maps over 80 TU for drag parameters of of 7×10^{-6}, 7×10^{-5} , and 7×10^{-4}, respectively.

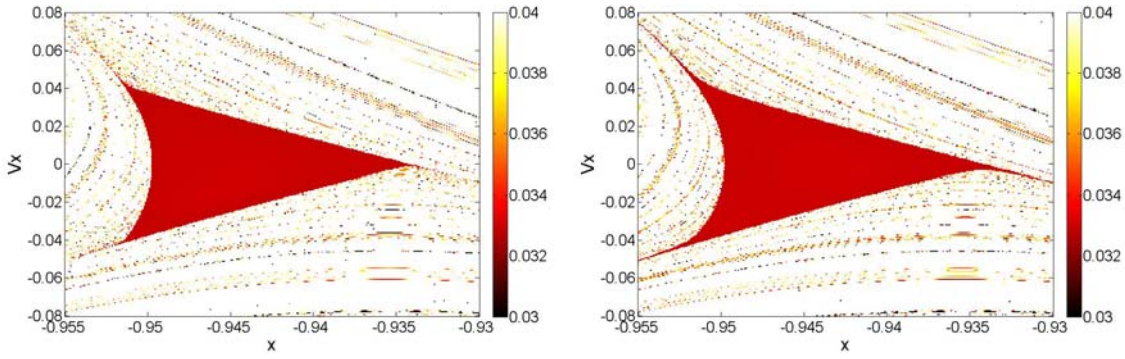

(a) (b)

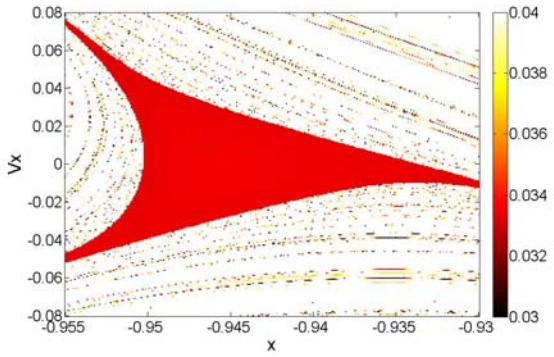

(c)

Fig. 3-20 (a-c), $\langle v^2 \rangle$ maps, values indicated by the color bars, of the distant retrograde region for drag parameters of 7×10^{-6}, 7×10^{-5} , and 7×10^{-4}, respectively. Integration time is 80 TU with a starting Jacobi constant of -1.5.

The evolution of capture orbits can be visualized by projecting into the *C*-*x* plane. Figure 3-21 shows the evolution of the capture orbit shown in the previous plot for 2,000 TU or approximately 3,800 years with a $\langle v^2 \rangle$ of 0.0714. The orbit oscillates about and slowly converges to the position of the central periodic orbit of the conservative system. Notice that the object migrates to a region of stability bounded by collision orbits. The collision map would closely resemble Fig. 3-11, making escape without collision impossible.

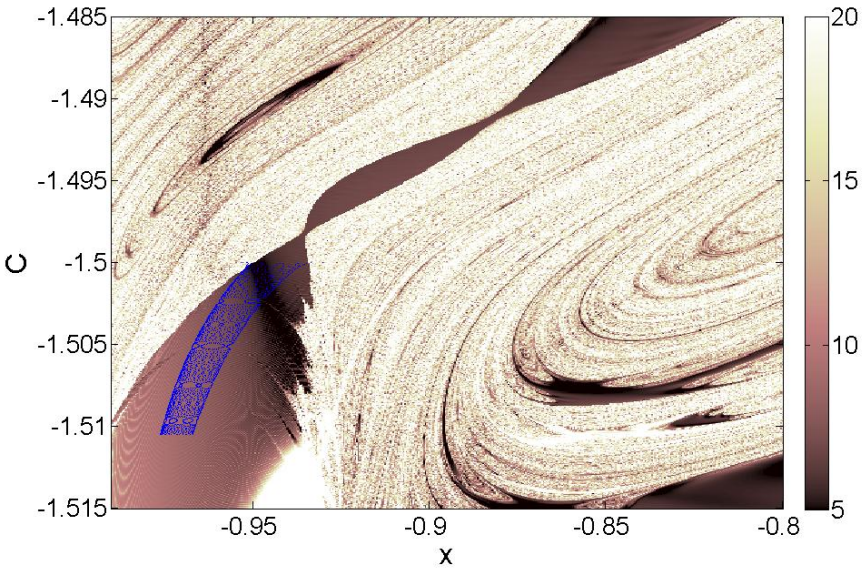

Fig. 3-21 FLI map with values indicated by the color bar of *C* versus *x* in the conservative system with a map integration time of 150 TU. The migration of a particle over a period of 2000 TU or 3800 years is shown in blue. The particle is subjected to nebular drag while traversing the stability region to lower energies.

It will be demonstrated in chapter 5 that there exists an energy threshold in the proximity of the disappearances of the stable region where energy dissipation is not guaranteed to stabilize the object. This is largely a result of the evolution of the geometry of the stable region through energy. Essentially, the rate of dissipation must be high enough so that the stable region may expand sufficiently to prevent escape. The opposite circumstance exists above *C*~-1.49 where

increases in energy have a stabilizing effect due to the expansion of the stable region. Thus, identification of this energy threshold in conjunction with this physical argument justifies the sudden drop off capture at approximately -1.495 in the literature [3]. This threshold is expected to change with inclination.

Realistically, a particle will migrate among the sun-centered resonant regions before capture as indicated by the Monte Carlo simulations of the previous section. Each of the stability islands are surrounded by manifolds of the bounding unstable periodic orbits. These manifolds compose a complicated border similar to Fig. 3-22 which displays the tangle surrounding the 4:3 resonant region. Close inspection reveals that the thick dark lines following the manifolds away from the region are not caused by short integration times. Rather these are lobes stretching away from the region which can intersect lobes originating from other regions. Particles trapped within these regions are subject to lobe dynamics delaying divergence of nearby initial conditions. It will be shown in chapter 5 that the lobes encompassing stable regions effectively delay divergence even if the BUPO possesses a high stability index. The area of phase space contained in the intersection determines the transport rate from one region to another [18]. Drag effectively widens this region, see Fig. 3-12, increasing the probability of capture.

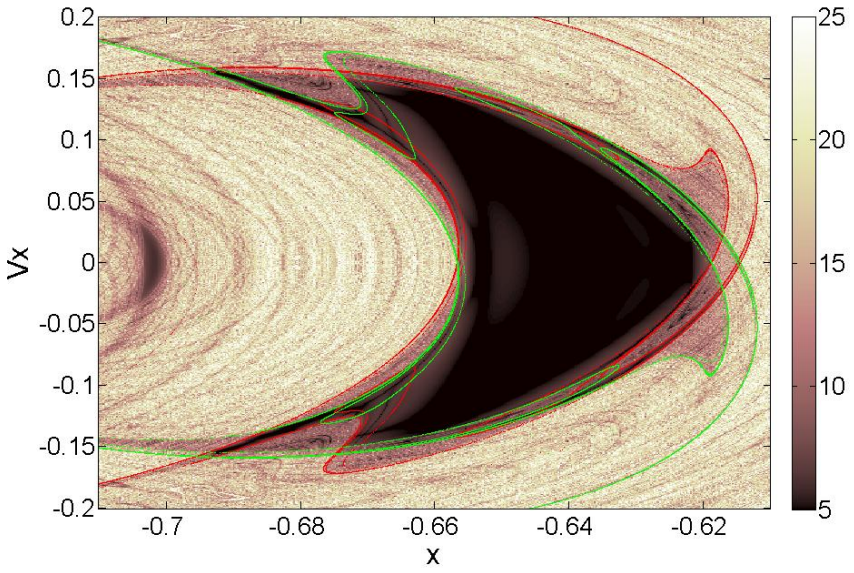

Fig. 3-22 Mean FLI map of the 4:3 resonance region integration time is 150 TU with an initial Jacobi constant of -1.49. Here the color bar indicates the FLI values for each initial condition. The stable and unstable manifolds are shown in green and red, respectively.

Numerous dynamical connections exist among the resonant and distant retrograde regions. Each of these connections makes up a segment of a complex dynamical chain. A particle leaving the vicinity of a resonant region along the chain will have some probability of visiting the exterior regions of other resonant zones and the distant retrograde region over some time span. In the conservative system, a particle must return to the region of original departure at some future time, although this time may be arbitrarily large [19]. In the dissipative system a particle will have a certain probability of either permanent capture into one of the stable regions or collision with Jupiter or the sun. Figure 3-23 shows many dynamical connections along the dynamical chain. An 18:12 unstable periodic orbit borders the 3:2 stability region.

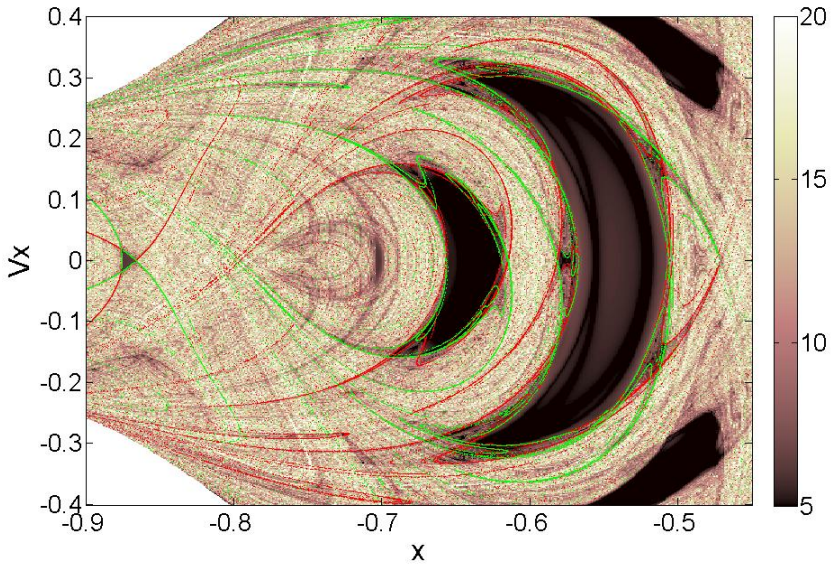

Fig. 3-23 Mean FLI map with an expanded view of the distant retrograde, 4:3, and 3:2 resonant islands surrounded by the stable and unstable manifolds of the BUPOs, shown in green and red, respectively. Here the color bar indicates the FLI value. The map integration time is 150 TU with an initial Jacobi constant of -1.49

The lobes generated by the hyperbolic points of this region enclose larger areas of the map compared to the lobes of the 4:3 region. This indicates larger transport rates into the region. Indeed, the Monte Carlo simulations of the previous sections demonstrated that the particles tend to collect near the 3:2 resonant island. This is consistent with the numerical simulations of Brunini [2]. Therefore, it can be concluded that distribution yielded by Monte Carlo simulation give an indication of the phase space volume encompassed by the lobes surrounding the stable regions.

Summary and Extension

This chapter presented new developments and an original viewpoint to the analysis of the capture of irregular satellites in the outer solar system utilizing the CR3BP. It is the first to indentify the precise mechanisms responsible for satellite capture in the context of both the

dissipative and conservative systems. Additionally, it is the first to physically describe the statistics of temporary and permanent capture from the perspective of phase space structures. A number of new developments resulted from these main contributions. These are emphasized in the following summary.

In conjunction with manifold seeding, collision mapping and the inclusion of nebular drag the methodologies provide a means for the global visualization of phase space and the classification of capture and escape orbits. In particular, the role of the BUPOs and their manifolds was analyzed by manifold theory and relative FLI values. The lobes of BUPOs where shown to be responsible for orbits of extended capture. Additionally, their evolution with energy creates a barrier between the stable orbits and the chaotic sea at lower energies. The relationship between the conservative and dissipative system was investigated, demonstrating that orbits on a capture trajectory follow the stable manifolds of the conservative system. A new mapping parameter was introduced which decreased computation time by a factor of three in the dissipative problem. A methodology was presented to identify sets of non-collision, insertion trajectories into the distant retrograde region.

These developments provide a physical interpretation of the statistical results found here and within the literature. The relative sizes of the lobes dictate the probability that a captured object originated from any individual resonant region. The orbital element distributions of the BUPO closely resemble original distributions of objects destined for capture. Moreover, based on the geometry of the stable region with energy a hypothesized mechanism for an energy threshold for capture was presented. This phenomenon is explored in greater detail in the sun-Earth system for low-thrust propulsion in chapter 5. Certainly, a detailed investigation of nebular drag at range of initial energies will verify this result in the sun-Jupiter system.

Another immediate extension is to apply similar techniques to three-dimensions where some inclinations increase the probability of capture. This is a function of the geometry of the

lobes with both inclination and energy. The problem may be simplified by constraining initial conditions to hyper-planes corresponding to a preferred parameter. Certainly, this chapter lays the foundation for such an undertaking. The eccentricity of Jupiter must be addressed in future work since it has been shown to affect the probability of capture [16]. Such an extension will build on the developments of this chapter. Although this chapter reports significant results, chapters 4 and 5 build on these developments to construct transfers to stable and sticky distant retrograde orbits in the sun-Earth system. Observations of particular importance include the prominent regions of collision outside of the stable distant retrograde region, the geometry of the stable region with energy, the role of the BUPOs and associated homoclinic tangles, the variation of capture times within the lobes, and the predictability of capture orbits in the dissipative system.

Once in a DRO, a spiral in or spiral out maneuver can be executed. The spiral out maneuver may be advantageous to interplanetary travel, since highly energetic yet stable orbits are attainable. A simple spiral out trajectory can be modeled in similar manner to drag, but with a forcing term of opposite sign. Similar transfers have been investigated in the Jupiter-Europa system, although these relied on optimization methods [8]. These methods could yield lower cost trajectories, since "thrust-free" transfers can be identified via connections on the dynamical chain.

References

[1] Hamilton, D., "Jupiter's Moonopoly", *Nature*, Vol. 423, pp. 235-236, 2003.

[2] Brunini, A., "On the satellite capture problem. Capture and stability regions for planetary satellites", *Celestial Mechanics and Dynamical Astronomy*, Vol. 64, No. 1, 1996.

[3] Astakhov, S.A., Burbanks, A.D., Wiggins, S., and Farrelly, D., "Chaos-assisted capture of irregular moons", *Nature*, Vol. 423, pp. 264-267, 2003.

[4] Hénon, M. and Guyot, M., "Stability of Periodic Orbits in the Restricted Problem", *Periodic orbits, stability and resonances. Proceedings of a symposium conducted by the University of Sao Paulo, the Technical Institute of Aeronautics of Sao Jose´ dos Campos, and the National Observatory of Rio de Janeiro, at the University of Sao Pau*, pp. 349-374, 1970.

[5] Wilczak, D. and Zgliczyński, P., "Heteroclinic Connections Between Periodic Orbits in Planar Restricted Circular Three-body Problem. Part II", *Communications in Mathematical Physics*, Vol. 259, pp. 561-576, 2005.

[6] Koon, W., Lo, M., Marsden, J., and Ross, S., "Heteroclinic Connections Between Periodic Orbits and Resonance Transitions in Celestial Mechanics", *Chaos*, Vol. 10, No. 2, 2000.

[7] Lam, T., "Exploration of distant retrograde orbits around Europa", *Advances in Astronautical Sciences*, Vol. 120, pp. 135-153, 2005.

[8] Demeyer, J and Gurfil P., "Transfer to Distant Retrograde Orbits using Manifold Theory", *Journal of Guidance, Control, and Dynamics*, Vol. 30; No. 5, 2007.

[9] Ocampo, C., and Rosborough, G., "Transfer Trajectories for Distant Retrograde Orbiters of the Earth", *Advances in the Astronautical Sciences*, Vol. 82, Pt. 2, pp. 1177-1200, 1993.

[10] Villac, B.F., "Mapping long-term stability regions using the fast Lyapunov indicator", *Advances in the Astronautical Sciences*, Vol. 120, No. 2, 1421-1442, 2005.

[11] Villac, B.F., Lara, M., "Stability maps, global dynamics and transfers", *Advances in the Astronautical Sciences*, Vol. 123, No. 3, pp. 1983-2002, 2006.

[12] Morbidelli, A., *Modern Celestial Mechanics: Aspects of Solar System Dynamics*, Taylor and Francis, New York, 2002.

[13] Alvarez, A. and Roig, F., "The role of the resonant "stickiness" in the dynamical evolution of Jupiter family comets", *Dynamics of Populations of Planetary Systems Proceedings IAU Colloquium*, No. 197, 2005.

[14] Jewitt, D., Shepphar, S. and Kleyna, J., "The Strangest Satellites in the Solar System", *Scientific American*, August 2006.

[15] Astakhov, S., Burbanks, A., Wiggins, S. and Farrely, D., "Dynamics of Capture in the Restricted Three-Body Problem," *Order and Chaos in Stellar and Planetary Systems, ASP Conference Series*, Vol. 316, 2004.

[16] Astakhov, S. and Farrely, D., "Capture and Escape in the Elliptic Restricted Three-Body Problem," *Monthly Notices of the Royal Astronomical Society*, Vol. 354, pp. 971-979, 2004.

[17] Wisdom, J., "The Resonance Overlap Criterion and the Onset of Stochastic Behavior in the Restricted Three-Body Problem, *The Astronomical Journal*, Vol. 85, No. 8, 1980.

[18] Dellnitz, M., Junge, O., Koon, W., Lekien, F., Lo, M., Marsden, J., Padberg, K., Preis, R., Ross, S., and Thiere, B., "Transport in Dynamical Astronomy and Multibody Problems", *Chaos*, Vol. 15, No. 3, pp.699-727, 2005.

[19] Wiggins, S., *Introduction to Applied Nonlinear Dynamical Systems and Chaos*, Springer-Verlag, New York, 1990.

Chapter 4

Transfers to Periodic Distant Retrograde Orbits

The last chapter introduced techniques for the analysis of the satellite capture problem in the sun-Jupiter system. This chapter outlines a methodology for the construction of optimal spacecraft transfers, in terms of transfer time and ΔV, from low-Earth orbit (LEO) to the stable periodic orbit lying at the center of the distant retrograde region. Since the CR3BP can be used a basic model for many regions throughout the solar system, the qualitative results transcend both celestial mechanics and astrodynamical applications. This chapter takes a more detailed look at the dynamics outside of the stable distant retrograde region in the sun-Earth system. Of importance is the region between the stable region and the Lyapunov orbits with their associated manifold tubes. A sequence of physical arguments predicts the existence of collision orbits in this chaotic region of space.

Collision orbits in the vicinity of the distant retrograde region are well-documented in works involving satellite capture. This chapter expands on the result of the last by utilizing the orderly arrangement of collision regions and a dynamical analysis to facilitate a focused sampling of phase space. This limited sampling provides an accurate guess for predictor-corrector algorithms for an arbitrary number of transfer types. A procedure is outlined that calculates favorable insertion points in terms of transfer time and ΔV. The relationship between families of transfer orbits and the morphology of phase space near the distant retrograde region is discussed.

Stable retrograde orbits about the Earth in the Earth-sun system, modeled by the circular restricted three-body problem (CR3BP), exist for nearly all energies and altitudes. These orbits typically refer to stable periodic distant retrograde orbits (SPDROs) or quasi-periodic distant retrograde orbits (QPDROs) residing outside of the L_1 and L_2 equilibrium points. They have received the attention of the astrodynamics community, because of the ability to avoid near-Earth

phenomena including stellar occultation and thermal perturbations for applications such as spaceborne telescopes, radio imaging of the sun [1], and solar storm warning systems [2]. L_2 halo and Lissajous orbits have also been suggested [3] as a location for spaceborne telescopes, but they require orbit maintenance throughout the lifetime of the telescope at a limited range of distances from the Earth. Trajectory design from LEO to a SPDRO in the sun-Earth system has been performed using impulsive and low-thrust propulsion with both direct and indirect optimization [4]. The most relevant to this study are those utilizing impulsive methods. Notable discoveries are the A1 and A2 transfers by Ocampo and Rosborough [2]. The drawback of these transfers is that they can reach only specific range of SPDRO sizes, because they require the computation of an Earth return periodic orbit for an initial guess. Demeyer and Gurfil addressed this limitation by extending these transfers using manifold theory coupled with a direct shooting method and a Monte Carlo optimization scheme, yet they investigated only one transfer type [1].

For large ranges of mass ratios and energies in the CR3BP there exists a stable region of distant retrograde orbits surrounded by a large region of chaotic orbits. The stable region is composed of bounded chaotic orbits and QPDROs encompassing a SPDRO often classified as family f [5]. As discussed in the previous chapter an unstable periodic orbit, referred to as a bounding unstable periodic orbit (BUPO), classified as family g3 [5], lies at the fringes of the stable region with its entangled manifolds marking the border. This chapter explores the design space by finding families of transfer orbits from a circular LEO to a SPDRO using a dynamical analysis in addition to differential correction and numerical continuation.

Each transfer uses two impulsive maneuvers, one to leave LEO and another to insert into a SPDRO. These families are computed for ranges of parking orbit altitudes, SPDRO sizes, constants of motion, and insertion points. An initial guess for the numerical algorithms is provided by an analysis of the phase space between the BUPO and Lyapunov orbit at the same energy. An orderly arrangement of collision regions are uncovered that facilitate a focused

sampling of phase space. This efficient method arrives at a favorable guess for an arbitrary number of transfer families. The number of collision regions increases indefinitely with transfer time, as a result, an arbitrary number of transfer families can be found. Thus, this chapter presents a methodology that by-passes the difficulty of generating an Earth return periodic orbit for an initial guess. In addition it expands on previous studies by allowing the insertion point to be modified for an arbitrary number of transfer trajectories. It provides access to a large range of SPDRO sizes for all transfer types utilizing a single starting transfer orbit for each type. Since the algorithms navigate a large range of insertion points for each family at a set SPDRO, favorable trajectories in terms of transfer time and ΔV can easily be identified.

Utilizing these methods, the design space is explored in an automated manner without the sophistication of more complex optimization routines or convergence to a local minimum. Moreover, the approach illuminates the intimate relationship between the geometry of transfer trajectories and the dominating morphological features of phase space near the smaller primary. This provides physical explanations for trends that have gone unexplained in the literature.

The evolution of ΔV and transfer time with energy and SPDRO size is presented in conjunction with a detailed study of these relationships Rapid changes in the transfer parameters with insertion point are shown to be caused by crossing distinct regimes of motion marked by the Lyapunov orbits and their manifolds. Using the developed techniques favorable insertion points are identified in terms of ΔV and transfer time. The variation of ΔV with parking orbit altitude is linear with no significant differences in transfer time. The discovery of an unstable periodic orbit corresponding to each family of transfer trajectories results as a by-product of the continuation method. In the sun-Earth system these orbits are known as the aforementioned Earth return periodic orbits [2]. Thus, these methods produce, in an orderly fashion, periodic orbits that pass especially near the second primary.

ΔV values for the first family of transfer orbits reaching small SPDROs agree within two percent of the optimal transfers found by Deymeyer and less then one percent of a case investigated by Ocampo (see Figure 10 in Ref. 1 and Table 1 in Ref. 2), providing verification of the procedure. At large SPDRO altitudes, 4M km or higher, generated trajectories require less ΔV than those found by Deymeyer for the first family, but at the cost of higher transfer times. In that study, lower transfer times were a result of lifting the restriction that the transfer orbit intersects the SPDRO tangentially. Application of these tools gives an analyst a complete set of reference trajectories in order to apply the low-thrust trajectory design procedures, such as those developed by Ocampo [6], for any system where the CR3BP can be used as an approximation. These developments are used a stepping stone to address the topic of the next chapter which includes direct insertion into so called sticky orbits.

Phase Space Analysis

As in Ref. 2, an augmented 'Earth plus Moon' model is adopted. This approximation entails combining the Earth and Moon into the second primary. In addition, the radius of the parking orbit is increased, so that the circular orbit velocity is that of parking orbit of a specific altitude about Earth. A realistic multi-body simulation proved that this modification provides accurate results for the duration of the transfer [2]. All plots in this chapter have their origins shifted to the location of the Earth with the positive *x*-axis pointing towards the sun.

The stable distant retrograde region is composed of three distinct types of motion corresponding to periodic, quasi-periodic and bounded chaotic orbits. The bounded chaotic orbits are expected by recalling the Poincaré-Birkoff fixed point theorem discussed in chapter 2. QPDROs encompass the central SPDRO at all but two values of Jacobi constant where the stable region disappears. Figure 4-1a shows an SPDRO and a Lyaponuv orbit about L_1 [7] where the

arrows indicate the direction of motion. A mean FLI stability mapping on a surface of section (SOS) of $y = 0$ and $\dot{y} < 0$, Figure 4-1b, reveals a mixed phase space composed of both chaotic and stable orbits. Recall that the lightest shades indicate the greatest divergence of nearby initial conditions. The triangular region constitutes the stable distant retrograde region. Note that the term "stable region" will refer to this region although thin layers of bounded chaotic orbits exist within it. Dark regions on the top and bottom of the map constitute chaotic bundles of sun-centered orbits whose divergence time is much greater than orbits surrounding the distant retrograde region.

Homoclinic points of the L_1 Lyapunov orbit are evidenced by the intersections of the stable and unstable manifolds, H_oP. These are orbits that first depart from the Lyapunov orbit along its unstable manifold then approach it asymptotically along its stable manifold as time goes to infinity. Heteroclinic points marked, H_eP, of the BUPO and the Lyapunov orbit indicate orbits that diverge from the BUPO along its unstable manifold and asymptotically converge to the Lyapunov orbit along its stable manifold. The opposite circumstance is indicated at H_eP where $\dot{x} < 0$. The frontier of the stable region is marked by a homoclinic tangle of the manifolds exuded by the BUPO, an unstable period-3 periodic orbit on the map. As discussed in the previous chapter, the BUPO is integral to understanding the dynamics near this region. Its stable and unstable manifolds dictate direct transport into and out of the so called sticky regions that border the surviving KAM tori containing the deformed quasi-periodic orbits of the two-body problem. These sticky regions retain motion that is sometimes referred to as "stable chaos" where a particle exhibits a dynamical lifetime longer than is predicted by the Lyapunov time [8].

Collisions are well documented for orbits passing near the distant retrograde region [9-11]. These collision orbits are ubiquitous at low energies extending to the border of the stable region in the CR3BP [9, 11]. The relative placement of phase space structures and a few geometric arguments predict the existence of both collision and transfer orbits terminating on the

SOS at $\dot{x} = 0$. Note that transfer orbits which terminate on this hyperplane will always intersect a SPDRO tangentially due to its symmetry.

The BUPO exhibits purely retrograde motion with respect to the Earth, whereas the L_1 Lyapunov orbit, an Earth return orbit at certain energies, switches between prograde and retrograde motion. Therefore, starting at the L_1 Lyapunov orbit and decreasing the *x*-coordinate at the same energy on the SOS at $\dot{x} = 0$, one expects to encounter collisions with Earth as the orbits evolve from prograde/retrograde to purely retrograde motion. Due to continuity, in a regularized coordinate system, immediately before these collisions an orbit passing especially near the Earth in the prograde direction is expected. This implies the band of collisions will be accompanied by a curve corresponding to the termination points of a family of transfer orbits just before the second maneuver.

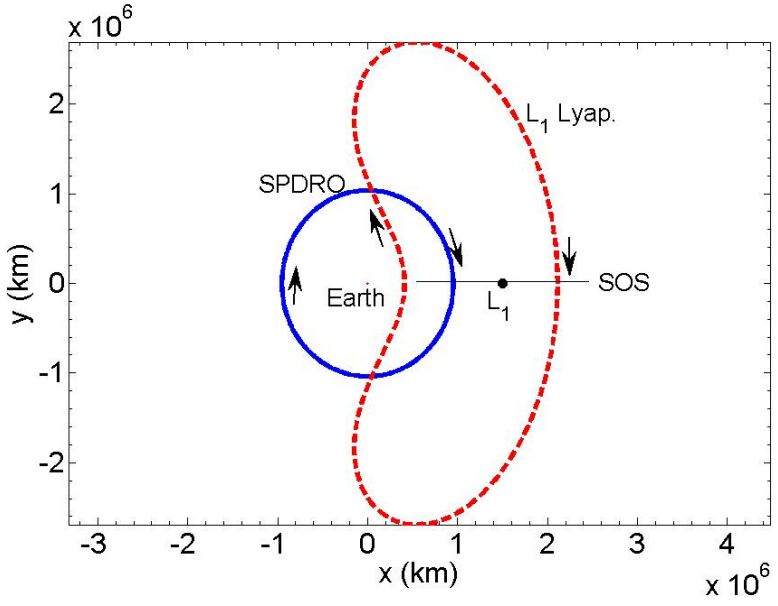
x 10^6
2
1
0
-1
-2
y (km)
-3
-2
-1
0
1
2
3
4
x (km)
x 10^6
L1 Lyap.
SPDRO
Earth
L1
SOS

(a)

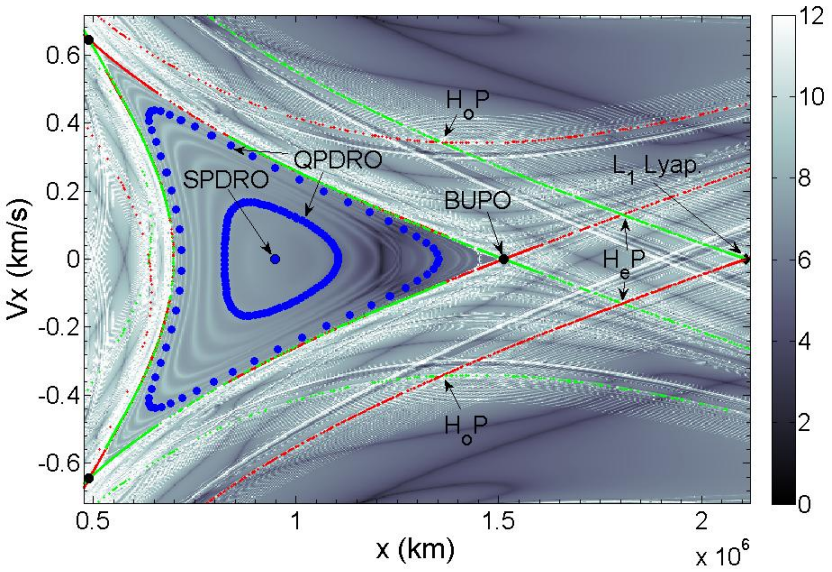
0.6
0.4
0.2
0
-0.2
-0.4
-0.6
Vx (km/s)
0.5
1
1.5
2
x (km)
x 10^6
12
10
8
6
4
2
0
HoP
QPDRO
SPDRO
BUPO
L1 Lyap.
HeP
HoP

(b)

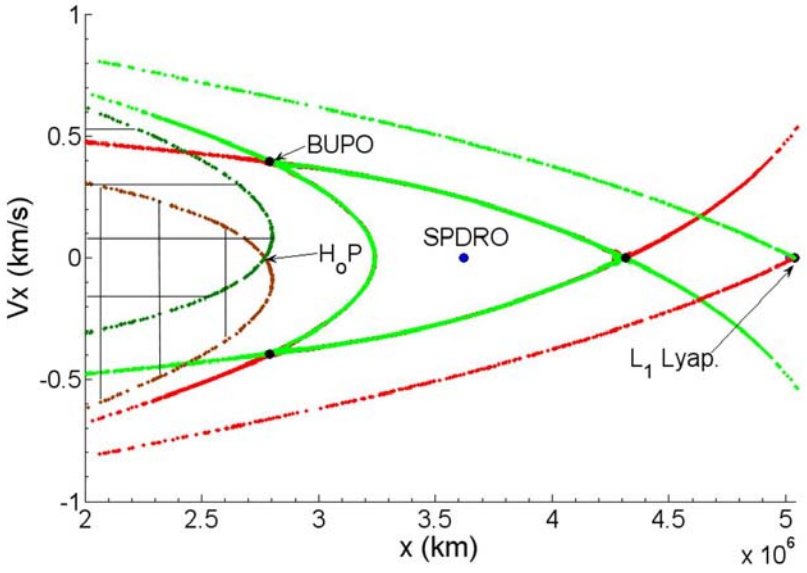

(c)

Fig. 4-1 Orbits and maps of the distant retrograde region. (a) SPDRO and Lyapunov orbit about L_1. (b) FLI stability mapping at the indicated SOS, C= -1.5001. Here the color bar indicates the FLI value. The stable distant retrograde region composed of QPDROs is indicated by the dark triangular region, with the SPDRO lying at the center. Stable and unstable manifolds of the BUPO and the L_1 Lyapunov orbit are shown in green and red, respectively. (c) =-1.4997, Manifolds of the BUPO and L_1 Lyapunov orbit. The stable and unstable manifold tubes of the L_2 Lyapunov orbit are indicated by the horizontal and vertical hatching.

On the opposite side of the stable region lie the unstable and stable manifold tubes of the L_2 Lyapunov orbit, displayed in Figure 4-1c, containing orbits that have been transported directly from or will be transported directly to the region exterior to the Earth's orbit. These tubes discussed in chapter 2, correspond to three of the nine possible classes of motion near the center manifold. In general, these tubes intersect forming a homoclinic point, marked H_oP, corresponding to an orbit that, moving either forward or backwards in time, asymptotically approaches the L_2 Lyapunov which exhibits both prograde and retrograde motion. Thus, starting at the homoclinic point and moving in the positive *x*-direction to the edge of the stable region the

orbits evolve from prograde/retrograde motion to purely retrograde, implying the existence of collisions and accompanying transfer orbits.

This provides impetus for the construction of a collision map near the distant retrograde region. Figure 4-2a shows such a map over a year where black and white indicate no collision and collision with the Earth, respectively. Initial conditions are found by setting $\dot{x} = 0$ on the SOS for a range of energies. Integrating these initial conditions forward and backwards over an arbitrary time period yields an orbit segment symmetric about the *x*-axis. Thus, white marks an orbit that both originates and terminates at the Earth's surface. The continuations of stable and unstable periodic orbits are indicated on the map. Notice there are two prominent ribbons of collision orbits lying between the L_1 Lyapunov orbit and the BUPO. Two others trace paths on the opposite side of the SPDRO between the stable region the homoclinic point formed by the intersection of the invariant manifold tubes of the L_2 Lyapunov orbit. Sets of orbits such as these are used to specify a narrow search region for transfer orbits.

A simulation of two years, Fig. 4-2b, bears additional regions of collisions branching from the vicinity of the four most prominent regions. The number of distinct sets of collision orbits increases with the simulation time. It is argued below that each region corresponds to a unique transfer orbit indicating that this method can be used to find an arbitrary number of transfer orbits.

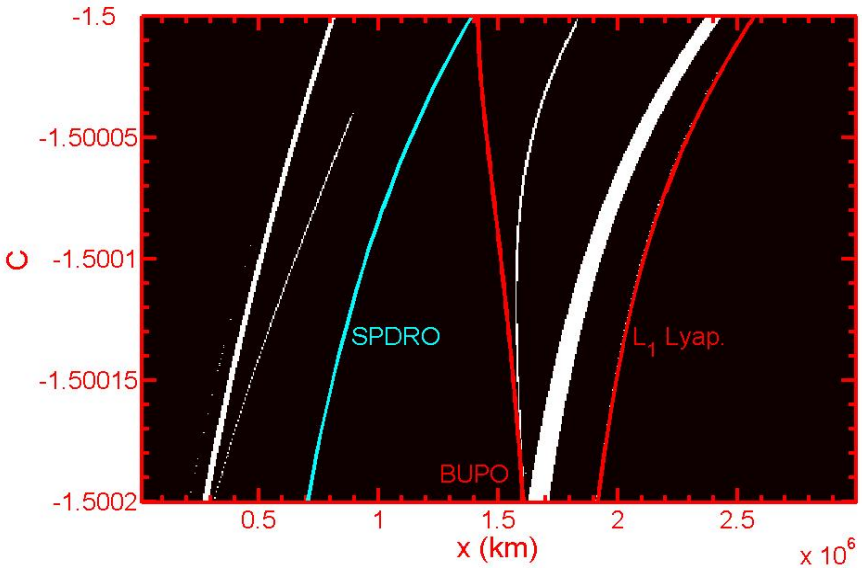

(a)

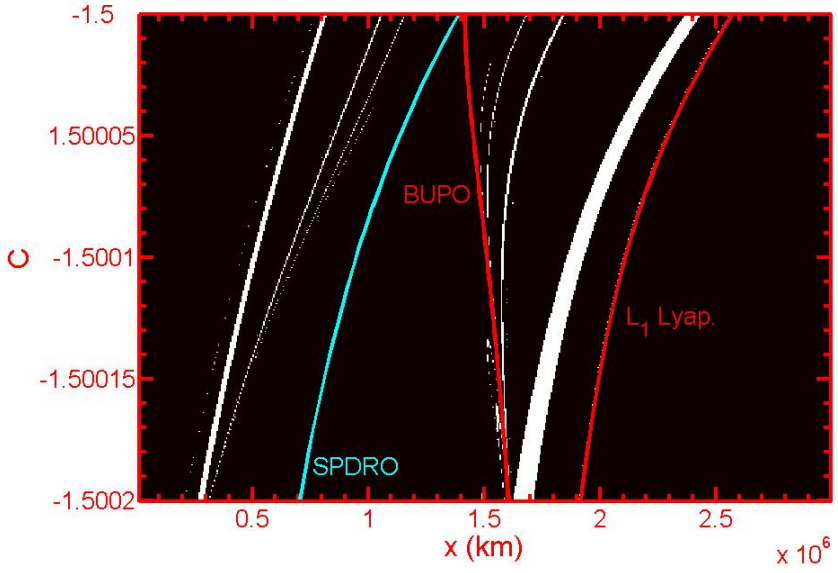

(b)

Fig. 4-2 Collision maps over a period of one and two years are shown in (a) and (b).

The key observation is that for some bounded time period each band of collisions tested marks the transition between prograde/retrograde and retrograde motion. First note that each

band of collisions and the corresponding transfer trajectory are generally associated with an unstable periodic orbit, an Earth return orbit. For instance, the thickest band is associated with the L_1 Lyapunov orbit. Projected into the x-$\dot{y}$ plane the manifolds of the unstable periodic orbit, lying symmetric about the x-axis, break the SOS into four quadrants. Following each orbit within the band to the surface of the Earth the eigenvectors of the unstable periodic orbit will rotate, corresponding to the rotation of the invariant manifolds, to the point corresponding the half period of the Earth return orbit. Each orbit will remain bound by the stable and unstable manifolds unless transported to another region. Since each band is continuous for detectable regions along the x-axis we assume that there has been no significant divergence of the orbits when propagated backwards to the surface of the Earth. Thus, it is concluded that the orbits will cross in physical space in a manner consistent with the rotation of the eigenvectors along the unstable periodic orbit.

The points of collision roughly coincide with the half period corresponding to a symmetric image of the eigenvectors in the x - $\dot{x}$ plane. On a surface of section, this has the effect of restoring or reversing the original order of orbits in terms of placement along the x-axis. Therefore, points within the collision band initially departing along parallel trajectories (propagating backwards) will unravel into nearly parallel trajectories before striking the Earth.

Inspection of Fig. 4-1b and c reveals that any orbit on a collision trajectory with Earth must lie to the left of the of L_1 Lyapunov orbit. Orbits to right comprise sun-centered orbits which turn away from the vicinity of the distant retrograde region. Moving backwards in time these orbits will evolve looping around the Earth an arbitrary number of times but must be transported back continuously to the region of phase space lying above the unstable manifolds of the L_1 Lyapunov orbit until collision. Otherwise, the orbit will escape into a sun-centered orbit interior to the Earth's orbit. An equivalent argument can be made for the L_2 Lyapunov orbit,

where crossing the threshold of the unstable manifold results to escape into a sun-centered orbit exterior to the Earth.

For energies corresponding to the existence of stable distant retrograde orbits, the distance between the Earth and the closest approach of either Lyapunov orbit is small as they penetrate deep within Earth's Hill sphere. Therefore, the final segment of a collision trajectory must approach one of the Lyapunov orbits in physical space before collision. In fact, along the *x*-axis, an Earth return orbit must lie between the Lyapunov orbit and Earth's center of mass at its half period. Since both orbits strike the *x*-axis perpendicularly and are of the same energy these orbits lie close together in phase space on the final approach to Earth. Thus, they experience similar accelerations along the segment approaching the half period.

Information pertaining to the relative spacing of the orbits before final approach can be deduced by recalling that Liouville's theorem which states that volumes are preserved for conservative Hamiltonian systems. Sampling along $\dot{x} = 0$, the end conditions of a group of collision orbits correspond to a one-dimensional curve in the *x*-$\dot{y}$ plane. Suppose this curve is given a small thickness in the remaining dimensions so that it fills a volume in phase space. As the volume evolves backwards in time it will twist and elongate in phase space becoming thinner with time.

A characteristic of the Lyapunov orbit is that starting from the SOS in Fig. 4-1b and integrating in negative time over half of a period the eigenvector of the stable manifold has its largest component in the *y*-direction. In fact, stretching in physical space dominates stretching in velocity until the orbits reach the vicinity of the Hill sphere. Due to similar accelerations, the Earth return orbits of higher periods share this characteristic over their final segment. Moreover, the expansion is more dramatic, since their stability indices are much larger than the Lyapunov orbits and the volumes have had a greater opportunity to stretch during the longer time period. These volumes experience a dramatic lengthening in physical space until they reach the vicinity

of Earth where the orbits travel on familiar hyperbolic orbits of the two-body problem. Since the order of the orbits along the *x*-axis has been preserved and the length in physical space has expanded, the orbits inhabiting a collision band will sequentially strike a large portion of the Earth at unique positions.

Near the Earth, the edges of the collision bands correspond to hyperbolic orbits which intersect the Earth tangentially at perigee in both the retrograde and prograde directions. Thus, each collision band shown in Fig. 4-2 is expected to mark a transition between prograde/retrograde and retrograde motion. By the intermediate value theorem it is concluded that each band will correspond to the existence transfer orbit. These arguments can be extended to collisions with a hypothetical body whose radius is that of a circular LEO, facilitating the initial guess for a transfer orbit. Because the order of the orbits are reversed or preserved, the position along the *x*-axis of a collision band is a monotonic function of an angle specifying the position on the Earth's surface or parking orbit. Thus, only one search direction is needed to find a transfer orbit.

Initial Guess

The results of the last section are utilized by a simple linear interpolation/extrapolation routine to find the particular orbit that passes near the Earth in the prograde direction at a specific altitude. This orbit will be used as a starting point for the differential correction and numerical continuation algorithms. Consider a point on a parking orbit where two angles α_p and β_p, defined $\alpha_p = \tan^{-1}\left[y/\left(x+1-\mu\right)\right]$ and $\beta_p = \tan^{-1}\left(V_y/V_x\right)$, determine the direction of the radius and velocity vectors, respectively. For a circular parking orbit $\beta_p = \alpha_p + \pi/2$, equivalently $\mathbf{r}_p \cdot \mathbf{v}_p = 0$. Note this relationship can be proven in both the inertial and rotating reference frames

for a circular parking orbit. Transfer orbits that have an initial velocity parallel to the parking orbit and a final velocity parallel to a SPDRO are energetically efficient, since no propulsive force is spent rotating the velocity vector. Therefore, we seek transfer orbits that begin with $\beta_o = \beta_p$, $\alpha_o = \alpha_p$, and $r_o = r_p$. Since SPDROs are symmetric about the *x*-axis the latter condition is automatically satisfied by constraining the search to the hyperplane, $\dot{x} = 0$.

An initial guess for the first differential correction algorithm is found by randomly sampling a small number of points near a ribbon of collision orbits. Sampled points are integrated backwards until they intersect the parking orbit. α_o and β_o at the intersection are recorded, shown as hollow squares in Fig. 4-3, where more than a necessary number of points have been sampled for demonstration. Linear interpolation/extrapolation is then used to find a guess that comes reasonably close to $\beta_o = \beta_p$ and $\alpha_o = \alpha_p$ along a monotonic function. As a result of isolating small regions of collisions, the orbit characteristics vary linearly at the intersection with the parking orbit.

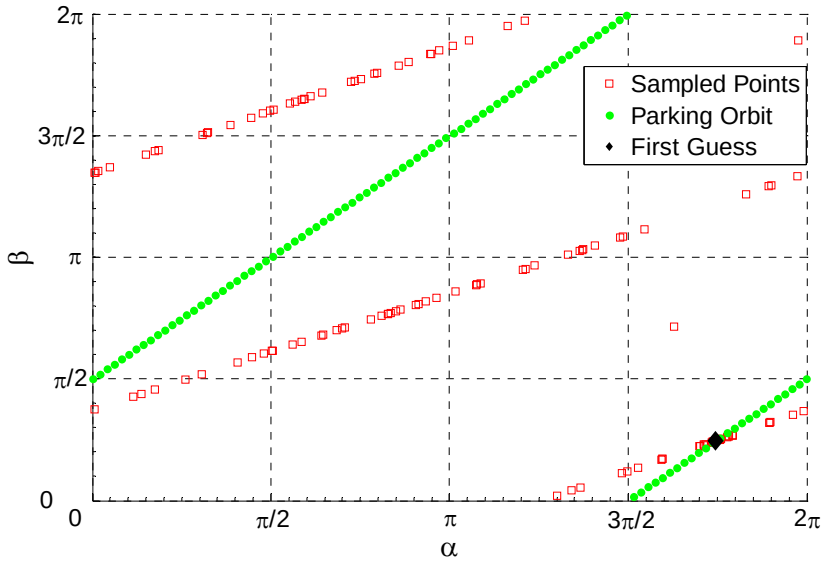

Fig. 4-3 α versus β for a circular parking orbit, solid circles, and sampled transfer orbits, hollow squares. The initial guess for the predictor-corrector algorithm is indicated by the diamond.

This procedure supplies a single guess for each transfer family at a particular value of Jacobi constant. Thus, only a small segment of a one-dimensional curve is sampled with one search direction along a monotonic function. Using only this guess, a predictor-corrector algorithm generates transfer orbits for arbitrary SPDRO sizes each corresponding to a unique transfer energy. Two others modify the parking orbit altitude and the insertion point on the SPDRO. Similarly, this procedure can be applied to transfer orbits which terminate on the negative *x*-axis on the opposite side of the Earth. The approach lifts the restriction of acquiring an Earth return periodic orbit for each transfer orbit. Such orbits are difficult to attain without an accurate guess.

Predictor-Corrector Algorithms

The method to navigate the design space can be described as follows. First, for a given parking orbit altitude an initial guess is calculated using the methodology outlined above. This guess is refined using differential correction, yielding a transfer trajectory that departs from the parking orbit tangentially and terminates perpendicularly to the *x*-axis, $\dot{x} = 0$. By construction, the transfer orbit intersects a SPDRO tangentially. Starting from this nominal orbit, two algorithms are used to modify size of the parking orbit and SPDRO for trajectories terminating on the *x*-axis. The latter case involves numerical continuation of the transfer trajectory through a range of energies, each having access to a distinct SPDRO. Once the desired SPDRO and parking orbit altitude have been reached, a third algorithm modifies the trajectory so that favorable insertion points can be found. These algorithms, outlined below, provide an automated procedure to navigate the design space. Additionally, the results describe the relationship among families of transfer trajectories and the dominant features of phase space near the second primary.

Predictor-Corrector for Transfers to the *x*-axis

The algorithm to find transfer orbits that terminate on the *x*-axis is built in a similar manner to one that applies continuation to locate symmetric periodic orbits, such as those plotted in Fig. 4-2. The terminal constraints remain the same while the constraints on the initial conditions are replaced by new conditions dictated by the parking orbit and the Jacobi constant of the transfer orbit. Specifically, a set of initial conditions satisfying the constraints will be differentially corrected until the final velocity in the *x*-direction is zero for a specified constant of motion. After differential correction the predictor step is performed to rectify any violations of the constraints incurred during differential correction, for example energy. Once again,

differential correction is performed until the final velocity in the *x*-direction is zero. This procedure is repeated until the constraints and end conditions are satisfied to specified tolerance. To access a range of SPDROs, the constraint on the Jacobi constant is modified to a new value during the prediction step and process is continued.

Consider a transfer orbit, $\mathbf{X}(\mathbf{X}_o, t)$, from time $t = 0$ to its terminal state at $t = T$, where $\mathbf{X}_o = \mathbf{X}(\mathbf{X}_o, 0) = \begin{bmatrix} x_o & y_o & \dot{x}_o & \dot{y}_o \end{bmatrix}^T$ and $\mathbf{X}_1 = \mathbf{X}(\mathbf{X}_o, T) = \begin{bmatrix} x_1 & y_1 & \dot{x}_1 & \dot{y}_1 \end{bmatrix}^T$. Expanding to first order about $(\mathbf{X}_o, T)$,

$$\delta \mathbf{X}_1 = \Phi(T)\,\delta \mathbf{X}_o + \frac{\partial \mathbf{X}_1}{\partial t}\delta T \tag{4.1}$$

where $\Phi(T) = \dfrac{\partial \mathbf{X}_1}{\partial \mathbf{X}_o}$ is the 4×4 state transition matrix. Eq. (4.1) provides the variation of the final state as a function of small changes in the initial conditions and transfer time. The SPDROs possess symmetry about the *x*-axis. Therefore, a particular transfer orbit will possess a terminal velocity parallel to a SPDRO if $\dot{x}_1 = 0$ at $y_1 = 0$. Using this property, a differential correction scheme can be established where $\delta \dot{x}_1 = -\dot{x}_1$ at each iteration. Expanding Eq. (4.1) and choosing the third element,

$$\delta \dot{x}_1 = \Phi_{31}\delta x_o + \Phi_{32}\delta y_o + \Phi_{33}\delta \dot{x}_o + \Phi_{34}\delta \dot{y}_o + \ddot{x}_1 \delta T \tag{4.2}$$

furnishes one equation and five unknowns.

Four constraints are required in order to develop a differential correction routine. y_1 will be numerically forced to zero, since we seek transfer trajectories that terminate on the *x*-axis. As a result, $\delta y_1 = 0$ and δT can be eliminated by utilizing the second element of Eq. (4.1),

$$\delta T = -\frac{\Phi_{21}}{\dot{y}_1}\delta x_o - \frac{\Phi_{22}}{\dot{y}_1}\delta y_o - \frac{\Phi_{23}}{\dot{y}_1}\delta \dot{x}_o - \frac{\Phi_{24}}{\dot{y}_1}\delta \dot{y}_o \tag{4.3}$$

Considering the constant of motion, provides another constraint.

$$\delta C = C_{x_o}\delta x_o + C_{y_o}\delta y_o + C_{\dot{x}_o}\delta \dot{x}_o + C_{\dot{y}_o}\delta \dot{y}_o \tag{4.4}$$

where the subscripts indicate partial derivatives. Solving for $\delta \dot{y}_o$,

$$\begin{aligned} \delta \dot{y}_o &= -\frac{C_{x_o}}{C_{x_o}}\delta x_o - \frac{C_{y_o}}{C_{x_o}}\delta y_o - \frac{C_{\dot{x}_o}}{C_{x_o}}\delta \dot{x}_o + \frac{\delta C}{C_{x_o}} \\ &:= R_1\delta x_o + R_2\delta y_o + R_3\delta \dot{x}_o + R_4 \end{aligned} \tag{4.5}$$

where $\delta C = 0$ for differential correction. Furthermore, $\delta C = -\left(C_o - C_{xfer}\right)$ if a prediction step is required to access new transfer energies where C_o and C_{xfer} are the current and desired Jacobi constant. Two additional constraints can be formulated by restricting the starting velocity to be parallel to a circular parking orbit. Accordingly, since the parking orbit is circular, the velocity of the transfer orbit in the rotating reference frame will be perpendicular to the radius with respect to the second primary, $\mathbf{r}_{2o} \cdot \mathbf{v}_o = 0$. Taking the variation of this expression,

$$\delta\left(r_{2o} \cdot v_o\right) := \Delta DP = \dot{x}_o\delta x_o + \dot{y}_o\delta y_o + \left(x_o + 1 - \mu\right)\delta \dot{x}_o + y_o\delta \dot{y}_o \tag{4.6}$$

yields,

$$\begin{aligned}\delta\dot{x}_o &= -\frac{\dot{x}_o}{\left(x_o+1-\mu\right)}\delta x_o - \frac{\dot{y}_o}{\left(x_o+1-\mu\right)}\delta y_o - \frac{y_o}{\left(x_o+1-\mu\right)}\delta\dot{y}_o + \frac{\Delta DP}{\left(x_o+1-\mu\right)} \\ &:= C_1\delta x_o + C_2\delta y_o + C_3\delta\dot{y}_o + C_4\end{aligned} \tag{4.7}$$

Since we consider only circular parking orbits, $\Delta DP = -\left(r_{2o}\cdot v_o\right)$ if the initial guess violates the constraint, otherwise, $\Delta DP = 0$. Taking the variation of the squared radius with respect Earth,

$$\delta\left(r_{2o}^2\right) = \delta\left(h_p + R_\oplus\right)^2 = 2y_o\delta y_o + 2\left(x_o+1-\mu\right)\delta x_o \tag{4.8}$$

where h_p and $R_\oplus$ are the altitude of the corrected parking orbit and the normalized radius of Earth, respectively. Solving for δx_o,

$$\delta x_o = -\frac{y_o}{\left(x_o+1-\mu\right)}\delta y_o + \frac{\delta\left(h_p+R_\oplus\right)^2}{2\left(x_o+1-\mu\right)} := D_1\delta y_o + D_2 \tag{4.9}$$

Here $\delta\left(h_p+R_\oplus\right)^2$ can be set to finite value for a prediction step or if the initial guess violates the constraint. Combining Eqs. (4.1)-(4.9) a predictor-corrector routine can be constructed with the following equations,

$$\begin{aligned}\delta y_o &= -\frac{\dot{x}_1 + V_1D_2 + V_3}{V_1D_1 + V_2} \\ \delta x_o &= D_1\delta y_o + D_2 \\ \delta\dot{x}_o &= C_1^*\delta x_o + C_2^*\delta y_o + C_3^* \\ \delta\dot{y}_o &= R_1\delta x_o + R_2\delta y_o + R_3\delta\dot{x}_o + R_4\end{aligned} \tag{4.10}$$

where,

$$V_1 = U_1 + U_3 C_1^* \qquad V_2 = U_2 + U_3 C_2^* \qquad V_3 = U_4 + U_3 C_3^*$$
$$U_1 = T_1 + T_4 R_1 \qquad U_2 = T_2 + T_4 R_2 \qquad U_3 = T_3 + T_4 R_3 \qquad U_4 = T_4 R_4$$
$$C_1^* = \frac{C_1 + C_3 R_1}{1 - C_3 R_3} \qquad C_2^* = \frac{C_2 + C_3 R_2}{1 - C_3 R_3} \qquad C_3^* = \frac{C_3 R_4 + C_4}{1 - C_3 R_3}$$
$$T_1 = \Phi_{31} - \frac{\ddot{x}_1 \Phi_{21}}{\dot{y}_1} \qquad T_2 = \Phi_{32} - \frac{\ddot{x}_1 \Phi_{22}}{\dot{y}_1} \qquad T_3 = \Phi_{33} - \frac{\ddot{x}_1 \Phi_{23}}{\dot{y}_1} \qquad T_4 = \Phi_{34} - \frac{\ddot{x}_1 \Phi_{24}}{\dot{y}_1}$$

Given a reasonable guess the algorithm will typically converge within a few iterations. Integrating the initial conditions until time $2T$, instead of performing the second maneuver yields a return orbit due to symmetry. These orbits are used as a starting point to navigate the design space. Figure 4-4 shows F1 transfers, to be discussed, constructed using this algorithm at a variety of energies. Each accesses a distinct SPDRO via a two tangential burns.

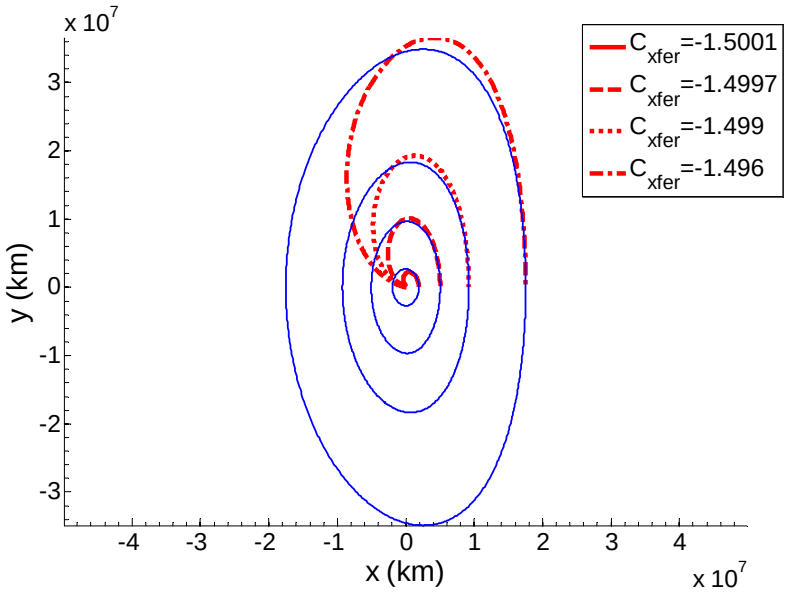

Fig. 4-4 F1 transfers at C=-1.5001, -1.4997, -1.499, and -1.496.

Predictor-Corrector for Variable Parking Orbit Altitudes

Once a nominal transfer orbit has been found using the aforementioned procedure, the initial parking orbit altitude can be modified. Suppose we want to find transfers to the same SPDRO, terminating on the *x*-axis, for a range of parking orbit altitudes. A single SPDRO can be specified by setting x_{1set}; therefore, we seek convergence conditions $x_1 = x_{1set}$ and $\dot{x}_1 = 0$ where $\delta x_1 = -\left(x_1 - x_{1set}\right)$ and $\delta \dot{x}_1 = -\dot{x}_1$. Keeping the constraints of the previous algorithm with the exception of energy yields the following corrections to the initial conditions.

$$\begin{bmatrix} \delta y_o \\ \delta \dot{y}_o \end{bmatrix} = \begin{bmatrix} V_{11} & V_{12} \\ V_{21} & V_{23} \end{bmatrix}^{-1} \begin{bmatrix} \delta x_1 - V_{13} \\ \delta \dot{x}_1 - V_{23} \end{bmatrix}$$
$$\delta x_o = D_1 \delta y_o + D_2 \tag{4.11}$$
$$\delta \dot{x}_o = C^*_{R1} \delta x_o + C^*_{R2} \delta y_o + C^*_{R3}$$

where $C^*_{R1} = C_1 D_1 + C_2 \quad C^*_{R2} = C_3 \quad C^*_{R3} = C_1 D_2 + C_4$. All undefined variables are provided in Appendix.

In most cases the algorithm requires only three steps to modify the transfer from a parking orbit altitude of 200 to 2000 km, resulting from linear variations in the initial conditions of the transfer orbit. The exceptions are the F2 and F5 transfers which draw especially close to each other with increasing SPDRO size. For these exceptional cases, as many as a few thousand steps are required depending on the energy. ΔV requirements depend linearly on the parking orbit altitude and the transfer time is nearly constant as a result of the scale of the problem, small second derivatives. F1 transfers starting from a range of parking orbit altitudes are displayed in Fig. 4-5.

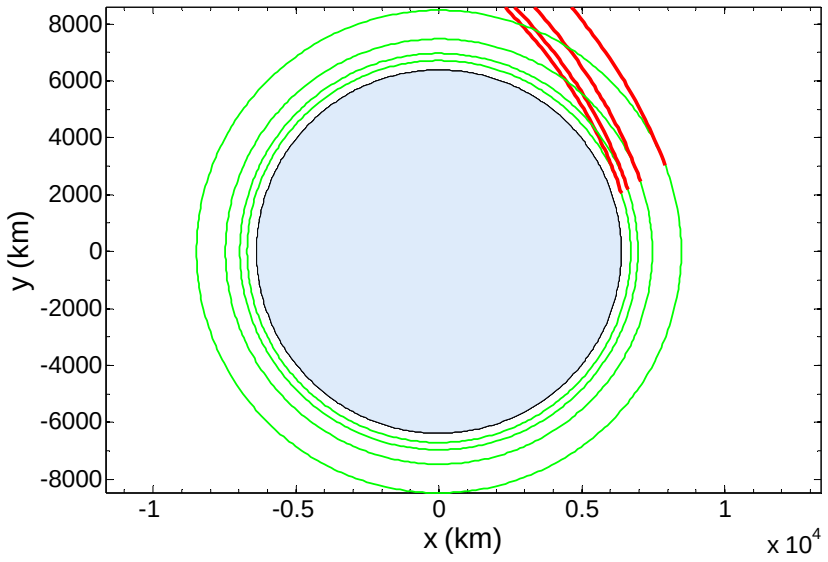

Fig. 4-5 F1 transfers starting from unadjusted parking orbit altitudes of 250, 500, 1000, and 2000 km.

Predictor-Corrector for Variable Insertion Points

Suppose the dependence of ΔV and transfer time on the insertion point is sought for a particular SPDRO. Assuming that a transfer to this SPDRO starting at a specific altitude, terminating on the *x*-axis, and a time series of the SPDRO are available, the algorithm is developed as follows. First the final directions of the radius and velocity vectors are specified by two angles α'_f and β_f where $\hat{\mathbf{r}}_{2f} \cdot \hat{\mathbf{j}} = \cos\alpha'_f$, $\hat{\mathbf{v}}_f \cdot \hat{\mathbf{i}} = \cos\beta_f$, and the "hat" indicates a unit vector. Based on the time series the magnitude of the final radius is specified by $r_{2f} = \sqrt{(x_1 + 1 - \mu)^2 + y_1^2}$. Taking the variations of these expressions yields three linear constraints on the final state, namely, $\delta y_1 = -A_1/A_2\,\delta x_1 + \delta CA/A_2$, $\delta \dot{x}_1 = -B_2/B_1\,\delta \dot{y}_1 + \delta CB/B_1$, and $\delta x_1 = \left[-y_1/(x_1 + 1 - \mu)\right]\delta x_1 + \delta RS_1/\left[2(x_1 + 1 - \mu)\right] := F_1 \delta x_1 + F_2$ where $\delta CA = \delta\left(\cos\alpha'_f\right)$, $\delta CB = \delta\left(\cos\beta_f\right)$, and $\delta RS_1 = \delta\left(r_{2f}^2\right)$. Placing the same constraints on the initial radius and

velocity as the previous algorithms while lifting the energy constraint and leaving transfer time to be determined, Eq. (4.1) can be modified to give the following corrections,

$$\begin{bmatrix} \delta y_o \\ \delta \dot{y}_o \\ \delta T \end{bmatrix} = \begin{bmatrix} T_{11} & T_{12} & T_{13} \\ T_{21} & T_{22} & T_{23} \\ U_1 & U_2 & U_3 \end{bmatrix}^{-1} \begin{bmatrix} \delta x_1 - T_{14} \\ \delta y_1 - T_{24} \\ cor3 \end{bmatrix} \tag{4.12}$$

where $\delta x_o = D_1 \delta y_o + D_2$, $\delta \dot{x}_o = E_1 \delta y_o + E_2 \delta \dot{y}_o + E_3$, and $cor3 = -T_{34} - \left(B_2 / B_1\right) T_{44} + \delta CB / B_1$. The remaining variables are defined in Appendix . As before, δDP_o and δRS_o will be finite for a prediction step and set to zero during corrections. The initial conditions are modified until α'_f , β_f , and r_{2f} match the target values to a specified tolerance. An alternative version, Algorithm B provided in Appendix A, can be formulated that avoids singularities at $\dot{y}_1 = 0$, $x_1 + 1 - \mu = 0$, and $x_o + 1 - \mu = 0$.

The combination of these formulations is sufficient to access large regions of insertion points, but fail if the transfer trajectory evolves into a collision orbit or if the local gradients are sufficiently large, thereby forcing the stepsize to become lower than the conversion tolerances. The algorithms, however, can still find at least one of the favorable insertion points (there are generally two) in terms of minimum ΔV and transfer time without a large penalty. Inspection of the data and comparisons with past studies verifies this assertion.

Collision orbits are of no use to most spacecraft missions, therefore the algorithm is terminated once a collision has been reached. This avoids the added complexity of using a regularized version of the algorithm. In addition, the ranges, corresponding to especially large gradients, which require a prohibitively small stepsize are omitted. They generally correspond to suboptimal conditions in terms of minimizing either the transfer time or ΔV and may be

impractical to space missions due to their sensitivity. These ranges can include transfers of high energy where families become prohibitively close in phase space or those which approach the curves of zero velocity (CZV). These characteristics will be demonstrated later. To deal with these omissions two transfer orbits terminating on the *x*-axis, on either side of the Earth, are used as starting points to navigate the design space. This method simplifies the algorithm and reduces computation time allowing a large range of insertion points to be accessed. Figure 4-6 shows the modification of an F1 transfer to various insertion points.

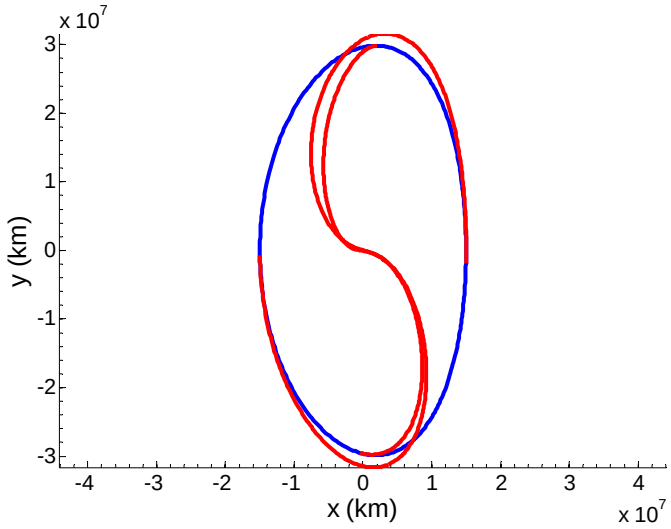

Fig. 4-6 F1 transfers to insertion points of α=7, 91, 178, and 274 deg.

Application and Results

Transfers Terminating on the *x*-axis

Five transfer types starting at a parking orbit altitude adjusted from a nominal value of 200 km and terminating on the *x*-axis are considered using the procedure outlined above. Figure

4-7 shows the termination point of five families of transfer orbits versus Jacobi constant in normalized units and their relative positions to the SPDROs, BUPOs, and Lyapunov orbit about L_1. F1-3 correspond to Ocampo's class A, B, and C transfers for a range of larger SPDROs [1, 2]. Notice that the transfer families parallel the major bands of collision orbits. Additional collision regions, not investigated in this study, imply the existence of more transfer families.

The bands represent a mapping of the subset of initial conditions starting on the Earth's surface at a particular energy striking the SOS, indicated in Figure 4-7a, perpendicularly. Since the volume of these initial conditions is preserved, as time is increased the detection of orderly bands in this and other regions of space becomes more difficult due to chaotic stretching and mixing. The new bands become thinner as the aggregate volume of orbits originating at the Earth's surface stretches with time. Close inspection of Fig. 4-7b reveals that the thickness of collision bands scales inversely with the transfer time of the corresponding transfer.

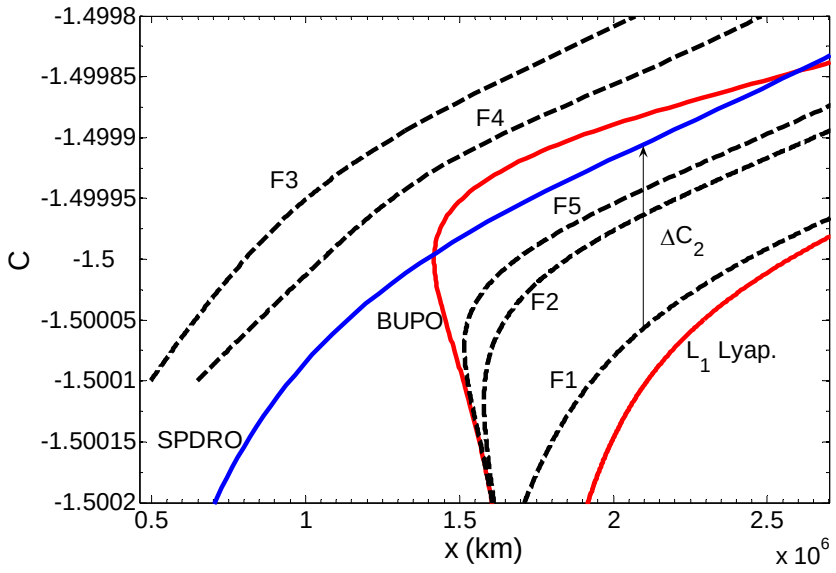

(a)

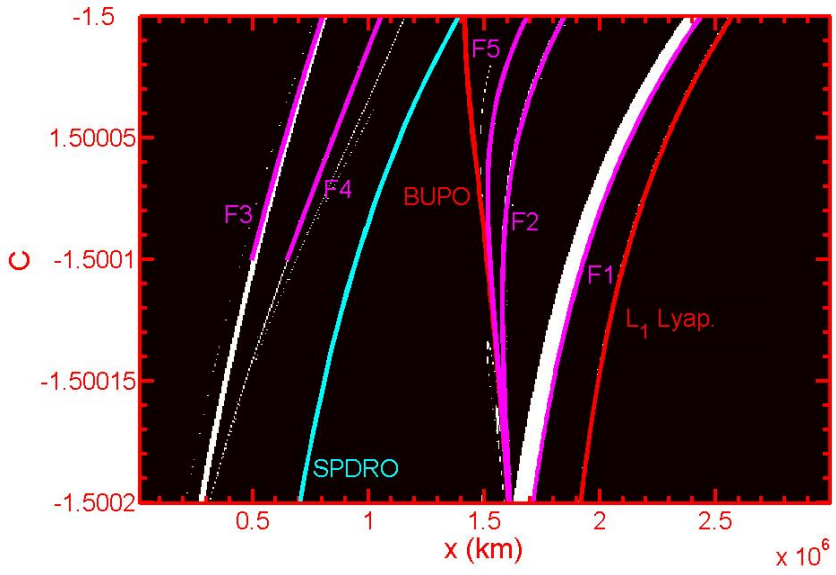

(b)

Fig. 4-7 (a) Termination point of five families of transfer orbits versus Jacobi constant (normalized units). (b) Termination points plotted on a forward collision map of two years. White and black indicate collision and no collision, respectively.

The intersections of the SPDRO and BUPO curves indicate the disappearance of the stable island surrounding the SPDRO. Therefore, these distances, approximately 1.48 and 2.60 M km, should be avoided when seeking a stable orbit or a large stable region. Figure 4-8 displays each transfer for a Jacobi constant of -1.5. At a set energy each transfer has access to a distinct SPDRO.

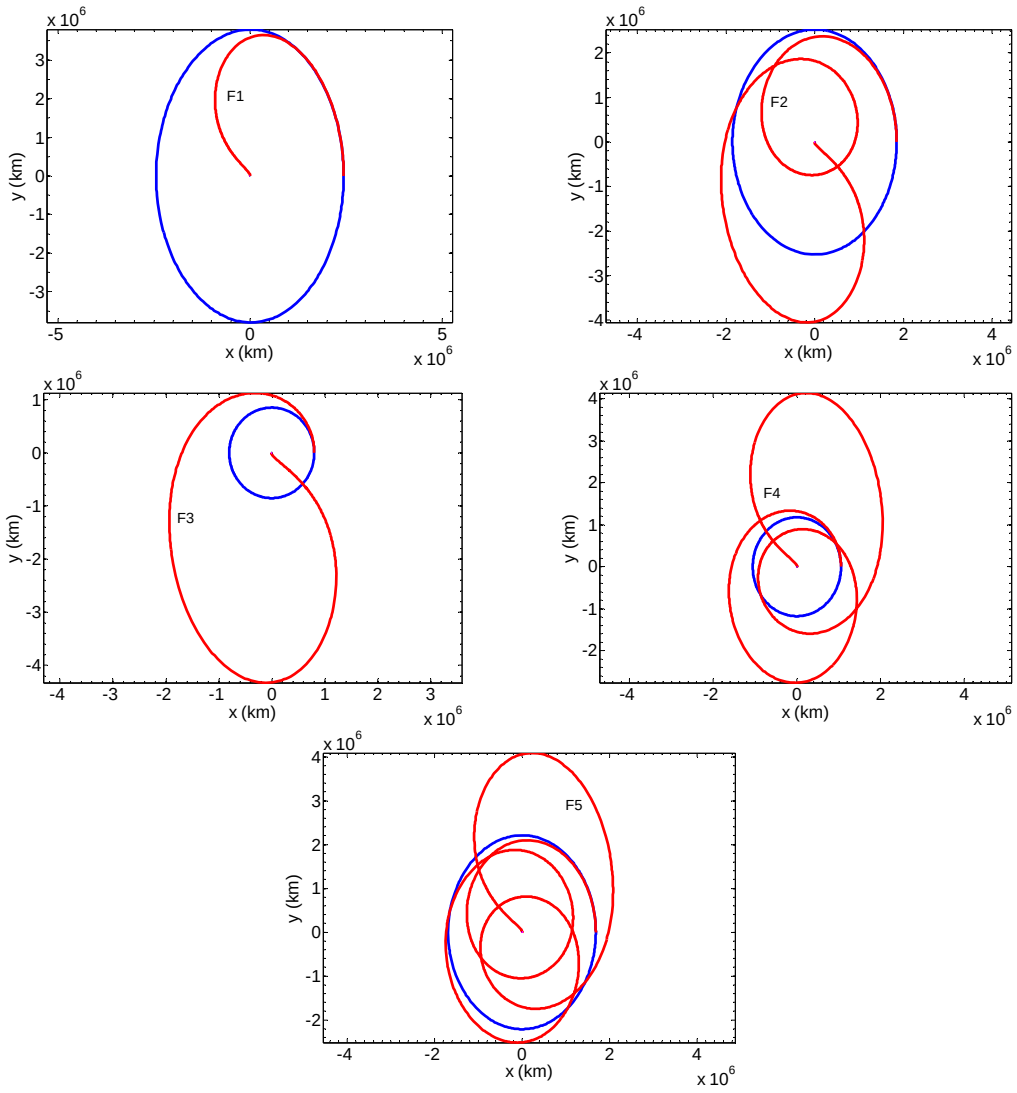

Fig. 4-8 F1-5 transfers at a Jacobi constant of -1.5.

The change in velocity required by each maneuver can be cast in terms of the velocities and change in Jacobi constant by

$$\Delta V_1 = \frac{2\Delta C_1}{V_o + V_p} \quad \Delta V_2 = \frac{2\Delta C_2}{V_1 + V_{SPDRO}} \tag{4.13}$$

Here V_o and V_p are the velocities of the transfer and parking orbits at the point of departure. V_1 and V_{SPDRO} are the velocities of the transfer orbit and SPDRO at the point of insertion. Inspection of Fig. 4-7a reveals that F3 and F4 must reduce their energies via retroburns for the second maneuver. Therefore, these transfers are generally less efficient, except for especially small SPDROs, than those lying under the SPDRO curve. Each SPDRO is specified by its distance along the *x*-axis from the center of the Earth measured away from the sun. This distance, referred to as SPDRO size, is chosen because it marks the maximum amplitude along the *x*-axis. This specification is necessary because of the asymmetry conspicuous for larger SPDROs shown in Fig. 4-9.

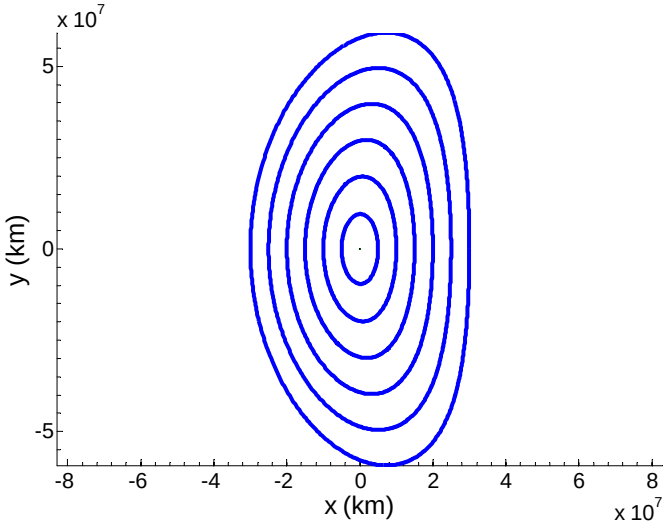

Fig. 4-9 SPDROs of sizes 5, 10, 15, 20, 25, and 30 M km from inner to outer.

Figures 4-10a and b show the variation of total ΔV, ΔV_T, for each family with SPDRO size. F2 and F5 transfers yield moderate savings over F1 transfers from 1.6 M km to 5 M km. This advantage comes at the price of increased transfer times that enlarges with SPDRO size, shown in Fig. 4-10c and d. At larger SPDROs F2 and F5 transfers hold no advantage as the curves of ΔV_T approach the same values. Notice that the F1, F2, and F5 transfers are incapable of accessing orbits smaller than about 1.6 M km. This characteristic can be accounted for by inspection of Fig. 4-7. The expansion of the zone between the SPDRO and BUPO with decreasing energy, largely a stable region filled with QPDROs and bounded chaotic orbits, forces certain families to turn sharply away from smaller SPDROs. As a result, the families which must perform retro-burns, F3 and F4, are superior at these sizes, yet impose a great penalty on ΔV_T and transfer time at moderate to large SPDROs. The final *x*-positions of the F3 and F4 transfers are not prohibited from reaching these smaller sizes. Geometrically, on the hyperplane $\dot{x}_1 = 0$ and across decreasing energy surfaces these families evolve nearly parallel to the SPDRO resulting in a delayed divergence of the transfer parameters.

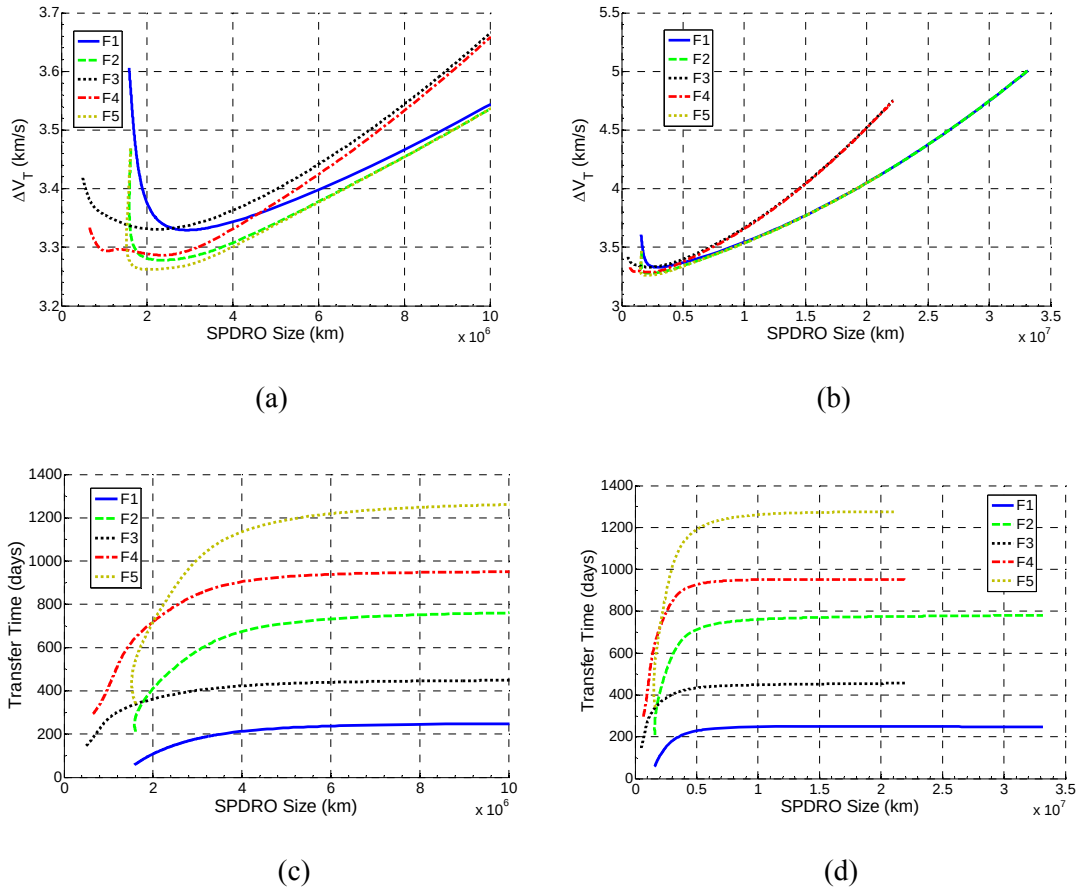

Fig. 4-10 (a) and (b), Variation of ΔV_T with SPDRO size. (c) and (d),Variation of transfer time with SPDRO size.

Figures 4-11a and b show that ΔV_1 is the largest of the maneuvers. The increase of ΔV_1 from minimum values to those corresponding to the maximum SPDRO sizes tested for F1 and F2 transfers is approximately 37% and 36%. F5 displays a similar growth rate paralleling F1 and F2. F3 and F4 evolve along a steeper gradient for ΔV_1 both increasing by 36% for a reduced range in SPDRO size.

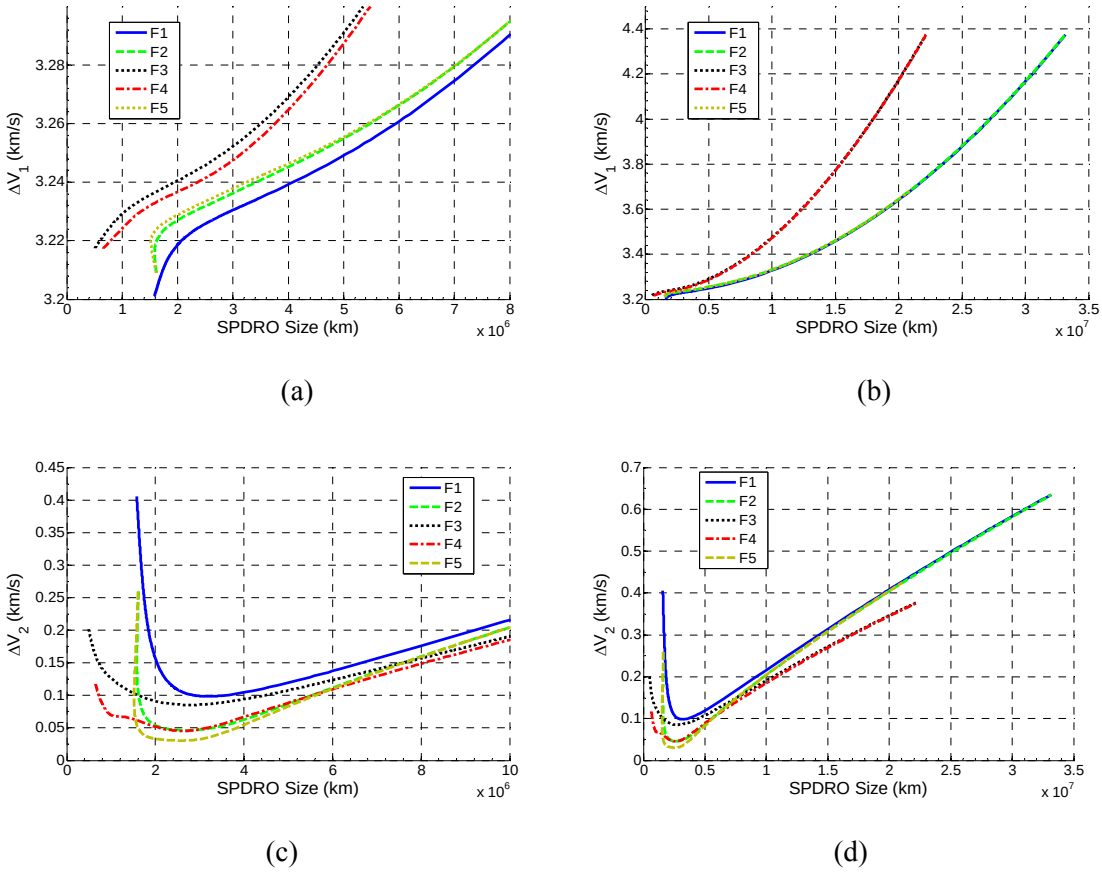

Fig. 4-11 (a) and (b), ΔV_1 versus SPDRO size. (c) and (d), ΔV_2 versus SPDRO size.

The second burn is a comparatively small stabilizing maneuver, yet is responsible for the divergence of ΔV_T for F1, F2, and F5 at lesser SPDRO sizes due to the expansion of the stable region. Although delayed for F4 and F3, all transfers eventually experience an increase in ΔV_2 with decreasing SPDRO size. ΔV_2 possesses an increased share of ΔV_T with increasing SPDRO size exceeding 10% for F1, F2, and F5 at the largest SPDROs tested. F3 and F4 experience a lesser increase due to the evolving shape of the stable region.

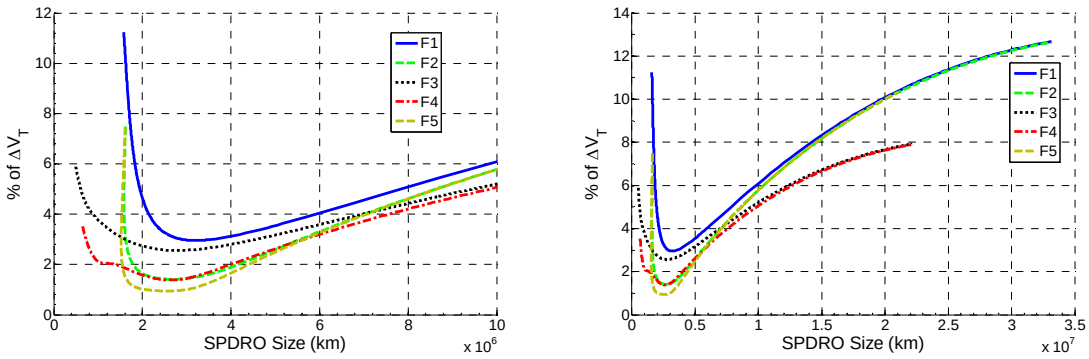

Fig. 4-12 ΔV_2 as percentage of ΔV_T.

Geometrically, by simple arguments of dimensionality, the transfer orbits are physically forbidden from entering the stable region, see Table 2-1. Therefore, these trends can be understood by visualizing the second maneuver as a shift of the stable region and the SPDRO, by increasing or decreasing the energy, to the location of the terminal point of the transfer. The magnitude of ΔV_2 to perform this shift as a function of distance and energy is determined by the slope of the SPDRO curve in Fig. 4-7a. For instance, the impulse required to shift the SPDRO from 0.8 to 1.2 M km is greater than a shift from 2 to 2.4 M km. This characteristic in conjunction with the expanding stable region at lower energy forces a divergence of ΔV_2.

As energy is increased the location of the terminal points of the transfer orbits draw closer to each other and the boundary of the expanding stable region with one side marked by the BUPO. Given the constant of motion, as the transfers approach the same physical location they must approach the same velocity. In particular, the F1, F2, and F5 and, F3 and F4 transfers converge to the same values.

The starting Jacobi constant has little variation for any position corresponding to initial conditions on a circular parking orbit. Each transfer starts from a unique position, α_p, at a given energy. Decreasing the SPDRO size also causes the two groups of transfer orbits approach the same energy and velocity. Thus by Eq. (4.13), ΔV_1 and ΔV_2 for each of the two groups approach

the same values as SPDRO size is increased or decreased. The convergence of transfer families can be physically described by the evolution of phase space structures in the distant retrograde region with energy.

The manifolds of the hyperbolic point corresponding to the L_1 Lyapunov orbit, Fig. 4-13b, on the SOS break it into four distinct quadrants labeled from one to four. Orbits contained within these quadrants are en route to distinct regions of motion, viz., the IR, ER, and OR, the interior, exterior, and outer regions respectively. Terminal points greater than the mapping of the L_1 Lyapunov orbit, quadrant 3, originate from sun-centered orbits interior to the Earth's orbit turning away from its vicinity indicated by the arrow. Points in quadrant 1 just below the manifolds of the BUPO are purely retrograde orbits largely contained in the stable region. See also the nine classes of motion discussed in chapter 2 via linearization about the collinear points.

By the arguments given in a previous section, there exist orbits that pass especially near the Earth in the prograde direction lying outside of the stable region. Thus, on the SOS the F1, F2, and F5 transfer orbits can only exist between the hyperbolic point corresponding to the L_1 Lyapunov orbit and the fringe of the stable region. As energy is increased the relative distance diminishes forcing a decreased separation between the F1, F2, and F5 transfers near the edge of the stable region.

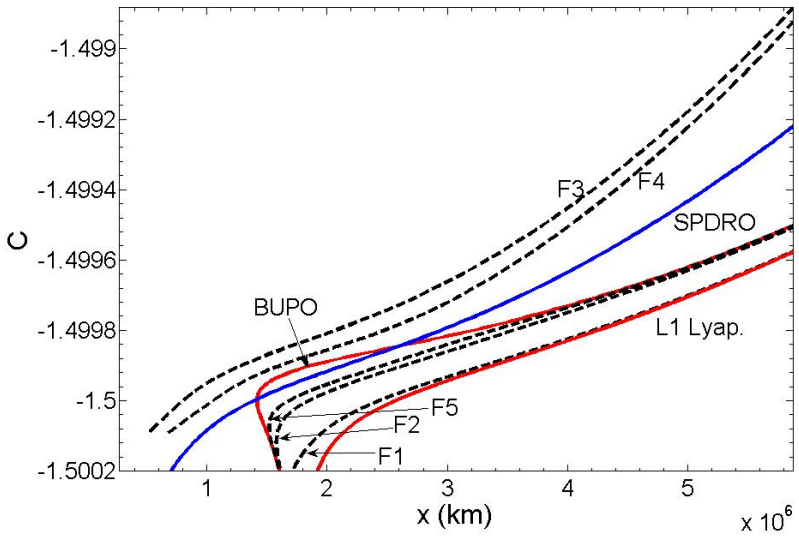

(a)

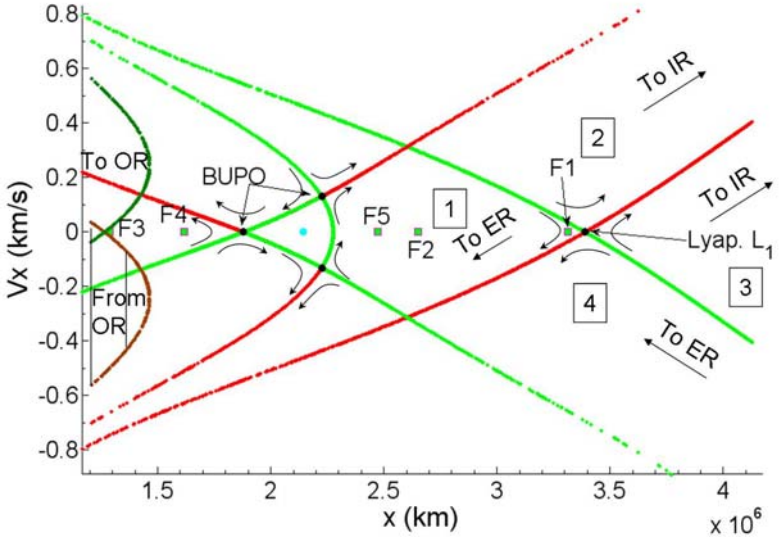

(b)

Fig. 4-13 Position of transfer families and phase space structures. (a) Termination point of five families of transfer orbits versus Jacobi constant along with the continuation of the SPDRO, BUPO, and L_1 Lyapunov orbit. (b) Map of the manifolds of the L_1 and L_2 Lyapunov orbits and BUPO at C=-1.4999. The stable and unstable manifolds of the L_1 Lyapunov orbit and BUPO are shown green and red, respectively. The unstable manifold "tube" of the L_2 Lyapunov orbit is indicated by the hatched region. The termination point of each family is indicated by the labeled squares.

F3 and F4 transfers which terminate at *x*-values just below the fringe of the stable region closest to Earth are bounded by both the stable region and the unstable manifold "tube" of the L_2 Lyapunov orbit, indicated by the hatched region in Fig. 4-13b. By Fig. 4-8, orbits traveling through the tube cannot be F3 and F4 transfers since it is filled with orbits originating directly from sun-centered orbits exterior to the Earth. As energy is increased the tube enlarges, see the progression of Fig. 4-13b and Fig. 4-14a and b, consistent with the enlargement of the L_2 Lyapunov orbit, in conjunction with an expansion of the stable region. The net effect is similar to the previous case involving the convergence of the transfer orbits to each other and the fringe of the stable region.

In all cases, this convergence, in conjunction with the expansion of the stable region and an increase in the slope of the SPDRO curve in Fig. 4-13a, causes ΔV_2 to increase as a greater energy change is needed to shift the location of the SPDRO to the termination point of the transfer orbits. This increase is not as drastic for F3 and F4, Fig. 4-11c and d, as the stable region takes on a crescent-like shape reducing the distance between the terminal points of the transfers and the SPDRO.

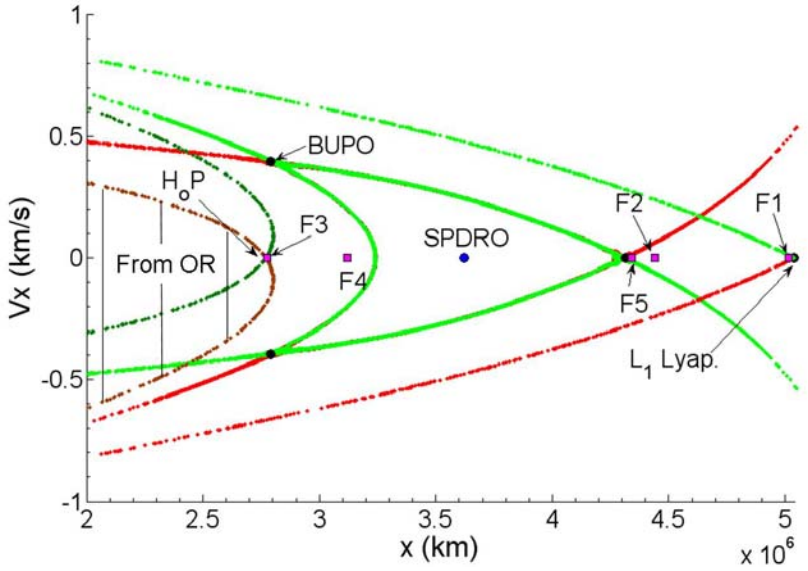

(a)

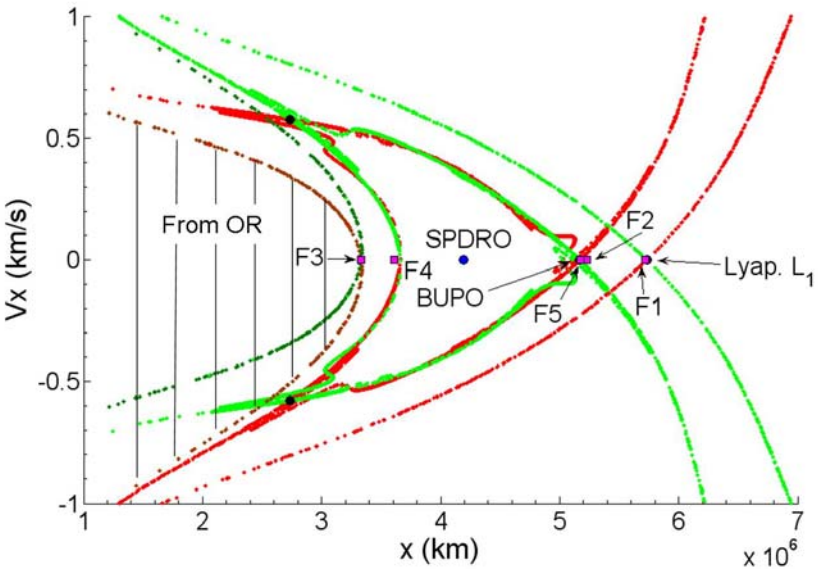

(b)

Fig. 4-14 Evolution of phase space structure with energy. (a) Map of the manifolds of the BUPO and L_2 Lyapunov orbits at C=-1.4997. The unstable manifold tube of the L_2 Lyapunov orbit is indicated by the hatched region. The termination point of each family is indicated by the labeled squares. (b) Map at C=-1.4996 illustrating the expansion of the unstable manifold tube of the L_2 Lyapunov orbit. The reduced relative distance between the edge of the tube and stable region compresses F3 and F4 into a smaller region. F1, F2, and F5 converge in a similar manner.

Earth Return Periodic Orbits

The previous section described transfers which terminate perpendicularly to the *x*-axis. As the transfers are continued through energy the initial conditions start from a unique position and velocity on the parking orbit. For each transfer, an energy will be reached where $\dot{x}_o$ (V_{xo}) is zero. These points are evident in Fig. 4-15 displaying the evolution of V_{xo} with energy for each transfer family. Due to symmetry, these particular transfers correspond to half of an unstable periodic orbit, specifically an Earth return orbit. Since each band of collision orbits, shown in Fig. 4-7b, corresponds to a unique transfer family, a periodic orbit that passes near the Earth in the prograde direction at a specific altitude can easily be found. Thus, this procedure can generate an arbitrary number Earth return periodic orbits as a growing number of collision bands can be detected by increasing the simulation time.

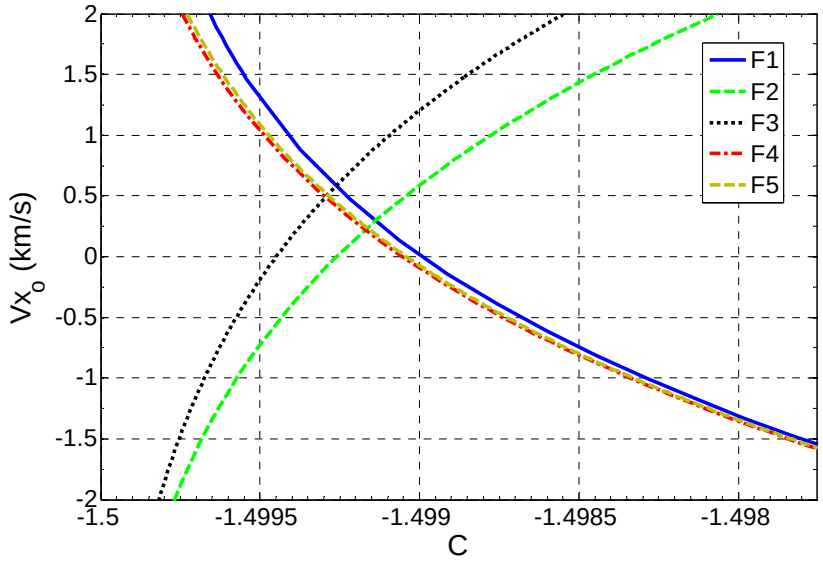

Fig. 4-15 Variation of Vx_o with energy for each transfer family.

Figure 4-16 shows unstable periodic orbits corresponding to the F1-5 transfers passing near the Earth at an altitude adjusted from 200 km in the prograde direction. The first corresponds to the well-known Lyapunov orbit about L_1. Because of the low mass ratio, another set of periodic orbits can be found that are nearly symmetric images about the second primary, for example the Lyapunov orbit about L_2. Since similar structures of collision orbits are present at other mass ratios, the method has applications throughout the solar system. In particular, the orbits may have application for science missions which require a number of close approaches without a reduction in energy. Note that this procedure can also be used to generate periodic orbits that extend to other regions of space or pass near the second primary in the retrograde direction. These orbits are generated by following the opposite edge of a collision region.

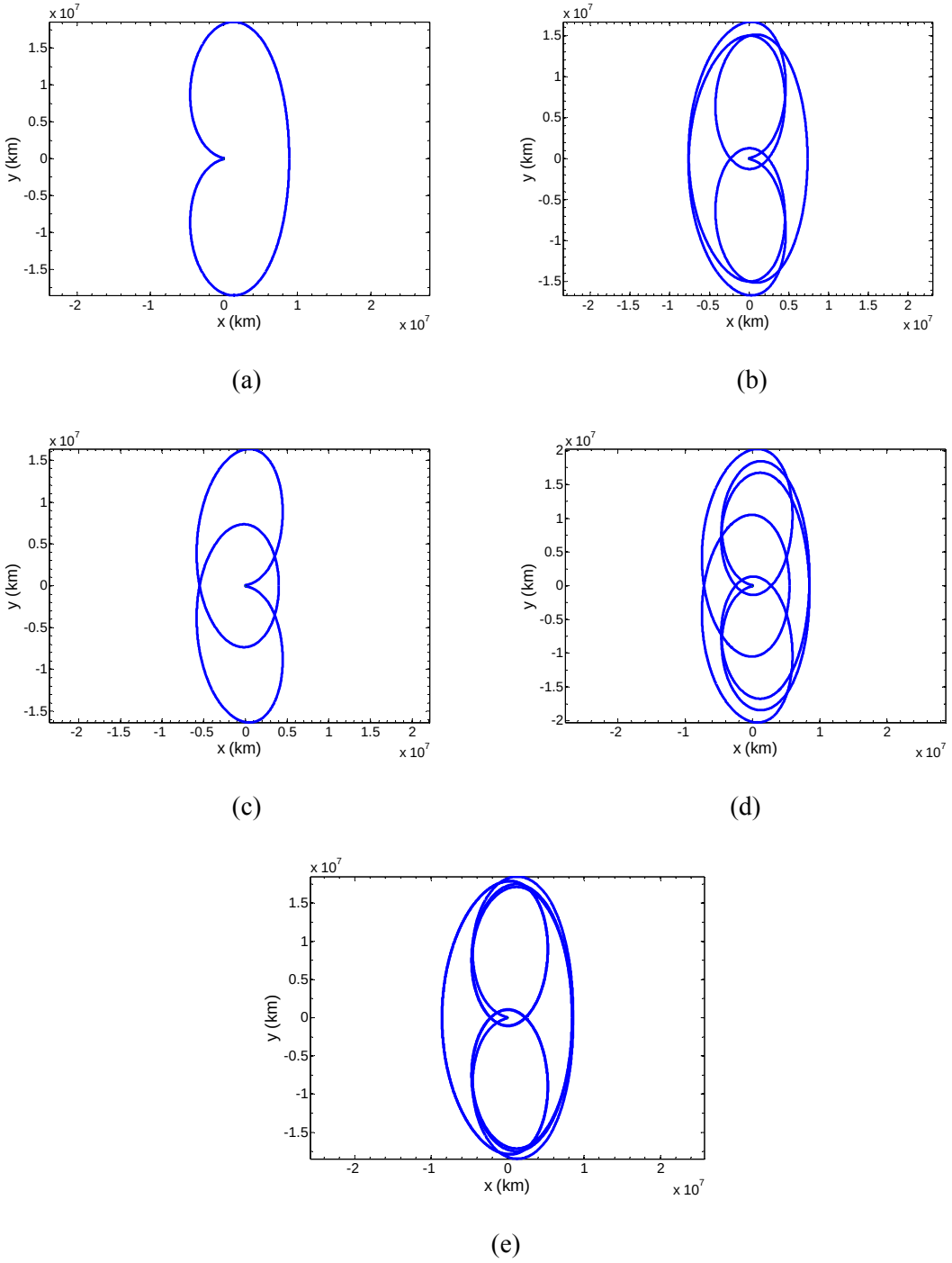

Fig. 4-16 Unstable periodic orbits, Earth return orbits, corresponding to the F1-5 transfers plotted in (a) through (e) in that order, with periods of approximately 494, 1495, 847, 1869, and 2504 days, respectively.

Variable Parking Orbit Altitude

The spacecraft starts on a circular parking orbit for all transfers in this study. Therefore, it is assumed to reside in its initial orbit for a short duration implying that the effects of J_2 (Earth's oblateness), third body perturbations, atmospheric drag, and other unmodeled forces are negligible. Figure 4-17 shows that the variation of ΔV_T with parking orbit altitude is nearly linear for a range of unadjusted altitudes. Predominantly, fewer than ten steps are required by the algorithm to navigate the range of parking orbit altitudes. The exceptions are the F2 and F5 transfers which draw especially close to each other with increasing SPDRO size. In these atypical cases, as many as a few thousand steps are required.

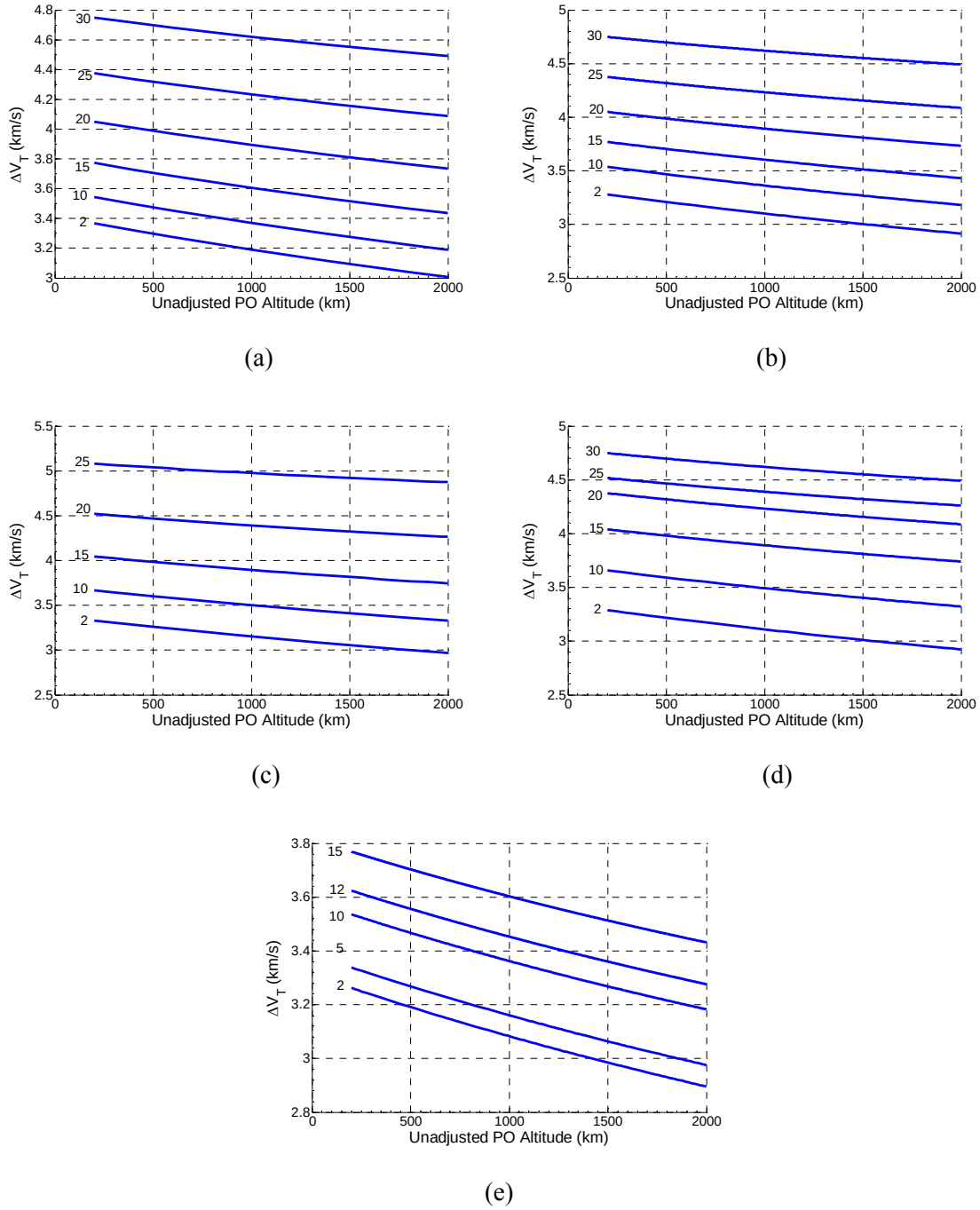

Fig. 4-17 Variation of ΔV_T with unadjusted parking orbit altitude at the indicated SPDRO sizes in M km. Plots (a-e) correspond to F1-5 in that order.

These simple trends can be understood by noticing the relative scales of the problem. A change of altitude from 200 km to 2000 km spans yields an energy change that is small fraction of that of the SPDRO. Since the transfers do not naturally transition into a different regime of motion (ie. another transfer type), a first order Taylor series expansion yields an accurate approximation.

The expression for ΔV_T which depends on the adjusted parking orbit altitude, h_p, and the starting position $\alpha_p\left(h_p\right)$. Here α is a function of only the altitude since there is a unique starting position corresponding to each altitude at a constant SPDRO size. Thus,

$$\begin{aligned}\Delta V_T\left(h_p\right) &= \Delta V_1\left(h_p\right) + \Delta V_2\left(h_p\right) = V_o\left(h_p\right) - V_p\left(h_p\right) + V_{DRO} - V_1\left(h_p\right) \\ &:= V_{SPDRO} - V_p\left(h_p\right) + f\left(h_p\right)\end{aligned} \tag{4.14}$$

and

$$\Delta V_T\left(h_p\right) \approx V_{SPDRO} - V_{po} + f\left(h_{po}\right) + \left(\frac{V_{po}}{2\left(R_\oplus + h_{po}\right)} + f'\left(h_{po}\right)\right)\Delta h_p \tag{4.15}$$

Here $(*)'$ indicates a derivative with respect to altitude and h_{po} indicates an unadjusted reference altitude. The truncation error depends on the upper bound of the second derivative and Δh_p^2. $\Delta V_T''\left(h_p\right)$ and $f''\left(h_p\right)$ are small for each family over the range of parking orbit altitudes. Thus, linear extrapolation yields accurate results for typical parking orbit altitudes with errors in the range $|E| \le S\Delta h_p^2/6$ where S is the upper bound on $\Delta V_T''\left(h_p\right)$. Given two points on the curve f' can be calculated yielding an estimate for the percent change in ΔV_T,

$$\%\left(\Delta V_T\right)=\frac{\Delta V_T\left(h_p\right)-\Delta V_T\left(h_{po}\right)}{\Delta V_T\left(h_{po}\right)}\times 100\%=\frac{\Delta V_T'\left(h_{po}\right)}{\Delta V_1\left(h_{po}\right)+\Delta V_2\left(h_{po}\right)}\Delta h_p\times 100\% \quad (4.16)$$

The numerator changes little with increasing SPDRO size, yet ΔV_T increases for all transfers after a SPDRO size of approximately 3 M km. Therefore, the savings as a percentage of the original transfer decreases with increasing SPDRO size. Equivalently, the energetic advantage, relative to the target SPDRO, of increasing the altitude at launch becomes smaller as the SPDRO size is increased.

Figure 4-18 shows the typical behavior of transfer time, in this case an F1 transfer to a 20 M km SPDRO, with unadjusted parking orbit altitude. The transfer time increases by two thousandths of a percent. All simulations displayed no significant variation in transfer time with unadjusted parking orbit altitude. Therefore, the approximations of $T'\left(h_p\right)\approx 0$ and $T\left(h_p\right)\approx T\left(h_{po}\right)$ hold over a large range of parking orbit altitudes.

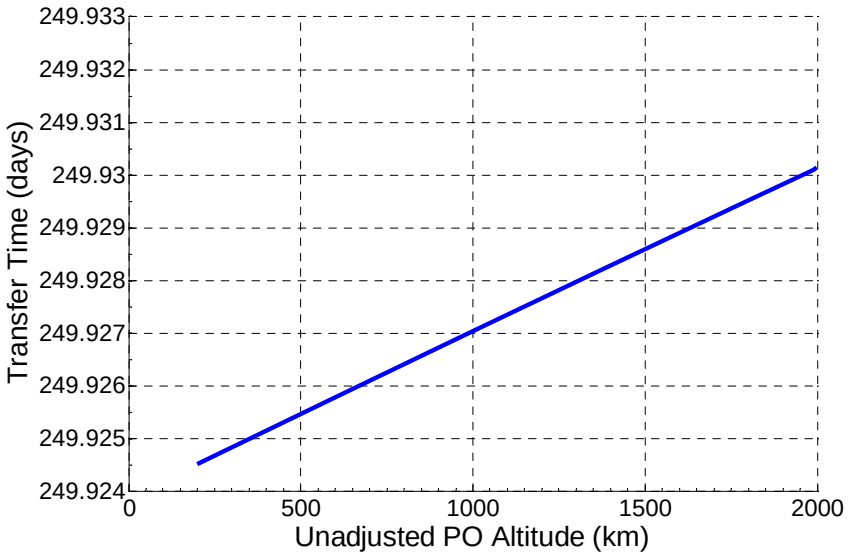

Fig. 4-18 Variation of transfer time with unadjusted parking orbit altitude for an F1 transfer to a 20 M km. SPDRO.

Based on these results the design space can be reduced by dropping extensive sampling of parking orbit altitudes. This comes with the understanding that the ΔV requirements depend linearly on the parking orbit altitude and the transfer time is nearly constant as a result of the scale of the problem, a small second derivative, and the existence of each transfer type over a large altitude range. Generally, moderate adjustments of the parking orbit altitudes yield a reduction in ΔV_T of a few percent. These returns diminish with larger SPDRO sizes as the slopes shown in Fig. 4-17 change little with SPDRO size.

Variable Insertion Points

Using the last of the algorithms, a favorable insertion points for transfer orbits satisfying the constraints, in terms of transfer time and ΔV_T can be found for any SPDRO. For a particular orbit, the position of an insertion point is defined as an angle that increases in the clockwise direction coinciding with retrograde motion, $\alpha_i = -\cos^{-1}\left(\hat{r}_{2DRO} \cdot \hat{i}\right)$. Restricting the transfer orbit to intersect the SPDRO tangentially results in larger transfer times and smaller ΔV_T values than those found by Demeyer [1] for F1 transfers to larger SPDROs. Using the described methods, β_f can easily be modified to find shorter transfer times at the cost of higher impulses; however, this tradeoff will not be explored.

In general, there exist two minimums, in terms of transfer time and ΔV_T, on either side of the Earth that are superior. Of these, one is slightly advantageous, positioned approximately 180 deg. from the other. Recalling that Hill's problem possesses symmetry about the origin, this characteristic results from a low mass ratio. Thus, ΔV_T and transfer time values for $\alpha_i \in \left[-90^\circ, 90^\circ\right]$ become identical to $\alpha_i \in \left[90^\circ, -90^\circ\right]$ as the mass ratio goes to zero.

Figure 4-19 shows the variation of ΔV and transfer time with α_i for an F1 transfer to a 30×10^6 km SPDRO. Notice the small segment conspicuously missing in the first plot. This corresponds to a region where the stepsize became prohibitively small. The spikes shown in Fig. 4-19b are not discontinuities, but places where the gradients are large. High gradients are most likely the result of crossing the manifolds of the Lyapunov orbits. A simple example of such a transition will be given below. If the stepsize and integration tolerances are set to sufficiently small values the algorithm will find all points on these curves. In many cases, this task is limited by the Runge-Kutta 7-8 integrator used in this study. Practically this is not necessary as values close to overall minimums can be identified inside regions with tractable tolerances and step sizes.

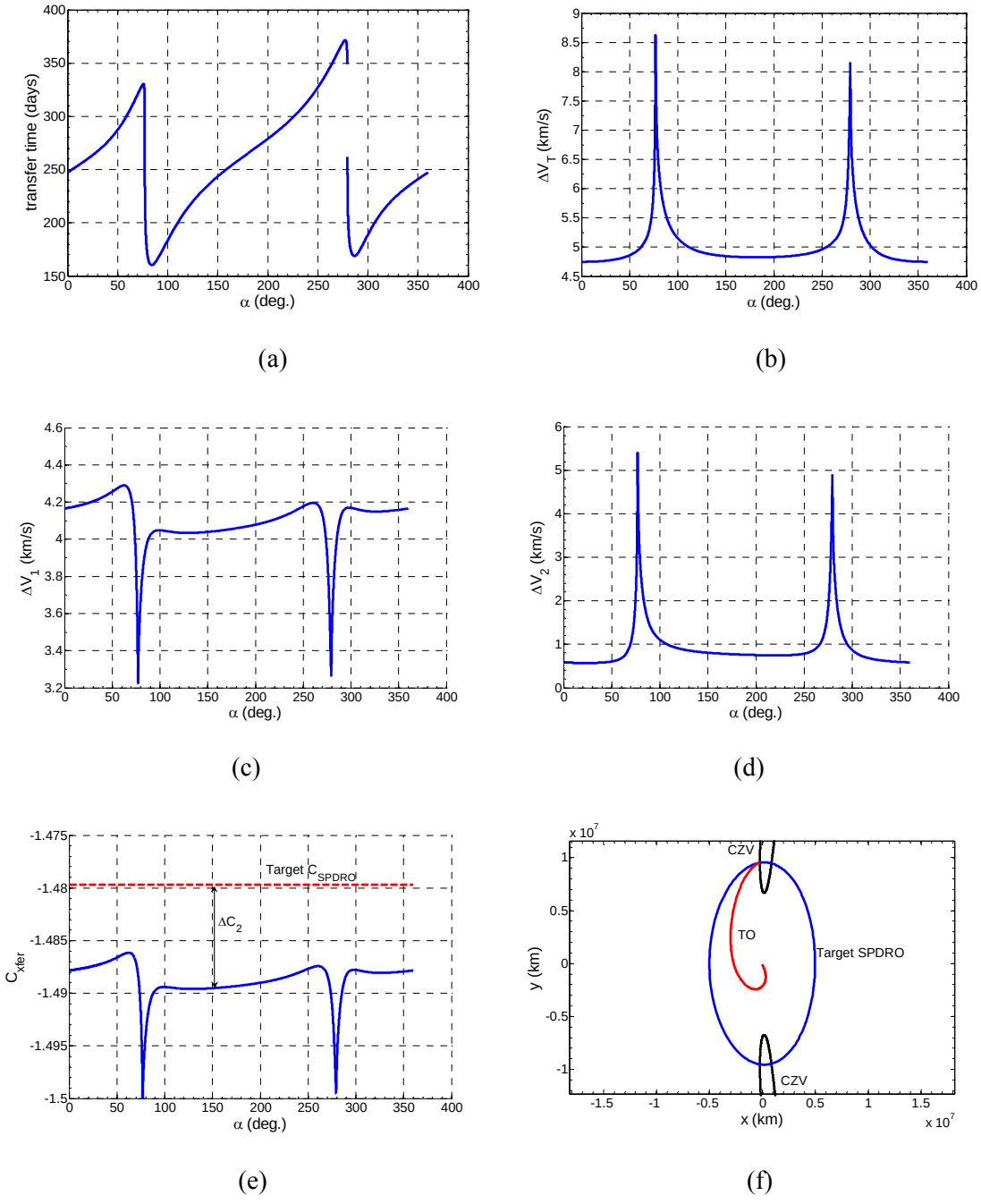

Fig. 4-19 Transfer characteristics versus insertion point. (a-d) Variation of transfer time and ΔV with insertion point for an F1 transfer to a 30×10^6 km SPDRO. (e) Transfer energy versus α with the target SPDRO energy represented by the dotted line. (f) A transition orbit terminatinsg near the CZV at the transfer energy.

Favorable insertion points are found where a proper balance among the maneuvers exists. The spikes in ΔV_T are caused by rapid increases in ΔV_2 exhibited by transition orbits, TOs, which bridge the gap among regions of motion. As before, the effect of the second maneuver can be visualized as a shift of the stable region by modification of energy. The change in energy required to shift the SPDRO at the transfer energy to the physical location of the terminal points of the transfer increases significantly at these spikes, ΔC_2 in Fig. 4-19e. This suggests, verified in Fig. 4-19f, that the transfer orbits approach the curves of zero velocity, labeled CZV, making convergence to a tangential intersection difficult. The slow approach to the CZV by the spacecraft imposes the highest transfer times. Similar trends exist for F2 and F5 transfers, yet the opposite circumstance is exhibited by F3 and F4 where high terminal velocities (high transfer energies) exist within regions of high gradients. The geometry of the stability region changes with both the insertion point and C_{xfer}. Therefore, the precise nature of these processes is difficult to visualize; however, rapid changes in the trajectory of transfer orbit provides insight.

These acute changes are essentially caused by crossing the distinct regimes of motion marked by the Lyapunov orbits and their intersecting manifolds. This phenomenon is simplest to visualize for the F1 transfers which, for certain SPDRO altitudes, closely shadow one of the Lyapunov orbits. Figure 4-20 displays two such orbits along with a TO following the manifolds of a smaller L_2 Lyapunov orbit (not shown), yet precariously positioned between two types of motion. The missing data in Fig. 4-20b shows where the stepsize became prohibitively small. These orbits mark the rapid changes in transfer time and ΔV with the insertion point. The other families are subject to exchanges among the manifold tubes of each Lyapunov orbit which become larger and more complex with increasing energy. As the insertion point is modified, each family of transfer orbits must, at some point, switch between distinct regimes of motion. For the families which exhibit particularly high transfer energies during transition this results in the discovery unique orbits whose paths deviate far distances from the target SPDRO. Presently,

such orbits are of only academic interest for spacecraft applications in the Earth/Moon-sun system, since the ΔV requirements are an order of magnitude larger than required at alternative insertion points.

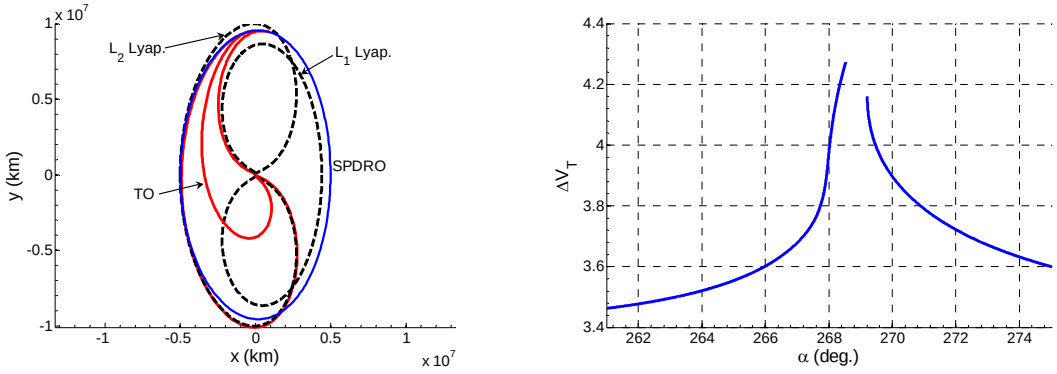

(a) (b)

Fig. 4-20 Evolution of transfer orbits at high gradients. (a) Two transfer trajectories shadowing the L_2 and L_1 Lyapunov orbits and a transition orbit, marked TO, with insertion points of α=262.4, 275.4, 267.8, respectively, to a 5×10^6 km SPDRO. (b) ΔV_T versus α for transfers to the same SPDRO.

Figure 4-21 shows the minimum values of ΔV_T and transfer times found using the described procedure. Although there are modest decreases in ΔV_T relative to transfers to the *x*-axis, changing the point of insertion can yield large reductions in transfer time confirmed by comparing Figs. 4-10 and 4-21. The same trends are exhibited in Fig. 4-21 as those exhibited by transfers terminating on the *x*-axis, indicating that the arguments involving the converging of phase space structures hold at arbitrary points of insertion.

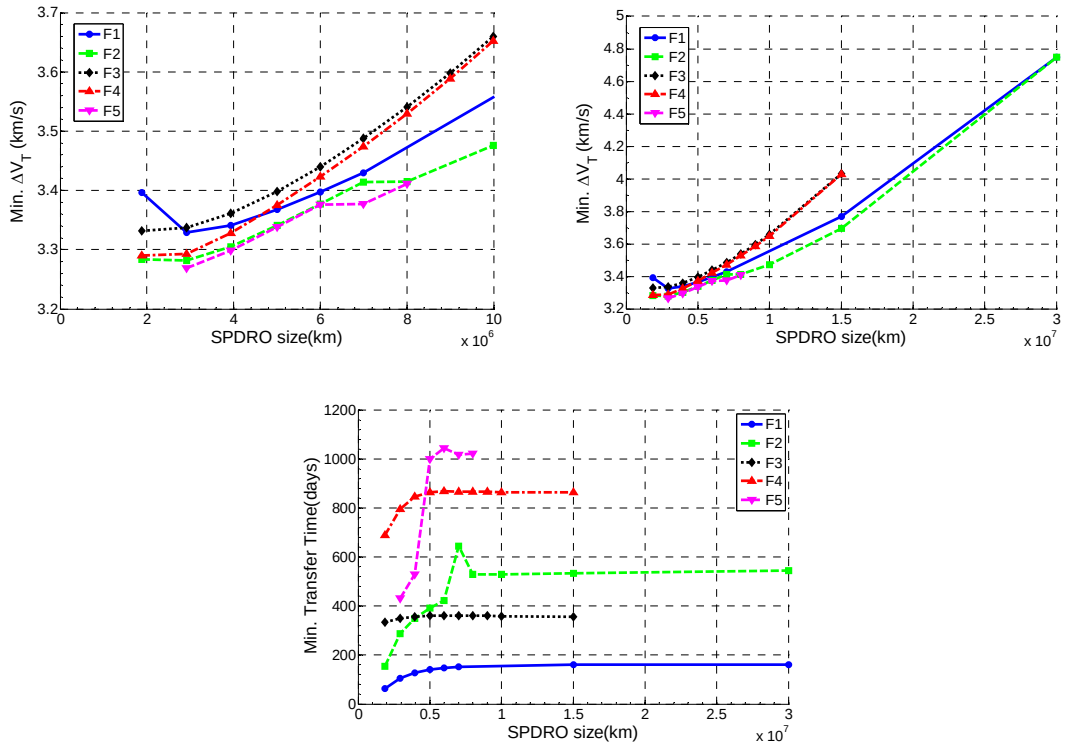

Fig. 4-21 Variation of transfer time and ΔV with insertion point for a 30×10^6 km SPDRO.

Figure 4-22 shows that an F1 transfer to a 3.93 M km SPDRO can achieve a minimum transfer time that is 39% less than equivalent transfer to the *x*-axis with a 6% increase in ΔV_T. This large reduction in travel time with modest increases in ΔV_T for F1 transfers was observed by Demeyer for nontangential intersections with the SPDRO [1]. Targeting alternate insertion points for F5 transfers can also lead to large decreases in transfer time especially at small SPDROs. Although the curves depend on the location of the peak transfer time, the cost of targeting the insertion point of minimum transfer time becomes quite high for F3 and F4 transfers. For instance, ΔV_T must be more than doubled to reach the minimum transfer time for transfers to a 15 M km SPDRO. A savings of no more than few percent in ΔV_T can be realized by changing the insertion point. In many cases this is accompanied by large increases in transfer time.

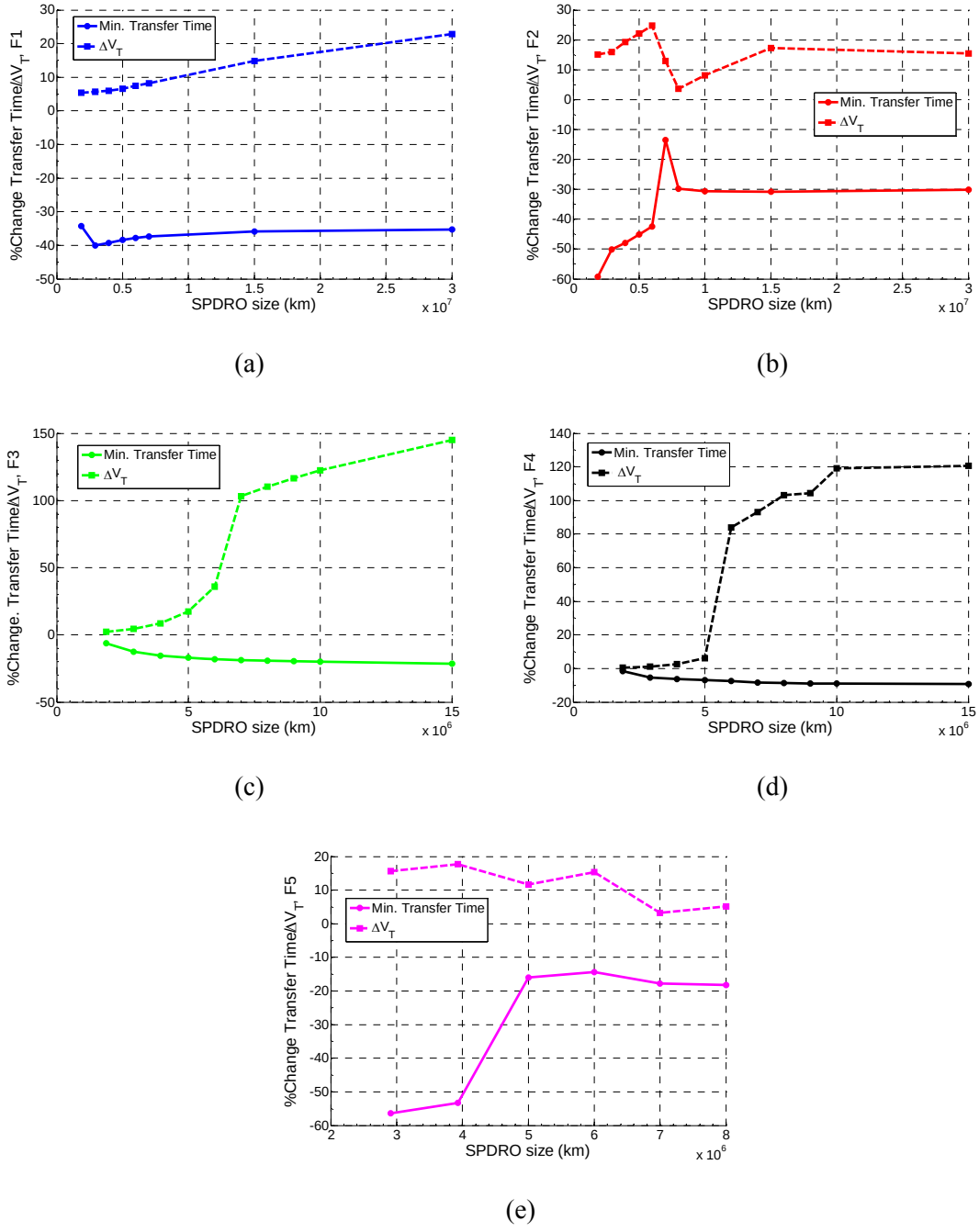

Fig. 4-22 Percent change in transfer time and ΔV_T at insertion points corresponding to the minimum transfer time relative to transfers terminating on the *x*-axis. Plots (a-e) correspond to F1-F5 transfers in that order.

For F1 transfers if the insertion point is modified in the positive direction from 0 to 180 deg., the data will connect continuously, at least within several significant digits, with data produced by modifying the insertion point from 180 to 0 deg. Inspection of Fig. 4-19a verifies this property. This characteristic, however, does not hold for all families at all SPDRO sizes and, in fact, may be the exception and not the rule. For example, Fig. 4-23a shows transfer time versus insertion point for a 15×10^6 km F2 transfer where the stating point, directions of continuation, and algorithm failure points are indicated. The solid and dotted lines indicate transfer orbits that have been modified from 0 and 180 deg., respectively. Those terminating at approximately α=80 deg., Fig. 4-23b and c, indicate distinct transfer orbit geometries. Each display the characteristics of the F2 transfer's single loop about Earth, although the second appears to be evolving into a different transfer type. Study of this process is difficult given numerical limitations, but it could be evolving into an F4 transfer.

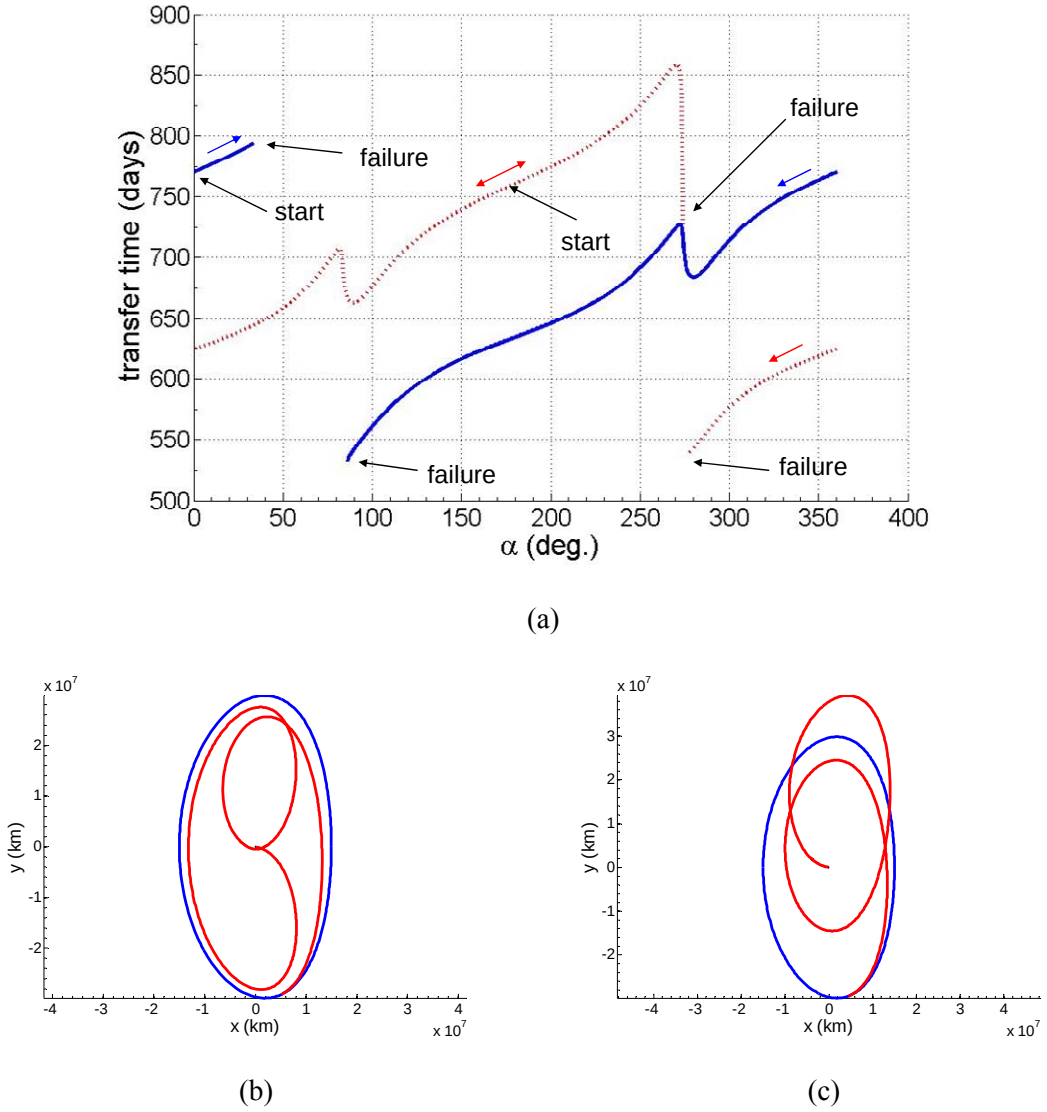

Fig. 4-23 Geometry and evolution of F2 transfers. (a) Variation of F2 transfer time with insertion point for a 15×10^6 km SPDRO starting from α=0 deg. (solid line) and α=180 deg.(dotted line). (b) and (c), transfer orbits continued from α=0 and 180 deg., respectively, terminating at approximately α=80 deg.

In this case, all insertion points must be accessed beginning at each of the two starting points to find the global minimums. Generally, the algorithms described in the previous sections will not access all insertion points given just one starting point, because of numerical limitations. The penalty for this shortcoming is not large, because of the small mass ratio. A transfer close to

one of the two superior minimums will generally be found with the knowledge that another can be located with a separation of approximately 180 deg. Figure 4-23 clearly demonstrates that the design space is multimodal. Methodologies involving local gradient searches will fail if the initial guess is close to a local minimum.

The minimum ΔV values found for the F1 transfers fall within 2% of optimal values calculated by Demeyer providing verification of the results. The analysis is performed without extensive random sampling or "blackbox" optimization codes. This provides a geometric description of the design space, ensuring that favorable insertion points are found for an arbitrary number of transfer types. With the availability of collision maps, a focused random sampling is needed solely for the initial guess to start the continuation algorithm for transfers terminating on the *x*-axis. As a result, the initial sampling is modest along a one-dimensional monotonic curve at a single Jacobi constant value. From here, the design space can be accessed for any transfer type due to the development of continuation algorithms. Since this procedure lends well to computer automation it may be useful for the planning of future space missions.

Summary and Extension

This work presented in this chapter resulted from an extension of the dynamical analysis presented in chapter 3. It represents an original study in the field of astrodynamics solving a number of complications prevalent in the literature. Essentially the problem of finding an initial guess has been automated for an arbitrary number of transfer families along a one-dimensional monotonic function. The continuation algorithms vastly expanded the design space available for analysis. The results reveal the intimate relationship among previously unexplained parameter trends and the evolution of phase space structure. These physical explanations will serve as the

foundation for transfers of greater complexity. In addition, this chapter constitutes the first major study on the evolution of transfer families with insertion point.

In particular, the existence of collision orbits in the vicinity of the distant retrograde region has been known for sometime and is often cited in works involving satellite capture. Indeed, processes such as the collisions of comets and asteroids with planets and the accretion of the outer planets are fundamentally similar to the cause of delivering a spacecraft to a SPDRO. A methodology that thoroughly and reliably explores the design space of two-impulse transfers to SPDROs. Core to this approach was a single guess for each transfer family followed by application of differential correction and continuation algorithms which plotted the terminal points of the transfer orbit along side of the major phase space structures.

A few geometric arguments hypothesized the existence of collision regions and accompanying transfer orbit between the Lyapunov orbits, their manifolds, and the stable region. This was verified by a focused sampling of candidate transfer orbits near the fringes of the collision region to arrive at an initial guess for the differential correction and continuation algorithms. The search involved following linear trends along a one-dimensional monotonic function. The subset of the results that was comparable to past studies using dissimilar methods agreed within a few percent. Aside from the initial guess, this study distinguished itself developing a procedure that could access a large range SPDRO sizes starting from any parking orbit altitude for all transfer types, with the capability of modifying the insertion point for an arbitrary number of transfer families.

The geometric approach illuminated the relationship between the transfer orbits and the morphology of phase space near the distant retrograde region. Specifically, the expansion of the stable region for low SPDRO sizes accounted for the divergence of the ΔV requirements. By examination of a set of hyperbolic points and the manifolds mapped on the SOS, it was shown that transfer families must exist within certain regions space which contract with increasing

energy. This contraction, primarily caused by the widening of the stable region, forces the terminal points of the transfer families closer together near the fringes of the stable region. This has an overall effect of decreasing the relative difference in ΔV_T among two sets of families. An Earth return periodic orbit resulted as a by-product of the procedure for each transfer type providing a reliable method for their calculation. Trajectories such as these could be applicable to science mission which require a number of close approaches to the second primary without a significant reduction in energy.

The ΔV requirements of the transfer orbits display a nearly linear variation with the range parking orbit altitudes. Additionally, the transfer time displays little change. These results simplify design trade-offs with parking orbit altitude. Choosing an insertion point off of the *x*-axis provided modest savings in ΔV_T, but is more useful to reduce the transfer time by a substantial amount. Modification of the insertion point yielded slow variations in the transfer orbit properties except for small ranges where acute changes take place. These occurrences are caused by the transfer orbits evolving across distinct regimes of motion marked by the Lyapunov orbits and their manifolds. Further research must be conducted in order to fully understand the evolution of transfer orbits with insertion point, such as F2 transfers, continued from starting points on either side of the Earth.

Experimentation with alternative integration routines may negate a few of the previously described limitations. By straightforward modifications of these algorithms, adjustments to the transfers can be investigated including lifting the constraint that the transfer trajectory intersects the SPDRO tangentially. Another extension is to investigate direct insertion into Lyapunov orbits with the use of retro-burns. Such transfers would need a relatively small ΔV_2 at both low and high energies due to the structure of phase space. The boundaries of the collision bands can be followed in the same manner as the transfer families. Thus, a future celestial mechanics

application may be to quantify the area of these bands in phase space in order to quantify collision probabilities.

It has been shown that most SPDROs are surrounded by a stable region of quasi-periodic orbits intermixed with bounded chaotic orbits. A spacecraft may substantially reduce ΔV_2 by inserting into QPDRO instead of a SPDRO. Additionally, if the spacecraft has no thrusting capabilities the manifolds of the BUPO can temporarily capture the spacecraft in the vicinity of the distant retrograde region. In this case the spacecraft becomes trapped in a sticky region of space where a particle exhibits a prolonged dynamical. The latter two topics are addressed in the next chapter.

References

[1] Demeyer, J. and Gurfil, Pini, "Transfer to Distant Retrograde Orbits Using Manifold Theory", *Journal of Guidance, Control, and Dynamics*, Vol. 30, No. 5, 2007, pp. 1261-1267.

[2] Ocampo, C., and Rosborough, G., "Transfer Trajectories for Distant Retrograde Orbiters of the Earth", *Advances in the Astronautical Sciences,* Vol. 82, No. 2 , pp. 1177–1200,199,.

[3] Lo, M., "Lissajous Trajectories for SIRTF", *Advances in Astronautical Sciences*, Vol. 76, No. 2, pp. 1229-1248, 1992.

[4] Ocampo, C., and Rosborough, G., "Multiple-Spacecraft Orbit Transfer Problem: The No-Booster Case," *Journal of Guidance, Control, and Dynamics*, Vol. 22, No. 5, pp. 650–657, 1999.

[5] Hénon, M., "Numerical Exploration of the Restricted Problem. VI. Hill's Case: Non-Periodic Orbits", *Astronomy and Astrophysics*, Vol. 9, 1970, pp. 24-36.

[6] Ocampo, C., "Trajectory Optimization for Distant Earth Satellites and Satellite Constellations," Ph.D. Thesis, Department of Aerospace Engineering Sciences, Univ. of Colorado, Boulder, CO, 1996.

[7] Szebehely, V., *Theory of Orbits: The Restricted Problem of Three Bodies*, Academic Press, New York, 1967.

[8] Alvarez, A. and Roig, F., "The role of the resonant "stickiness" in the dynamical evolution of Jupiter family comets", *Dynamics of Populations of Planetary Systems Proceedings IAU Colloquium*, No. 197, 2005.

[9] Brunini, A., "On the satellite capture problem. Capture and stability regions for planetary satellites", *Celestial Mechanics and Dynamical Astronomy*, Vol. 64, No. 1, 1996, pp. 79-92.

[10] Lam, T., "Exploration of distant retrograde orbits around Europa", *Advances in Astronautical Sciences*, Vol. 120, pp. 135-153, 2005.

[11] Scott, C. and Spencer, D., "Stability Mapping of Distant Retrograde Orbits and Transport in the Circular Restricted Three-Body Problem", *AIAA/AAS Astrodynamics Specialist Conference and Exhibit, August 18-21, 2008, Honolulu, HI*, AIAA 2008-6431.

Chapter 5

Transfers to Sticky Distant Retrograde Orbits

This chapter extends the material presented in both chapters 3 and 4. A single impulse transfer takes the spacecraft to the fringes of the stability region where it can reside for an extended period of time on a sticky orbit. Here the spacecraft can either follow an uncontrolled orbit, subject to the natural dynamics, or perform a stabilizing impulsive or low-thrust maneuver into a stable quasi-periodic orbit. These transfers have the benefit of delayed escape from the Earth region and fuel savings over comparable transfers to the central periodic orbit presented in the previous chapter. This chapter presents the first study to consider both sticky orbits and to develop a design procedure to access them. Therefore, all developments and results presented in this chapter are new to the field of astrodynamics.

Here, the use of sticky orbits near the distant retrograde region in the sun-Earth system is explored. These orbits are of value to spacecraft that have little or no propulsive means and must rely on the natural dynamics of the system. The previous chapter presented a novel methodology to find families of transfer trajectories to stable periodic distant retrograde orbits (SPDROs), see also Ref. 1. The method facilitated an accurate guess and automated exploration of the design space using predictor-corrector routines. The key observation, pertinent to this chapter, entailed the convergence of the transfer families to the edge of the stable region with energy. Also extended are the results of chapter 3 which divulged the dynamical mechanisms responsible for satellite capture in the sun-Jupiter system. This chapter takes a more detailed look at these mechanisms within the framework of a spacecraft transfer in the sun-Earth system.

In the field of solar system dynamics, sticky phenomenon has been a topic of research for sometime. The number of comets or asteroids surviving simulations, avoiding collision or

ejection from the solar system, has been found to be much larger than predicted by a diffusion or random walk approximation. Sticky regions of space have been identified that retain motion where a particle exhibits a dynamical lifetime longer than is predicted by the Lyapunov time [2]. In fact, a two-stage depletion rate has been observed for objects moving in the solar system. The first, consistent with a random walk approximation, involves an exponential depletion rate. After a certain time period, this approximation must be switched to a depletion rate dictated by a power law. The phenomenon has been attributed to resonant stickiness. Specifically, objects tend to reside for extended periods of time near the stable resonant islands on a Keplerian map for three-body systems throughout the solar system [3]. An equivalent phenomenon has been observed in accurate symplectic integrations of the solar system.

Stability maps reveal that a sizeable stable region encompasses the central SPDRO, classified as family *f* [4], at nearly all energies. As discussed in the previous two chapters the distant retrograde region consists of periodic, quasi-periodic, and bounded chaotic orbits. The frontier of the stable region is marked by a homoclinic tangle of the manifolds exuded by an unstable periodic orbit. Chapter 3 discussed in some detail the role of the BUPOs in capture phenomena. The BUPO at the fringe of the stable distant retrograde region was classified as family g3 by Hénon [4]. It was shown that the stable and unstable manifolds form loops, known as lobes, which dictate direct transport into and out of the sticky regions contiguous to the stable regions. The reader is also directed to Ref. 5.

A numerical experiment similar to the Monte Carlo simulations of chapter 3 is performed along with a linear analysis near the hyperbolic points. It is found that even in the case of high stability indices, a continuous cycling of the spacecraft through the lobe dynamics acts to amplify the period of capture. In addition, this chapter extends the basic analysis of chapter 3 by exploring the evolution of the homoclinic tangle with energy. The overall effect on capture probability, capture time, and collision probability is examined.

Just as there are orderly bands of collision orbits across energy surfaces for orbits that pierce the sun-Earth line perpendicularly [1], there exist analogous structures at a set energy with no other constraints on the orbits. In particular, bands of collision orbits are bound by iterates of the stable or unstable manifolds depending on the direction of time. A differential-correction routine is developed that modifies the terminal radial velocity on an energy surface, in the absence of a final maneuver, for transfers terminating at the sun-Earth line following these bands. This allows the transfer families to be mapped on a surface of section (SOS) revealing their relationship to the structure of phase space in the distant retrograde region. These geometric relationships facilitate near-term predictions of the fate of the transfer families in terms of collision, escape, or capture.

For spacecraft applications the length of time a spacecraft will reside in a certain region on human timescales is of interest. In particular, this chapter focuses on orbits which exhibit a prolonged lifetime near the stable distant retrograde region in the sun-Earth system. Instead of macroscopic measures, such as the depletion rate of objects randomly scattered throughout the system, continuous one-dimension curves of orbits are isolated, as they appear on maps, corresponding to end conditions of the transfer families discussed in the last chapter with modified radial velocities. These maps reveal that the families traverse lobes formed by the BUPO. With this information, a subset of orbits, accessible by a direct transfer from low-Earth orbit, are isolated which exhibit an extended capture time near the distant retrograde region.

Developments in this chapter facilitate the preliminary design of three new transfers. The first utilizes a single maneuver throughout the entire transfer to depart from low-Earth orbit. The spacecraft then coasts into the fringes of the stable distant retrograde region followed by an extended capture period. The transfer inserts the satellite directly into the lobes formed by the manifolds of the BUPO otherwise known as a sticky orbit. Stable regions are inaccessible without a change in energy; therefore, the spacecraft cannot be permanently captured without a

second maneuver. Essentially the same dynamical phenomenon thought to be responsible for the slow rate of decay of populations of Jupiter-family comets and asteroids is exploited. In chapter 3 it was shown that capture within the lobes are responsible for the capture of planetary satellites on retrograde orbits. Such natural trajectories can be used by a spacecraft that has little or no propulsive means, such as the one proposed in the Regatta-Astro program of the former Soviet Union [6].

The second transfer involves two impulsive maneuvers. The first is an impulsive maneuver from low Earth orbit to an orbit of extended capture at the fringes of the distant retrograde region. After a coasting phase, a small impulsive stabilizing maneuver is then performed to insert the spacecraft into a stable quasi-periodic distant retrograde orbit (QPDRO). If this type of orbit is desirable, the transfer can result in significant fuel savings compared to direct insertion into the SPDRO. The third involves a simple low-thrust control method analogous to nebular drag to stabilize the spacecraft after the initial transfer. This type of maneuver could be used for both fuel savings and if unmodeled forces render station keeping necessary. Additionally, the initiation of spiral-in and spiral-out transfers is investigated from the sticky orbits.

Differential Correction

A differential correction routine similar, to the first introduced in the last chapter, is developed. Consider a transfer orbit, $\mathbf{X}(\mathbf{X}_o,t)$, from time $t=0$ to its terminal state at $t=T$, where $\mathbf{X}_o=\mathbf{X}(\mathbf{X}_o,0)=\begin{bmatrix} x_o & y_o & \dot{x}_o & \dot{y}_o \end{bmatrix}^T$ and $\mathbf{X}_1=\mathbf{X}(\mathbf{X}_o,T)=\begin{bmatrix} x_1 & y_1 & \dot{x}_1 & \dot{y}_1 \end{bmatrix}^T$. Expanding to first order about $(\mathbf{X}_o,T)$,

$$\delta \mathbf{X}_1 = \Phi(T)\delta \mathbf{X}_o + \frac{\partial \mathbf{X}_1}{\partial t}\delta T \tag{5.1}$$

where $\Phi(T) = \partial \mathbf{X}_1 / \partial \mathbf{X}_o$ is the 4×4 state transition matrix. Equation (5.1) provides the variation of the final state as a function of small changes in the initial conditions and transfer time.

Here, transfers which terminate on the *x*-axis at a set radial velocity, $\dot{x}_{1set}$ and energy are sought. For a large range of energies a solution at $\dot{x}_{1set} = 0$ is provided for each transfer family using the algorithms developed in the previous chapter. This solution is used as starting point to continue transfer trajectories into those that do not intersect the *x*-axis perpendicularly. A differential correction routine can be established where $\delta \dot{x}_1 = -(\dot{x}_{1set} - \dot{x}_1)$ at each iteration. The solutions are found consecutively starting at $\dot{x}_{1set} = 0$.

Expanding Eq. (5.1) and choosing the third element,

$$\delta \dot{x}_1 = \Phi_{31}\delta x_o + \Phi_{32}\delta y_o + \Phi_{33}\delta \dot{x}_o + \Phi_{34}\delta \dot{y}_o + \ddot{x}_1 \delta T \tag{5.2}$$

furnishes one equation and five unknowns. Four constraints are required in order to develop a differential correction routine. The first is provided by numerically forcing y_1 to zero, thus $\delta y_1 = 0$. Constraining the transfer to an energy surface gives the second, while the remaining two are established by constraining the transfer orbit to depart tangentially from a circular parking orbit of constant radius. Combining all of the constraints yields a predictor-corrector routine specified by the following equations,

$$
\begin{aligned}
\delta y_o &= -\frac{-\left(\dot{x}_{1set} - \dot{x}_1\right) + V_1 D_2 + V_3}{V_1 D_1 + V_2} \\
\delta x_o &= D_1 \delta y_o + D_2 \\
\delta \dot{x}_o &= C_1^* \delta x_o + C_2^* \delta y_o + C_3^* \\
\delta \dot{y}_o &= R_1 \delta x_o + R_2 \delta y_o + R_3 \delta \dot{x}_o + R_4
\end{aligned}
\tag{5.3}
$$

with all remaining variables defined in the Appendix. The algorithm will typically converge within a few iterations given a suitable guess. Figure 5-1 displays multiple F1 and F2 transfers terminating on the *x*-axis at *C*=-1.499 constructed using the described algorithm.

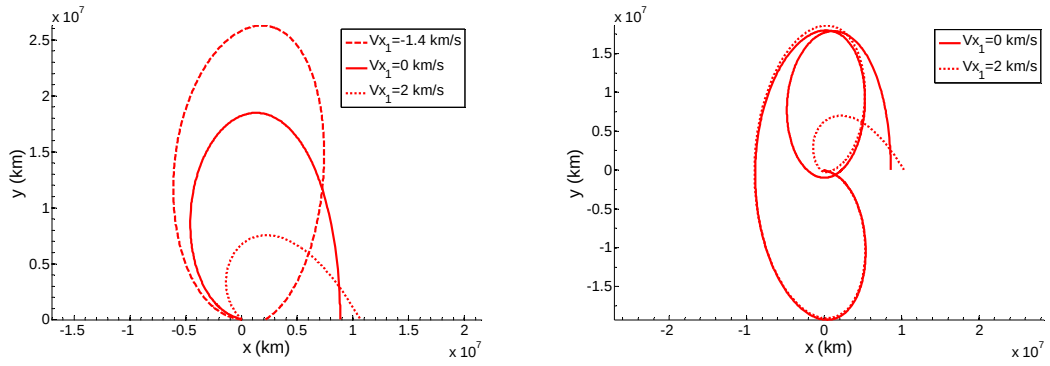

(a) (b)

Fig. 5-1 (a) and (b), F1 and F2 transfers terminating on the *x*-axis at the indicated terminal velocities, *C*=-1.499.

Phase Space Structure

The augmented 'Earth plus Moon' model used in the last chapter is adopted. The masses of the Earth and Moon are combined into the second primary. Additionally, the radius of the parking orbit is increased, so that the circular orbit velocity is that of parking orbit of a specific altitude about Earth. The accuracy of this approximation has been confirmed in Ref 2. Plots in

this chapter have their origins shifted to the location of the Earth with the positive *x*-axis pointing towards the sun.

Figure 5-2a shows a SPDRO and a Lyapunov orbit about L_1 at the same energy, *C*=-1.5001. A mean FLI stability map [5] at an SOS of $y = 0$ and $\dot{y} < 0$, Fig. 5-2b, reveals a mixed phase space composed of both chaotic and stable orbits. Since the SPDRO returns to its original position on the map after one iteration, it classified as a period-1 periodic orbit. The BUPO returns to its original position after three iterations, a period-3 periodic orbit, and lies at the fringes of the stability region indicated by the three black dots at the corners of triangular region.

There are an infinite number of homoclinic points formed by the intersections of the manifolds of the BUPO. The resulting homoclinic tangle is of particular importance to the satellite capture problem and the spacecraft transfers discussed in this chapter. Heteroclinic connections, marked H_eP indicate complex and chaotic dynamics, yet build dynamical chains making it possible for a spacecraft to travel among distinct regions of space on a particular energy surface. Using the continuation algorithms the relationship between the transfer families and segments of the dynamical chain are uncovered.

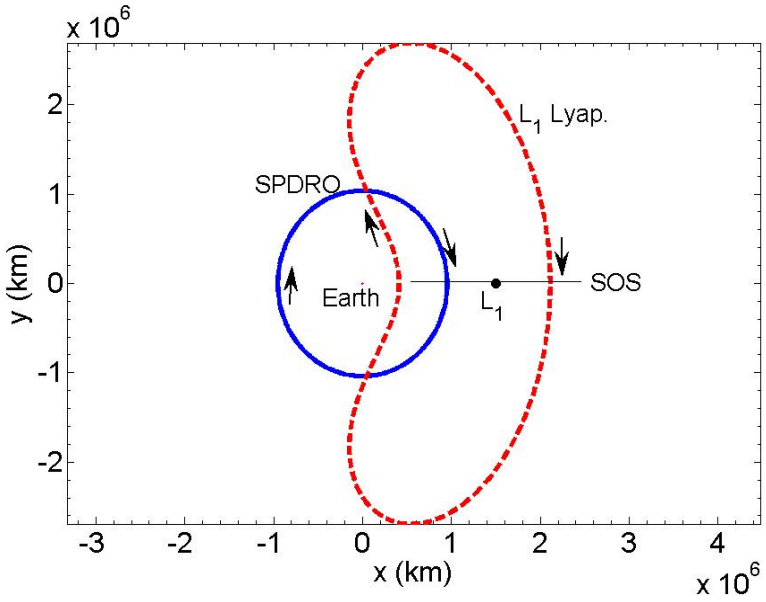

(a)

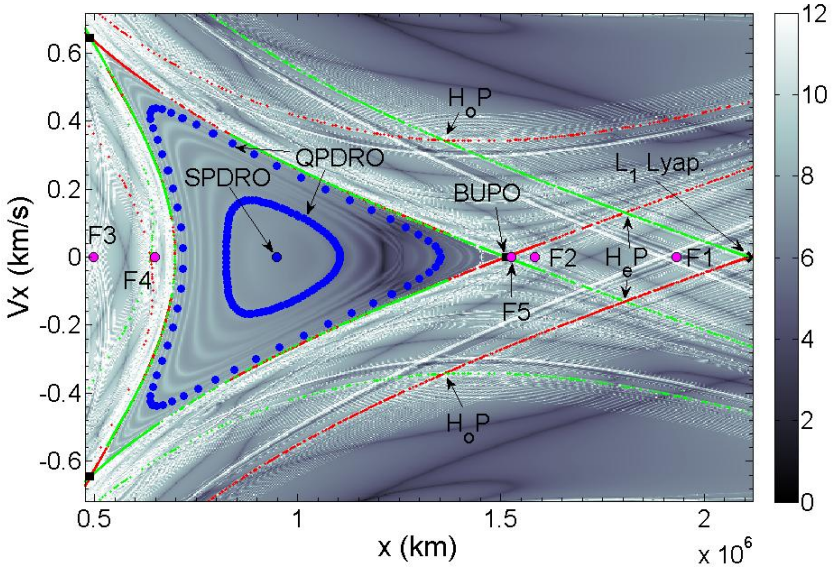

(b)

Fig. 5-2: Orbits, FLI map, and phase space structure near the distant retrograde region. (a) SPDRO and Lyapunov orbit about L_1. (b) Mean FLI stability map at the indicated SOS. The stable distant retrograde region composed of QPDROs is indicated by the dark triangular region, with the SPDRO lying at the center. Stable and unstable manifolds of the BUPO and Lyapunov orbit are shown in green and red, respectively. The termination points of the F1-5 transfers piercing the *x*-axis perpendicularly are shown at this energy level, C= -1.5001.

After a number of physical arguments, the last chapter exploited the orderly arrangement of collision orbits on the hyperplane $Vx = 0$ to arrive at starting guesses for all transfers terminating perpendicularly to the *x*-axis, marked F1-5 on Fig. 5-2b. The collision map, collisions shown in white, along with the continuations of F1-5 transfers through energy is displayed in Fig. 5-3a. These transfers closely follow major bands of collision orbits near the distant retrograde region. A transfer family can be found for each band of collision orbits, which increase in number with the simulation time. Thus, there exist an arbitrary number of transfer families.

F1, F2, and F5 transfers terminating perpendicularly to the *x*-axis are bound between the stable region and the mapping of the L_1 Lyapunov orbit. As energy is increased the distance between the expanding stable region and the Lyapunov orbit diminishes decreasing the relative separation of the terminal points of the transfers. Thus, the transfers converge to the border of the stability region as demonstrated in the last chapter. Similarly, F3 and F4 are bound between the unstable manifold tube (see Ref. 7) of the L_2 Lyapunov orbit and the border of the stable region. As discussed in the previous chapter, the net effect is similar to the prior case involving the convergence of the transfer to the boundary of the stable region.

The arrangement of collision bands on the hyperplane indicates that analogous regions exist for arbitrary values of *Vx*. Figure 5-3b verifies this assumption on a backwards collision map of the distant retrograde region at *C*=-1.5001 along with the unstable manifolds of the BUPO and the L_1 Lyapunov orbit.

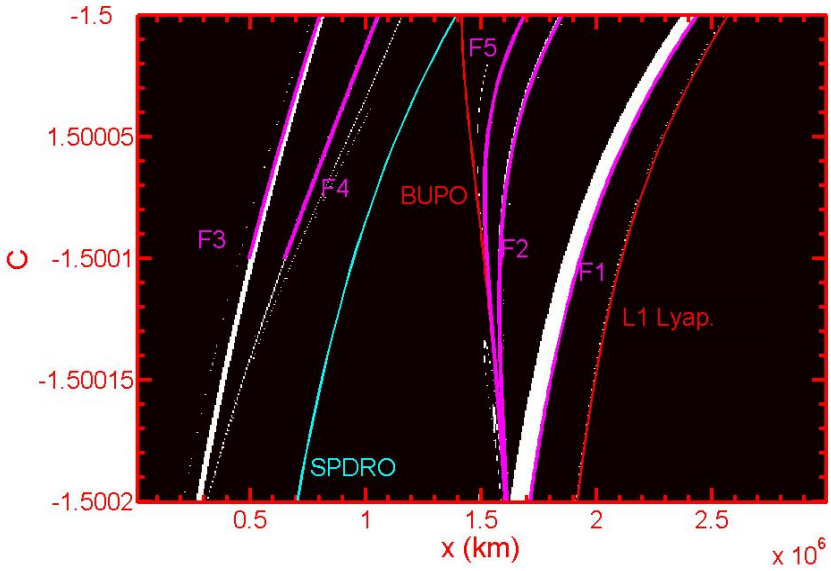

(a)

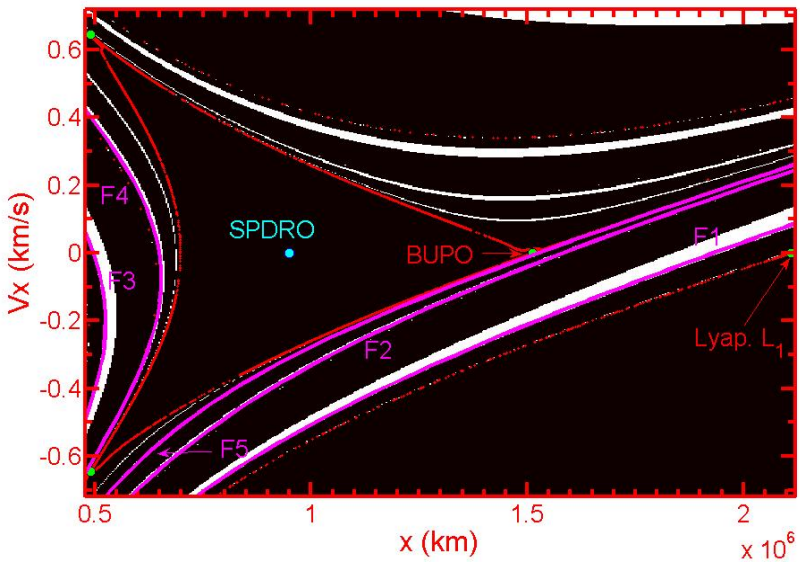

(b)

Fig. 5-3 Backward collision maps over a period of two years. (a) Continuations through Jacobi constant of termination points of F1-5 transfers, SPDRO, BUPO, and L_1 Lyapunov orbit are labeled. (b) The termination points of the F1-5 transfer families with variable *Vx* are shown at *C*= -1.5001.

Unstable manifolds separate diverging regions of motion for backward propagations [5]. Notice that the map of the unstable manifolds of the L_1 Lyapunov orbit and BUPO bound the numerous bands of collision orbits. Using the differential correction scheme outlined in the last section, *Vx* can be adjusted for all transfer families. These families, following the regions of collision orbits, are also confined by the images of the unstable manifolds. F1-5 follow collision orbits that cross $Vx = 0$, yet there are a number of regions that do not cross this hyperplane suggesting the existence of additional transfer families.

The bands are essentially a mapping of the volume of initial conditions starting on the Earth's surface to a SOS on the *x*-axis with $\dot{y} < 0$. This, of course, excludes the set of all collision orbits striking the *x*-axis with $\dot{y} > 0$. By Liouville's theorem the total volume of these initial conditions are preserved. As these orbits are propagated forward in time the detection of orderly bands in this and other regions of space becomes more difficult as they are subjected to chaotic mixing. This suggests that as the simulation time is increased the new bands of collisions will become thinner as the aggregate volume of orbits originating at the Earth's surface stretches with time. In fact, the thickness of collision bands, corresponding to a particular transfer, scales inversely with the transfer time. Using the methodologies of the previous chapter it is possible to follow the boundaries of the major bands in the same manner that transfer families are continued through energy and *Vx*.

As stated, future collisions can be inferred from backwards simulations by noting that a collision on a backwards map at (*x*,*Vx*) implies a collision at (*x*,-*Vx*) on a forward map. This property indicates that iterates of the stable manifolds will separate and bound the collision regions on forward maps. In the absence of a second burn, the near-term fate of each transfer trajectory can be predicted by motion in the neighborhood of the unstable periodic orbits, the geometry of the stable and unstable manifolds, and by the structure of the collision orbits on forward map. Figure 5-4a reveals the complicated structure of phase space showing multiple

crossings of each transfer family with collision regions at C= -1.4999. A transfer to one of the bands implies an imminent collision in the absence of a second maneuver.

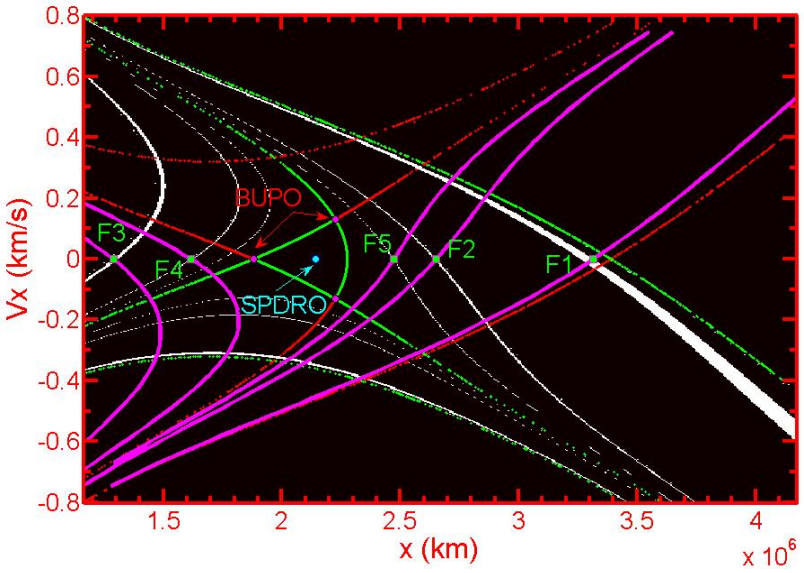

(a)

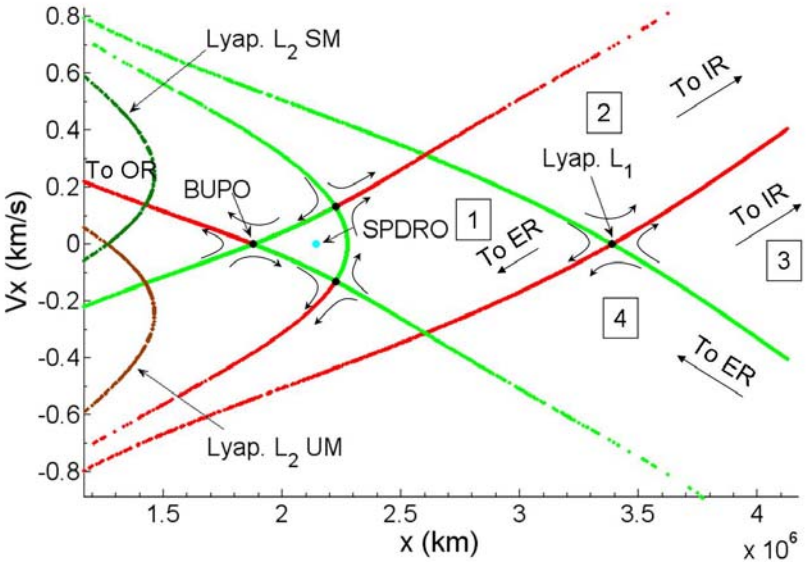

(b)

Fig. 5-4 *C*= -1.4999, Phase space structure and transfer families. (a) Forward collision map over a period of two years including the manifolds of the BUPO and L_1 Lyapunov orbit and continuations of the F1-5 transfers through *Vx* with no second burn. (b) Map of the manifolds of the L_1 and L_2 Lyapunov orbits and BUPO. The stable and unstable manifolds of the L_1 Lyapunov orbit and BUPO are shown in green and red on both maps. Boundaries of the stable and unstable manifold tubes of the L_2 Lyapunov orbit appear on the left side of the plot.

Figure 5-4b shows the manifolds of the Lyapunov orbits separate orbits en route to distinct regions of motion, viz., the interior, Earth, and outer regions, denoted by IR, ER, and OR, respectively. The interior and outer regions contain sun-centered orbits interior and exterior to the orbit of the Earth. The manifolds of the L_1 Lyapunov orbit divide the phase space into four quadrants, labeled on through four, with the local directions of motion indicated by the arrows. See also the nine classes of motion discussed in chapter 2. Notice that all transfers lie in either the first or second quadrant. The first quadrant contains the distant retrograde region, while only the first and fourth contain collision orbits over a two year period. In the first, an orbit will pass through the Earth region at least once before escaping to the OR, colliding with Earth, or evolving to either quadrant 1 or 2. The stable distant retrograde region constitutes the set of orbits that are transported back to quadrant 1 indefinitely. Depending on the position on the map, transfers to the second quadrant may circumnavigate the Earth before departing to the IR. These orbits, however, pose no near-term risk of collision. A segment of the first iterate of the stable manifold tube of the L_2 Lyapunov orbit is marked by the indicated loop on the left side of the plot. All orbits inside of this loop escape immediately to the outer region. Continuations of F3 and F4 pass through this region.

The Role of the BUPO and its Manifolds

Monte Carlo Simulations

Chapter 3 provided clear evidence that the regions of longest capture about the second primary in the CR3BP exist within the nebulous boundary of the stable distant retrograde region. Two types of temporary capture are distinguished. The first are extended capture orbits evolving

within the lobes of the stable manifold. These orbits are characterized by modest to drastic increases capture times compared to nearby orbits. The second are capture orbits outside of the lobes. These orbits have a fleeting presence near the distant retrograde region excluding those that lie close to the stable manifold at a low stability index.

The fringe of the distant retrograde region is characterized by the homoclinic tangle of the BUPO with motion governed by lobe dynamics. The lobes are the small regions of phase space enclosed by segments of the stable and unstable manifolds, see lobe "L" in Fig. 5-7a, see chapter 3 and Refs. 8 and 9 for more details on lobe dynamics. Chapter 3 showed that capture time within the lobes themselves can vary drastically as demonstrated on a mean FLI map, see Fig. 3-15 and the corresponding text.

To demonstrate that the lobes are the primary mechanism for extended capture and to rule out any unconsidered factors, a simple numerical experiment can be performed similar to the Monte Carlo simulation of chapter 3. Here, the simulations at variable energies seek the relationships between lobe geometry, energy, and probability of capture of collision.

At a given energy, orbits are propagated from initial conditions uniformly sampled on a circle in physical space whose radius is some multiple of the radius of the Hill sphere. To avoid contamination of the results, care is taken to ensure that this circle does not intersect the stable region. Under such a circumstance some surviving particles would not be of a capture origin since they would have been initialized within the stable region. In the following cases, a multiplicative factor of one is used. The simulation continues until the particle collides with the planet, escapes from the planetary region, or survives after some maximum time. For those that survive, the avenues of capture, escape, and regions of extended capture are revealed by recording the first and last intersections of the surviving orbits with the surface of section. In dynamical astronomy, a similar procedure has been used to attain capture statistics, in terms of orbital element distributions, of captured objects and collision probabilities for particles

bombarding the Hill sphere [10-12]. This dissertation is the first to utilize the approach to reveal the dynamical mechanisms responsible for prolonged capture.

The first intersections of orbits surviving a simulation of ten years lie inside or near lobes of the stable manifold, shown in Fig. 5-5. The squares, marking the last intersection before reaching the maximum simulation time are trapped very near or within the homoclinic tangle or departing along the unstable manifold. The number of surviving particles outside of the lobes goes to zero as simulation time is increased. This results from initial conditions of maximum capture lying within the lobes, as will be demonstrated later. Notice that there are many more surviving particles at C=-1.499 near the distant retrograde region, because the relatively large width of the lobes intersecting the Hill sphere. In both cases, all surviving members reside on retrograde orbits at the final intersection.

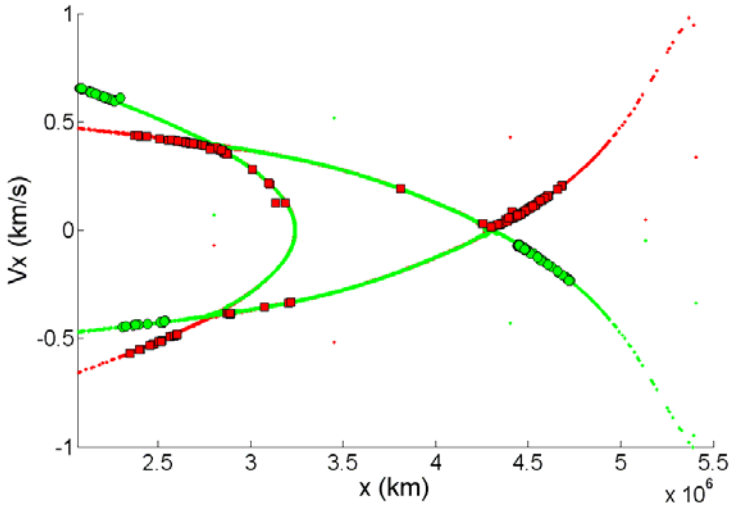

(a)

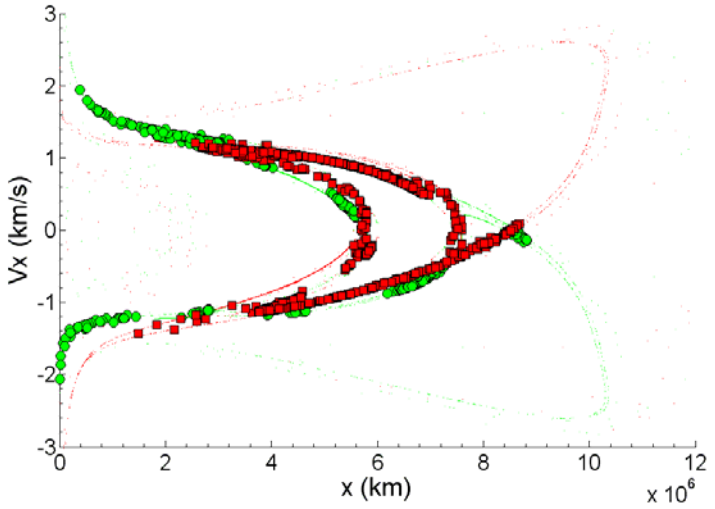

(b)

Fig. 5-5 First and last intersections, shown as circles and squares, of surviving members of 5×10^5 particles over 10 year simulations. Initial conditions are uniformly sampled on a circle with a radius matching the Hill sphere. Stable and unstable manifolds of the BUPO are shown in green and red, respectively. (a) C= -1.4997, The simulation terminates upon collision or escape beyond a distance of 20 times the radius of the Hill sphere. There are 183 survivors, 8,524 collisions, and 491,293 escapes. (b) C= -1.499, Simulation terminates after collision or until particle reaches 30 times the radius of the Hill Sphere. There are 939 survivors, 5,508 collisions, and 493,553 escapes.

The results show that only orbits which become trapped within or very near to the lobes survive for a simulation longer than ten years. Specifically, initial conditions within them will be cycled through the local, lobe dynamics, before departing within those stretching along the unstable manifold. Delaying divergence from the region, this process facilitates an extended capture period. In other words, the manifolds of the BUPO essentially act as gate keepers to the fringes of the stable distant retrograde region, the location of extended capture. It will be shown in later sections that the continuations of the transfer families through *Vx* which intersect the lobes of the stable manifold reveal orbits of extended capture which cycle through the homoclinic tangle of the BUPO.

Stability Index

A local analysis yields information pertaining to the rate of convergence or divergence from the BUPO appearing as a hyperbolic point on the SOS. For orbits passing near the BUPO lying outside of lobes or departing along the unstable manifold, an estimate of the rate of divergence from the distant retrograde region can be obtained. Since the CR3BP is a conservative system, two eigenvalues of the monodromy matrix are one while the remaining two come in a reciprocal pair. For two degrees-of-freedom, a single stability index is used,

$$k = \lambda + \frac{1}{\lambda} \tag{5.4}$$

where λ is one of the reciprocal pair with $\lambda \in \Re$, $\lambda > 1$, although either of the pair will give the same value. The orbit is considered linearly stable if $|k| \leq 2$. The stability index is closely related to a map representing the linearized dynamics near a hyperbolic point. Translating the origin of the coordinate system to the hyperbolic point, linearizing the equations of motion, and performing

a linear change of coordinates with the eigenvectors enables a map to be constructed for objects near a hyperbolic point,

$$\begin{bmatrix} x_{n+1} \\ y_{n+1} \end{bmatrix} = \begin{bmatrix} \lambda & 0 \\ 0 & \frac{1}{\lambda} \end{bmatrix} \begin{bmatrix} x_n \\ y_n \end{bmatrix} \tag{5.5}$$

Changes in the *x* and *y* coordinates correspond to movement in the direction of the unstable and stable manifolds, respectively. Neglecting other factors, the greater the stability index the faster a particle will diverge from the BUPO and the distant retrograde region. Figure 5-6 shows the evolution of the stability index as a function of Jacobi constant for the BUPO near the distant retrograde region,

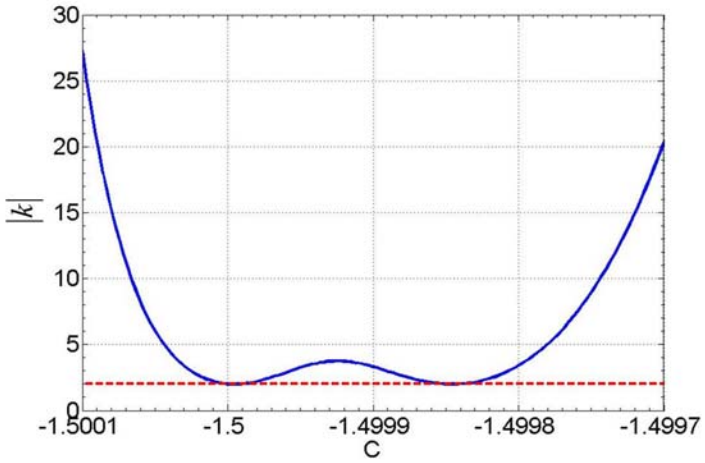

Fig. 5-6 Stability index versus Jacobi constant for the BUPO. The dotted line marks, $|k| = 2$, the stability threshold.

The stability index continues to increase for *C*<-1.5001 and *C*>-1.4997. The two points where $|k| = 2$ correspond to instances where the BUPO and SPDRO cross marking the disappearance of the stability region. This phenomenon, known as the "squeeze effect", is

generic for area preserving maps meeting a certain criteria [13]. It occurs when the rotation number near a fixed point approaches 1/3. The points of marginal stability mark a coalescing of the hyperbolic points into a single point and the existence of a monkey saddle those energies.

Equation (5.5) indicates that objects evolving in regions of small index values will exhibit slow divergence from the hyperbolic point. This suggests that for small ranges of energy, orbits outside of the lobes may also exhibit lengthy capture times. In fact, close inspection of Fig. 5-5 reveals that most of the points surviving the simulation at C=-1.4997 lie just outside of the lobes. This is due to a small stability index and a low probability of a randomly generated initial condition lying inside of the lobes due to their small size. In contrast, nearly all of the surviving particles at C=-1.499 lie inside of the lobes due to a high stability index and a high probability of generating such an initial condition.

Although orbits of maximum capture time lie inside of the lobes, the existence of a small stability index may be sufficient to achieve transfers requiring temporary capture. These ranges correspond to a small subset of energies where targeting the lobes is difficult. It will be demonstrated that at C= -1.4999 none of the transfers pass through lobes of appreciable size. At greater energies the stability index becomes two or three orders of magnitude larger. In these cases, the lobe dynamics necessarily recycle the object back to the vicinity of hyperbolic points to achieve a lengthy capture.

Single Impulse Transfers

A class of transfers utilizing single impulsive maneuver tangential to a circular parking orbit with an uncorrected altitude of 200 km is demonstrated. In the last chapter it was established that ΔV varies linearly while transfer time remains approximately constant for parking orbit altitudes from 200 to 2000 km. Therefore, a constant uncorrected parking orbit altitude of

200 km is used for all transfer orbits in this chapter. The goal is to find a transfer to the fringes of the distant retrograde region which maximizes the period of temporary capture before collision or escape to the OR or IR. Here, capture time lasts from when the transfer terminates on the *x*-axis until the spacecraft collides with Earth or evolves into a sun-centered orbit. As in the previous section the simulation terminates for the latter case when the radius of the spacecraft's orbit with respect to the Earth passes a certain threshold. This threshold is a multiple of the radius of Earth's Hill sphere with a multiplicative factor that increases with energy.

Transfer Characteristics

Figures 5-7a and b show lobes stretching along the stable manifold emanating from the first intersection of the BUPO at *C*=-1.5001 and -1.4997. As the lobes of the stable manifold approach the BUPO they intersect the unstable manifold an infinite number of times forming an infinite number of lobes. This essential creates a thin region along the stable manifold characterized by a high capture periods. The spike in capture time at approximately 1.519 M km in Fig. 5-10a is a manifestation of this effect. Notice that the lobes of the stable manifold are all contained on one side of the stable manifold emanating from the first crossing of the BUPO, the lone dot indicated in Fig. 5-7a and b. In fact, orbits on the upper side of the stable manifold will approach then turn directly away from the distant retrograde region characteristic of quadrant 3 as seen in Fig. 5-4b. Thus, at all energies the stable manifold emanating from the first crossing of the BUPO acts as a separatrix between two regions with one containing all orbits of extended capture.

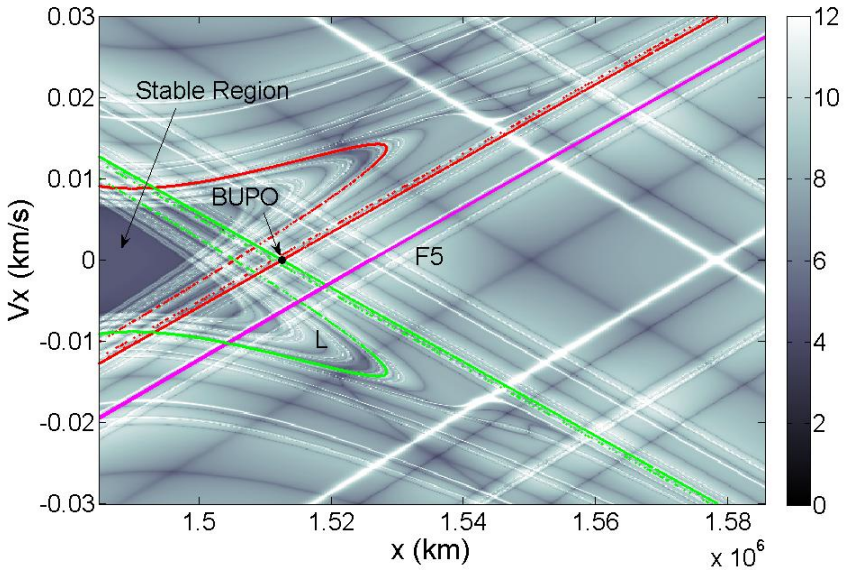
Stable Region
BUPO
F5
L
Vx (km/s)
x (km)
x 10^6
0.03
0.02
0.01
0
-0.01
-0.02
-0.03
1.5
1.52
1.54
1.56
1.58
12
10
8
6
4
2
0

(a)

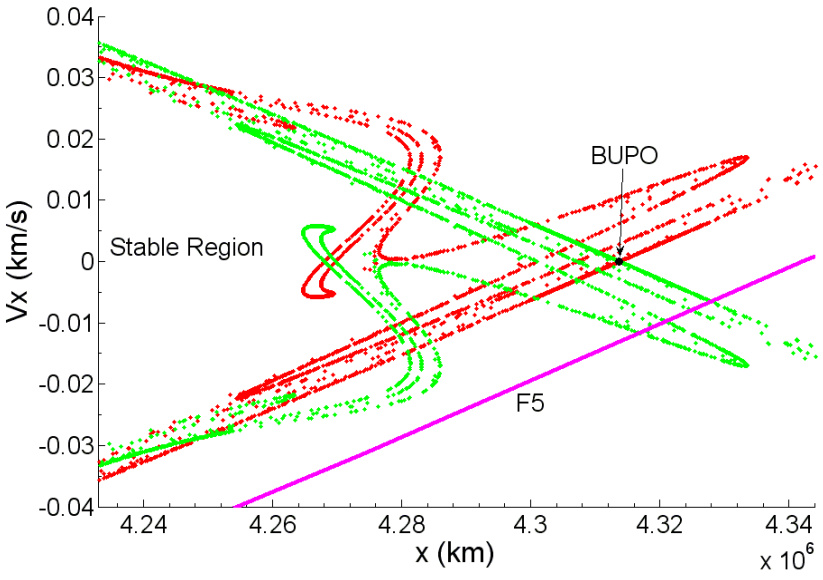
BUPO
Stable Region
F5
Vx (km/s)
x (km)
x 10^6
0.04
0.03
0.02
0.01
0
-0.01
-0.02
-0.03
-0.04
4.24
4.26
4.28
4.3
4.32
4.34

(b)

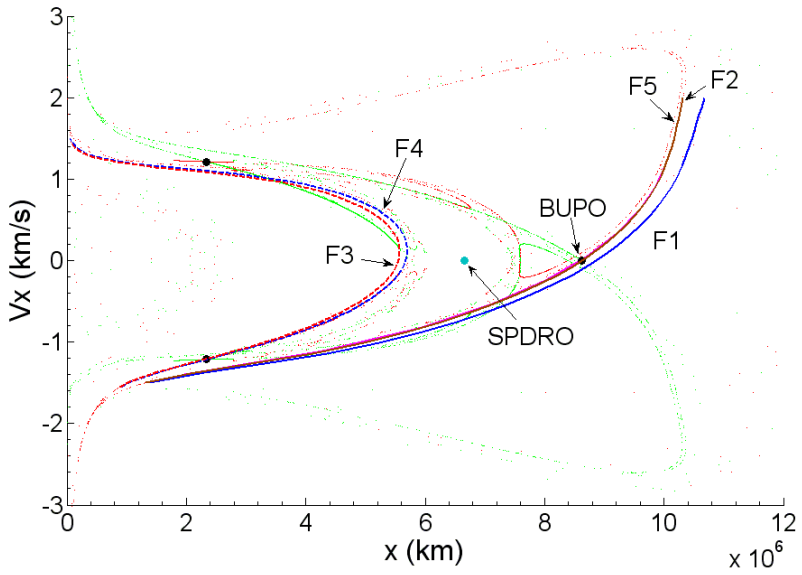

(c)

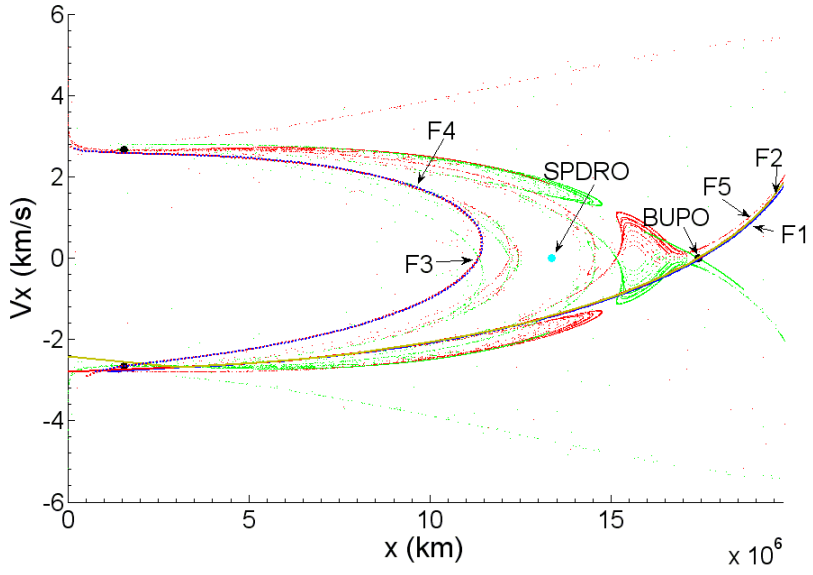

(d)

Fig. 5-7: Continuations of the F1-5 transfers at the specified energies are labeled. The stable and unstable manifolds of the BUPO at C= -1.5001, -1.4997, -1.499, and -1.496 are shown green and red, respectively. Plot (a) includes a mean FLI stability map.

Within the approximation of the CR3BP exact targeting of the stable manifold will yield an infinite capture time as the spacecraft asymptotically approaches the BUPO. Practically, orbits will never precisely follow the stable manifold due to unmodeled forces. For this reason, the area encompassed by the lobes is investigated. A single impulse F5 transfer traverses large regions encompassed by the lobes for a large energy range. For the lowest energies tested, C=-1.5001 and C=-1.4997, it is the only transfer that passes through any of appreciable size. The combination of increased lobe size and decreased relative distance among transfer families with energy provides more design options. Sizeable regions of extended capture are available to all transfer families at C=-1.499 and -1.496 and are shown in Figs. 5-7c and d.

F1, F2, and F5 transfers approach the same ΔV requirements as energy is increased. Likewise, F3 and F4 display the same behavior as was discussed in-depth in chapter 4. ΔV can be cast in terms of initial velocity of the transfer orbit, V_o, the velocity of the parking orbit, V_p, a constant, and the change in energy, ΔC.

$$\Delta V = \frac{2\Delta C}{V_o + V_p} \Rightarrow V_o^2 = V_p^2 + 2\Delta C \tag{5.6}$$

The variation of ΔV with final Jacobi constant for single impulse transfers, Fig. 5-8, is nearly identical for all cases. Each transfer starts from a unique position at a given energy. Despite this fact, ΔV is nearly identical for all transfers, because the starting Jacobi constant, thus V_o, has little variation for any position corresponding to initial conditions on a circular parking orbit. Therefore, the cost, in terms of ΔV, for each single impulse transfer to the sticky region is nearly identical.

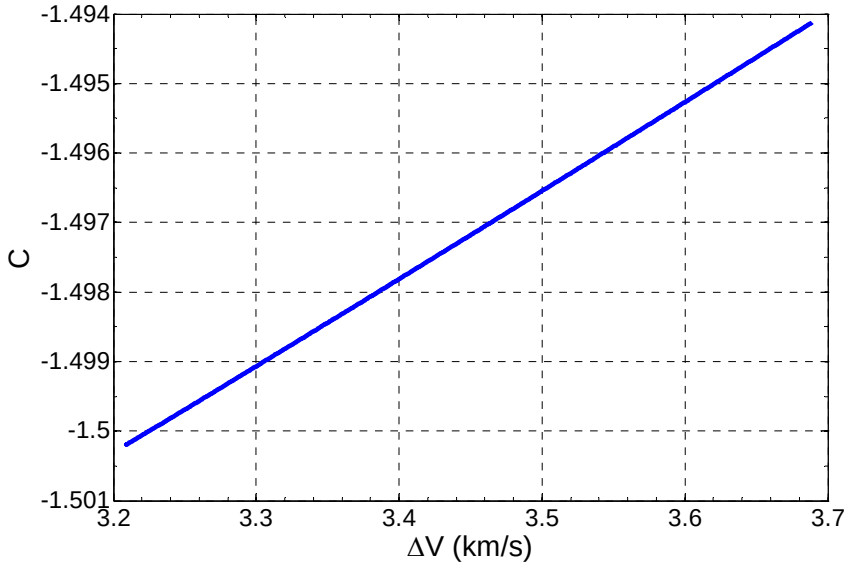

Fig. 5-8 *ΔV* versus final Jacobi constant for all single impulse transfers.

The variation of *ΔV* with *Vx* and *x*-position for each transfer family at a set energy is on the order of cm/s for all cases examined in this study. Thus, there is negligible penalty in *ΔV* for targeting the regions of extended capture. However, the transfer time displays significant variation. There is as much as a 63, 26, 29, 14, and 12% decrease from the maximum time at *C*=-1.499 for the F1-5 curves shown in Fig. 5-9a. Similar trends exist at the remaining energies. In general, the transfer time decreases with increasing *Vx*.

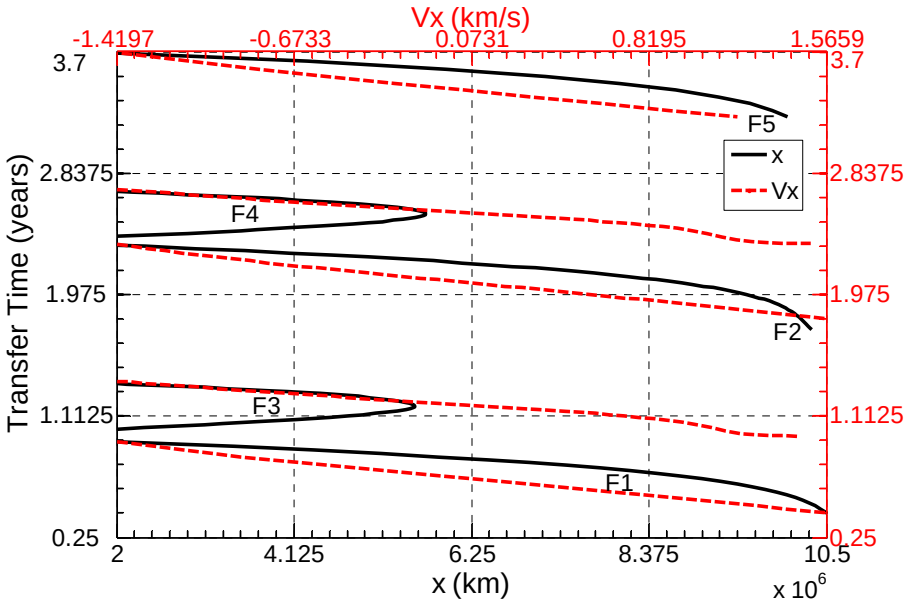

(a)

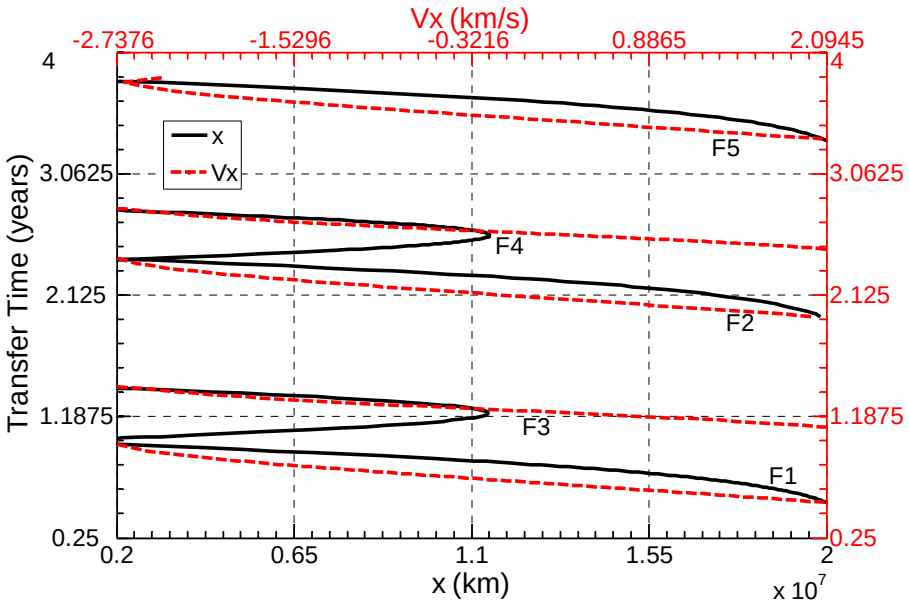

(b)

Fig. 5-9 Transfer time versus *x* (solid) and *Vx* (dotted) for single impulse transfers at (a) *C*=-1.499 and (b) *C*=-1.496.

Capture

Figure 5-10 shows capture time versus the terminal point of the transfer for selected regions near and within the lobes displayed in Fig. 5-7. At *C*=-1.5001 the minimum capture times for single impulse F5 transfers to lobe "L" are higher, by at least a few years, than transfers in the surrounding region. This capture time decreases before reaching the vicinity of the stable manifold, at approximately 1.519 M km, where the lobes stretch long distances into the surrounding space. Although capture times are longer within the lobes, they can vary significantly. The largest lobe traversed by the F5 transfer at *C*=-1.5001 extends from 1.504 to 1.515 M km along the transfer. Under the idealization of the CR3BP, the shortest capture time within this lobe is about 6 years while the longest lasts in excess of 300 years. Similar trends exist for all energies. For example, at *C*=-1.499 capture times of at least 5 years exist from approximately 5.45 to 7.35 Mkm with a maximum of nearly 100 years.

The orbits of exceptionally long capture times, off the scale of the plots, lie within small regions of phase space. Therefore, it is reasonable to assume that these orbits will be sensitive to perturbations. Realistically, a spacecraft would evolve from its nominal orbit into one possessing a lesser capture within the lobes. Ideal for spacecraft applications, large regions of extended capture orbits from 10 to 20 years exist for a wide range of energies surrounding the exceptionally persistent orbits.

The manifolds as well as the width of the lobes intersecting a single impulse F5 transfer change significantly with energy. The approximate widths of the largest lobe intersected by the F5 transfer at *C*=-1.5001 and -1.4997 are 11,000 and 4,000 km., respectively. However in both cases, a narrow target range of less than 5 m/s in *Vx* is required. Under some circumstances nature compensates with a low stability index. For instance, at *C*=-1.4997, the stability index is approximately 20. As a result, Fig. 5-10b shows that capture times of approximately ten years are

possible outside of lobes. Taken together, a transfer with a minimum capture time of slightly below ten years is possible with a target lengths in radial position and velocity of 18,725 km and 9 m/s.

By C=-1.499 large lengths of the transfer, on the order of millions of kilometers, are contained within the homoclinic tangle as its width and complexity increases with energy. This is accompanied by enlarged target ranges for Vx of over 100 m/s for the largest capture times. These characteristics also exist for C=-1.496 where inserting within ranges 0.5 M km. and 40 m/s in radial position and velocity yields a capture time of at least 12.5 years for one target region. For both C=-1.499 and -1.496 capture times above 10 years are contained exclusively within the lobes. This is due to an increase in stability index by at least two orders of magnitude compared to the previous cases. Thus, despite the short timescales for divergence from the BUPO the lobe dynamics continuously cycle the spacecraft through the region.

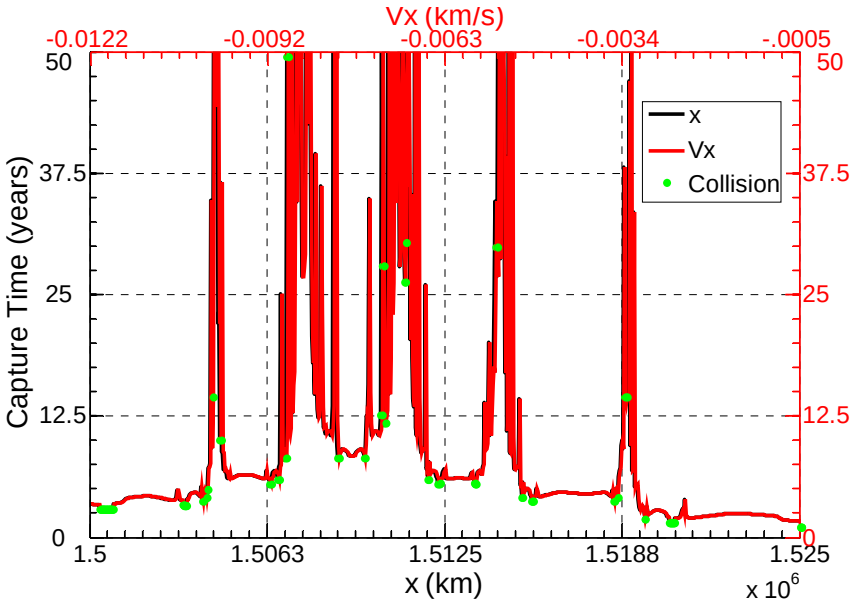
Vx (km/s)
-0.0122
-0.0092
-0.0063
-0.0034
-.0005
50
37.5
25
12.5
0
Capture Time (years)
x
Vx
Collision
1.5
1.5063
1.5125
1.5188
1.525
x (km)
x 10^6

(a)

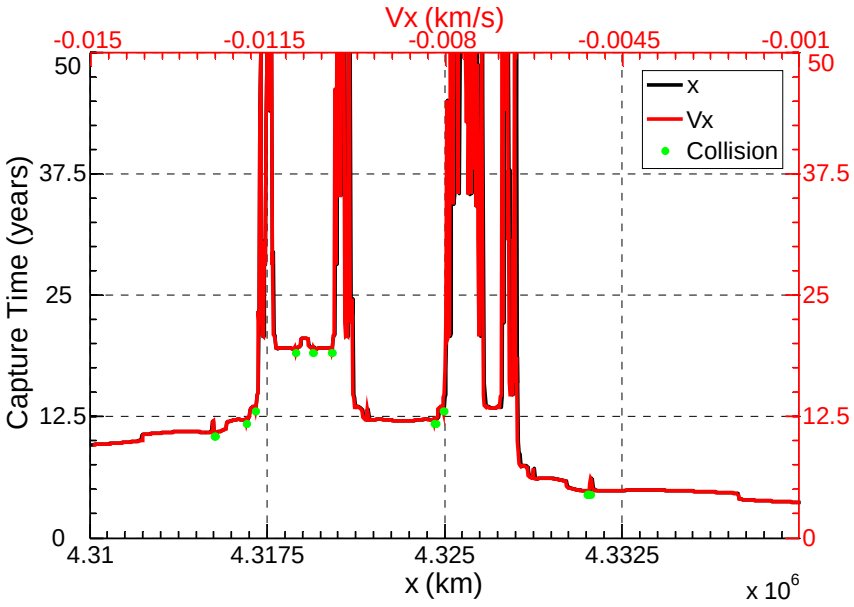
Vx (km/s)
-0.015
-0.0115
-0.008
-0.0045
-0.001
50
37.5
25
12.5
0
Capture Time (years)
x
Vx
Collision
4.31
4.3175
4.325
4.3325
x (km)
x 10^6

(b)

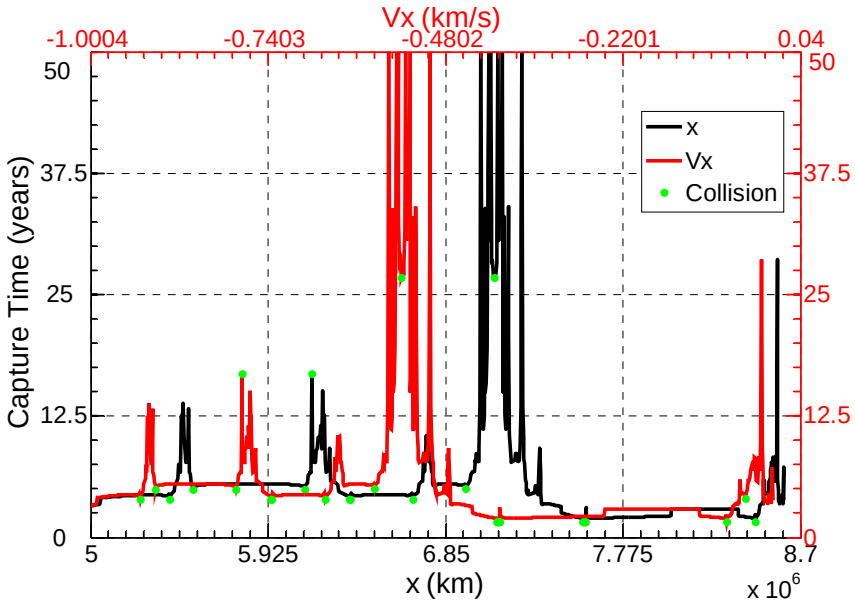

(c)

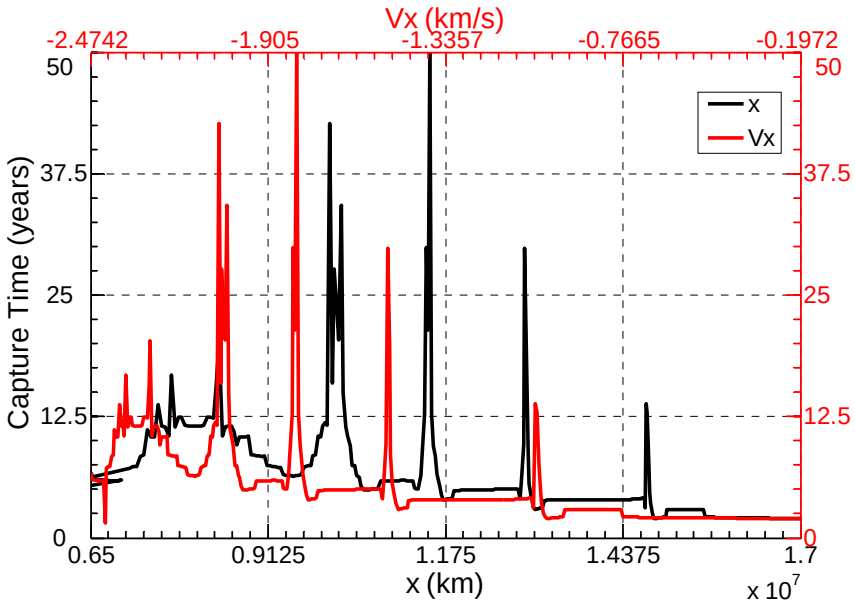

(d)

Fig. 5-10 Variation of capture time with *x*-position at *C*=-1.5001, -1.4997, -1.499, and -1.496 for F5 transfers. The simulations were terminated upon collision, indicated by the dots, or after deviating a distance of 20, 20, 30 and 40 times the radius of the Hill sphere, respectively.

All transfer families intersect sizable regions of the homoclinic tangle at larger energies.

Fig. 5-11 displays capture times for F1-4 transfers at *C*=-1.499. A comparison reveals that the F5

transfer possesses larger regions of persistent capture orbits. This is a direct result of the larger lengths of the F5 transfer crossing the lobes of the BUPO. Since the lobes generally become thinner with increasing distance from the stability zone the transfers closest to the stability region exhibit larger lengths of extended capture.

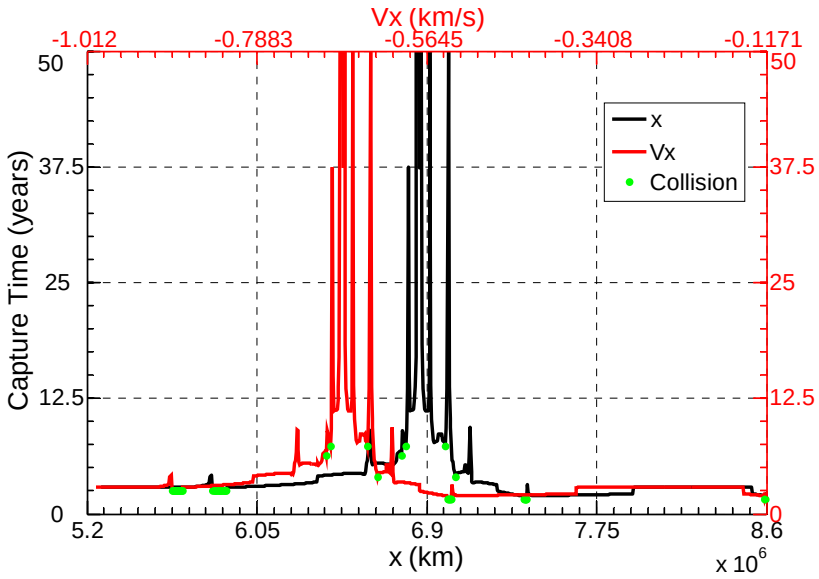

(a)

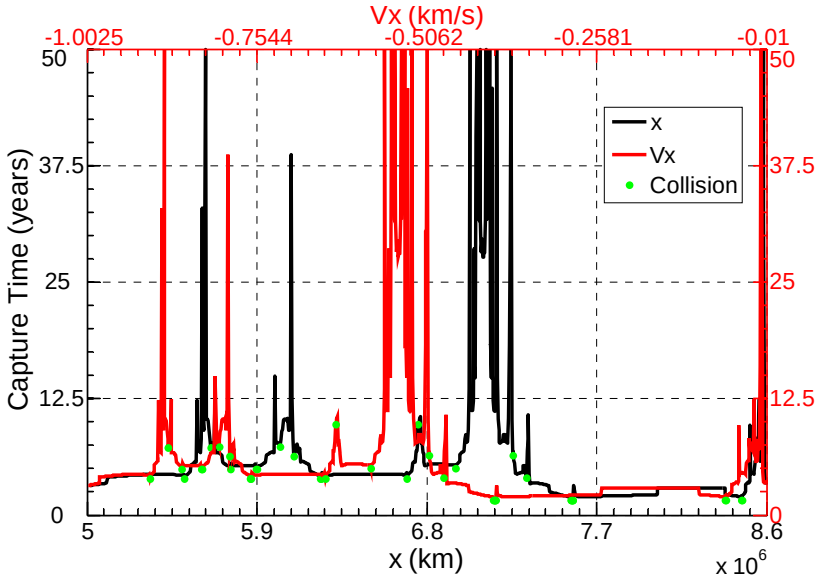

(b)

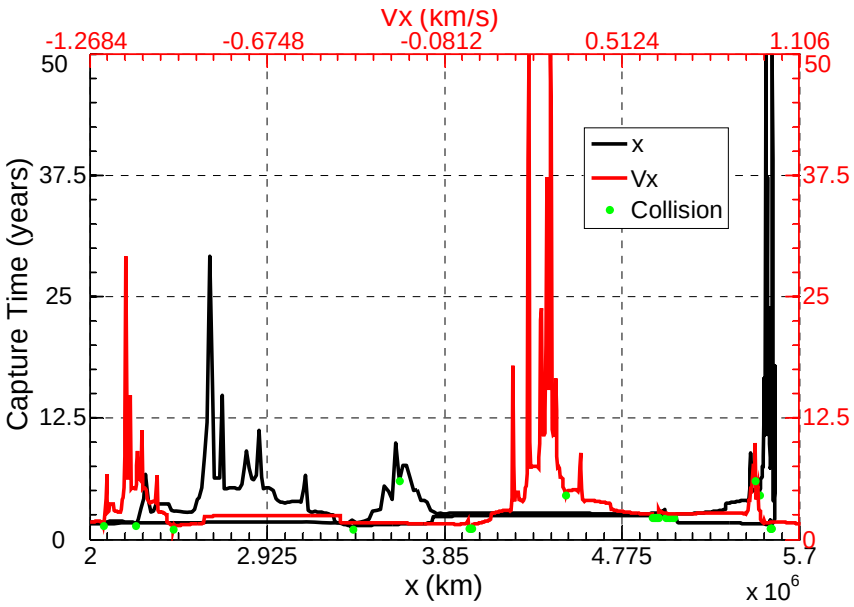

(c)

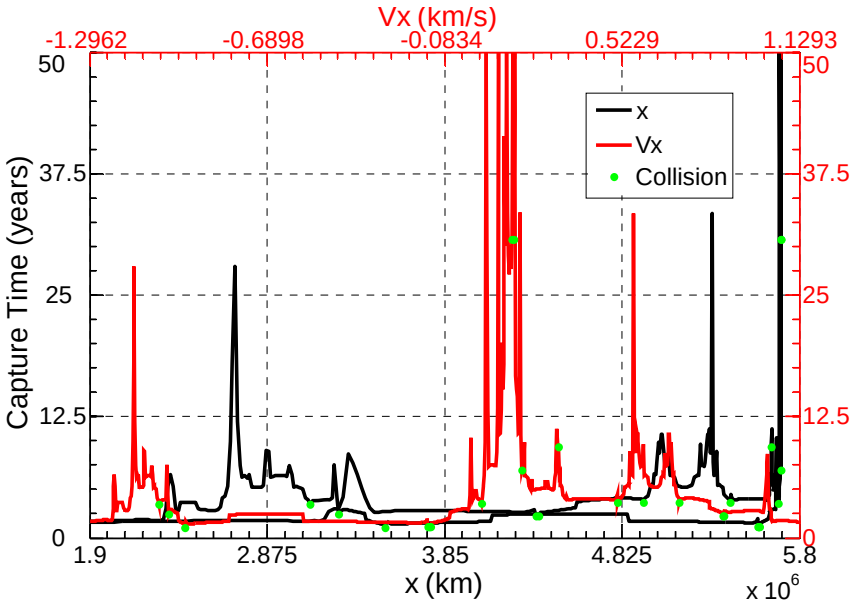

(d)

Fig. 5-11 Variation of capture time with *x*-position at *C*=-1.499 for F1-4 (a-d). The simulations were terminated upon collision, indicated by dots, or after deviating a distance 30 times the radius of the Hill sphere.

Collision orbits, indicated by the dots in Figs. 5-10 and 5-11, are concentrated in small pockets of space. Inspection of Fig. 5-4a reveals that a finite collision probability can be expected. In general, the lobes stretching along the unstable manifold of the BUPO cross bands of collision orbits on the forward map. The probability of collision appears to drop with energy as the collision bands become thinner. This conclusion is verified by the statistics given in the caption of Fig. 5-5. For the randomly generated orbits, a collision at C=-1.4997 is 55% more likely than a collision at C=-1.499. Further simulations, show that a collision at C=-1.4999 is 53% and 137% more likely than at C=-1.4997 and -1.499.

Figure 5-12 displays the approximate maximum amplitude along the Earth-sun line of captured orbits along with the boundary of the Hill sphere of the Moon and Venus as they cross the SOS. The maximum amplitude is estimated by taking the difference between points on the mapping of the BUPO.

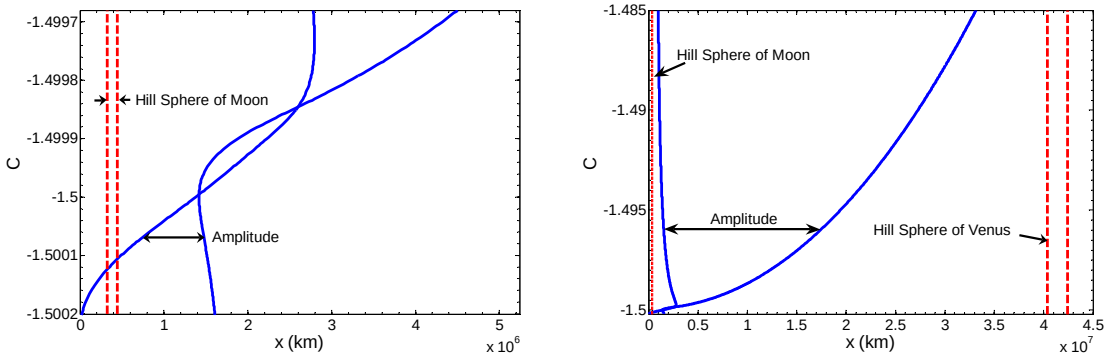

(a) (b)

Fig. 5-12 Approximate amplitude along x-axis of temporarily captures orbits with energy.

Time-dependent perturbations due to the Moon are important at the lowest energies where orbits within the stability zone repeatedly cross its orbit. The amplitude grows large with increasing energy approaching the Hill spheres of the Moon and Venus on either side. The edge

of the oscillatory region draws within 500,000 km of the Moon's Hill sphere in Fig. 5-12b. Long-term effects of fourth and fifth-body perturbations will undoubtedly effect the capture time. However, for wide ranges of energies, due to the spacecraft's distance from the nearest fourth-body, the perturbations could take years to build up leaving the fundamental results presented here intact. Moreover, another study has concluded that solar radiation pressure and the Moon's gravitational perturbation do not significantly affect QPDROs ranging from 1-2 M km. over a period of 5 years [14]. There is a possibility that the spacecraft could have a close approach to the Moon following its release from the distant retrograde region. Both the probability and outcome of such an event requires the use of a more sophisticated model, although it is likely more of a risk at lower energies.

Figure 5-13 shows examples of persistent capture orbits at a variety of energy levels. Science objectives may be achievable during the transit orbit as large segments lie within bounds defined by the amplitude of captured orbits.

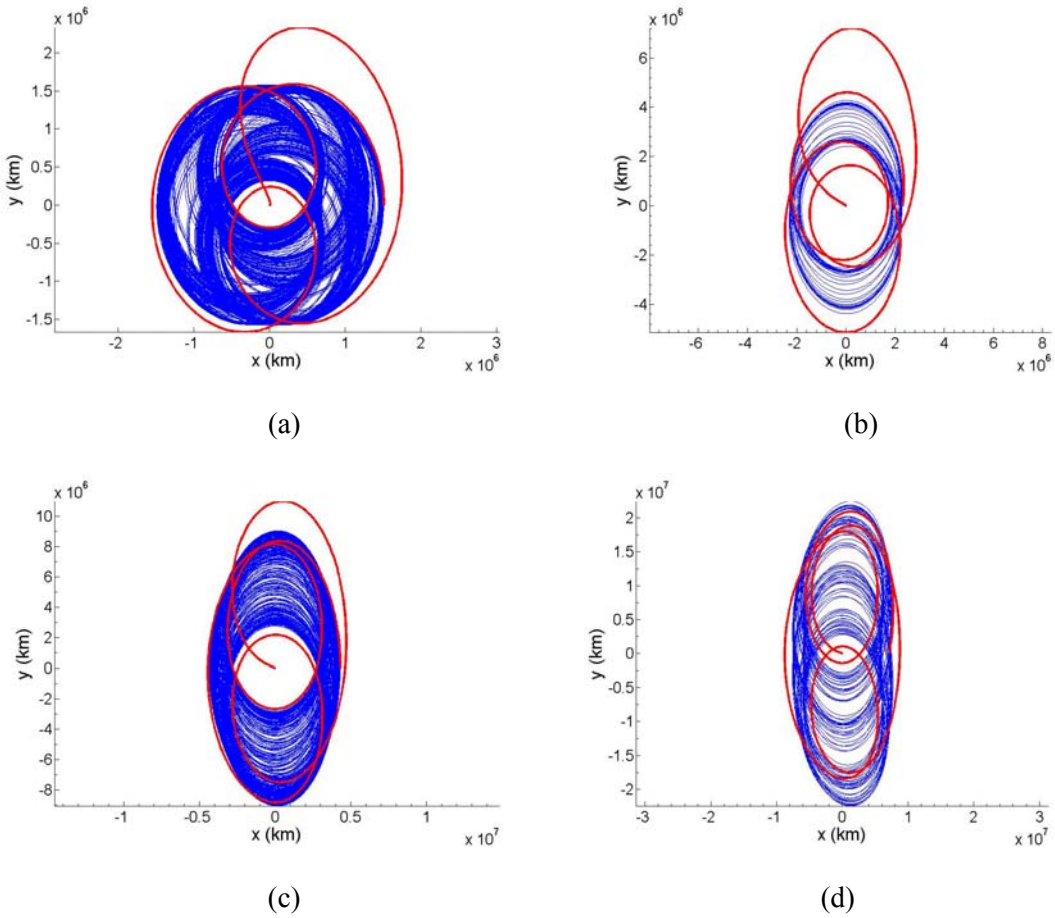

Fig. 5-13 Extended capture orbits at C=-1.5001, -1.4999, -1.4997, and -1.499 via an F5 transfer.

Stabilization Maneuver to a Quasi-Periodic Orbit

In the last chapter, two burn transfers to SPDROs were investigated. Here it is assumed that the spacecraft has little or no propulsive means to perform a second burn. For large ranges of energies a single impulse F5 transfer places the spacecraft near to the stable region within the sticky homoclinic tangle of the BUPO. The variation of ΔV with target V_x for the F5 transfer family for all energies tested is no more than a few cm/s. Given practical constraints of orbit determination and the presence of unmodeled forces this indicates that small corrective

maneuvers may be necessary during the transfer. More importantly, there is negligible penalty for inserting the spacecraft directly into an orbit which has an extended dynamical lifetime near the distant retrograde region. This allows for incremental stabilization of spacecraft via a series of small impulsive maneuvers or a low-thrust propulsion system. Here, the requirements of a single impulse stabilization maneuver is studied at the energy of the transfer and coasting orbit. This methodology can be advantageous to the two-burn methodology, presented in chapter 4, where the spacecraft would be lost in the event of an engine failure.

Figure 5-14 shows the mapping of an F5 transfer to an orbit of extended capture and the subsequent stabilization of the spacecraft near the distant retrograde region at C=-1.4997. The ΔV required to stabilize the spacecraft on the energy surface depends on its exact position and the thickness of the homoclinic tangle. In this case, a stabilizing maneuver of approximately 8 m/s is chosen to take place after the spacecraft has coasted for 2.6 years. Note the time of the final burn was arbitrarily chosen to coincide with the third crossing of the positive x-axis after the transfer. In general, this burn can be performed at any surface of section other than the x-axis. The geometry of the stable region on the surface of section must be determined before the sign of ΔV_x can be specified. This is evident on the leftmost concave border of the stability region where the sign of ΔV_x can be either positive or negative. ΔV_y is determined by the constant of motion.

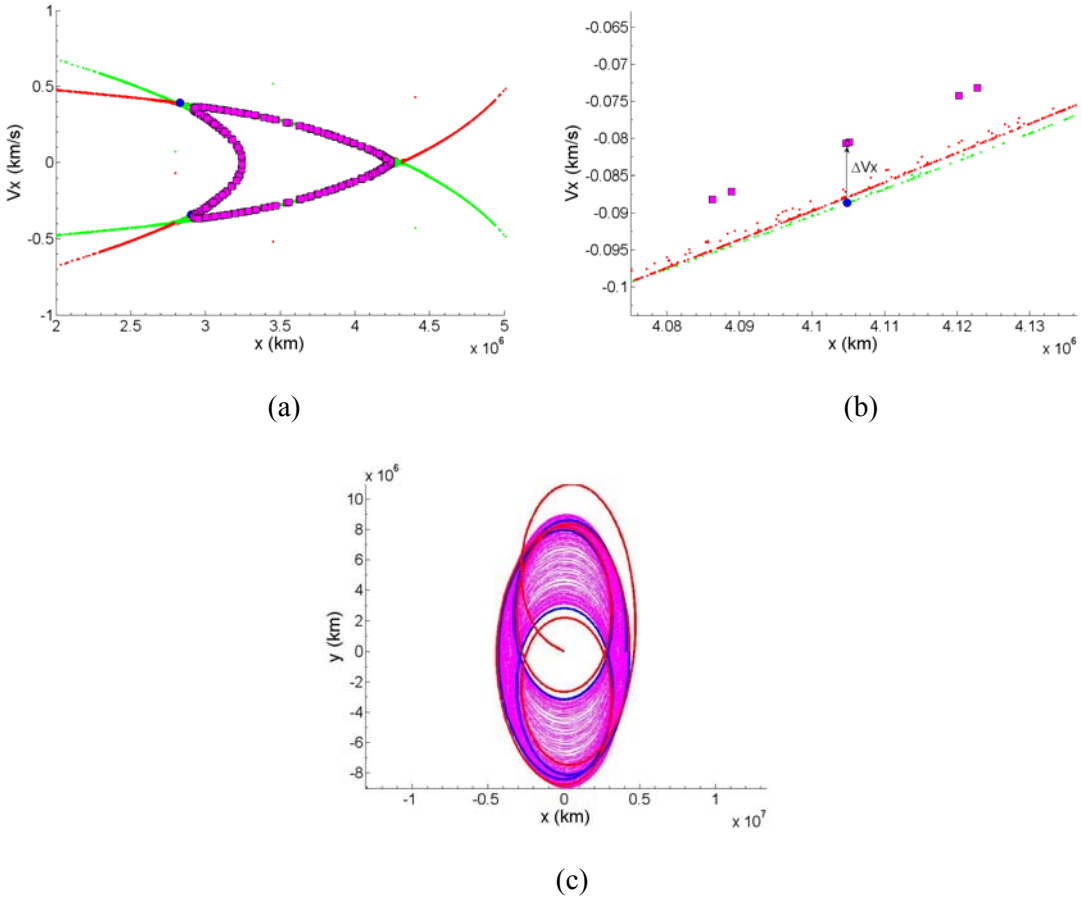

Fig. 5-14 Impulsive stabilizing maneuver at C=-1.4997. (a) Mappings of the stable and unstable manifolds of the BUPO are shown in green and red. The mapping of the coast and final orbit is indicated by circles and squares. (b) Close-up of the final maneuver point. Mappings of the stable and unstable manifolds of the BUPO are shown in green and red. (c) The transfer, coast, and final orbits in physical space are shown in red, blue, and magenta, respectively.

Similarly, Fig. 5-15 shows a stabilization maneuver of 18.7 m/s, 5.8 years after a single impulse F5 transfer at C=-1.499. In this case, at the sixth crossing of the x-axis the spacecraft is positioned favorably relative to the stable region for the second maneuver. The size of the maneuver has the potential to be much smaller for energies corresponding to thin homoclinic tangles. For instance, under the assumptions of the CR3BP a maneuver of less than 1 m/s will

stabilize a spacecraft at C=-1.4999. Inspection of Fig. 5-4a shows that an F5 maneuver must target the thin lobes stretching very near the stable manifold.

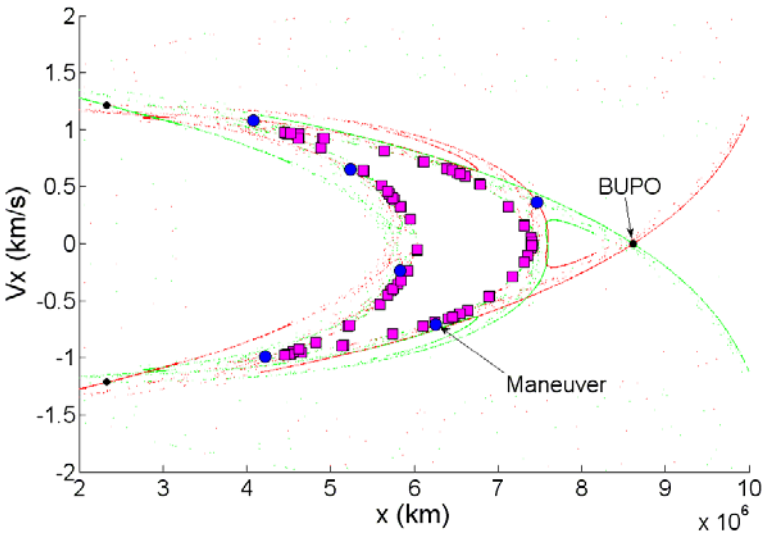

(a)

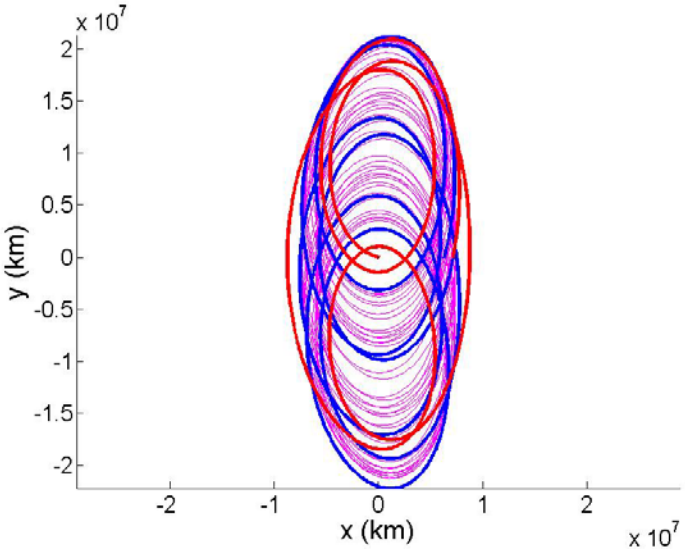

(b)

Fig. 5-15 Impulsive stabilizing maneuver at C=-1.499. (a) Mappings of the stable and unstable manifolds of the BUPO. The mapping of the coast and final orbit is indicated by the large circles and squares. (b) The transfer, coast, and final orbits in physical space are shown in red, blue, and magenta, respectively.

The size of these maneuvers can be compared with the ΔV required for the second impulsive transfer to the SPDRO, the central periodic orbit, for transfers terminating perpendicular to the x-axis in chapter 4. For these transfers, the last maneuvers to the SPDROs are approximately 44 and 127 m/s for C=-1.4997 and -1.499. A stabilizing maneuver to the fringes of the stability region translates to a ΔV savings of 82% and 85% over transfers to the central periodic orbit. Thus, if a QPDRO is acceptable to the mission considerable fuel savings can be realized.

After the initial stabilizing burn, a series of similar maneuvers can be performed to reduce the amplitude of the QPDRO or to compensate for unmodeled forces. Since the energy is kept constant, all propulsive effort is put into changing the direction of the velocity vector. This suboptimal procedure comes with negligible penalty for small modifications of the amplitude. In the first example, the velocity vector is turned only by a tenth of a degree. Application of optimal control theory may be worthwhile for large modifications of the QPDRO amplitude. Here the spacecraft would enter into an orbit of extended capture and end in a QPDRO of a greater energy after an optimal series of impulsive maneuvers. Generally, insertion into a stable QPDRO will enable the incremental modification of the orbit via series of small impulsive maneuvers or by a continuous low-thrust system.

Low-Thrust Stabilization

Just as chapter 3 showed a small force due to drag in the opposite direction of the velocity vector in the rotating frame can have a stabilizing effect in the sticky region, this section shows that a small thrust-acceleration in either direction parallel to the velocity can have an analogous effect. The notions of stable and unstable manifolds do not apply to time-dependent

systems, such as the CR3BP with a period of thrust. Therefore, the target area must be defined by some other means. This section uses primarily FLI maps to identify regions of capture for spacecraft utilizing a simple control law. Due to the short duration of the thrust segment relative to the period of escape, maps based on average velocity are less useful for this application. However, relationships similar to those derived in chapter 3 provide insight into the effects of thrust-acceleration on energy. These relationships may serve as the foundation for an optimal control algorithm, where maximizing the average velocity must be balanced with stability.

The system is time-dependent, yet the time-scales dictate that evolving structures such as those discussed in chapter 2 do not appear on these maps. Rather the effect of such evolving structures is essentially averaged over the time period. The maps provide clear discernment among permanent capture and escape regions. Both are composed of initial conditions corresponding to orbits that are on either stable or chaotic orbits.

Consider a constant, low-thrust maneuver in the direction of the velocity vector. The time-dependent equations take similar form to Eq. (3.1),

$$\begin{aligned} \ddot{x} - 2\dot{y} &= \Omega_x + H(t)a_x \\ \ddot{y} + 2\dot{x} &= \Omega_y + H(t)a_y \end{aligned} \tag{5.7}$$

where $a_x = a\,\dot{x}/v$, $a_x = a\,\dot{y}/v$, $v = \sqrt{\dot{x}^2 + \dot{y}^2}$, a is the normalized value of thrust-acceleration. $H(t)$ is the Heaviside step function,

$$H(t) = \begin{cases} 0, & t < t_1 \\ 1, & t_1 < t < t_2 \\ 0, & t > t_2 \end{cases} \tag{5.8}$$

where t_1 and t_2 mark the times at the beginning and end of the thrust segment. There is no constant of motion, yet a simple expression for the change in Jacobi constant and average velocity during the thrust segment can be derived.

$$\begin{aligned} &\frac{dC}{dt} = C_x\dot{x} + C_y\dot{y} + C_{\dot{x}}\ddot{x} + C_{\dot{y}}\ddot{y} = av \\ &\Rightarrow \Delta C := C_2 - C_1 = a\left(t_2 - t_1\right)\langle v\rangle := a\Delta t\langle v\rangle \\ &\Rightarrow \langle v\rangle = \frac{\Delta C}{a\Delta t} \end{aligned} \tag{5.9}$$

where $\langle v\rangle = \frac{1}{\Delta t}\int_{t_1}^{t_2} v\,dt$ is the average velocity of the spacecraft during thrust and, C_2 and C_1 are the Jacobi constants at the start and end of the thrust segment. Note that $\langle v\rangle > 0$. Eq. (5.9) states that the greatest change in energy occurs when the velocity is maximized. This result is comparable to a simple impulsive maneuver performed in the two-body problem. Assuming that the radial distance stays constant, a small sudden change in velocity yields the following change in energy

$$E = \frac{1}{2}V^2 - \frac{\mu}{r} \Rightarrow \delta E = V\delta V \tag{5.10}$$

where μ is the gravitational parameter; and, of course, change in two-body energy is maximized with velocity.

After transfer to the sticky distant retrograde the spacecraft may begin an extended low thrust control segment either with are against the direction of the velocity vector with respect to the rotating reference frame. Chapter 3 revealed that the geometry of the capture region extends along the stable manifold and can encompass large portions of the sticky region depending on the

drag parameter. Comparison of Figs. 5-16 and 5-10 shows the effect that a small acceleration can have on orbits within the sticky region. In this case a=-1×10^{-5} DU/TU^2 or approximately -5.9×10^{-5} mm/s^2. For a 100 kg spacecraft this amounts to approximately 5.9×10^{-3} N of thrust falling with the range of electrothermal and electrostatic propulsion systems. Realizing that this force is less than the weight of a paper clip, 9.81×10^{-3} N, on Earth's surface, reveals that it is quite small. The acceleration is two orders of magnitude greater than the acceleration due to the gravity of Moon 0.5 M km from its center of mass. At 1 and 2 M km, it is three and four orders of magnitude greater. This is consistent with the force of solar pressure on 1 m^2 of advanced, highly reflective area of solar sail at the radius of Earth's orbit, approximately 1×10^{-5} N. The build-up and relevance of unmodeled forces will depend on the geometry of the orbit and spacecraft, but certainly must be considered in future studies, especially in the case of relatively low thrust-accelerations close to a fourth-body.

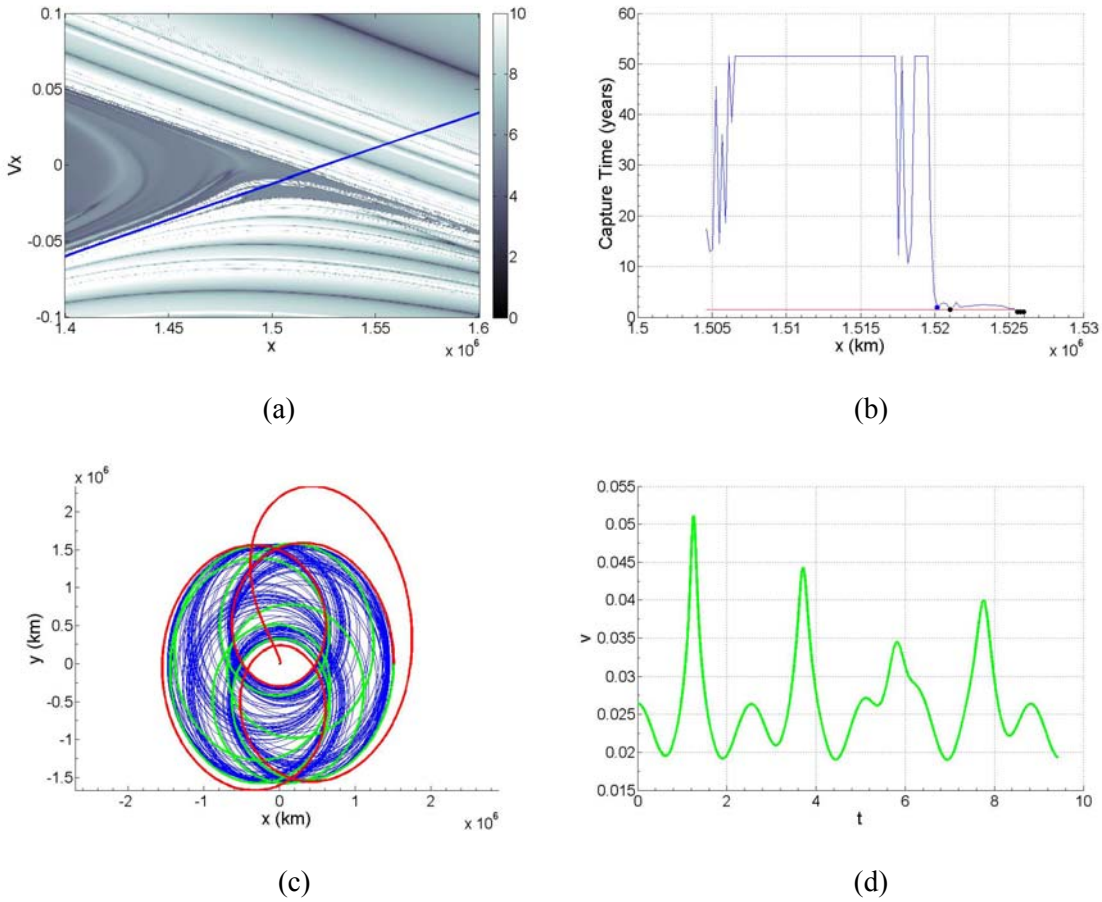

Fig. 5-16 Low-thrust stabilizing maneuver starting from C_1=-1.5001, a=-1×10^{-5}, thrust time of 1.5 years. (a) Forward FLI map with 15 year simulation after thrusting period displaying the capture and escape regions. (b) and (c) Capture time versus x position along the F5 transfer family. (d) Transfer, thrust, and capture orbits are shown in red, green and blue respectively, $\langle v \rangle = 0.026$.

The forward FLI map clearly indicates a distinct region of permanent capture beginning at approximately 1.507 M km. Also, indicated is the erratic region at approximately 1.505 M km. with capture times ranging from 15 to 45 years. This region appears as dark as the capture region, because the FLI map involves a simulation that lasts only 15 years after the thrusting period. Thus, this simple control law yields a sizeable region of permanent capture. As a consequence, capture and stabilization of spacecraft via simple control laws are robust to targeting, orbit determination, and modeling errors.

A more dramatic example, demonstrating a spiral-down transfer from C=-1.4997 to C=-1.50007, with a=-1×10^{-3} (0.59 N for a 100 kg spacecraft) is shown in Fig. 5-17d. A region of permanent capture akin to Fig. 3-16 can be identified in Fig. 5-17a. Thus, a spacecraft need not be on a stable orbit before initiating a spiral-in transfer, although any initial condition within the triangular region facilitates a stable course to permanent capture. Similar trajectories may be of use to a spacecraft requiring ballistic capture followed by an extended maneuver which both stabilizes and delivers the spacecraft closer to the second primary.

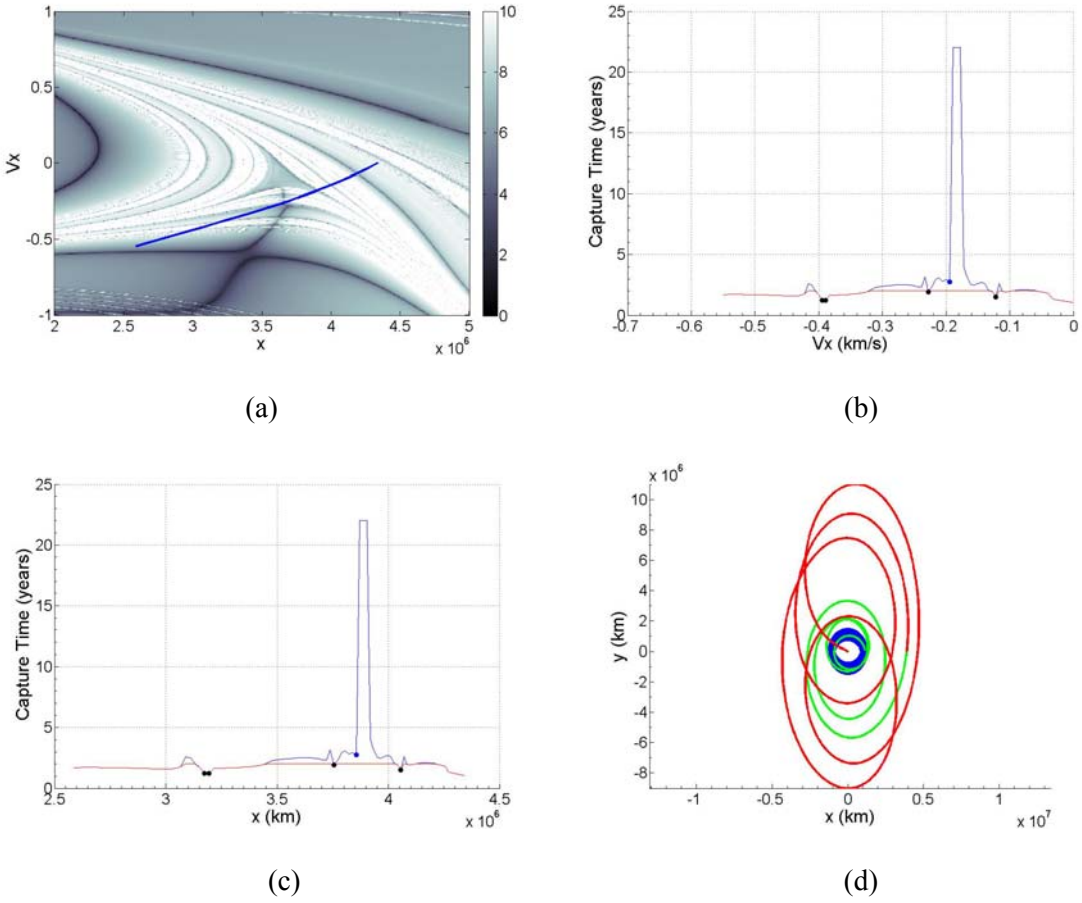

Fig. 5-17 Spiral-down transfer starting from C=-1.4997, a=-1×10^{-3}, thrust time of 2 years (a) Forward FLI map displaying the capture and escape regions. End conditions of the F5 transfer family are shown in blue. (b) and (c) Capture time versus x and Vx position along the F5 transfer family. Red and blue lines indicate the thrust and capture segments, while the dots indicate a collision orbit. (d) Typical example of transfer, thrust, and capture orbit shown in red, green and blue, respectively, $\langle v \rangle = 0.03$.

For C=-1.5001, thrusting with the direction of the velocity vector causes a rapid destabilization of the spacecraft. This is not the case for most orbits above the energy of the second crossing of the BUPO and the SPDRO due to the expansion of the stable region. Essentially the thrust must be sufficient to expand the stable region before the spacecraft escapes. At lower energies, below the first crossing of the BUPO and SPDRO, an increase in energy leads

to an erosion of the stable region via the squeeze effect. C=-1.4997 appears to be an exceptional case where thrusting both with and against the direction of the velocity vector provides stabilization. This is most likely because the thrust-acceleration can be set large enough to quickly by-pass, before escape, the energies where the BUPO and SPDRO cross. In fact, considering the geometry of the stable region with energy it is logical to predict that a much larger capture region forms when thrusting in the direction of the velocity vector. This prediction is verified in Fig. 5-18 which displays a spiral out maneuver from C=-1.4997 to -1.4994 over a period of one year. Similar maneuvers are useful to substantially increase energy, analogous to a "coiled spring", without confinement to orbits far within the stable region and escape from an orbit centered about the second primary. From here a small maneuver will provide access to other regions of the solar system along the IPS.

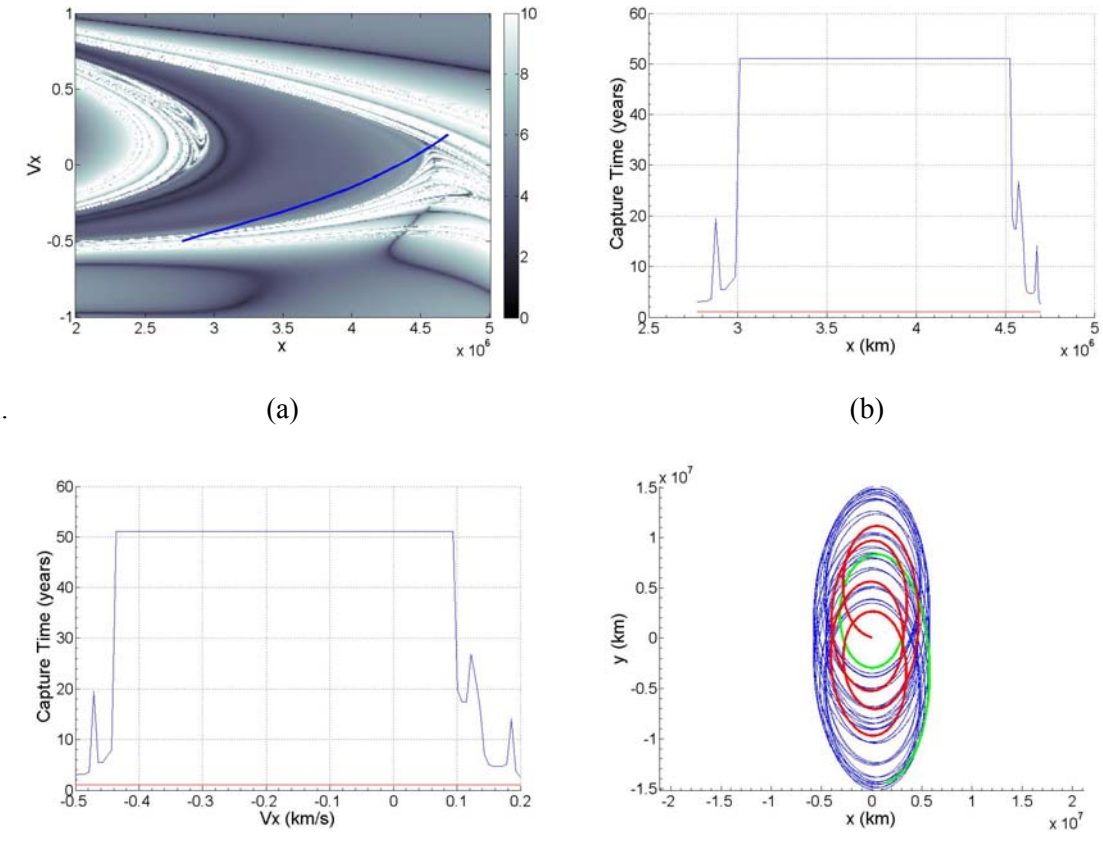

Fig. 5-18 Low-thrust stabilizing maneuver starting from C_1=-1.4997, a=1×10^{-3}, thrust time of 1 year (a) Forward FLI map displaying the capture and escape regions. End conditions of the F5 transfer family are shown in blue. (b) and (c) Capture time versus x and Vx position along the F5 transfer family. Red and blue lines indicate the thrust and capture segments, while the dots indicate a collision orbit. (zero in this case) (d) Typical example of transfer, thrust, and capture orbit shown in red, green and blue, respectively, $\langle v \rangle = 0.048$.

The magnitude of the acceleration affects not only the stability of the final orbit and the required length of thrust period, but the size of the target region. Figure 5-19 shows that reductions erode the capture/target region. The lower time rate of change of energy allows larger lengths of orbits to escape before the stable region expands by a sufficient amount.

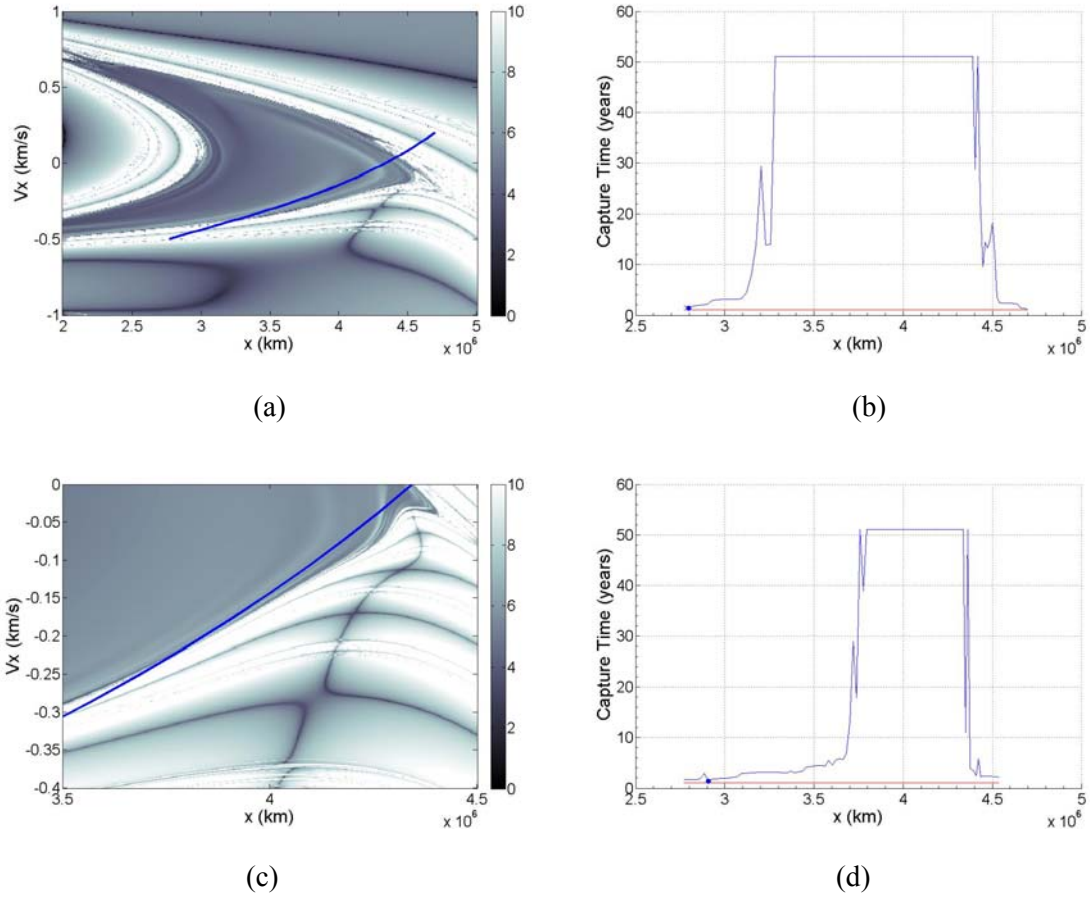

Fig. 5-19 Evolution of capture region with thrust magnitude starting from C_1=-1.4997, thrust time of 1 year, end conditions of the F5 transfer family are shown in blue. (a) and (c) Forward FLI map, where the color bar indicates the FLI values, displaying the capture and escape regions for a=5×10^{-4} and 1×10^{-4}. (b) and (c) Capture time versus x and Vx position along the F5 transfer family. Red and blue lines indicate the thrust and capture segments, while the dots indicate a collision orbit.

Figure 5-19(d) represents a set of more subtle stabilization maneuvers with a=1×10^{-4} DU/TU^2 or approximately 5.9×10^{-4} mm/s^2.

By the previous arguments, a spacecraft residing in the sticky region at energies above approximately -1.4998 can experience a stabilizing effect due to low-thrust propulsion in the

direction of the velocity vector. Fig. 5-18 shows a stabilizing maneuver at C=-1.499 with $a=5\times10^{-4}$ or approximately 3×10^{-3} mm/s^2.

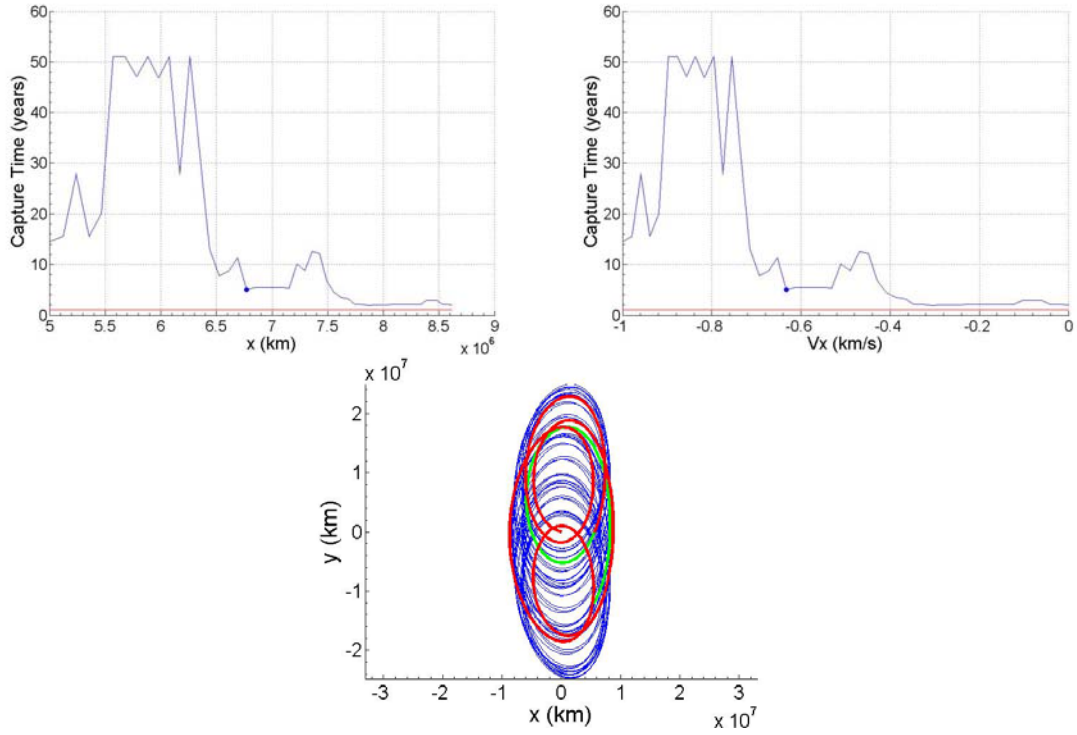

Fig. 5-20 Low-thrust stabilizing maneuver starting from C_1=-1.499, $a=5\times10^{-4}$, thrust time of 1 year. (a) and (b) Capture time versus *x* and *Vx* position along the F5 transfer family. (c) Transfer, thrust, and capture orbits are shown in red, green and blue, respectively.

Summary and Extension

This chapter entailed the development of spacecraft transfers to sticky distant retrograde orbits. Although direct transfers to sticky orbits may have been previously discovered by other means this is the first work to develop a systematic method for their construction. It follows that all of the maneuvers and resulting analyses initiated from the sticky region are new to

astrodynamics including the impulsive and low-thrust stabilization and, spiral-in and spiral-out transfers.

As in chapter 3, Monte Carlo simulations demonstrated that the manifolds of the BUPO which form lobes are the primary avenues of extended capture. Moreover, the fringes of the distant retrograde region harbor objects exhibiting the largest capture times for the range of energies tested. The analysis of chapter 3 was extended by considering the evolution of the lobes with energy and their effect on the probability of capture and collision. Additionally, the role of the stability index was investigated. For most energies capture times on the order of a decade are only achievable via capture within the lobes of the stable manifold. The exceptions are cases where the stability index reaches a relatively small value. These correspond to energies near two crossings of the BUPO and SPDRO marking the disappearance of the stability region. Nevertheless, captured objects closely follow the lobes of the BUPO for these cases. Additionally, bands of collision orbits become thinner with increasing energy reducing the collision probability of captured objects.

Prior developments provided a starting point for the continuations of the transfer families through radial velocity at a set energy. This yielded a valuable geometric description of the relationships between the transfer families and the morphology of phase space. Furthermore, the short-term fate of each transfer was predicted by its position on a SOS. Excluding energies corresponding to an exceptionally low stability index of the BUPO, at least one of the five transfer families passed through a sizeable lobe. At the highest energies tested, all transfers provided a substantial target region for extended capture within the lobes. Testing capture times along the one-dimensional curves formed by the transfer families on an SOS revealed that orbits lying within the lobes exhibited the highest capture times. However, orbits within them can display significant variations. Sizeable target regions exist within the lobes, in terms of radial position and velocity, except for energies where the BUPO possesses a relatively low stability

index. Because of the reduced timescales at these low values, capture time on the order of a decade are still achievable outside of the lobes.

Under the assumptions of the CR3BP a small stabilizing maneuver results in large ΔV savings over a direct transfer to the SPDRO. The timing of the maneuver was achieved by a visual inspection of the coast orbit on an SOS at y=0, Vx<0. As mentioned, the maneuver can take place anywhere along the coast orbit. As the spacecraft is cycled through the lobe dynamics its distance, in terms of all phase space coordinates, from the stability region will oscillate with time. Thus, there will exist optimal times in which to perform the stabilizing maneuver.

The sticky orbits were shown to be convenient staging points for low-thrust stabilization maneuvers. Simple low-thrust control of constant thrust-acceleration parallel to the velocity vector was investigated. It was shown that the efficacy of thrusting with or against the direction of the velocity vector depends on the initial energy and the evolution of the stable region with energy. An energy threshold was demonstrated near the crossings of the BUPO and SPDRO where the direction of the thrust-acceleration must be reversed for stabilization. A similar threshold most likely exists in the sun-Jupiter system marking a boundary in terms of energy where capture is impossible given a specific drag parameter. Additionally, the sticky region was shown to be convenient for initiation spiral-in and spiral-out transfers. These maneuvers may be useful for spacecraft traveling along the IPS.

The preliminary design of spacecraft trajectories, exploiting the phenomenon of sticky orbits, demonstrated promising results for future space missions in the Earth-sun system. The effects of fourth-body perturbations and other unmodeled forces remain open to investigation. A previous study has concluded that the perturbations of the Moon and solar pressure are negligible for QPDROs over a period of five years. However, planned attitude control maneuvers may have a stabilizing effect within the sticky region over a period of several years. Although transport rates can be completely described by the dynamical evolution of the lobes, the geometric

structure of the tangle is complex. The mathematical formalism available to describe the evolution of the lobes, involving many considerations such as turnstiles, self-intersection turnstiles, and multi-lobe turnstiles, may advance the concepts introduced in this study. The consolidation of techniques from optimal control theory and dynamics systems theory may be a fruitful concept. Preliminary results indicate that the application of small thrust-accelerations can dramatically extend the target region and period of capture. Important to both astrodynamics and the general satellite capture problem of dynamical astronomy, analogous orbits exist in three-dimensional space. These trajectories are relevant to transfers involving ballistic capture. Additionally, orbits out of the ecliptic plane can avoid interference by the local zodiacal cloud and may possess advantageous capture times. This chapter will serve as a foundation for analysis and design in systems characterized by higher dimension and alternate mass ratios.

References

[1] Scott, C. and Spencer, D., "Transfers to Periodic Distant Retrograde Orbits", *AIAA/AAS Astrodynamics Specialist Conference and Exhibit August 9-13, 2009, Pittsburgh, PA,* AAS 09-399.

[2] Alvarez, A. and Roig, F., "The role of the resonant "stickiness" in the dynamical evolution of Jupiter family comets", *Dynamics of Populations of Planetary Systems Proceedings IAU Colloquium*, No. 197, 2005.

[3] Malyshkin, L. and Tremaine, S., "The Keplerian Map for the Planar Restricted Three-Body Problem as a Model of Comet Evolution", *Icarus*, Vol. 141, 1999, pp. 341-353.

[4] Hénon, M., "Numerical Exploration of the Restricted Problem. VI. Hill's Case: Non-Periodic Orbits", *Astronomy and oAstrophysics*, Vol. 9, pp. 24-36, 1970.

[5] Scott, C. and Spencer, D., "Stability Mapping of Distant Retrograde Orbits and Transport in the Circular Restricted Three-Body Problem", *AIAA/AAS Astrodynamics Specialist Conference and Exhibit, August 18-21, 2008, Honolulu, HI*, AIAA 2008-6431.

[6] Dunham, D., "Astrodynamics-Natural Trajectories", *Space for Peace and Progress, 41st International Astronautical Congress, Dresden Germany, October 1990*.

[7] Koon, W., Lo, M., Marden, J., and Ross, S., "Heteroclinic connections between periodic orbits and resonance transitions in celestial mechanics", *Chaos*, Vol. 10, No. 2, 2000, pp. 427-469.

[8] Dellnitz, M., Junge, O., Koon, W., Lekien, F., Lo, M., Marsden, J., Padberg, K., Preis, R., Ross, S., and Thiere, B., "Transport in Dynamical Astronomy and Multibody Problems", *Chaos*, Vol. 15, No. 3, pp.699-727, 2005.

[9] Wiggins, S., *Introduction to Applied Nonlinear Dynamical Systems and Chaos*, Springer-Verlag, New York, 1990.

[10] Astakhov, S., Burbanks, A., Wiggins, S., and Farrely, D., "Chaos-Assisted Capture of Irregular Moons, *Nature*, Vol. 423, 2003.

[11] Astakhov, S., Burbanks, A., Wiggins, S. and Farrely, D., "Dynamics of Capture in the Restricted Three-Body Problem," *Order and Chaos in Stellar and Planetary Systems, ASP Conference Series*, Vol. 316, 2004.

[12] Astakhov, S. and Farrely, D., "Capture and Escape in the Elliptic Restricted Three-Body Problem," *Monthly Notices of the Royal Astronomical Society*, Vol. 354, pp. 971-979, 2004.

[13] Van Der Weele, J.P., Capel, H.W., Valkering, T.P., and Post, T., "The Squeeze Effect in Non-Integrable Hamiltonian Systems", *Physica A*, Vol. 147A, pp. 499-532, 1988.

[14] Gurfi, P. and Kasdin, N., "Practical Deep-Space Geocentric and Out-of-Ecliptic Orbits in the Sun-Earth Restricted Three-Body Problem", *Proceedings of SPIE*, Vol. 4854, 2003.

[15] Shadden, S.C., Lekien, F., and Marsden, J. E., “Definition and properties of Lagrangian coherent structures from finite-time Lyapunov exponents in two-dimensional aperiodic flows”, Physica D, Vol. 212, pp. 271-304, 2005.

Chapter 6

Conclusion

This dissertation identified the dynamical processes responsible for the placement of irregular satellites in the outer solar system. Essentially, a better understanding of the complex phenomena was achieved by reducing the problem to the relatively simple model of the circular restricted three-body problem. This model was demonstrated to contain the underpinnings of the dynamical phenomena associated with the capture of irregular satellites. Since these mechanisms are not unique to mass ratios corresponding to the outer planets, they have applications on human timescales for hypothetical spacecraft within the sun-Earth and the many moon-planet systems. Their identification facilitated the development of new techniques for analysis of capture phenomenon in the outer solar system and the construction and analysis of new spacecraft transfers and orbits. As a result, chapters 3-5 constitute original works in the fields of celestial mechanics and astrodynamics.

Each chapter addressed topics related to the dynamics of distant retrograde orbits lying within the bottleneck of the energy manifold. The philosophy was adopted that the fields of astrodynamics and celestial mechanics can not only be developed in parallel, but the same techniques for analysis can be utilized. The chapters were presented sequentially corresponding to the time of development. Therefore, it follows that the results of one chapter are intimately related to the others.

For example, the regions of collisions may be followed in a manner similar to the construction of transfer trajectories in chapter 4. Applied to the sun-Jupiter system they would facilitate the calculation of collision probabilities without random sampling. Chapter 4 also presented an automated method in order to identify families of unique transfer trajectories. These

correspond to distinctive paths resulting in collision with secondary body. Perhaps further analysis of known collisions, such as Shoemaker-Levy 9, will closely resemble a trajectory along a family of collision orbits. Similarly, the connections responsible for the transport of celestial bodies among resonant islands may be useful for spacecraft traveling within the Jovian or Saturnian systems.

The detailed evolution of the structures and associated parameters responsible for capture in the sun-Earth system was presented in chapter 5. The same analysis could be performed in the sun-Jupiter system in order to illuminate the relationship among evolving phase space structures with capture probability and the energy threshold of capture. The continuation algorithms of chapter 4 could yield orientations for families of insertion orbits, bound for the sticky orbits of chapter 5, with larger target areas and shorter transfer times. Moreover, major classes of transfer orbits still await analysis for applications in both chapter 4 and 5. These concepts have application to ballistic capture orbits, much like the one followed by Japan's Hiten spacecraft.

The results of this dissertation provide the foundation for analysis in the three-dimensions and more complex versions of the restricted problem. The utilization of presented tools and future analytical work, such as averaging, will facilitate analysis of time-dependent perturbations. The three-dimensional problem adds two additional phase space dimensions. A focus on particular hyper-planes or a change to canonical coordinates would constitute the first steps to dealing with greater dimensionality. A patching of the structures investigated in this dissertation with the IPS would yield efficient transfer and capture orbits for spacecraft traveling among three-body systems. Ultimately, the developments presented here will act as the framework for interpretation for systems of greater complexity.

A consolidation of optimal control and dynamical systems theory will provide a detailed understanding of favorable trajectories. A dynamical analysis could provide an accurate guess for an optimal control algorithm. The resulting transfer, not attainable by the use of dynamical

systems theory alone, would be understood in the context of phase space structure. For instance, by chapter 5, one could reasonably predict, for the stabilization of a spacecraft on sticky orbit, that an optimal control algorithm would maximize thrust with the magnitude of velocity. The direction of this thrust would, of course, depend on the evolution of the stable region with energy. The future value of multidisciplinary effort on these challenging problems can not be overstated.

Appendix

Chapter 4 Variables

Predictor-Corrector for Variable Parking Orbit Altitudes

$$V = \begin{bmatrix} \Phi_{11}D_1 + \Phi_{12} + \Phi_{13}C^*_{R1} + \dot{x}_1 A_{R1} & \Phi_{13}C^*_{R2} + \Phi_{14} + \dot{x}_1 A_{R2} & \Phi_{11}D_2 + \Phi_{13}C^*_{R3} + \dot{x}_1 A_{R3} \\ \Phi_{31}D_1 + \Phi_{32} + \Phi_{33}C^*_{R1} + \ddot{x}_1 A_{R1} & \Phi_{33}C^*_{R2} + \Phi_{34} + \ddot{x}_1 A_{R2} & \Phi_{31}D_2 + \Phi_{33}C^*_{R3} + \ddot{x}_1 A_{R3} \end{bmatrix} \tag{A.1}$$

$$\begin{aligned} A_{R1} &= -\frac{\Phi_{21}}{\dot{y}_1}D_1 - \frac{\Phi_{22}}{\dot{y}_1} - \frac{\Phi_{23}}{\dot{y}_1}C^*_{R1} \quad A_{R2} = -\frac{\Phi_{23}}{\dot{y}_1}C^*_{R2} - \frac{\Phi_{24}}{\dot{y}_1} \\ A_{R3} &= -\frac{\Phi_{21}}{\dot{y}_1}D_2 - \frac{\Phi_{23}}{\dot{y}_1}C^*_{R3} \end{aligned} \tag{A.2}$$

Predictor-Corrector for Variable Insertion Points

Algorithm A.

$$T = \begin{bmatrix} \Phi_{11}D_1 + \Phi_{12} + \Phi_{13}E_1 & \Phi_{13}E_2 + \Phi_{14} & \dot{x}_1 & \Phi_{11}D_2 + \Phi_{13}E_3 \\ \Phi_{21}D_1 + \Phi_{22} + \Phi_{23}E_1 & \Phi_{23}E_2 + \Phi_{24} & \dot{y}_1 & \Phi_{21}D_2 + \Phi_{23}E_3 \\ \Phi_{31}D_1 + \Phi_{32} + \Phi_{33}E_1 & \Phi_{33}E_2 + \Phi_{34} & \ddot{x}_1 & \Phi_{31}D_2 + \Phi_{33}E_3 \\ \Phi_{41}D_1 + \Phi_{42} + \Phi_{43}E_1 & \Phi_{43}E_2 + \Phi_{44} & \ddot{y}_1 & \Phi_{41}D_2 + \Phi_{43}E_3 \end{bmatrix} \tag{A.3}$$

$$U_1 = T_{31} + \frac{B_2}{B_1}T_{41} \quad U_2 = T_{32} + \frac{B_2}{B_1}T_{42} \quad U_3 = T_{33} + \frac{B_2}{B_1}T_{43} \tag{A.4}$$

$$A_1 = \frac{-y_1\left(x_1+1-\mu\right)}{r_{2f}^3} \quad A_2 = \frac{1}{r_{2f}} - \frac{y_1^2}{r_{2f}^3} \tag{A.5}$$

$$B_1 = \frac{1}{v_1} - \frac{\dot{x}^2}{v_1^3} \quad B_2 = -\frac{\dot{x}_1\dot{y}_1}{v_1^3} \tag{A.6}$$

$$E_1 = C_1D_1 + C_2 \quad E_2 = C_3 \quad E_3 = C_1D_2 + C_4 \tag{A.7}$$

$$\delta y_1 = A^* = \frac{-\frac{A_1F_2}{A_2} + \frac{\delta CA}{A_2}}{1+\frac{A_1F_1}{A_2}} \tag{A.8}$$

$$\delta x_1 = F_1A^* + F_2 \tag{A.9}$$

Algorithm B. The final directions of the radius and velocity vectors are specified by two angles α_f and β_f, where $\hat{r}_{2f}\cdot\hat{i} = \cos\alpha_f$ and $\hat{v}_f\cdot\hat{j} = \cos\beta_f'$. $\hat{v}_f\cdot\hat{i} = \cos\beta_f$. Based on the time series the magnitude of the final radius is specified by $r_{2f} = \sqrt{\left(x_1+1-\mu\right)^2 + y_1^2}$. The three linear constraints on the final state vector become: $\delta x_1 = -A_2'/A_1'\,\delta y_1 + \delta CA/A_1'$, $\delta\dot{y}_1 = -B_1'/B_2'\,\delta\dot{x}_1 + \delta CB/B_2'$, and $\delta y_1 = \left[-\left(x_1+1-\mu\right)/y_1\right]\delta x_1 + \delta RS_1/\left(2y_1\right) := F_1'\delta x_1 + F_2'$ where $\delta CA = \delta\left(\cos\alpha_f\right)$, $\delta CB = \delta\left(\cos\beta_f'\right)$, and $\delta RS_1 = \delta\left(r_{2f}^2\right)$.

$$T' = \begin{bmatrix} \Phi_{11}D_1' + \Phi_{12} + \Phi_{13}E_1' & \Phi_{13}E_2' + \Phi_{14} & \dot{x}_1 & \Phi_{11}D_2' + \Phi_{13}E_3' \\ \Phi_{21}D_1' + \Phi_{22} + \Phi_{23}E_1' & \Phi_{23}E_2' + \Phi_{24} & \dot{y}_1 & \Phi_{21}D_2' + \Phi_{23}E_3' \\ \Phi_{31}D_1' + \Phi_{32} + \Phi_{33}E_1' & \Phi_{33}E_2' + \Phi_{34} & \ddot{x}_1 & \Phi_{31}D_2' + \Phi_{33}E_3' \\ \Phi_{41}D_1' + \Phi_{42} + \Phi_{43}E_1' & \Phi_{43}E_2' + \Phi_{44} & \ddot{y}_1 & \Phi_{41}D_2' + \Phi_{43}E_3' \end{bmatrix} \tag{A.10}$$

$$U_1' = T_{41} + \frac{B_1}{B_2} T_{31} \quad U_2' = T_{42} + \frac{B_1}{B_2} T_{32} \quad U_3' = T_{43} + \frac{B_1}{B_2} T_{33} \tag{A.11}$$

$$A_1' = \frac{1}{r_{2f}} - \frac{\left(x_1 + 1 - \mu\right)^2}{r_{2f}^3} \quad A_2' = -\frac{y_1 \left(x_1 + 1 - \mu\right)^2}{r_{2f}^3} \tag{A.12}$$

$$B_1' = -\frac{\dot{x}_1 \dot{y}_1}{v_1^3} \quad B_2' = \frac{1}{v_1} - \frac{\dot{y}_1^2}{v_1^3} \tag{A.13}$$

$$E_1' = C_1' + C_2' D_1 \quad E_2' = C_3' \quad E_3' = C_2' D_2 + C_4' \tag{A.14}$$

$$C_1' = -\frac{\dot{x}_o}{y_o} \quad C_2' = -\frac{\dot{y}_o}{y_o} \quad C_3' = -\frac{x_o + 1 - \mu}{y_o} \quad C_4' = \frac{\Delta DP}{y_o} \tag{A.15}$$

$$\delta x_1 = A'^* = \frac{-\frac{A_2' F_2'}{A_1'} + \frac{\delta CA}{A_1'}}{1 + \frac{A_2' F_1'}{A_1'}} \tag{A.16}$$

$$\delta x_1 = F_1' A'^* + F_2' \tag{A.17}$$

Chapter 5 Variables

$$R_1 = -\frac{C_{x_o}}{C_{x_o}} \quad R_2 = -\frac{C_{y_o}}{C_{x_o}} \quad R_3 = -\frac{C_{\dot{x}_o}}{C_{x_o}} \quad R_4 = \frac{\delta C}{C_{x_o}} \quad \delta C = -\left(C_o - C_{xfer}\right) \tag{A.18}$$

$$C_1 = -\frac{\dot{x}_o}{(x_o + 1 - \mu)} \quad C_2 = -\frac{\dot{y}_o}{(x_o + 1 - \mu)} \quad C_3 = -\frac{y_o}{(x_o + 1 - \mu)} \quad C_4 = \frac{\Delta DP}{(x_o + 1 - \mu)} \tag{A.19}$$
$$\Delta DP = -(\mathbf{r}_{2o} \cdot \mathbf{v}_{2o})$$

$$D_1 = -\frac{y_o}{(x_o + 1 - \mu)} \quad D_2 = \frac{\delta(h_p + R_\oplus)^2}{2(x_o + 1 - \mu)} \tag{A.20}$$

where $\mathbf{r}_{2o}$, $\mathbf{v}_{2o}$ are the current radius and velocity with respect to the Earth. C_o and C_{xfer} are the current and desired Jacobi constant of the transfer orbit.

$$C_1^* = \frac{C_1 + C_3 R_1}{1 - C_3 R_3} \quad C_2^* = \frac{C_2 + C_3 R_2}{1 - C_3 R_3} \quad C_3^* = \frac{C_3 R_4 + C_4}{1 - C_3 R_3} \tag{A.21}$$

$$\begin{aligned} T_1 &= \Phi_{31} - \frac{\ddot{x}_1 \Phi_{21}}{\dot{y}_1} \quad T_2 = \Phi_{32} - \frac{\ddot{x}_1 \Phi_{22}}{\dot{y}_1} \\ T_3 &= \Phi_{33} - \frac{\ddot{x}_1 \Phi_{23}}{\dot{y}_1} \quad T_4 = \Phi_{34} - \frac{\ddot{x}_1 \Phi_{24}}{\dot{y}_1} \end{aligned} \tag{A.22}$$

$$\begin{aligned} U_1 &= T_1 + T_4 R_1 \quad U_2 = T_2 + T_4 R_2 \\ U_3 &= T_3 + T_4 R_3 \quad U_4 = T_4 R_4 \end{aligned} \tag{A.23}$$

$$V_1 = U_1 + U_3 C_1^* \quad V_2 = U_2 + U_3 C_2^* \quad V_3 = U_4 + U_3 C_3^* \tag{A.24}$$

VITA

Christopher James Scott

Christopher was born in Altoona, Pennsylvania on June 28, 1981. He and his brother, Justin D. Scott, sons of James and Elizabeth Scott, were raised in the village of Glasgow, Pennsylvania. After receiving his diploma from Glendale Jr./Sr. High School in 1999, he earned a Bachelor of Science degree in Aerospace Engineering with highest distinction and honors from the Pennsylvania State University in 2003. As an undergraduate he was awarded a number of scholarships including the Donald G. and Jayne L. Steva Scholarship in Aerospace Engineering. In the summer of 2004 he participated in the Space Scholars Program at the Air Force Research Laboratory in Albuquerque, New Mexico conducting research on satellite formation flying. He was awarded the National Defense Science and Engineering Graduate Fellowship the same year. In 2005, he received his Master of Science degree in Aerospace Engineering from the Pennsylvania State University before admission as a Ph.D. candidate. He received fellowships multiple times from the Pennsylvania State University's College of Engineering Recruitment Fund and won the Pennsylvania Space Grant Consortium Graduate Fellowship in 2007. In the summer of 2008 he worked with the Precision Formation Flying Control team at the Jet Propulsion Laboratory. At the 2009 AAS/AIAA Astrodynamics Specialist Conference in Pittsburgh, Pennsylvania he was selected for the John V. Breakwell Student Travel Award. Throughout his graduate studies he has served as a teaching assistant for number of courses including orbit and attitude control of spacecraft, spacecraft design, space science and technology, space propulsion, and astronautics. He serves as a reviewer for the Journal of Guidance, Control, and Dynamics. His research interests include formation flying and the application of dynamical systems and optimal control theory to spacecraft dynamics and control.